TU Delft

Delft University of Technology

Spiraling Towards Understanding In Vitro Min Protein Surface Patterns

Meindlhumer, S.

DOI
10.4233/uuid:a8ae3d6f-17f6-4d40-8374-1eaffbf18879

Publication date
2024

Document Version
Final published version

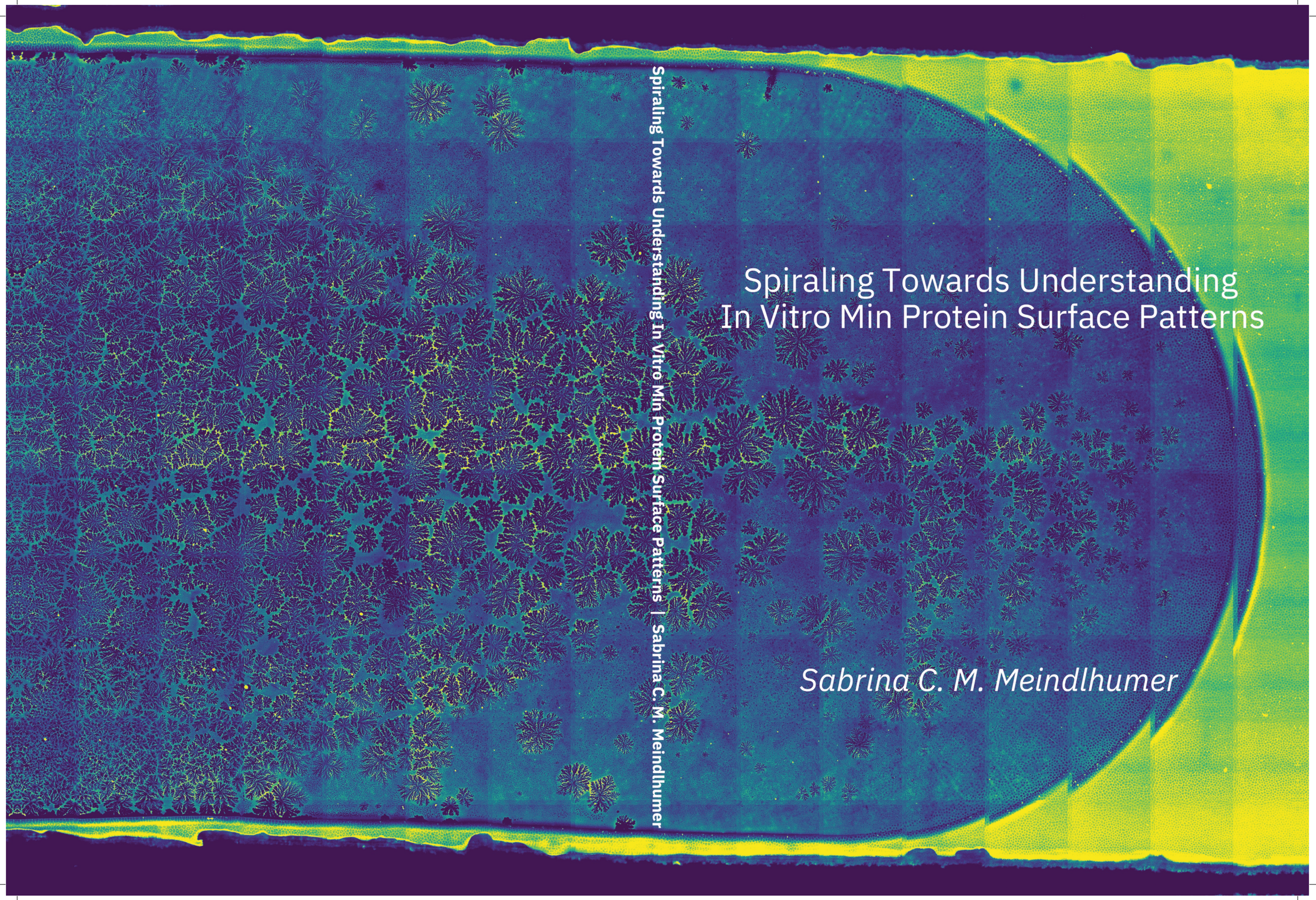
Citation (APA)
Meindlhumer, S. (2024). *Spiraling Towards Understanding In Vitro Min Protein Surface Patterns*. [Dissertation (TU Delft), Delft University of Technology]. https://doi.org/10.4233/uuid:a8ae3d6f-17f6-4d40-8374-1eaffbf18879

Important note
To cite this publication, please use the final published version (if applicable).
Please check the document version above.

Copyright
Other than for strictly personal use, it is not permitted to download, forward or distribute the text or part of it, without the consent of the author(s) and/or copyright holder(s), unless the work is under an open content license such as Creative Commons.

Takedown policy
Please contact us and provide details if you believe this document breaches copyrights.
We will remove access to the work immediately and investigate your claim.

This work is downloaded from Delft University of Technology.
For technical reasons the number of authors shown on this cover page is limited to a maximum of 10.



Spiraling Towards Understanding In Vitro Min Protein Surface Patterns | Sabrina C. M. Meindlhumer

Spiraling Towards Understanding In Vitro Min Protein Surface Patterns

Sabrina C. M. Meindlhumer

SPIRALING TOWARDS UNDERSTANDING IN VITRO MIN PROTEIN SURFACE PATTERNS

SPIRALING TOWARDS UNDERSTANDING IN VITRO MIN PROTEIN SURFACE PATTERNS

Dissertation

for the purpose of obtaining the degree of doctor
at Delft University of Technology
by the authority of the Rector Magnificus Prof.dr.ir. T.H.J.J. van der Hagen
chair of the Board for Doctorates
to be defended publicly on
Wednesday 11th September 2024 at 17:30 o'clock

by

Sabrina Christina Michaela MEINDLHUMER

Diplom-Ingenieurin in Biophysics,
Johannes Kepler Universität, Linz, Austria,
born in Linz, Austria.

This dissertation has been approved by the promotors.

Composition of the doctoral committee:

Rector Magnificus,	chairperson
Prof.dr. C. Dekker,	Delft University of Technology, promotor
Prof.dr. A.M. Dogterom,	Delft University of Technology, promotor
Independent members:	
Dr.ir. L. Laan,	Delft University of Technology
Prof.dr. M. Loose,	Institute of Science and Technology Austria
Prof.dr. S.J. Tans,	Delft University of Technology
Dr. J.W. Zwanikken,	Delft University of Technology
Prof.dr.ir. S.J.J. Brouns,	Delft University of Technology, reserve member
Other members:	
Prof.dr. E. Frey,	Ludwig Maximilian University of Munich, Germany

Keywords: biophysics; pattern formation; surface patterns; in vitro; Min protein

Printed by: Proefschriftspecialist

Style: TU Delft House Style, with modifications by S. Meindlhumer

Cover: Tile-stitched fluorescence microscope image of static Min patterns on a supported lipid bilayer, which is gradually being damaged by an air bubble moving further into the flow channel.

Copyright © 2024 by S. Meindlhumer

ISBN 978-94-6384-622-6

An electronic version of this dissertation is available at
`http://repository.tudelft.nl/`.

To all the failed experiments:
You paved the way.

CONTENTS

Summary xi

Samenvatting xiii

Zusammenfassung xv

1 Introduction 1
- 1.1 Patterns across scales . . . 2
  - 1.1.1 Fundamental mechanisms and terminology . . . 2
  - 1.1.2 Turing patterns . . . 4
  - 1.1.3 Studying biological pattern formation . . . 5
  - 1.1.4 Intracellular pattern formation . . . 7
- 1.2 Min protein pattern formation . . . 9
  - 1.2.1 Discovery and fundamentals of modeling . . . 9
  - 1.2.2 In vivo and in vitro studies of Min proteins . . . 12
  - 1.2.3 In vitro Min protein surface patterns . . . 12

References . . . 15

2 Quantitative analysis of surface wave patterns of Min proteins 23
- 2.1 Introduction . . . 24
- 2.2 Image processing methodology . . . 27
- 2.3 Pattern analysis strategies . . . 28
  - 2.3.1 Global parameters . . . 28
  - 2.3.2 Local parameters . . . 33
- 2.4 Discussion . . . 37
- 2.5 Supplementary Information . . . 39
  - 2.5.1 Methods . . . 39
  - 2.5.2 Online Content . . . 39
  - 2.5.3 Supplementary Figures . . . 41
  - 2.5.4 Appendix A: Demo Global Analysis . . . 49
  - 2.5.5 Appendix B: Demo Local Analysis . . . 62

References . . . 80

3 Directing Min protein patterns with advective bulk flow 85
- 3.1 Introduction . . . 86
- 3.2 Results . . . 88
  - 3.2.1 MinE-to-MinD concentration ratio determines the propagation direction . . . 88
  - 3.2.2 Model reductions and mechanistic explanation of upstream propagation . . . 91

3.2.3 Hysteresis and transition to upstream propagation by increasing flow rate . . . 93
3.3 Discussion . . . 96
3.4 Methods . . . 98
3.4.1 Mathematical model . . . 98
3.4.2 Sample preparation . . . 100
3.4.3 Image acquisition . . . 101
3.4.4 Image analysis . . . 101
3.5 Supplementary Theoretical Methods . . . 102
3.5.1 Setup . . . 102
3.5.2 Eliminating the vertical bulk dimension . . . 105
3.5.3 Summary of models and parameters used . . . 106
3.5.4 Switch model . . . 107
3.5.5 Reduced switch model . . . 108
3.5.6 Skeleton model . . . 110
3.5.7 Mapping the full switch model to the reduced switch model . . . 111
3.5.8 Details of hysteresis sweeps . . . 112
3.5.9 Details of simulations with disabled MinE advection . . . 115
3.5.10 Wave speed vs flow speed . . . 116
3.5.11 Linear Stability Analysis . . . 116
3.5.12 Other models of Min protein dynamics . . . 118
3.5.13 Persistent MinE membrane binding . . . 118
3.5.14 Loose, et al. model . . . 119
3.5.15 Bonny, et al. model . . . 119
3.6 Supplementary Experimental Methods . . . 121
3.6.1 Chemicals . . . 121
3.6.2 Preparation and handling of SUVs . . . 121
3.6.3 Protein purification and labeling . . . 122
3.6.4 Flow cell preparation and assembly . . . 122
3.6.5 Min pattern acquisition . . . 123
3.7 Supplementary image and data analysis . . . 124
3.7.1 General information . . . 124
3.7.2 Image processing and representation . . . 124
3.7.3 Image representation . . . 125
3.7.4 Local wave crest propagation analysis . . . 125
3.7.5 Analysis and visualization of local wave crest analysis results . . . 126
3.7.6 Spatial autocorrelation analysis . . . 127
3.8 Supplementary Data . . . 129
3.8.1 Concentration/ratio change in closed-circle settings . . . 129
3.8.2 Flow-independent time evolution of wave propagation velocity . . . 130
3.8.3 Effect of flow reversal . . . 133
3.8.4 Wave-crest velocity dependence on flow . . . 134
3.8.5 Wavelength dependence on flow . . . 135
3.8.6 Positional dependence . . . 136
3.8.7 Overview on closed-circle experiments . . . 137

3.8.8 Local velocity analysis: closed-circle experiments . . . 139
3.8.9 Overview on additional/control experiments . . . 145
3.8.10 Local velocity analysis: additional/control data . . . 147
3.9 Supplementary Movie captions . . . 152
3.10 Author's Correction . . . 153
References . . . 158

4 Quantifying the effect of MinE membrane binding on pattern formation 165
4.1 Introduction . . . 166
4.1.1 Background & motivation . . . 166
4.1.2 Recent advances . . . 168
4.2 Results . . . 170
4.2.1 Aim of this project . . . 170
4.2.2 Large-scale acquisitions of patterns . . . 171
4.2.3 Classification and quantification of patterns . . . 174
4.3 Discussion . . . 178
4.4 Materials & Methods . . . 179
4.4.1 SUV preparation . . . 179
4.4.2 Protein purification, His-tag removal and labelling . . . 180
4.4.3 Slide preparation and cleaning . . . 180
4.4.4 Sample preparation . . . 180
4.4.5 Fluorescence microscopy . . . 181
4.4.6 Image acquisition, rendering and analysis . . . 181
4.5 Supplementary Information . . . 182
4.5.1 Experimental data: overview . . . 182
4.5.2 Supplementary Figures . . . 185
References . . . 196

5 Designing surface patterns based on DNA oligomers 199
5.1 Introduction . . . 200
5.1.1 Minimum requirements for pattern formation . . . 200
5.1.2 DNA-based oscillators . . . 201
5.1.3 A mass-conserving DNA-based surface pattern system . . . 203
5.2 Results Part I: Design of a pattern-forming system . . . 204
5.2.1 Components and mechanisms . . . 204
5.2.2 Strand-displacement reactions . . . 204
5.2.3 Helicase as a tool for disassembly . . . 205
5.2.4 Initial design . . . 207
5.2.5 Cooperativity . . . 209
5.2.6 Two-step detachment model . . . 211
5.3 Results Part II: Experimental testing of the DNA-based system . . . 213
5.3.1 Testing the system with surface fluorescent imaging . . . 213
5.3.2 Testing kinetic rates with bulk fluorescence . . . 214
5.3.3 Simulation-guided sequence redesign . . . 217

5.4 Discussion & Outlook 219
5.5 Materials & Methods 221
References 222

6 Conclusions and outlook to future research **227**
References 231

Acknowledgements **235**

Curriculum Vitæ **239**

List of Publications **241**

SUMMARY

This thesis contains the results and conclusions obtained from over four years of PhD research, which were dedicated primarily to the study of Min protein surface patterns. This research is meant to contribute to our understanding of how pattern formation occurs in nature by considering Min proteins (MinD and MinE) as a well-established model system that is known to be capable of forming surface patterns on lipid membranes *in vitro*. Its minimal requirements make the Min protein system accessible to both experimental and theoretical researchers, and hence continue to spark the interest for collaborations between these groups.

Beyond the research on pattern formation, Min proteins are also of interest for the field of synthetic cell research. As the *in vivo* role of Min proteins in bacterial cells is the correct positioning of the division machinery, they are also a promising candidate for future integration into synthetic cells. With my research, I hope to contribute by providing a better understanding of the reaction mechanisms underlying the Min protein system, also making their integration into complex systems more straightforward.

Chapter 1 provides an introduction into the field of Min protein research. Here, I introduce the overall framework and terminology that will keep reoccurring throughout all following chapters. The chapter starts with a bird-eye-perspective on the research of pattern formation, soon focusing on intracellular pattern formation and, in particular, surface patterns formed by Min proteins. By presenting both the foundations of Min protein patterns and the context within which it is studied, I hope to explain our motivation for gaining a yet deeper understanding of the models underlying Min protein patterns.

Chapter 2 presents an image-analysis method developed specifically for analyzing Min protein surface patterns as they are observed *in vitro*. This includes introducing suggestions for pre-processing of image stacks, as well as strategies for obtaining quantitative information from the image data. The main focus is on quantities such as characteristic lengths and velocities of the patterns, as these properties are relatively straightforward to access and allow for direct comparison to simulation outcomes later on. The methods presented in this chapter are, with some modifications, used for the data presented in chapters 3 and 4.

In line with the collaborative spirit of the Min research field, the work presented in chapters 3, 4 and 5 was performed in collaboration with the theoretical biophysics group of Prof. Dr. Erwin Frey, whose members are interested in developing improved models and simulations of the Min protein system.

Chapter 3 presents the findings of a study which focused on how Min protein patterns will respond to bulk flow. In short, we find that when exposed to flow, Min protein patterns tend to align perpendicular to the flow direction, and that, surprisingly, they can either travel with or against the flow direction, depending on the concentration ratio between MinD and MinE. This finding provided new insight into the system's underlying reaction mechanism.

Chapter 4 presents the current status and experimental results of an ongoing collaboration, which aims to improve our understanding of the role of MinE membrane binding on the Min reaction cycle. To contribute to this effort, I measured, over a range of MinD and MinE concentrations, the patterns formed with MinE-wildtype as well as a truncated MinE mutant lacking the capacity for membrane binding. Importantly, this screening is complemented by a quantification of the patterns' properties, allowing for comparison to simulation results.

Chapter 5 summarizes the current status of an ambitious project that aims to use DNA oligomers to bottom-up construct a pattern-forming system inspired by the minimalism of the Min protein system. I argue that establishing such a system would open up a vast amount of potential for future research, and proceed to present the conceptual and experimental research that has been performed for this project up to the moment of this writing.

SAMENVATTING

Dit proefschrift bevat de resultaten en conclusies die zijn verkregen in meer dan vier jaar promotieonderzoek, dat hoofdzakelijk was gewijd aan het bestuderen van oppervlaktepatronen van Min eiwitten. Dit onderzoek is bedoeld om bij te dragen aan ons begrip van hoe patroonvorming plaatsvindt in de natuur door Min eiwitten (MinD en MinE). Het Min system wordt beschouwd als een goed gevestigd modelsysteem dat in staat is ruimtelijke patronen te vormen op lipide membranen *in vitro*. De minimale eisen van het Min eiwitsysteem maken het toegankelijk voor zowel experimentele als theoretische onderzoekers, waardoor het een dankbaar onderwerp is voor samenwerkingen tussen deze groepen.

Naast het onderzoek naar patroonvorming zijn Min eiwitten ook interessant voor het vakgebied van synthetisch celonderzoek. Aangezien de *in vivo* rol van het Min system binnen bacteriële cellen de juiste positionering van de delingsmachinerie is, zijn ze ook een veelbelovende kandidaat voor toekomstige integratie in synthetische cellen. Met mijn onderzoek hoop ik hieraan bij te dragen door een beter begrip te bieden van de reactiemechanismen van het Min systeem, waardoor de integratie ervan in complexe systemen eenvoudiger wordt.

Hoofdstuk 1 geeft een inleiding in het veld van het Min-eiwitonderzoek. Hier introduceer ik het algemene kader en de terminologie die terug zal komen in alle volgende hoofdstukken. Het hoofdstuk begint met een overzicht van het onderzoek naar patroonvorming, waarbij al snel wordt ingezoomd op intracellulaire patroonvorming en met name op oppervlaktepatronen gevormd door Min eiwitten. Door zowel de basis van Min-eiwitpatronen als de context waarin het wordt bestudeerd te presenteren, hoop ik onze motivatie uit te leggen waarom we een nog dieper begrip trachten te krijgen van de Min-eiwitpatronen.

Hoofdstuk 2 presenteert een beeldanalysemethode die specifiek is ontwikkeld voor het analyseren van Min-eiwitoppervlaktepatronen zoals ze *in vitro* worden waargenomen. Dit omvat suggesties voor de voorbewerking van beeldstapels, evenals strategieën voor het verkrijgen van kwantitatieve informatie uit de beeldgegevens. De nadruk ligt vooral op grootheden zoals karakteristieke lengtes en snelheden van de patronen, omdat deze eigenschappen relatief eenvoudig te verkrijgen zijn en een latere vergelijking met simulatieresultaten mogelijk maken. De methoden die in dit hoofdstuk worden gepresenteerd, worden met enkele aanpassingen gebruikt voor de metingen die worden gepresenteerd in hoofdstukken 3 en 4.

Zoals gewoonlijk in het in het Min-onderzoeksveld, is het werk dat wordt gepresenteerd in hoofdstukken 3, 4 en 5 uitgevoerd in samenwerking met de theoretische biofysica-

groep van Prof. Dr. Erwin Frey, wier leden geïnteresseerd zijn in het ontwikkelen van verbeterde modellen en simulaties van het Min eiwitsysteem.

Hoofdstuk 3 presenteert de bevindingen van een studie die zich richt op hoe Min eiwitpatronen reageren op bulkstroming van de vloeistof boven het oppervlak. Kort gezegd vinden we dat Min eiwitpatronen geneigd zijn zich loodrecht op de stroomrichting uit te lijnen wanneer ze aan stroming worden blootgesteld, en dat ze verrassend genoeg ofwel mèt of tégen de stroomrichting kunnen bewegen, afhankelijk van de concentratieverhouding tussen MinD en MinE. Deze bevinding levert nieuw inzicht op in het onderliggende reactiemechanisme van het systeem.

Hoofdstuk 4 presenteert de huidige status en de experimentele resultaten van een lopende samenwerking, die tot doel heeft ons begrip van de rol van MinE-membraanbinding in de Min reactiecyclus te verbeteren. Om bij te dragen aan deze inspanning, heb ik patronen gemeten over een scala aan MinD- en MinE-concentraties, gevormd met wildtype MinE en met een ingekorte MinE-mutant die niet in staat is tot membraanbinding. Belangrijk is dat deze screening wordt aangevuld met een kwantificering van de eigenschappen van de patronen, waardoor vergelijking met simulatieresultaten mogelijk is.

Hoofdstuk 5 vat de stand van zaken samen van een ambitieus project dat tot doel heeft om DNA oligomeren te gebruiken om bottom-up een patroonvormend systeem te construeren dat is geïnspireerd op het minimalisme van het Min eiwitsysteem. Ik betoog dat het opzetten van een dergelijk systeem een enorme potentie heeft voor toekomstig onderzoek, en presenteren er vervolgens van het conceptuele en experimentele onderzoek dat is uitgevoerd voor dit project tot aan het moment van schrijven.

ZUSAMMENFASSUNG

Diese Dissertation beinhaltet die Resultate und Schlussfolgerungen, die aus vier Jahren PhD-Forschungsarbeit hervorgegangen sind und deren hauptsächliches Themengebiet die Min Protein Musterbildung darstellt. Ziel dieser Forschungsarbeit ist, zu unserem Verständnis der Musterbildung in der Natur beizutragen, indem wir Min Proteine studieren (MinE und MinD). Min Proteine sind bekannt als ein etabliertes Modelsystem, das dazu in der Lage ist, in einer *in vitro* Umgebung Muster auf Oberflächen, nämlich Lipidmembranen, zu formen. Seine minimalen Anforderungen machen das Min Protein System sowohl experimentellen als auch theoretischen Forscher*innen zugänglich, weshalb es einen attraktiven Forschungsgegenstand in Kollaborationen zwischen diesen Gruppen darstellt.

Zusätzlich zu Grundlagenforschung im Bereich der Musterbildung sind Min Proteine auch für Forschung im Bereich von synthetischen Zellen von Interesse. Die *in vivo* Aufgabe von Min Proteinen in Bakterienzellen ist die korrekte Positionierung der Zellteilungs-Maschinerie. Daher werden Min Proteine als vielversprechende Kandidaten für die Integration in zukünftige synthetische Zellen gesehen. Ich hoffe, mit meiner Forschung einen Beitrag dazu geleistet zu haben, den zugrundeliegenden Reaktionsmechanismus des Min Protein Systems besser zu verstehen, und ihre Integration in komplexe Systeme zu erleichtern.

Kapitel 1 stellt eine Einführung in das Forschungsfeld der Min Protein Musterbildung dar. Hier führe ich das theoretische Grundgerüst sowie die Terminologie ein, die in den nachfolgenden Kapiteln verwendet wird. Das Kapitel beginnt mit einem Überblick über die Forschung im Bereich der Musterbildung, wobei der Fokus früh auf intrazelluläre Musterbildung und in weiterer Folge auf Min Protein Musterbildung gelegt wird. Indem ich die Fundamente der Min Protein Musterbildung sowie den Kontext der Forschung daran erörtere, hoffe ich, zu motivieren warum ein tieferes Verständnis der dem Min Protein System zugrundeliegenden Modelle für die Forschung interessant ist.

Kapitel 2 stellt eine Bild-Analyse-Methode vor, die speziell für Min Protein Oberflächenmuster entwickelt wurde, die man *in vitro* beobachten kann. Das beinhaltet die Einführung von Vorverarbeitungsschritten von Bilderserien, sowie von Strategien für die Extrahierung quantitativer Informationen aus dem Bildmaterial. Der Fokus liegt auf dem Erhalt charakteristischer Längen und Geschindigkeiten der Muster, da diese Eigenschaften verhältnissmäßig einfach zu erfassen sind und in weiterer Folge einen direkten Vergleich zu Simulationsergebnissen erlauben. Die Methodik, die in diesem Kapitel präsentiert wird, wird – mit notwendigen Modifikationen – auf die in Kapitel 3 und 4 präsentierten Daten angewandt.

Ganz im Sinne der kollaborativen Haltung des Min Protein Forschungsfeldes wurde die in Kapitel 3, 4 und 5 präsentierte Arbeit in Kollaboration mit der auf Theoretische Biophysik spezialisierten Gruppe von Prof. Dr. Erwin Frey durchgeführt. Die Mitglieder dieser Gruppe sind daran interessiert, Modelle des Min Protein Systems zu entwickeln und zu verbessern.

Kapitel 3 stellt die Ergebnisse einer Studie vor, in derern Rahmen untersucht wurde, wie Min Protein Muster auf Massenfluss der Flüssigkeit im Reservoir über der Oberfläche reagieren. Zusammengefasst zeigen unsere Ergebnisse, dass Min Protein Oberflächenmuster dazu tendieren, sich im rechtem Winkel zur Flussrichtung auszurichten und entweder in oder gegen die Flussrichtung laufen können. Die Richtung der Muster wird hier vom Konzentrationsverhältnis zwischen MinD und MinE beeinflusst. Die Ergebnisse dieser Studien liefern neue Erkenntnisse über den zugrundeliegenden Reaktionsmechanismus des Min Systems.

Kapitel 4 stellt den derzeitigen Stand sowie die experimentellen Ergebnisse einer laufenden Kollaboration vor, deren Ziel es ist, die Rolle von MinE Membranbindung auf den Reaktionszyklus von Min Proteinen besser zu verstehen. Um hierzu beizutragen, nahm ich Messungen über ein Spektrum von MinD und MinE Konzentrationen vor und klassifizierte die Muster, die mit MinE-Wildtype gebildet wurden oder mit einem MinE-Mutant, dem die Befähigung zur Membranbindung fehlt. Über die Messung hinausgehendend wurde auch eine Quantifizierung der Mustereigenschaften durchgeführt, um einen Vergleich zu Simulationsergebnissen zu erlauben.

Kapitel 5 enthält eine Zusammenfassung des derzeiten Standes eines ambitionierten Projektes, welches darauf abzielt, ein musterbildenes System von Grund auf aufzubauen unter Verwendung von DNA-Oligomeren. Ziel ist die Konstruktion eines minimalen Systems, wobei das Min Protein System wichtige Inspiration darstellt. Ich argumentiere, dass die erfolgreiche Etablierung eines solchen Systems enormes Potential für zukünftige Forschung bieten würde. In weiterer Folge stelle ich die konzeptionelle und experimentelle Arbeit vor, die bis zu diesem Zeitpunkt an diesem Projekt geleistet wurde.

1

INTRODUCTION

Patterns inevitably surround us. Intriguingly, patterns can emerge spontaneously out of an initially homogeneous distribution of components or molecules from a combination of intermolecular interactions and (diffusive) transport – a process that was famously conceptualized for biological systems by Alan Turing. Patterns fulfill a broad range of vital functions in biology. Nowadays, we know and study many pattern-forming systems across various scales, both on the multi- and single-cellular level. The Min protein system is the prime example of an intracellular pattern-forming system, as it forms pole-to-pole oscillations on the inner membrane of E. coli bacteria, thereby guiding the division machinery to the cell's central circumference. When reconstituted in vitro, Min proteins were shown to form surface patterns on lipid bilayers, which opened up a wide range of possibilities for scientific studies. As a minimalistic pattern-forming system, Min proteins have become a model system for both theoretical and experimental life scientists, and they continue to teach us about the foundations of pattern formation to this day.

This chapter first provides a general overview of the field of pattern formation, with a particular focus on intracellular systems, and proceeds to describe what we know about the reaction cycle of Min proteins. We clarify that Min proteins are of special interest to this research field, as they constitute a minimalistic system that holds the capacity to form a rich variety of surface patterns.

1

1.1. PATTERNS ACROSS SCALES

1.1.1. FUNDAMENTAL MECHANISMS AND TERMINOLOGY

The Oxford English Dictionary defines the noun "pattern"[1] as

> "I. A model, example, or copy.
> II. A regular or decorative arrangement."

with each definition containing multiple sub-categories of additional meaning.
Of particular interest here is definition II.11.b., which reads:

> "*Science.* An arrangement or relationship of elements, *esp.* one which indicates or implies an underlying causative process other than chance."

In other words, a pattern is the visible or detectable outcome of a process that is currently taking place or has occurred previous to the observation. The word "arrangement" implies spatial order, but as this is not specified, it can in principle also refer to a regular emergence of a state or property over time.

Traveling through our world, we can discover patterns in an immeasurable multitude of appearances. A look through a telescope reveals that galaxies and planetary systems arrange themselves in characteristic recurring patterns.[1, 2] Satellite images or even just looking up at the sky may present us with imagery of magnificent cloud formations. [3] A bird-eyes view of a landscape or large-scale ecosystem reveals patterned arrangements in geological formations, vegetation growth, or animal territories.[4, 5] Animal fur and skin present stunning pigmentation patterns, such as stripes or spots[6, 7] – constituting examples of multicellular pattern formation. (Please consider Fig. 1.1A for an illustration.) [8, 9] Zooming in even further, patterns are observed transiently at certain stages of intracellular processes, in particular processes that require imposing some form of directionality – such as embryonic development or cell division.[10]

Having become aware of the frequent occurrence of patterns in our natural world, there are many fundamental, tightly connected questions that one can ask about them, such as: How exactly do these patterns emerge? Can we find underlying physical principles? What roles (if any) do they fulfill once they have emerged? The study of pattern formation deals with these questions and aims to identify and describe the physicochemical principles underlying the patterns found throughout our world.

[1] Oxford English Dictionary (www.oed.com), keyword "pattern", accessed 2023-11-26.

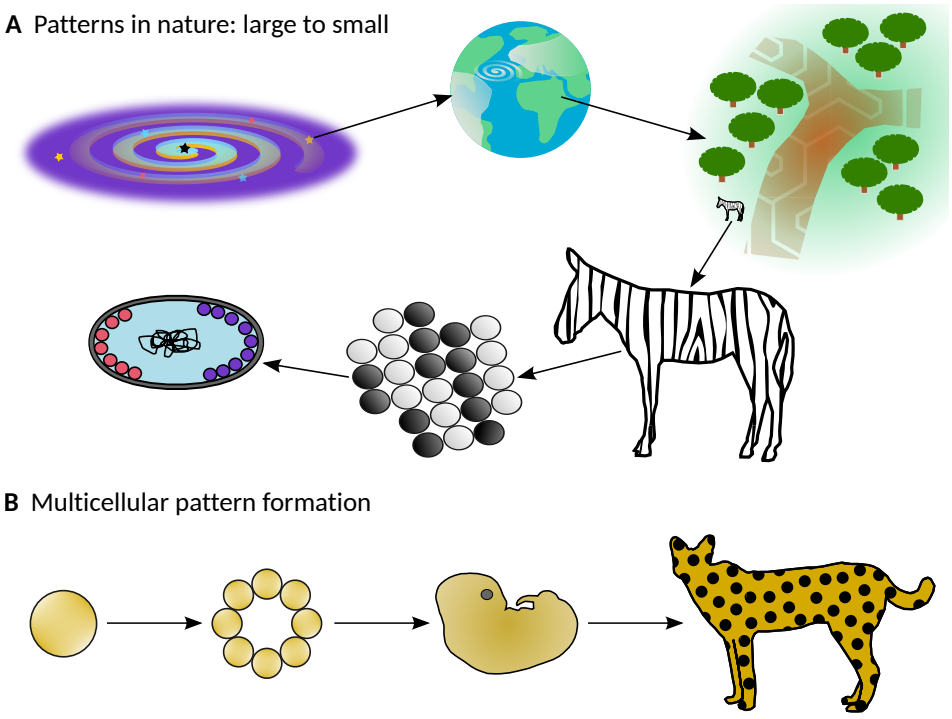


Figure 1.1: **Patterns in nature. A** Patterns emerge in our natural world in all scenarios and sizes. We see them manifested in the spatial arrangement in galaxies,[1, 2] in cloud formations in our atmosphere,[3] in geological formation and ecosystems,[4, 5] as well as in the shape and appearance of living creatures, with pigmentation patterns constituting are a visibly striking example of multicellular pattern formation[6, 7]. Even within cells, pattern-forming reactions occur within single molecules, as will be described in section 1.1.4. **B** During embryonic development, an initially symmetrical arrangement of cells needs to break this symmetry for tissue to differentiate and eventually form the complex shape of a multicellular organism. Alan Turing considered this process (in an idealized, mathematically more accessible form) in his seminal article "The chemical basis of morphogenesis"[11], as described in the text.

From a general point of view, regular structures can emerge from collective processes of a system's components (often molecules) that are often referred to as *self-organization* or *self-assembly*.[12, 13] In these cases, structure is a consequence of specific interactions between the system's components. Though the terminology is not used consistently across scientific fields, a distinction between self-assembly and self-organization can be made based on thermodynamics:[13]

Self-assembly refers to order emerging as a system strives toward a thermodynamic equilibrium, i.e. as it minimizes its total internal free energy. That includes phenomena like the formation of crystalline structures, or the formation of lipid bilayers in biology. These processes happen voluntarily without external energy input and result in static structures. Self-organization, in contrast, occurs outside the thermodynamic equilibrium. The resulting patterns may present as apparently static or as dynamic, but require constant energy supply in order to be maintained. [12, 13]

Self-organization is of particular interest to biology as it deals with fundamental questions such as how life is sustained as a non-equilibrium process, and how form and function relate to one another. If the formation of a pattern is the result of an assembly of molecules, this means that at one point in time, order is or was created from disorder. Spatiotemporal structure emerges as components organize into a heterogeneous arrangement, arising out of an initially homogeneous distribution. This apparently contradicts the second law of thermodynamics, which states that entropy – loosely interpreted as "disorder" – increases over time. However, this holds for a closed system which does not receive energy from the outside,[12] and living systems can not be described as such.

1.1.2. TURING PATTERNS

In 1952, Alan Turing published a paper titled "The chemical basis of morphogenesis"[11]. In this work, Turing brought up the question of how a spatial arrangement of any component can emerge within a biological system. Specifically, he referred to spontaneous symmetry breaking such as it is observed during embryonic development, during which an embryo starts out from a spherical state and evolves into a highly differentiated, complex shape (see Fig. 1.1B). To address this issue, Turing considered an idealized, symmetrical system in the form of a ring of cells, with components that are able to diffuse laterally between them. These components are purposefully unspecified and very generally referred to as form-giving "morphogens".[11, 14]

Turing found that while diffusion will homogeneously spread these morphogens among the cells, there will always be small, transient inhomogeneities within their distribution. Over time, one would expect these fluctuations to average to zero at every position. However, Turing could show that if one assumes there to be a reaction taking place within the cells which would *amplify* a deviation from the average concentration, the expected outcome changes drastically. Turing could describe this system mathematically via a set of reaction-diffusion equations.[11, 14] By performing a mathematical procedure referred to as linear stability analysis, Turing showed how the spatial concentration profile can be disassembled into a series of Fourier modes with their own amplitudes and growth rates. Negative growth rates will lead to a decay of the mode. However, modes with a positive rate will keep growing. Hence, if the parameters of the overall systems are such that an instability is created, the system will develop into a heterogeneous steady state, commonly referred to as a pattern. [11, 10, 9]

Turing calculated some exemplary patterns for his idealized system and found it capable of forming both dynamic patterns (i.e., traveling waves within the morphogen concentration profile) and stationary patterns (from standing morphogen concentration waves), with the latter bearing similarity to animal fur.[11, 15, 14] Nowadays, the term "Turing pattern" is used to refer to a pattern that emerges from spontaneous symmetry breaking via lateral diffusive coupling.[12, 15, 10]

1.1.3. STUDYING BIOLOGICAL PATTERN FORMATION

While Turing's work was preceded by the theoretical and experimental work of others (in particular on chemical oscillatory systems), he ingenuously combined knowledge from different scientific disciplines – in particular mathematics, chemistry and biology – to address a fundamental question of life.[12, 14]

At the time of its publication, Turing's paper did not yet receive the attention that it does today within the life science community, but was rather overshadowed by other discoveries for decades.[12, 14] However, in the meantime, important insights were gained into other types of reaction-diffusion mechanisms found in purely chemical systems, such as the Belousov–Zhabotinsky (BZ) system. The BZ system was found capable of forming spatial patterns in the form of traveling waves.[12, 14, 16].

Interest in pattern formation in biology increased gradually starting from the 1970s onwards, as the availability of computers also made the required calculations considerably easier. In a series of publications, different types of pattern-forming phenomena were conceptualized in a form similar (though not identical) to how Turing had proposed.[14] So far, it could be established that pattern formation, on a very general level, can result from a combination of [9, 17]

- specific reactions (i.e. reactions between the involved components),
- transport (often, though not necessarily, diffusive transport), and
- guiding cues (for example, geometrical or chemical cues).

By relying on these commonly identified features, pattern formation occurs among an astonishingly wide range of biological scenarios.[10, 6, 7] A given pattern's description requires reaction terms and approaches to modeling that adequately capture the key features of its underlying mechanisms, and numerous different models have been proposed and applied so far.[18, 10, 9]

A by now well-known and frequently applied example is the activator/inhibitor model originally proposed by Gierer and Meinhardt in 1972[19], which presents a reconceptualized version of Turing's reaction scheme.[8, 14] In the activator/inhibitor model, a short-range "activator" stimulates its own local production in an autocatalytic reaction, while it is counteracted by a long-range "inhibitor" which promotes its degradation. [8, 10] This model has so far been successfully adapted and applied to a number of problems, such as embryonic development (morphogenesis) of multicellular organisms[20], including processes such as skin pigmentation[8, 6].

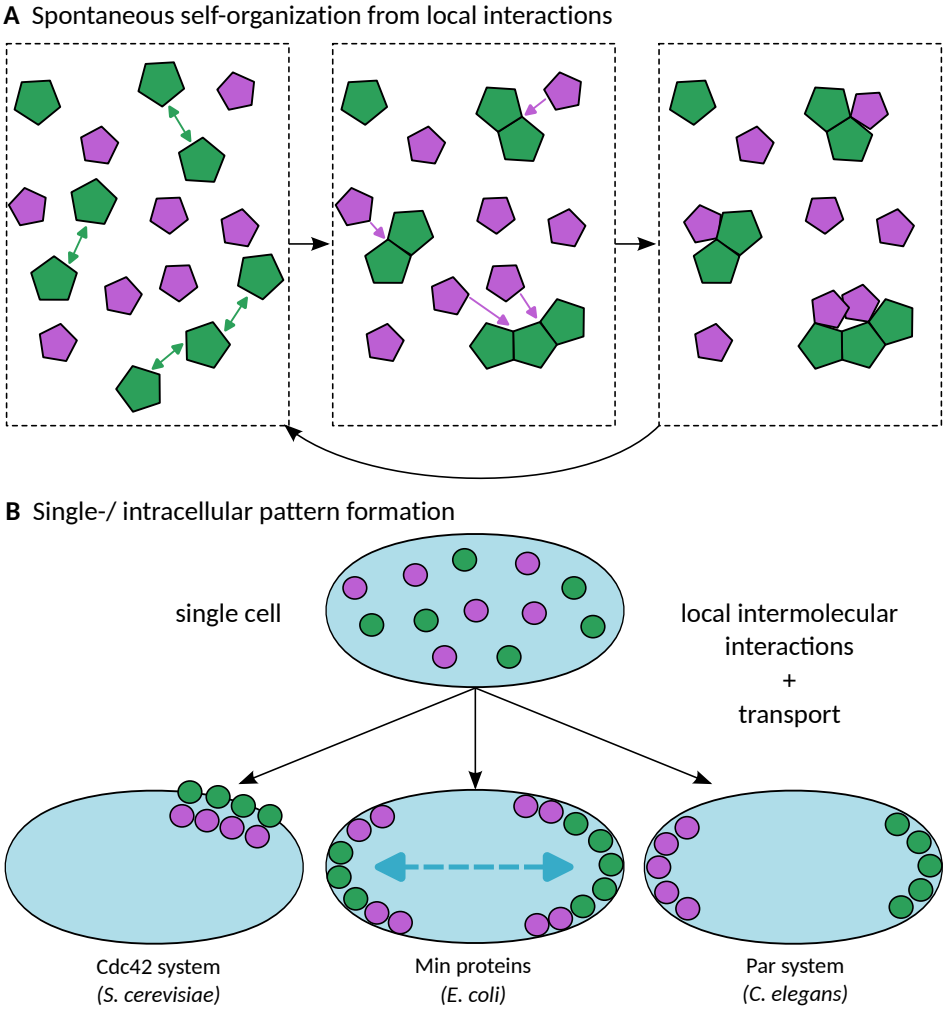


Figure 1.2: **Principles of self-organization. A** An abstract representation of a container (such as a single cell) within which a group of molecules (typically proteins) interact with each other. In the given example, the green molecules have an affinity for each other and cluster. Subsequently, the purple species interacts with the clusters and disassembles them. If this were to happen in bulk, no semi-permanent pattern would form. Intracellular patterns typically form on membranes, with the cell's bulk acting as a transport layer. **B** Examples of membrane patterns that can emerge within a single cell, presented in highly simplified illustrations. The Cdc42 system from eukaryotic *Saccharomyces cerevisiae* relies on the complex interaction of several proteins to determine the site where the budding off of a daughter cell occurs.[10, 21] In *Escherichia coli* bacteria, the mid-cell division site is determined by pole-pole-oscillations of Min proteins.[22] In the single-cell-stage of the multicellular organism *Caenorhabditis elegans*, the posterior-anterior axis of the developing embryo is determined by the action of the complex Par protein system.[23] As intricate and diverse as these pattern-forming systems are, they all rely on an interplay of local interactions, transport, and guiding cues.[17]

1.1.4. INTRACELLULAR PATTERN FORMATION

For multicellular organisms, self-organization is evidently of crucial importance, as it governs embryonic morphogenesis and consequently, allows our bodies to adopt their highly complex shape.[20]. However, even on a subcellular level, pattern formation could be shown to fulfill a variety of vital functions. Typically, it is found in processes which require imposing some form of directional or positional preference of components within the cell, such as during cell division. [10, 17]

A famous example thereof is the Min protein system of *Escherichia coli* (*E. coli)*, comprising the proteins MinD, MinE, and MinC, which perform dynamic pole-pole oscillations that locate the division apparatus in a way that enforces symmetrical cell division.[22] This system which will be described in detail in section 1.2 below. However, a number of other systems continue to be explored, both in bacteria and eukaryots. Another bacterial representative would be the ParABS system, which is essential for bacterial chromosome segregation and was found to rely on working principles similar to those of the Min system, to which it is evolutionarily close.[24] Further, analogues of the Min system from *E. coli* also exist in other bacteria,[25] such as in *Bacillus subtilis*.[26] This system does not contain MinE, but MinD, MinC and MinJ, which are recruited to the cell poles by the curvature-sensing protein DivIVA, leading to stationary spatial gradients instead of an oscillatory pattern.[27, 26] An eukaryotic example would be the partitioning defective (Par) proteins system from *Caenorhabditis elegans*, which defines the posterior-anterior axis in the single-cellular embryo. [23] Yet another eukaryotic example is given by the Cdc42 system from baker's yeast (*Saccharomyces cerevisiae*), which divides asymmetrically and employs a pattern-forming at the budding site, requiring the action of several components, including regulatory and scaffolding proteins.[10, 21] Fig. 1.2B provides a (highly simplified) schematic representation of the types of patterns found within single cells as a result of intracellular pattern formation.

Intracellular patterns are of particular interest to the study of pattern formation, as they provide useful model systems and allow for both *in vivo* and *in vitro* experiments. Analogous to multicellular patterns, they emerge from a combination of specific intermolecular reactions (cf. Fig. 1.2A) and transport. The molecules here are generally proteins which fulfill certain roles within the cell. The transport processes distribute these proteins through the cytosol and can be facilitated by diffusion, advective flows within the cell, or active transport by motor proteins. If conditions are met, patterns can form on intracellular membranes or other surfaces within the cell to which proteins can bind. The patterns will be influenced by cues like the cell's geometry or biochemical processes taking place within the cell.[17]

A common feature of these intracellular systems is their reliance on mass-conserving dynamics. As protein production and degradation are slow and resource-intensive processes, the pattern-forming dynamics rely on the amount of protein already present within the cell at the moment of initiation. This has considerable implications for modeling, as widely used approaches such as the activator-inhibitor model (which relies on autocatalytic production and degradation) are not applicable.[28, 29]

Importantly, the dynamics rely on cycling of proteins between different conformational states, a property sometimes referred to as the “switching paradigm”. Conformational changes can be induced as the protein interacts with another component within the cell, such as a membrane or another protein, or as it performs nucleotide triphosphate (NTP) hydrolysis. Cycling between NTP-bound and -unbound state is crucial, as NTPs are the main source of energy within the cell. As pattern formation occurs outside the thermodynamic equilibrium, the system relies on constant energy input to maintain its heterogeneous steady state, which is provided by NTP hydrolysis. Notably, conformational switching of proteins can greatly affect their kinetic properties as well as their (membrane) bindings affinities, but does not affect the total amount of protein within the cell.[28, 29, 17]

In order for the system to be capable of pattern formation, the reaction cycle has to include some form of feedback mechanism, providing a nonlinear element that amplifies rather than eliminates inhomogeneities in spatial distribution – meaning, it requires some process which makes the whole system unstable towards perturbations. Reaction mechanisms which can provide such a nonlinear element include cooperative binding or competition for binding sites.[28, 17]

1.2. MIN PROTEIN PATTERN FORMATION

1.2.1. DISCOVERY AND FUNDAMENTALS OF MODELING

In 1967, Adler et al. published a study entitled "Miniature Escherichia coli cells deficient in DNA", reporting on the formation of anucleate minicells (i.e. cells without genetic material, which were thus nonviable).[30] Such minicells were later shown to exhibit mutation of the *minB* gene locus, which encodes the protein MinD, MinE and MinC.[31] Soon after, it was found that these Min proteins do in fact inhibit the membrane binding of the protein FtsZ, a crucial member of the bacterial cell division machinery, which assembles at the cell's central circumference. As Min proteins would locate preferentially at the poles of the rod-shaped bacterium, FtsZ would be the least inhibited at the center and hence, bind and act there.[25, 32]

Strikingly, Raskin and de Boer discovered in 1999 that Min protein organize not only spatially, but also temporally, as their membrane concentration oscillated between the cell's pole at a timescale of about one minute.[33]. MinC, the key component for inhibiting FtsZ, was found to oscillate between the poles along with MinD and MinE, leading the FtsZ assembly at the cell's central plane and formation of the division plane.[34, 35] In 2001, Meinhardt and de Boer[32] suggested a key sequence of actions for the local Min protein reaction scheme, which in short went as follows: 1. MinD binds to the membrane, from where it recruits both MinC and MinE. 2. MinE accumulates on the membrane. 3. MinE displaces MinD and MinC from the membrane. Computer simulations based on this model indeed yielded spatio-temporal patterns in the form of pole-to-pole oscillations, which were in good agreement with experimental observations.[33, 35]

Since then, models of the Min protein system have continuously evolved and incorporated new experimental data as it was provided.[36, 37, 10] Some early key findings included that MinD is an ATPase that upon acquiring adenosine triphosphate (ATP) can bind to phospholipids, and that MinE stimulates membrane-bound MinD to perform hydrolysis of ATP, triggering its release from the membrane.[38, 39, 40]. Another aspect that was found to be important was a higher diffusive mobility of Min protein in bulk as opposed to those bound to the membrane.[36] Current models assign a diffusion constant of about 10 $\mu m^2 s^{-1}$ to cytoplasmic Min protein[41], which is assumed to be at least a factor 100 higher than for their membrane-bound counterparts.[28, 17].

Generally, as is also the case with other pattern-forming systems, the Min system's dynamics can be described by a set of partial differential equations which include both diffusion and reaction terms. These reaction terms can differ between individual models, based on what assumptions on intermolecular interactions it includes. [42, 10, 17] Based on these sets of equations, both stochastic models (i.e. simulating the paths and interactions of single molecules) and deterministic models (i.e. working with averaged concentrations of molecules over time) have been developed for the Min system.[37]

1

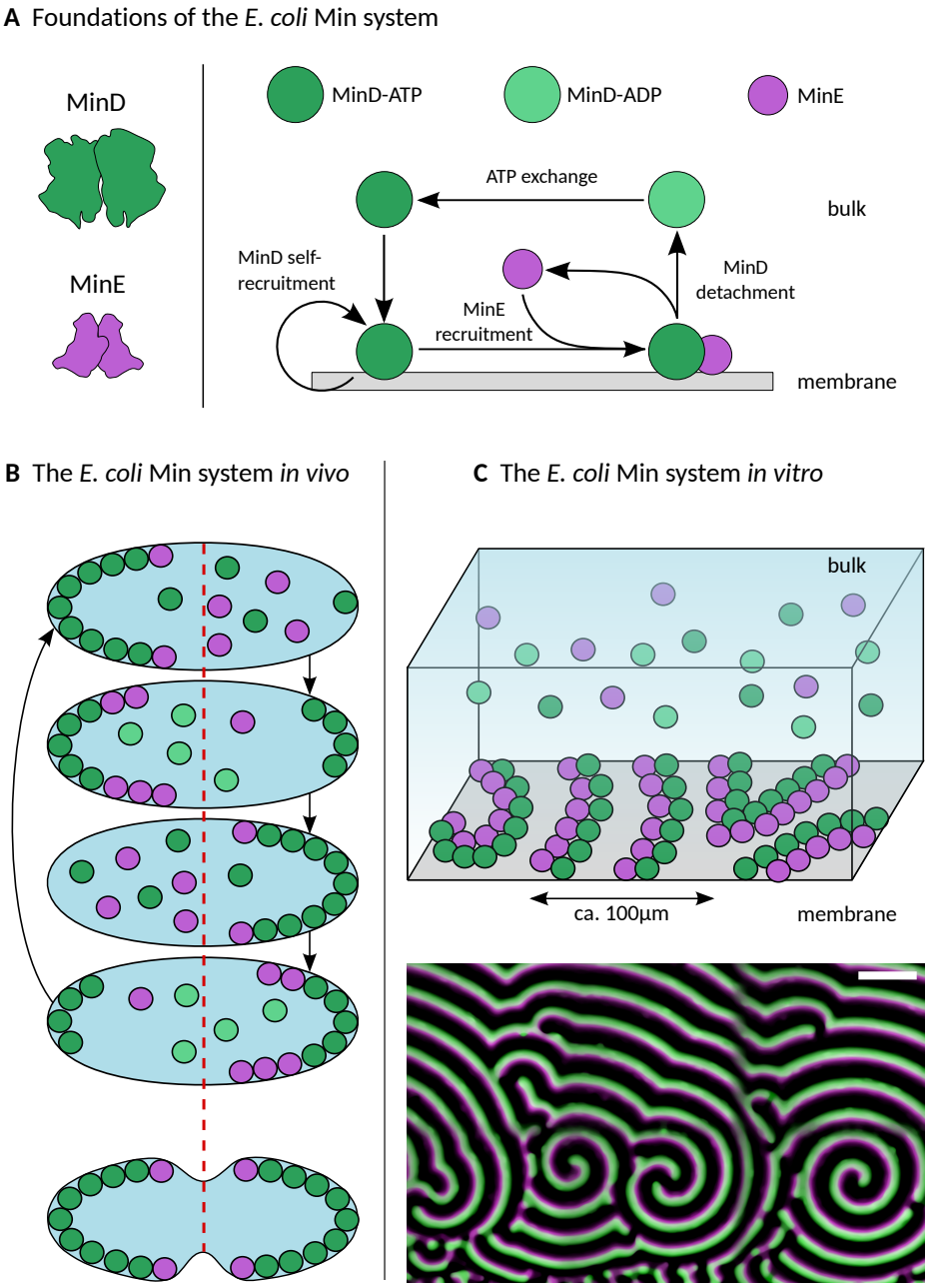


Figure 1.3: **Min protein pattern formation.** (Figure caption on next page.)

Figure 1.3: **Min protein pattern formation.**
A Left: schematic depictions of dimeric MinD and MinE inspired by Protein Data Base (PDB)[2]structures 3Q9L[43] and 2KXO[44], respectively.[22] Right: MinD and MinE are further simplified for subsequent illustrations by dark-green spheres for MinD-ATP, light-green spheres for MinD-ADP and purple spheres for MinE. A model illustration of the minimal MinD-MinE reaction cycle: MinD-ATP binds to the membrane surface, from where it recruits both more MinD to its vicinity and MinE. MinE stimulates MinD to facilitate ATP hydrolysis and release from the membrane. MinD-ADP and MinE return to the bulk. MinD-ADP undergoes ATP exchange and is available for the next reaction cycle. [10, 45]
B *In vivo*, Min proteins perform pole-pole-oscillations along the long axis of the *E. coli* bacterium. These lead to the time-averaged membrane concentration of Min proteins to be the lowest at the cell's central circumference (indicated by a red dashed line). As Min proteins inhibit the binding of FtsZ (via MinC, which is not shown in the depiction, but is recruited by MinD), cell division will preferentially occur at this site. [46, 22]
C *In vitro* studies of the Min system typically rely on reconstitution of purified Min protein on supported lipid bilayers.[47, 22] This can be done in a variety of sample chamber geometries[48, 49] and conditions[50], providing control and important insight into the inner workings of the Min system. Top: A schematic depiction of an *in vitro* experimental setting. Bottom: A fluorescence microscopy acquisition of Min proteins on a supported lipid bilayer (surface density of MinD in green and of MinE in magenta). Scale bar is 100 μm. Measured on an anionic lipid membrane (matching the charge density of the *E. coli* membrane) at concentrations of 1 μM MinD and 1 μM MinE, supplemented with 2.5 mM adenosine triphosphate (ATP).

As mentioned, the reaction terms used in these models need to include some form of feedback or nonlinear behavior in order to give rise to a lateral instability.[10] Min models incorporate this either by assuming cooperative binding of MinD to the membrane (referred to as "cooperative attachment" models) or by assuming that once MinD proteins are membrane-bound, attractive forces between them tend to cluster them together ("aggregation current" models).[37] Over time, it has become clear that for a number of reaction networks, simulations are able to produce the observed pole-pole oscillations upon modelling MinD, MinE and ATP within a container, described by a reaction-diffusion mechanism.[36, 51]

[2] PDB entry 3Q9L for *Escherichia coli* MinD-ATP available at: https://www.rcsb.org/structure/3Q9L [2024/07/13]
PDB entry 2KXO for *Neisseria gonorrhoeae* MinE available at: https://www.rcsb.org/structure/2KXO [2024/07/13]

1.2.2. IN VIVO AND IN VITRO STUDIES OF MIN PROTEINS

Over the years, the Min system has been studied extensively *in vivo* (cf. Fig. 1.3B). Research efforts include fluorescence imaging of labelled Min protein in both wildtype and bioengineered bacteria[35, 33] as well as within bacteria enclosed in artificially crafted environments[52, 53, 54]. *In vitro* studies of the Min system, however, constitute an essential contribution to the research field, as they offer new insight into the structural and mechanistic properties of these proteins. That includes the determination of crystal structures[55, 43] as well as studies on MinD's ATPase activity and the interaction between Min proteins and phospholipids[40, 56, 57, 58].

All of these research efforts – and certainly more than cited here so far – contributed to the body of knowledge of Min proteins that we have today. The following two paragraphs very briefly summarize the current state of knowledge on MinD and MinE from the reviews in references [46, 22].

We know that monomeric MinD from *E. coli* is 270 amino acids long protein with a mass of about 30 kDa.[3] MinD is part of the Walker A family of ATPases, as it carries the characteristic Walker A motif or "P-loop" (phosphate-binding loop) at its N-terminus. This motif, along with others (Walker B, switch regions I and II), is involved in ATP binding. ADP-bound MinD is monomeric and cannot bind the membrane, but upon replacing ADP by ATP, it dimerizes. Only upon dimerization, MinD becomes capable of binding to negatively charged phospholipid membranes. The negative membrane charge is essential, as binding is facilitated by a positively charged, C-terminal membrane-targeting sequence (MTS). [46, 22]

MinE, on the other hand, is small with only 88 amino acids and a mass of about 10 kDa.[4] MinE is what is called an ATPase-activating protein, as it stimulates membrane-bound MinD-dimers to hydrolyze ATP to ADP and release from the membrane. Similar to MinD, MinE has a positively charged MTS, though it is located at its N-terminus, as well as a topological specificity domain (TSD), which acts as a dimerization site. By themselves, MinE-dimers have a weak membrane affinity as the MTS is hidden within their hydrophobic core, from which it emerges upon association with already membrane-bound MinD.[46, 22]

1.2.3. IN VITRO MIN PROTEIN SURFACE PATTERNS

Min protein research was greatly enriched by the discovery that purified Min proteins are able to form surface patterns not only on the bacterium's inner membrane, but also on supported lipid bilayers *in vitro*, first reported by Loose et al. in 2008. [59] The authors reported surface patterns in the form of traveling wave fronts, some of which would form spirals, with wavelengths of up to 100 μm, propagating along the surface.[59]

[3] UniProt entry for *E. coli* MinD: https://www.uniprot.org/uniprotkb/P0AEZ3/entry [2024/04/19]
[4] UniProt entry for *E. coli* MinE: https://www.uniprot.org/uniprotkb/P0A734/entry [2024/04/19]

This finding opened up a whole class of new experiments, and in concert, new testing grounds for modeling on the Min system. Since then, the Min system has become what is often referred to as a "paradigm for intracellular pattern formation", as due to its simplicity and versatility, it can be used to study pattern formation on a rather generalized level. Studying surface pattern formation *in vitro* provides a whole realm of possibilities when it comes to environmental conditions which the system can be exposed to. Min protein surface patterns were found to respond with high sensitivity to changes in experimental conditions, allow to infer their responses back to the models and gradually, improve them.[46, 47, 10, 29, 22]

So far, Min protein surface patterns have been studied *in vitro* (cf. Fig. 1.3C) for a range of experimental settings, including for different concentrations of MinD and MinE[60], on patterned surfaces[61] and within different sample chamber geometries – such as within microchambers [48] and for different bulk heights[49, 62] –, as well as in association with membrane cargo (other than MinC)[63, 64]. Further Min patterns have been studied for different lipid compositions and buffer conditions, and the pattern's wavelengths were found to respond to changes in anionic charge.[50] Notably, based on the finding that there appears to be very little difference between Min surface patterns on *E. coli* lipids and patterns on phospholipid mixtures of comparable anionic charge density, many *in vitro* experiments have been performed with minimal phospholipid mixtures rather than with *E. coli* lipids.[65, 48, 66, 49, 67]

An early important finding achieved by single-molecule imaging was the discovery of "MinE persistent membrane binding", i.e. the capacity of MinE to linger on the membrane for a short time after MinD has been released.[68] In more recent years, several other techniques, such as high-speed atomic force microscopy[69] and particle tracking [70, 71], have been applied additionally to study the Min system's inner working. Still, optical imaging of surface patterns continues to be of great interest.

Denk et al. reported in 2018 on the importance of the "MinE switch", that being the capacity of MinE to undergo a conformational switch from an active into a latent state, shortly after having been released from the membrane.[45] They could show that in experiments with MinE mutants lacking the ability to switch, surface patterns were only formed within a very constricted range of MinE:MinD concentration ratios – in stark contrast to patterns with MinE-wildtype, which would still form patterns for MinE:MinD ratios of 10 and beyond. Based on this finding, the formerly used *skeleton model* of Min pattern formation (MinD binds and recruits more MinD - MinD recruits MinE - membrane release of MinD and MinE) was extended by MinE conformational switching into what was called the *switch model*, which considers the different kinetic rates of active and latent MinE.[45]

While the dynamic traveling wave pattern was clearly the most studied for the longest time, other pattern types were found for limiting as well as very high protein concentrations – not all of them dynamic.[60] Vecchiarelli et al. (2016) identified static "amoeba" patterns at high, and dynamic "mushroom" or "burst" patterns at low protein concentrations.[60]

Importantly, in 2019, Glock et al. reported [72] a technical point that placement of the residual tags from protein purification on MinE had a drastic influence on pattern formation. They showed that positioning the purification tag in proximity to MinE's N-terminal MTS rendered the protein more active in its ATPase-activating function, which lead to the surface patterns leaning heavily towards the so-far predominantly observed traveling wave patterns. Relocating or removing the purification tag, however, led to the observation of several previously unknown static patterns, subsequently classified as "spots", "inverse spots", "labyrinth" and "mesh" patterns.[72]

The open challenge in Min research remains to reconce all of these recent as well as upcoming experimental findings under the umbrella of a single model. This model would need to include all (relevant) intermolecular interactions between Min proteins as well as their (environmentally dependent) kinetic rates and properties. Such a model would then, in theory, allow to accurately determine the resulting pattern (or range of possible patterns) in advance of an experiment for any given setting, for situations *in vivo* and *in vitro* alike. Obtaining such a model would be a huge step forward in our understanding of protein pattern formation. Contributing to this research effort is a main motivation of the work presented in this thesis.

REFERENCES

[1] Markus J. Aschwanden et al. “Order out of Randomness: Self-Organization Processes in Astrophysics”. In: *Space Science Reviews* 214.2 (Mar. 2018), p. 55. ISSN: 0038-6308, 1572-9672. DOI: 10.1007/s11214-018-0489-2. URL: http://link.springer.com/10.1007/s11214-018-0489-2 (visited on 02/22/2024).

[2] Shankar C. Venkataramani and Alan C. Newell. “Pattern dark matter and galaxy scaling relations: Is dark matter the self-organized behavior and manifestation of things we already knew?” In: *The European Physical Journal Special Topics* 230.9 (Aug. 2021), pp. 2139–2165. ISSN: 1951-6355, 1951-6401. DOI: 10.1140/epjs/s11734-021-00196-9. URL: https://link.springer.com/10.1140/epjs/s11734-021-00196-9 (visited on 04/07/2022).

[3] Juliane Rosemeier and Peter Spichtinger. “Pattern formation in clouds via Turing instabilities”. en. In: *Mathematics of Climate and Weather Forecasting* 6.1 (Jan. 2020), pp. 75–96. ISSN: 2353-6438. DOI: 10.1515/mcwf-2020-0104. URL: http://access.portico.org/stable?au=phzpj8468gf (visited on 07/12/2024).

[4] Max Rietkerk and Johan van de Koppel. “Regular pattern formation in real ecosystems”. In: *Trends in Ecology & Evolution* 23.3 (Mar. 2008), pp. 169–175. ISSN: 01695347. DOI: 10.1016/j.tree.2007.10.013. URL: https://linkinghub.elsevier.com/retrieve/pii/S0169534708000281 (visited on 04/07/2022).

[5] Robert M. Pringle and Corina E. Tarnita. “Spatial Self-Organization of Ecosystems: Integrating Multiple Mechanisms of Regular-Pattern Formation”. In: *Annual Review of Entomology* 62.1 (Jan. 31, 2017), pp. 359–377. ISSN: 0066-4170, 1545-4487. DOI: 10.1146/annurev-ento-031616-035413. URL: http://www.annualreviews.org/doi/10.1146/annurev-ento-031616-035413 (visited on 01/08/2020).

[6] Shigeru Kondo, Masakatsu Watanabe, and Seita Miyazawa. “Studies of Turing pattern formation in zebrafish skin”. In: *Philosophical Transactions of the Royal Society A: Mathematical, Physical and Engineering Sciences* 379.2213 (Dec. 27, 2021), p. 20200274. ISSN: 1364-503X, 1471-2962. DOI: 10.1098/rsta.2020.0274. URL: https://royalsocietypublishing.org/doi/10.1098/rsta.2020.0274 (visited on 12/09/2021).

[7] Marcelo De Gomensoro Malheiros, Henrique Fensterseifer, and Marcelo Walter. “The leopard never changes its spots”. In: 39.4 (Aug. 2022).

[8] Shigeru Kondo and Takashi Miura. “Reaction-Diffusion Model as a Framework for Understanding Biological Pattern Formation”. In: *Science* 329.5999 (Sept. 24, 2010), pp. 1616–1620. ISSN: 0036-8075, 1095-9203. DOI: 10.1126/science.1179047. URL: https://www.science.org/doi/10.1126/science.1179047 (visited on 04/07/2022).

[9] François Schweisguth and Francis Corson. “Self-Organization in Pattern Formation”. In: *Developmental Cell* 49.5 (June 2019), pp. 659–677. ISSN: 15345807. DOI: 10.1016/j.devcel.2019.05.019. URL: https://linkinghub.elsevier.com/retrieve/pii/S1534580719303910 (visited on 01/08/2020).

[10] J. Halatek, F. Brauns, and E. Frey. "Self-organization principles of intracellular pattern formation". In: *Philosophical Transactions of the Royal Society B: Biological Sciences* 373.1747 (May 26, 2018), p. 20170107. ISSN: 0962-8436, 1471-2970. DOI: 10.1098/rstb.2017.0107. URL: https://royalsocietypublishing.org/doi/10.1098/rstb.2017.0107 (visited on 11/22/2019).

[11] Alan Turing. "The chemical basis of morphogenesis". In: *Philosophical Transactions of the Royal Society of London. Series B, Biological Sciences* 237.641 (Aug. 14, 1952), pp. 37–72. ISSN: 2054-0280. DOI: 10.1098/rstb.1952.0012. URL: http://www.royalsocietypublishing.org/doi/10.1098/rstb.1952.0012 (visited on 11/22/2019).

[12] Eric Karsenti. "Self-organization in cell biology: a brief history". In: *Nature Reviews Molecular Cell Biology* 9.3 (Mar. 2008), pp. 255–262. ISSN: 1471-0072, 1471-0080. DOI: 10.1038/nrm2357. URL: https://www.nature.com/articles/nrm2357 (visited on 11/17/2023).

[13] Julianne D Halley and David A Winkler. "Consistent concepts of self-organization and self-assembly". In: *Complexity* 14.2 (2008), pp. 10–17.

[14] Philip Ball. "Forging patterns and making waves from biology to geology: a commentary on Turing (1952) 'The chemical basis of morphogenesis'". In: *Philosophical Transactions of the Royal Society B: Biological Sciences* 370.1666 (Apr. 19, 2015), p. 20140218. ISSN: 0962-8436, 1471-2970. DOI: 10.1098/rstb.2014.0218. URL: https://royalsocietypublishing.org/doi/10.1098/rstb.2014.0218 (visited on 02/22/2024).

[15] Vladimir K. Vanag and Irving R. Epstein. "Pattern formation mechanisms in reaction-diffusion systems". In: *The International Journal of Developmental Biology* 53.5 (2009), pp. 673–681. ISSN: 0214-6282. DOI: 10.1387/ijdb.072484vv. URL: http://www.intjdevbiol.com/paper.php?doi=072484vv (visited on 04/12/2022).

[16] Andrea Cassani, Alessandro Monteverde, and Marco Piumetti. "Belousov-Zhabotinsky type reactions: the non-linear behavior of chemical systems". In: *Journal of Mathematical Chemistry* 59.3 (Mar. 2021), pp. 792–826. ISSN: 0259-9791, 1572-8897. DOI: 10.1007/s10910-021-01223-9. URL: https://link.springer.com/10.1007/s10910-021-01223-9 (visited on 04/08/2024).

[17] Tom Burkart et al. "Control of protein-based pattern formation via guiding cues". In: *Nature Reviews Physics* (May 16, 2022). ISSN: 2522-5820. DOI: 10.1038/s42254-022-00461-3. URL: https://www.nature.com/articles/s42254-022-00461-3 (visited on 05/25/2022).

[18] Dominik Thalmeier, Jacob Halatek, and Erwin Frey. "Geometry induced protein pattern formation: Supplement". In: (2016), p. 8.

[19] A. Gierer and H. Meinhardt. "A theory of biological pattern formation". In: *Kybernetik* 12.1 (Dec. 1972), pp. 30–39. ISSN: 0023-5946. DOI: 10.1007/BF00289234. URL: https://link.springer.com/10.1007/BF00289234 (visited on 02/22/2024).

[20] Zoe R. Sudderick and James D. Glover. “Periodic pattern formation during embryonic development”. In: *Biochemical Society Transactions* 52.1 (Feb. 28, 2024), pp. 75–88. ISSN: 0300-5127, 1470-8752. DOI: 10.1042/BST20230197. URL: https://portlandpress.com/biochemsoctrans/article/52/1/75/233994/Periodic-pattern-formation-during-embryonic (visited on 04/17/2024).

[21] Sophie Tschirpke et al. *A guide to the in vitro reconstitution of Cdc42 GTPase activity and its regulation*. preprint. Biochemistry, Apr. 24, 2023. DOI: 10.1101/2023.04.24.538075. URL: http://biorxiv.org/lookup/doi/10.1101/2023.04.24.538075 (visited on 11/17/2023).

[22] Beatrice Ramm, Tamara Heermann, and Petra Schwille. “The E. coli MinCDE system in the regulation of protein patterns and gradients”. In: *Cellular and Molecular Life Sciences* 76.21 (Nov. 2019), pp. 4245–4273. ISSN: 1420-682X, 1420-9071. DOI: 10.1007/s00018-019-03218-x. URL: http://link.springer.com/10.1007/s00018-019-03218-x (visited on 11/22/2019).

[23] Carsten Hoege and Anthony A. Hyman. “Principles of PAR polarity in Caenorhabditis elegans embryos”. In: *Nature Reviews Molecular Cell Biology* 14.5 (May 2013), pp. 315–322. ISSN: 1471-0072, 1471-0080. DOI: 10.1038/nrm3558. URL: http://www.nature.com/articles/nrm3558 (visited on 10/14/2021).

[24] Adrián Merino-Salomón, Leon Babl, and Petra Schwille. “Self-organized protein patterns: The MinCDE and ParABS systems”. In: *Current Opinion in Cell Biology* 72 (Oct. 2021), pp. 106–115. ISSN: 09550674. DOI: 10.1016/j.ceb.2021.07.001. URL: https://linkinghub.elsevier.com/retrieve/pii/S0955067421000788 (visited on 07/27/2022).

[25] Lawrence I Rothfield and Chun-Rui Zhao. “How Do Bacteria Decide Where to Divide?” In: *Cell* 84.2 (Jan. 1996), pp. 183–186. ISSN: 00928674. DOI: 10.1016/S0092-8674(00)80971-X. URL: https://linkinghub.elsevier.com/retrieve/pii/S009286740080971X (visited on 11/17/2023).

[26] Helge Feddersen et al. “Dynamics of the Bacillus subtilis Min System”. In: *mBio* 12.2 (Apr. 27, 2021). Ed. by Houra Merrikh, e00296–21. ISSN: 2150-7511. DOI: 10.1128/mBio.00296-21. URL: https://journals.asm.org/doi/10.1128/mBio.00296-21 (visited on 04/08/2024).

[27] Lauren R. Hammond, Maria L. White, and Prahathees J. Eswara. “¡vIVA la DivIVA!” In: *Journal of Bacteriology* 201.21 (Nov. 2019). Ed. by William Margolin. ISSN: 0021-9193, 1098-5530. DOI: 10.1128/JB.00245-19. URL: https://journals.asm.org/doi/10.1128/JB.00245-19 (visited on 11/10/2021).

[28] J. Halatek and E. Frey. “Rethinking pattern formation in reaction–diffusion systems”. In: *Nature Physics* 14.5 (May 2018), pp. 507–514. ISSN: 1745-2473, 1745-2481. DOI: 10.1038/s41567-017-0040-5. URL: http://www.nature.com/articles/s41567-017-0040-5 (visited on 11/27/2019).

[29] Erwin Frey et al. “Protein Pattern Formation”. In: *Physics of Biological Membranes*. Ed. by Patricia Bassereau and Pierre Sens. Cham: Springer International Publishing, 2018, pp. 229–260. ISBN: 978-3-030-00628-0 978-3-030-00630-3. DOI: 10.1007/978-3-030-00630-3_10. URL: http://link.springer.com/10.1007/978-3-030-00630-3_10 (visited on 10/14/2021).

[30] H. I. Adler et al. “MINIATURE *escherichia coli* CELLS DEFICIENT IN DNA”. In: *Proceedings of the National Academy of Sciences* 57.2 (Feb. 1967), pp. 321–326. ISSN: 0027-8424, 1091-6490. DOI: 10.1073/pnas.57.2.321. URL: https://pnas.org/doi/full/10.1073/pnas.57.2.321 (visited on 11/17/2023).

[31] Piet A.J. De Boer, Robin E. Crossley, and Lawrence I. Rothfield. “A division inhibitor and a topological specificity factor coded for by the minicell locus determine proper placement of the division septum in E. coli”. In: *Cell* 56.4 (Feb. 1989), pp. 641–649. ISSN: 00928674. DOI: 10.1016/0092-8674(89)90586-2. URL: https://linkinghub.elsevier.com/retrieve/pii/0092867489905862 (visited on 04/16/2024).

[32] H. Meinhardt and P. A. J. de Boer. “Pattern formation in Escherichia coli: A model for the pole-to-pole oscillations of Min proteins and the localization of the division site”. In: *Proceedings of the National Academy of Sciences* 98.25 (Dec. 4, 2001), pp. 14202–14207. ISSN: 0027-8424, 1091-6490. DOI: 10.1073/pnas.251216598. URL: http://www.pnas.org/cgi/doi/10.1073/pnas.251216598 (visited on 11/22/2021).

[33] David M. Raskin and Piet A. J. De Boer. “Rapid pole-to-pole oscillation of a protein required for directing division to the middle of *Escherichia coli*”. In: *Proceedings of the National Academy of Sciences* 96.9 (Apr. 27, 1999), pp. 4971–4976. ISSN: 0027-8424, 1091-6490. DOI: 10.1073/pnas.96.9.4971. URL: https://pnas.org/doi/full/10.1073/pnas.96.9.4971 (visited on 04/16/2024).

[34] Zonglin Hu and Joe Lutkenhaus. “Topological regulation of cell division in *Escherichia coli* involves rapid pole to pole oscillation of the division inhibitor MinC under the control of MinD and MinE”. In: *Molecular Microbiology* 34.1 (Oct. 1999), pp. 82–90. ISSN: 0950-382X, 1365-2958. DOI: 10.1046/j.1365-2958.1999.01575.x. URL: https://onlinelibrary.wiley.com/doi/10.1046/j.1365-2958.1999.01575.x (visited on 04/18/2024).

[35] David M. Raskin and Piet A. J. De Boer. “MinDE-Dependent Pole-to-Pole Oscillation of Division Inhibitor MinC in *Escherichia coli*”. In: *Journal of Bacteriology* 181.20 (Oct. 15, 1999), pp. 6419–6424. ISSN: 0021-9193, 1098-5530. DOI: 10.1128/JB.181.20.6419-6424.1999. URL: https://journals.asm.org/doi/10.1128/JB.181.20.6419-6424.1999 (visited on 04/16/2024).

[36] Joe Lutkenhaus. “Dynamic proteins in bacteria”. In: ().

[37] Karsten Kruse, Martin Howard, and William Margolin. “An experimentalist’s guide to computational modelling of the Min system”. In: *Molecular Microbiology* 63.5 (Mar. 2007), pp. 1279–1284. ISSN: 0950-382X, 1365-2958. DOI: 10.1111/j.1365-2958.2007.05607.x. URL: https://onlinelibrary.wiley.com/doi/10.1111/j.1365-2958.2007.05607.x (visited on 10/14/2021).

[38] Z. Hu, E. P. Gogol, and J. Lutkenhaus. "Dynamic assembly of MinD on phospholipid vesicles regulated by ATP and MinE". In: *Proceedings of the National Academy of Sciences* 99.10 (May 14, 2002), pp. 6761–6766. ISSN: 0027-8424, 1091-6490. DOI: 10.1073/pnas.102059099. URL: http://www.pnas.org/cgi/doi/10.1073/pnas.102059099 (visited on 11/22/2021).

[39] K. Suefuji, R. Valluzzi, and D. RayChaudhuri. "Dynamic assembly of MinD into filament bundles modulated by ATP, phospholipids, and MinE". In: *Proceedings of the National Academy of Sciences* 99.26 (Dec. 24, 2002), pp. 16776–16781. ISSN: 0027-8424, 1091-6490. DOI: 10.1073/pnas.262671699. URL: http://www.pnas.org/cgi/doi/10.1073/pnas.262671699 (visited on 11/22/2021).

[40] Laura L. Lackner, David M. Raskin, and Piet A. J. de Boer. "ATP-Dependent Interactions between *Escherichia coli* Min Proteins and the Phospholipid Membrane In Vitro". In: *Journal of Bacteriology* 185.3 (Feb. 2003), pp. 735–749. ISSN: 0021-9193, 1098-5530. DOI: 10.1128/JB.185.3.735-749.2003. URL: https://journals.asm.org/doi/10.1128/JB.185.3.735-749.2003 (visited on 11/22/2021).

[41] G Meacci et al. "Mobility of Min-proteins in Escherichia coli measured by fluorescence correlation spectroscopy". In: *Physical Biology* 3.4 (Nov. 2006), p. 255. DOI: 10.1088/1478-3975/3/4/003. URL: https://dx.doi.org/10.1088/1478-3975/3/4/003.

[42] Lukas Wettmann, Mike Bonny, and Karsten Kruse. "Effects of geometry and topography on Min-protein dynamics". In: *PLOS ONE* 13.8 (Aug. 30, 2018). Ed. by Lev Tsimring, e0203050. ISSN: 1932-6203. DOI: 10.1371/journal.pone.0203050. URL: https://dx.plos.org/10.1371/journal.pone.0203050 (visited on 10/13/2022).

[43] Wei Wu et al. "Determination of the structure of the MinD–ATP complex reveals the orientation of MinD on the membrane and the relative location of the binding sites for MinE and MinC". In: *Molecular Microbiology* 79.6 (Mar. 2011), pp. 1515–1528. ISSN: 0950-382X, 1365-2958. DOI: 10.1111/j.1365-2958.2010.07536.x. URL: https://onlinelibrary.wiley.com/doi/10.1111/j.1365-2958.2010.07536.x (visited on 04/19/2024).

[44] Houman Ghasriani et al. "Appropriation of the MinD protein-interaction motif by the dimeric interface of the bacterial cell division regulator MinE". en. In: *Proceedings of the National Academy of Sciences* 107.43 (Oct. 2010), pp. 18416–18421. ISSN: 0027-8424, 1091-6490. DOI: 10.1073/pnas.1007141107. URL: https://pnas.org/doi/full/10.1073/pnas.1007141107 (visited on 07/13/2024).

[45] Jonas Denk et al. "MinE conformational switching confers robustness on self-organized Min protein patterns". In: *Proceedings of the National Academy of Sciences* 115.18 (May 1, 2018), pp. 4553–4558. ISSN: 0027-8424, 1091-6490. DOI: 10.1073/pnas.1719801115. URL: http://www.pnas.org/lookup/doi/10.1073/pnas.1719801115 (visited on 07/28/2020).

[46] Martin Loose et al. “Min protein patterns emerge from rapid rebinding and membrane interaction of MinE”. In: *Nature Structural & Molecular Biology* 18.5 (May 2011), pp. 577–583. ISSN: 1545-9993, 1545-9985. DOI: 10.1038/nsmb.2037. URL: http://www.nature.com/articles/nsmb.2037 (visited on 11/22/2019).

[47] Kiyoshi Mizuuchi and Anthony G Vecchiarelli. “Mechanistic insights of the Min oscillator via cell-free reconstitution and imaging”. In: *Physical Biology* 15.3 (Mar. 1, 2018), p. 031001. ISSN: 1478-3975. DOI: 10.1088/1478-3975/aa9e5e. URL: http://stacks.iop.org/1478-3975/15/i=3/a=031001?key=crossref.18bf29cccb7b7223b142cdbecfc43d0d (visited on 11/22/2019).

[48] Yaron Caspi and Cees Dekker. “Mapping out Min protein patterns in fully confined fluidic chambers”. In: *eLife* 5 (Nov. 25, 2016), e19271. ISSN: 2050-084X. DOI: 10.7554/eLife.19271. URL: https://elifesciences.org/articles/19271 (visited on 11/22/2019).

[49] Fridtjof Brauns et al. “Bulk-surface coupling identifies the mechanistic connection between Min-protein patterns in vivo and in vitro”. In: *Nature Communications* 12.1 (Dec. 2021), p. 3312. ISSN: 2041-1723. DOI: 10.1038/s41467-021-23412-5. URL: http://www.nature.com/articles/s41467-021-23412-5 (visited on 06/03/2021).

[50] Anthony G. Vecchiarelli et al. “Differential affinities of MinD and MinE to anionic phospholipid influence Min patterning dynamics *in vitro*: Flow and lipid composition effects on Min patterning”. In: *Molecular Microbiology* 93.3 (Aug. 2014), pp. 453–463. ISSN: 0950382X. DOI: 10.1111/mmi.12669. URL: http://doi.wiley.com/10.1111/mmi.12669 (visited on 11/29/2019).

[51] Lukas Wettmann and Karsten Kruse. “The Min-protein oscillations in *Escherichia coli*: an example of self-organized cellular protein waves”. In: *Philosophical Transactions of the Royal Society B: Biological Sciences* 373.1747 (May 26, 2018), p. 20170111. ISSN: 0962-8436, 1471-2970. DOI: 10.1098/rstb.2017.0111. URL: https://royalsocietypublishing.org/doi/10.1098/rstb.2017.0111 (visited on 12/01/2021).

[52] Jaan Männik et al. “Robustness and accuracy of cell division in *Escherichia coli* in diverse cell shapes”. In: *Proceedings of the National Academy of Sciences* 109.18 (May 2012), pp. 6957–6962. ISSN: 0027-8424, 1091-6490. DOI: 10.1073/pnas.1120854109. URL: https://pnas.org/doi/full/10.1073/pnas.1120854109 (visited on 10/13/2022).

[53] Fabai Wu et al. “Symmetry and scale orient Min protein patterns in shaped bacterial sculptures”. In: *Nature Nanotechnology* 10.8 (Aug. 2015), pp. 719–726. ISSN: 1748-3387, 1748-3395. DOI: 10.1038/nnano.2015.126. URL: http://www.nature.com/articles/nnano.2015.126 (visited on 01/16/2020).

[54] Fabai Wu et al. “Multistability and dynamic transitions of intracellular Min protein patterns”. In: *Molecular Systems Biology* 12.6 (June 2016), p. 873. ISSN: 1744-4292, 1744-4292. DOI: 10.15252/msb.20156724. URL: https://www.embopress.org/doi/10.15252/msb.20156724 (visited on 10/07/2023).

[55] I. Hayashi. “Structural and functional studies of MinD ATPase: implications for the molecular recognition of the bacterial cell division apparatus”. In: *The EMBO Journal* 20.8 (Apr. 17, 2001), pp. 1819–1828. ISSN: 14602075. DOI: 10.1093/emboj/20.8.1819. URL: http://emboj.embopress.org/cgi/doi/10.1093/emboj/20.8.1819 (visited on 12/01/2021).

[56] Eugenia Mileykovskaya et al. “Effects of Phospholipid Composition on MinD-Membrane Interactions in Vitro and in Vivo”. In: *Journal of Biological Chemistry* 278.25 (June 2003), pp. 22193–22198. ISSN: 00219258. DOI: 10.1074/jbc.M302603200. URL: https://linkinghub.elsevier.com/retrieve/pii/S0021925820862504 (visited on 11/22/2021).

[57] Shirley Mazor et al. “Mutual effects of MinD–membrane interaction: I. Changes in the membrane properties induced by MinD binding”. In: *Biochimica et Biophysica Acta (BBA) - Biomembranes* 1778.11 (Nov. 2008), pp. 2496–2504. ISSN: 00052736. DOI: 10.1016/j.bbamem.2008.08.003. URL: https://linkinghub.elsevier.com/retrieve/pii/S0005273608002393 (visited on 11/22/2021).

[58] Lars D. Renner and Douglas B. Weibel. “MinD and MinE Interact with Anionic Phospholipids and Regulate Division Plane Formation in Escherichia coli”. In: *Journal of Biological Chemistry* 287.46 (Nov. 2012), pp. 38835–38844. ISSN: 00219258. DOI: 10.1074/jbc.M112.407817. URL: https://linkinghub.elsevier.com/retrieve/pii/S0021925820623468 (visited on 11/22/2021).

[59] Martin Loose et al. “Spatial Regulators for Bacterial Cell Division Self-Organize into Surface Waves in Vitro”. In: *Science* 320.5877 (May 9, 2008), pp. 789–792. ISSN: 0036-8075, 1095-9203. DOI: 10.1126/science.1154413. URL: https://www.science.org/doi/10.1126/science.1154413 (visited on 11/17/2021).

[60] Anthony G. Vecchiarelli et al. “Membrane-bound MinDE complex acts as a toggle switch that drives Min oscillation coupled to cytoplasmic depletion of MinD”. In: *Proceedings of the National Academy of Sciences* 113.11 (Mar. 15, 2016), E1479–E1488. ISSN: 0027-8424, 1091-6490. DOI: 10.1073/pnas.1600644113. URL: http://www.pnas.org/lookup/doi/10.1073/pnas.1600644113 (visited on 11/22/2019).

[61] Katja Zieske, Jakob Schweizer, and Petra Schwille. “Surface topology assisted alignment of Min protein waves”. In: *FEBS Letters* 588.15 (Aug. 1, 2014), pp. 2545–2549. ISSN: 00145793. DOI: 10.1016/j.febslet.2014.06.026. URL: http://doi.wiley.com/10.1016/j.febslet.2014.06.026 (visited on 01/14/2020).

[62] Laeschkir Würthner et al. “Bridging scales in a multiscale pattern-forming system”. In: *Proceedings of the National Academy of Sciences* 119.33 (Aug. 16, 2022), e2206888119. ISSN: 0027-8424, 1091-6490. DOI: 10.1073/pnas.2206888119. URL: https://pnas.org/doi/full/10.1073/pnas.2206888119 (visited on 11/02/2022).

[63] Yu-Ling Shih et al. “Active Transport of Membrane Components by Self-Organization of the Min Proteins”. In: *Biophysical Journal* 116.8 (Apr. 2019), pp. 1469–1482. ISSN: 00063495. DOI: 10.1016/j.bpj.2019.03.011. URL: https://linkinghub.elsevier.com/retrieve/pii/S0006349519301973 (visited on 10/13/2022).

[64] Beatrice Ramm et al. “A diffusiophoretic mechanism for ATP-driven transport without motor proteins”. In: *Nature Physics* 17.7 (July 2021), pp. 850–858. ISSN: 1745-2473, 1745-2481. DOI: 10.1038/s41567-021-01213-3. URL: http://www.nature.com/articles/s41567-021-01213-3 (visited on 10/05/2021).

[65] Beatrice Ramm et al. “The MinDE system is a generic spatial cue for membrane protein distribution in vitro”. In: *Nature Communications* 9.1 (Dec. 2018), p. 3942. ISSN: 2041-1723. DOI: 10.1038/s41467-018-06310-1. URL: http://www.nature.com/articles/s41467-018-06310-1 (visited on 01/17/2020).

[66] Tamara Heermann et al. “Local Self-Enhancement of MinD Membrane Binding in Min Protein Pattern Formation”. In: *Journal of Molecular Biology* 432.10 (May 2020), pp. 3191–3204. ISSN: 00222836. DOI: 10.1016/j.jmb.2020.03.012. URL: https://linkinghub.elsevier.com/retrieve/pii/S0022283620302333 (visited on 10/14/2021).

[67] Laeschkir Würthner et al. “Bridging scales in a multiscale pattern-forming system”. In: *arXiv:2111.12043 [nlin, physics:physics]* (Nov. 24, 2021). arXiv: 2111.12043. URL: http://arxiv.org/abs/2111.12043 (visited on 11/29/2021).

[68] Martin Loose, Karsten Kruse, and Petra Schwille. “Protein Self-Organization: Lessons from the Min System”. In: *Annual Review of Biophysics* 40.1 (June 9, 2011), pp. 315–336. ISSN: 1936-122X, 1936-1238. DOI: 10.1146/annurev-biophys-042910-155332. URL: https://www.annualreviews.org/doi/10.1146/annurev-biophys-042910-155332 (visited on 02/14/2024).

[69] Atsushi Miyagi et al. “High-Speed Atomic Force Microscopy Reveals the Inner Workings of the MinDE Protein Oscillator”. In: *Nano Letters* 18.1 (Jan. 10, 2018), pp. 288–296. ISSN: 1530-6984, 1530-6992. DOI: 10.1021/acs.nanolett.7b04128. URL: https://pubs.acs.org/doi/10.1021/acs.nanolett.7b04128 (visited on 06/28/2022).

[70] Tamara Heermann et al. “Mass-sensitive particle tracking to elucidate the membrane-associated MinDE reaction cycle”. In: *Nature Methods* 18.10 (Oct. 2021), pp. 1239–1246. ISSN: 1548-7091, 1548-7105. DOI: 10.1038/s41592-021-01260-x. URL: https://www.nature.com/articles/s41592-021-01260-x (visited on 10/15/2021).

[71] Eric D. B. Foley et al. “Mass photometry enables label-free tracking and mass measurement of single proteins on lipid bilayers”. In: *Nature Methods* 18.10 (Oct. 2021), pp. 1247–1252. ISSN: 1548-7091, 1548-7105. DOI: 10.1038/s41592-021-01261-w. URL: https://www.nature.com/articles/s41592-021-01261-w (visited on 04/19/2024).

[72] Philipp Glock et al. “Stationary Patterns in a Two-Protein Reaction-Diffusion System”. In: *ACS Synthetic Biology* 8.1 (Jan. 18, 2019), pp. 148–157. ISSN: 2161-5063, 2161-5063. DOI: 10.1021/acssynbio.8b00415. URL: https://pubs.acs.org/doi/10.1021/acssynbio.8b00415 (visited on 11/05/2021).

2

QUANTITATIVE ANALYSIS OF SURFACE WAVE PATTERNS OF MIN PROTEINS

The Min protein system is arguably the best-studied model systems for biological pattern formation. It exhibits pole-to-pole oscillations in E. coli bacteria as well as a variety of surface wave patterns in in vitro reconstitutions. Such Min surface wave patterns pose particular challenges to quantification as they are typically only semi-periodic and non-stationary. Here, we present a methodology for quantitatively analyzing such Min patterns, aiming for reproducibility, user-independence, and easy usage. After introducing pattern-feature definitions and image-processing concepts, we present an analysis pipeline where we use autocorrelation analysis to extract global parameters such as the average spatial wavelength and oscillation period. Subsequently, we describe a method that uses flow-field analysis to extract local properties such as the wave propagation velocity. We provide descriptions on how to practically implement these quantification tools and provide Python code that can directly be used to perform analysis of Min patterns.

This chapter has been published in Frontiers in Physics **10**, 930811 (2022) by Sabrina MEINDLHUMER, Jacob KERSSEMAKERS and Cees DEKKER.

2.1. INTRODUCTION

Pattern formation is a fascinating basic phenomenon that occurs across many scales, from galaxy formation all the way down to embryology and beyond. In chemistry and biology, self-organizing patterns emerge from the combination of specific intermolecular interactions and molecular transport processes.[1] Acting together, reaction and diffusion can result in inhomogeneous concentrations of molecules that constitute spatiotemporal patterns.[2] Such patterns provide useful functions as they impose directional or positional preferences on processes in cells and tissues.[3, 4, 5] Indeed, pattern formation is of vital importance for the description of a multitude of biological phenomena, ranging from bacterial and eukaryotic cell division[4], to embryonic development of multicellular organisms[3, 5], up to entire ecosystems[6].

For example, in *E. coli* bacteria, a pattern-forming mechanism acts to determine the central position of the rod-shaped cell, ensuring that the required protein-machinery is guided to the correct location to start a fully symmetric division into daughter cells. This particular pattern-forming system, formed by the Min proteins, relies on a reaction-diffusion mechanism and is widely considered to be the best-studied model system for intracellular pattern formation.[4, 7] As the moment of cell division approaches, Min proteins will periodically bind and unbind the inner membrane at the poles of the bacterium. When visualized by fluorescent labelling, the Min proteins are observed to oscillate from pole to pole with a period of approximately one minute. As a result, their temporally averaged concentration is minimized at the mid-cell location. One component of the Min system, MinC, exerts an inhibitory effect on a component of the cell division machinery. As the lowest concentration of MinC is found at mid-cell, the proteins that facilitate cell division will preferably bind there, and the cell gets divided evenly.[8]

While MinC is important for this downstream process, the pattern as such is formed by only two proteins, MinD and MinE. MinD is an ATPase that upon binding ATP can attach to the membrane, while MinE is its ATPase activator. MinE can bind to the membrane upon recruitment by membrane-bound MinD and subsequently facilitate MinD's ATP-consuming membrane detachment.[9, 10, 11, 7] The Min proteins thus constitute a pattern-forming model system with only 2 essential components, which is appealingly simple for both theoretical and experimental studies. A wide range of experiments have been reported that explore particular features of the Min system.[12, 9, 13] A multitude of Min protein models[14, 15] have been proposed, and continue to be developed as new molecular details are discovered.[16, 17, 10, 18]

Arguably, the most iconic images of Min protein patterns present themselves in *in vitro* studies of these proteins. Such experiments typically reconstitute Min proteins on supported lipid bilayers on a glass slide, with a fraction of Min proteins carrying a fluorescent label.[9] Min proteins exhibit mesmerizing dynamic membrane patterns in such an artificial *in vitro* environment: Over a wide range of concentrations, one encounters characteristic patterns such as rotating spirals or travelling planar wave fronts, with typical wavelengths in the order of tens of micrometers.[9, 12] An example is given in Fig. 2.1A, showing a snapshot image for labelled MinE. Examination of this image reveals vari-

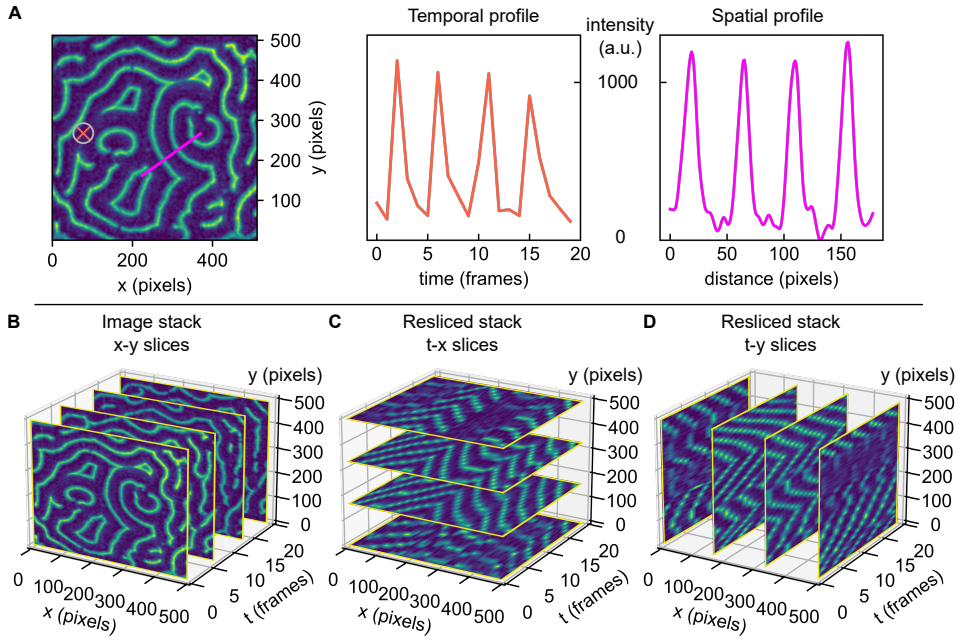


Figure 2.1: **Min acquisition stacks contain spatial and temporal information on the pattern.** Min protein surface patterns are dynamic in space and time. Min pattern acquisitions are 3D (x, y, t) matrices, containing the measured fluorescence intensity values for different coordinates. The information contained within this matrix can be accessed and visualized differently, dependent on what parameters are of interest. **A** Left: Example of a real MinE protein surface pattern. Middle: Fluorescence intensity over time at the surface position highlighted by orange cross in the image, for an image stack comprising 20 frames. Right: Fluorescence intensity trace along surface cross-section highlighted in magenta in the image. **B** 3D view of a Min protein acquisition stack with four example images (standard x-y slices) shown for demonstration. **C** 3D view of slice from A, resliced along constant y-directions, creating t-x slices. **D** 3D view of slice from A, resliced along constant x-directions, creating t-y slices.

ous features that are typical for Min patterns. For example, Min proteins exhibit planar waves, but these occur only locally and become less correlated on longer length scales. Min patterns thus organize in surface domains with one dominating type of pattern, such as spiral or planar wave fronts traveling in a certain direction. Boundaries between domains are recognizable by phase shifts.

Thorough quantitative analysis of Min patterns is nontrivial. While visual inspection is often sufficient to deduce the basic Min pattern, quantitative information is required to extract trends in the patterns' characteristic parameters, such as the average or local wavelength, oscillation period, or propagation velocity. For perfectly periodic Min patterns with only one type of pattern with a set orientation over the entire imaged sur-

face, analysis can easily be achieved by Fourier analysis. However, this is most often not possible due to the fact that real Min patterns are usually a patchwork of domains separated by phase-shift boundaries. The semi-periodic nature of Min patterns makes image analysis challenging, and so far there are no clear guidelines or standards on how to realise this without user bias. Extraction of quantitative parameters is typically performed by manual selection of individual surface positions,[19] line traces[20], or rectangular regions-of-interest[21, 12]. Plotting of fluorescence intensity along a defined axis allows to determine the pattern's local wavelength. Similarly, the temporal characteristics such as its oscillation period and wave propagation velocity can be measured by monitoring the intensity versus time at one spot,[19] see Fig. 2.1A for an illustration of these possible practices.

While these approaches are widely used, such manual selection is cumbersome, prone to user bias, and it underuses the vast amount of data in videos of Min patterns that could improve data accuracy. In the example given in Fig. 2.1A, the intensity profile of denoted line trace (magenta) shows approximately equidistant peaks that indicate the wavelength. However, selection of another spot or a slightly different trace that is not perpendicular to the wave fronts would have led to a deviating result. Furthermore, note how extending the trace over the region of the spiral domain would erroneously lead to the inclusion of shorter or longer wavelengths. Notably, these domain boundaries do not always remain stationary over the time of acquisition, and hence line traces would have to be carefully adapted for every single frame so as to adapt to possible reorientations of wave fronts (compare for example the domain variation over time in Supplementary Fig. 2.5A). In view of all these limitations, we conclude that an automated user-independent analysis of large regions is preferable, as it allows to obtain solid statistics on the patterns' characteristic features.

In this paper, we present a methodology for analyzing Min patterns that aims for thorough quantitation, easy usage, reproducibility, and user independence. We start by briefly proposing strategies for image cleaning. After that, we proceed to presenting strategies for global and local analysis of Min protein surface patterns. For extracting global parameters, we rely on calculating autocorrelation maps to examine the average periodic features of Min patterns, following other groups[16] as well as our own.[18] We treat a Min pattern acquisition stack as a threedimensional matrix containing information in space and time (x, y, t), and we propose strategies on how to efficiently access this information. Subsequently, we introduce an analysis pipeline which allows to quantify local properties of Min patterns, such as the wave propagation speed and direction of propagation. The approach we present here relies on the identification of individual wave crest points and their movement from one frame to the next. While other tools have been used to extract the directional preferences of Min surface wave propagation[22], our approach allows not only for obtaining large distributions of parameters, but also for accessing multiple parameters at the same time. For both global and local analysis, we offer guidance to researchers who would like to implement similar strategies for their own applications. Code is openly available and provided in Python 3[23].

2.2. IMAGE PROCESSING METHODOLOGY

Min patterns are phenomena that occur at lipid membranes. Accordingly, the most suitable forms of microscopy for *in vitro* experiments are those that acquire an imaging slab along the membrane-coated surface. Examples are total internal reflection fluorescence (TIRF) microscopy,[19, 12, 16, 24] laser scanning confocal microscopy[21, 22, 20, 25] or spinning disc confocal microscopy[18, 26]. Epifluorescence microscopy[27] is generally not suitable as it leads to high background signal from the fluorescent molecules in the bulk, significantly reducing the pattern's quality or even making it unrecognizable.

"Image cleaning" includes procedures and operations performed on microscope data that improve the overall quality of the image by making the features of interest better recognizable, while not distorting or removing essential components. Good image cleaning, where background and spurious contributions are removed, is important for successful quantitative analysis of Min protein patterns, as insufficient cleaning can lead the algorithms to fail to recognize the pattern as such. There are multiple imaging artefacts that need to be corrected. For example, local fluorescent impurities such as protein aggregates may give a static signal that is not part of the Min pattern. And depending on the microscope, illumination is typically inhomogeneous across the field-of-view. In many cases, researchers are interested in the time-dependent behavior of Min patterns, and for this, they acquire images at the same spatial positions at regular time intervals ranging from seconds to minutes. Consequently, Min proteins may bleach due to prolonged imaging.[18] Flow-cell setups with constant bulk flow may pose additional challenges in the form of objects entering and passing through the field-of-view or adhering to and spontaneously detaching from the surface.[26] We empirically found that the occurrence of imaging artefacts can vary strongly, depending on the experimental setup (specifically, the type of sample chamber and the surface preparation), protein concentration (higher concentrations may result in more aggregates), and experiment duration (the longer, the more aggregates occur).

With image cleaning, we aim to tackle all of these issues. Here, we propose a sequence of standard actions that we found to yield overall good results for a time series (several frames of the same sample position saved sequentially in an image stack) of images I_{movie} of *in vitro* Min surface patterns. Our protocol involves the following steps:

- Correct for fluorescence bleaching by normalizing each frame to its mean intensity value.
- Create an 'illumination correction map' I_{illum} by smoothing and averaging all movie images, and normalizing the images to their maximum intensity.
- Create a static background image I_{stat} by averaging over all the moving (surface pattern) features of all images in the stack. This background image then only contains static fluorescent features such as local specks, holes, and scratches.
- Correct each image via the following image operation: $I_{cor} = (I_{movie} - I_{stat})/I_{illum}$.
- At this point, there may still be some artefacts left, for example, those that appeared during the acquisition time and might thus not have been included in the static background image. Therefore, remaining bright or dark artefacts can be re-

moved manually or by thresholding.
– Images can finally be slightly smoothed to diminish effect of sharp edges and artefacts from the latter cropping.

In cases where it is required to explore Min patterns across very large areas, it may furthermore be of interest to stitch multiple fields-of-view of Min patterns into larger images.[28, 26] If the microscope's software does not offer an automatized solution for this, stitching can be achieved by good bookkeeping and a few lines of code. When planning to stitch images, it can be helpful to choose individual field-of-views in such a way that there is a bit of an overlap (e.g. 5 % of the width) between adjacent areas, as this makes it easier to correctly reassemble the full image afterwards. Note that in general, adjoining areas may not have exactly the same median intensity. Therefore, differences in median intensity levels between individual field-of-views need to be corrected for when assembling the stitched image. This way, the resulting large image will appear more homogeneous in brightness and stitching borders will be less visible.

2.3. PATTERN ANALYSIS STRATEGIES

2.3.1. GLOBAL PARAMETERS

In many cases, researchers are interested in quantifying parameters such as the average spatial wavelength and oscillation period of a Min pattern. For this purpose, they acquire image stacks of Min patterns at a certain surface region (x, y in pixel or distance units) and at regular time-intervals (t in time units or frames). However, the existence of domains within and dynamics of patterns make manual extraction of these parameters a laborsome task, and the results of such analyses (cf. Fig. 2.1A) may suffer from poor statistics and user bias. Here, it is important to realize that what we are interested in are essentially global, image-averaged parameters. In this section, we describe how quantification of such global parameters can be achieved by performing autocorrelation analysis[29] for different slices along time or space coordinates (x-y frames such as in Fig. 2.1B, t-x slices such as in Fig. 2.1C or t-y slices as in Fig. 2.1D). We start with spatial autocorrelation, aiming to quantify the wavelength, and then continue to present how temporal autocorrelation can be used to quantify the oscillation period of a pattern.

GLOBAL WAVELENGTH

Spatial autocorrelation analysis of an image essentially compares each pixel to other pixels around it, quantifying their (dis)similarity as a function of distance.[29] Starting from a single image frame as shown in Fig. 2.2A, an autocorrelation map can be calculated using routines from scientific libraries provided for most programming languages. Before performing these operations, the image should be normalized by a series of actions (subtraction of minimum intensity, division by summed-up total intensity and subtraction of mean intensity). Using standard functions supplied within most environments, a twodimensional autocorrelation map *crmx* can be calculated for an image frame *image*

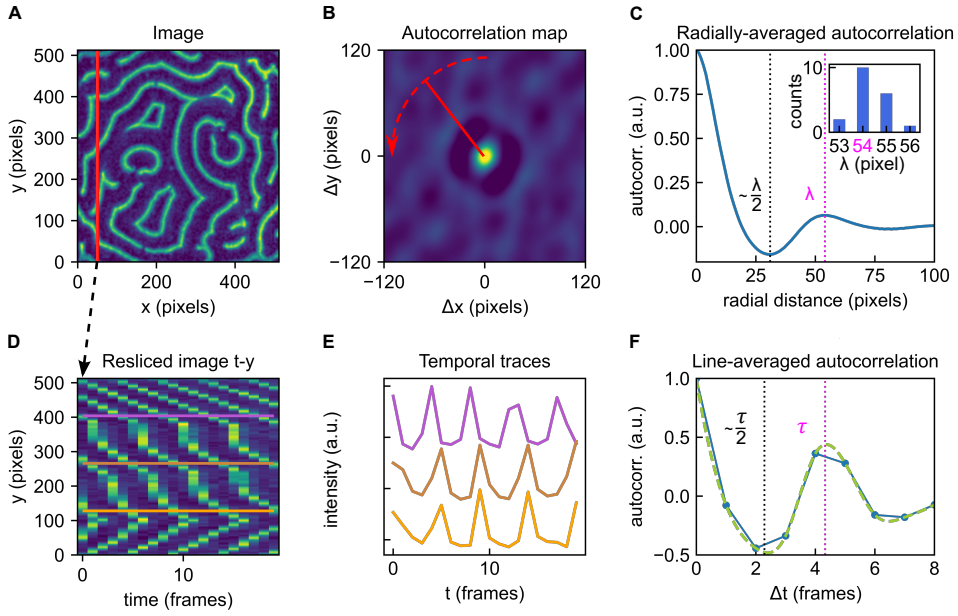


Figure 2.2: **Overview of the autocorrelation analysis pipeline to obtain global parameters. A** Example of a Min protein surface pattern, single frame. Color brightness indicates fluorescence intensity (a.u.). **B** Autocorrelation map of the frame shown in A. Color brightness indicates intensity. Red dashed line indicates radial averaging. **C** Averaged radial profile for the autocorrelation map shown in B. The first maximum after the central peak at distance zero is a measure of the the patterns global characteristic wavelength. The identified wavelength λ is highlighted by the magenta dashed line. The first valley is positioned at approximately $\lambda/2$ (black dashed line). Inset: the analysis presented in A-C can be performed for all individual frames within an image stack. Here, the collected results for 20 consecutive frames (image stack also represented in Fig. 2.1B) are shown in a histogram. A λ of 54 pixels is deduced. **D** Resliced image for fixed x; same as shown in Fig. 2.1D. **E** Selected temporal traces for the y-positions indicated in D. All point-traces shown in the kymograph in D will be included in the autocorrelation trace shown in F. **F** Line-averaged autocorrelation trace from point-traces (such as shown in E) in blue, cubic spline fit used for peak-detection in green. The first maximum after the central peak at $\Delta t = 0$ measures the average characteristic oscillation period of the pattern. The identified global oscillation of $\tau = 4$ frames is highlighted by the magenta dashed line. The first valley is positioned approximately at $\tau/2$ (black dashed line). The analysis pipeline illustrated in D-F can be performed for multiple slices (fixed x or y) of the image stack.

by the transformation

$$crmx = \text{real}(\text{ifft2}(\text{fft2}(image) \cdot \text{conj}(\text{fft2}(image)))) \tag{2.1}$$

with *fft2* calculating a two-dimensional discrete Fourier Transformation, *ifft2* calculating its inverse and *real* and *conj* returning the real part and complex conjugate of the input,

respectively. The four quadrants of the autocorrelation map can be re-arranged so as to place the position ($\Delta x = 0$, $\Delta y = 0$) in the center of the image, rather than having four partial peaks in the corners.

Close examination of the autocorrelation map in Fig. 2.2B reveals a general speckled pattern as well as a ring-shaped feature that is present around the center, which is characterized by a peak in intensity. As this central peak corresponds to a distance of zero, its high intensity is a consequence of the self-correlation of each pixel with itself. Moving radially outward from the center, one observes a decrease in intensity (negative autocorrelation) followed by a peak (positive autocorrelation). An easy way to extract the pattern's dominant wavelength is to perform an angular averaging of the profile around the central peak, where the radial line profiles are averaged over all angles, as illustrated by the red arrow in panel Fig. 2.2B. This leads to a profile as shown in Fig. 2.2C. The first minimum corresponds to the dark value from the autocorrelation map. Here, the first peak after the central peak identifies the pattern's global wavelength λ (magenta dashed line). The valley in fact corresponds to $\sim \lambda/2$ (black dashed line). Note that this value is not exactly half the wavelength, since Min profiles are typically somewhat asymmetrical (cf. Fig. 2.1A).

If, as often is the case, Min patterns display steady-state dynamics, then multiple time frames can be used to provide better statistics in estimating the global wavelength. Min patterns are routinely acquired at constant time intervals, which provides a series of sequential image frames, as represented in Fig. 2.1B. Calculating and analysing autocorrelation maps for several frames within such an image stack allows to collect a distribution of wavelengths, such as the histogram shown in the inset in Fig. 2.2C, summarising results for 20 consecutive frames. Indeed, for dynamic patterns, we recommend performing this analysis strategy for multiple (e.g. 10) frames and averaging the results to obtain a reliable value for the pattern's spatial wavelength. As Min patterns are typically dynamic, it is also possible that their wavelength changes over time, e.g., due to changes in external parameters. The spatial autocorrelation analysis presented here is however equally applicable to static patterns.

Identifying the peaks shown in Fig. 2.2C (and 2.2F, see following section) is trivial to the human eye, but not necessarily straightforward to automate. For our data, we achieved this via a simple algorithm that identifies the second local maximum of the trace. In doing so, we implicitly assume that the trace is fine enough to achieve sufficient accuracy and upsampling is not required. While a curve such as shown in Fig. 2.2C looks smooth to the eye, the original image data had a finite resolution, and accordingly, this curve contains small rags which an algorithm may erroneously detect as a local maximum. In many cases, this issue can be solved by smoothing the curve slightly before subjecting it to peak analysis. This can be achieved by applying a smoothing kernel stretching over a few pixels, for example a small fraction of the image dimension.

To avoid erroneous results, it is recommendable to plot at least one example trace (for one frame) and inspect whether the detected (averaged) wavelength position correctly co-localizes with the valley position. If no clear valley can be identified (characterized by a small or even vanishing intensity difference between the local minimum and maxi-

mum), the pattern may lack a recognizable periodicity, which could be an intrinsic property of the given pattern. Alternatively, this issue can also be encountered if insufficient image cleaning has been applied to the stack before analysis and the pattern is superimposed with too many artifacts, resulting in low autocorrelation. However, we find that this method is generally quite robust towards noise, as shown in Supplementary Fig. 2.6B.

Further, the ratio between image size and spatial wavelength is of importance. In Supplementary Fig. 2.7, a large-scale image stack is sequentially cropped to smaller sizes and global autocorrelation analysis as presented here is performed on randomly selected areas. Based on these results, we find that the standard deviation increases as the image sizes gets smaller, and estimate that the image dimension should be large enough to contain at least 5-10 full wavelengths for the presented algorithm to provide reliable results.

GLOBAL OSCILLATION PERIOD

Another global property of interest is the average oscillation period. This parameter describes how at any given point within the imaged region, the membrane protein density (which is proportional to the fluorescence intensity) can be expected to change over time. We quantify the global oscillation period of a Min pattern following a strategy that closely resembles the one presented for obtaining the global wavelength in the preceding section.

To obtain quantitative information on the temporal dynamics of Min patterns, Min patterns are typically acquired as time series. A time series such as the one shown in Fig. 2.1B is essentially a three dimensional (x, y, t) matrix, containing information on fluorescence intensity as a function of space and time. Notably, for temporal analysis to be reliable, image data has to be acquired at a rate above the Nyquist rate. Min patterns are characterized by point-wise temporal periodicity (compare the time evolution at a random sample position in Fig. 2.1A). Hence, when acquiring a time series, intervals have to be chosen short enough to ensure the acquisition of enough data to adequately depict the pattern's temporal dynamics. If consecutive acquisition times in a series are chosen very far apart, the pattern may even appear to travel towards the opposite direction. According to Nyquist theorem, for patterns of an oscillation period τ, consecutive images in a series have to be acquired at intervals spaced no longer than $\tau/2$ apart. In principle, the shorter these intervals are, the better the temporal dynamics can be characterized. Min protein patterns in lipid bilayer reconstitutions will typically exhibit wave propagation velocities of several $100\,\mathrm{nm\,s^{-1}}$ [12] and wavelengths around $50\,\mu\mathrm{m}$ [9]. This leads to an expected oscillation period in the order of minutes. Acquiring sufficient images to fulfill Nyquist theorem should therefore not be an issue in most microscope setups. In practice, finding the optimal imaging rate is a trade-off between achieving a high temporal resolution and minimizing fluorescence bleaching.

Upon analyzing a given Min pattern stack with respect to its temporal characteristics, we found that reslicing the stack along fixed spatial coordinates simplifies data processing and makes it more straightforward to access the temporal information contained within

the stack. Fig. 2.2D shows a (t, y) slice through our example image stack at fixed pixel position x. These t-x or t-y slices are collections of kymographs for all points along the cross-section at the fixed spatial coordinate. In Fig. 2.2E, we show example traces of these kymographs along selected y positions, which then correspond to individual surface locations (x,y) on the field-of-view shown in Fig. 2.2A. Analogous to the strategy presented for spatial global analysis, Eq. (2.1) can be used to obtain an autocorrelation map for this slice (cf. Supplementary Notebook *DEMO_MinDE_global_analysis.ipynb*, see section 2.5.2). To extract the pattern's global oscillation period, we consider the autocorrelation map's trace at $\Delta y = 0$ for $\Delta t \geq 0$, plotted in Fig. 2.2F. Including the $\Delta t \leq 0$ trace (going back in time) of the curve would not yield additional resolution, as it contains the same information as the positive trace (going back in time). This profile then immediately provides the averaged temporal autocorrelation trace for all points along one fixed spatial coordinate (as indicated for fixed x by the vertical line in Fig. 2.2A). If the line-averaged autocorrelation trace does not provide sufficiently high resolution to identify a minimum indicative of the oscillation period, imaging over a longer time and/or at shorter intervals could be necessary.

The first maximum of this curve beyond the central peak again identifies the predominant global oscillation period τ (magenta dashed line), while the first minimum is located at approximately $\tau/2$ (black dashed line). Statistics on τ can be collected by performing the analysis pipeline illustrated in Fig. 2.2D-F for multiple cross-sections at fixed y or x, that is, for multiple resliced frames as shown in Fig. 2.1C and 2.1D. Compared to the traces obtained from spatial autocorrelation, which are calculated via radial averaging, these temporal autocorrelation traces may appear rather coarse. A more advanced peak detection can be obtained with cubic-spline fitting and subsequent extreme point analysis. Further, the presented method for temporal autocorrelation analysis is less robust towards noise than spatial autocorrelation, as shown in Supplementary Fig. 2.6C. Adequate image preprocessing and cleaning is again of high importance. Image smoothing was found to slightly increase the detected oscillation period, albeit not above the error margins obtained for unsmoothed images, as shown in Supplementary Fig. 2.8.

Note furthermore that the propagation speed of a pattern may depend on the concentrations of all components, and may change over time. Therefore, for very long time series, it can make sense to split the stack up into multiple stacks of shorter total duration and perform analysis for subsequent sub-stacks (compare Supplementary Fig. 2.12). However, we estimate that an image stack needs to span the duration of a minimum length of 3 oscillation periods for the presented method to yield reliable results (cf. Supplementary Fig. 2.8).

2.3.2. LOCAL PARAMETERS

In this section, we present an analysis strategy that aims to quantify local parameters of Min patterns. These parameters include the local wave propagation velocity or characteristic local distances such as the distance between MinD and MinE wave crests. As we will describe in more detail, local parameters can be quantified by implementing two steps: (i) identification of wave crests for each frame within an image stack, and (ii) comparison of intensities at and around the identified crest points from one frame to the next.

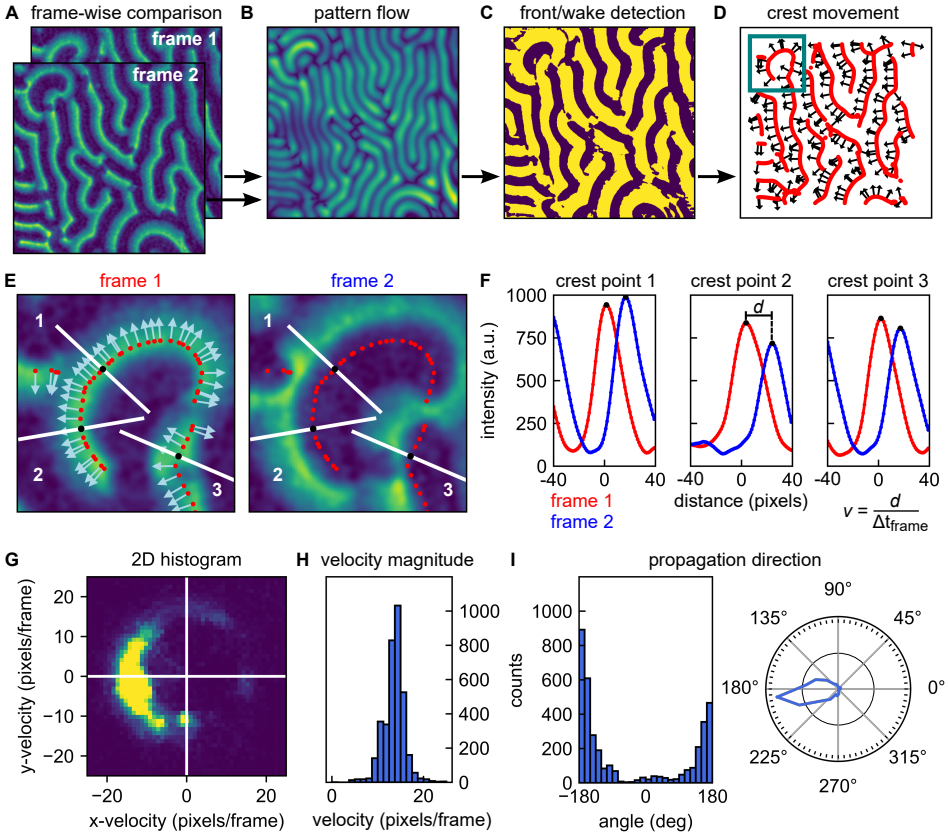


Figure 2.3: **Overview of analysis pipeline for determining local wave propagation velocities. A** Local analysis relies on sequential pairwise comparison of frames within an image stack. Example frames are here referred to as frame 1 and frame 2. **B** the Horn-Schunck algorithms is used to compute optical flow of the image pair (from frame 1 to frame 2) These return one vector per pixel, indicating the shift. Brightness indicates the vector magnitude. *Caption continues on next page.*

Figure 2.3: **C** Phase image of frame 1. The phase is determined by whether the wave intensity goes up ("front" of the wave, bright color) or down ("wake" of the wave, dark color) following the direction of the vector obtained from the optical flow analysis. **D** Wave crests can be identified by the transitions from front to wake as denoted in panel C. Red lines show the identified wave crest locations. Selected arrows indicate the direction of movement of the crests as determined from the optical flow. **E** Left: Zoom-in of frame 1 at the location highlighted in panel D. Wave crest points are indicated by red dots; direction of movement as identified by optical flow analysis are indicated by arrows. Right: Zoom-in of frame 2 at the same location. Crest points of frame 1 are indicated by red dots. In both images, 3 crest point positions are highlighted by white line traces parallel to the direction of propagation at these points (i.e., normal to the wave fronts). **F** Intensities versus distance along the white lines in panel E. Starting from the crests identified for frame 1 (red dots), intensities are sampled at discrete sub-pixel positions perpendicular to the wave front. Smoothed intensity traces are shown in red for frame 1 and in blue for frame 2. The translocation d of each crest position is then determined from the peak shift, allowing to calculate a velocity vector with magnitude v. Wave crest velocities can be calculated for each crest and each sequential pair of frames in an image stack. **G** Velocity distribution of a pattern can be visualized as a 2D histogram. **H** Velocity histogram that provides the average velocity magnitude v as well as the distribution of velocities within a given pattern. **I** Histogram of angles of the wave propagation vector (left) and an angular diagram denoting the occurrence of various pattern velocities (right). From the list of velocity vectors, we have immediate access to the propagation directions present within a pattern, the occurrence of which can be visualized in a histogram (left). The information can be represented as a polar histogram (right).

LOCAL WAVE PROPAGATION VELOCITY

The local wave propagation velocity is determined as the shift of individual crest points from one frame to the next. To calculate the local velocity, we first need to identify these crest points, and then determine their positional difference. We achieve this by applying optical flow analysis. Optical flow is defined by how brightness patterns move from one image to another[30, 31]. For our Min patterns, we estimate an optical flow vector field using Horn-Schunck algorithm[30, 32]. This algorithm works on a pair of sequential image frames (see Fig. 2.3A for example data, recorded for MinE) and returns a vector field, describing the estimated optical flow for each pixel from the first to the second frame. Fig. 2.3B shows the magnitude (indicated by image brightness) of the optical flow vectors obtained for our example image pair from Fig. 2.3A. Note that the collected optical flow vectors do not necessarily represent the local wave propagation velocities. The relation between the two measures will depend on the wave shape, making it hard to generalize.

As a first step to identifying the positions of the wave crests within the first frame, we use the information obtained from optical flow analysis to create a phase image. This phase image is essentially a binary map over the whole image, which indicates whether at any given point we are at the "front" ('ahead of the wave') or "wake" region of the wave

('behind the wave'). These regions are characterized by a decrease or increase in fluorescence intensity, respectively, along the direction of movement. If we consider any specific surface location and its corresponding vector obtained from optical flow, we can follow the direction of that vector over a short distance (say 3 pixels) within the same frame, and determine whether the fluorescence intensity is decreasing or increasing. The outcome of this procedure for our example frames is shown in Fig. 2.3C. Using this phase image, we can identify those positions in the image that make up the wave crests – which form the backbone structure of the pattern. Wave crests are identified by the positions at which a transition from the front to a wake region occurs. Fig. 2.3D shows the wave crests identified for the first frame in red. Subsequently, we need to determine the direction of wave propagation for these individual crest points. While we have a set of vectors available for distinct (x, y) positions from optical flow analysis, their directions will in general not be exactly normal to the wave crests due to noise. Therefore, we calculate vectors which are perpendicular to the lines of wave crests, and determine their correct directionality (pointing towards the front of the wave) using the information already present in the phase image. In Fig. 2.3D the direction of propagation is indicated by vectors at distinct crest points throughout the image for illustration. Following the procedure outlined here and in Fig. 2.3A-D, we thus effectively obtained (i) a list of positions, identifying the wave crest point positions, and (ii) a list of vectors, describing their direction of movement from the current to the next frame.

The next step is to quantify how far these crest points moved during the transition from the current to the next frame. Upon quantifying this positional shift, the velocity magnitude is given by this distance divided by the time that passed between the acquisition of subsequent frames. The procedure is illustrated in Fig. 2.3E-F for three example crest points. For each crest point, we considered the fluorescence intensity traces along the direction of movement at the given position (i.e., perpendicular to the wave front). Starting from the crest position, we plotted this trace up to a distance corresponding to roughly half the (global) wavelength of the pattern. Choosing this distance should ensure that the next frame's peak is still within the sampling range (provided that the time resolution of the acquisition stack is sufficiently high, cf. section 2.3.1). In Fig. 2.3E, the example traces along which intensities are plotted are highlighted in white. For sampling positions along this trace which are located off the pixel grid, intensities can be estimated by interpolation. This yields an intensity trace at sub-pixel resolution. This intensity trace will have a maximum located very close to the center of the originally determined crest position, with a small offset that can be attributed to the additional smoothing step performed before optical flow analysis, and is generally not significant (cf. Supplementary Fig. 2.9 and adjoined table).

Next, we performed exactly the same procedure at the same positions on the next frame. As shown in Fig. 2.3E and Fig. 2.3F, these positions are now no longer centered around the maximum of the intensity trace, but offset from them by a certain distance. This distance is the positional shift that we need to obtain for quantification of the local wave propagation velocity. Performing peak fitting allows to identify the two traces' peak values and measure the shift d in crest peak position at sub-pixel resolution.

Performing this analysis for all identified crest points along all sequential pairs of frames in an stack eventually yielded a list of velocity vectors with components (v_x, v_y) at frame n for a wave crest at position (x, y). Image smoothing is an important technical aspect of the local analysis presented here. We first perform a light image smoothing (with a limited initial smoothing kernel) to de-noise the image and to simplify peak detection such as shown in Fig. 2.3F. For optical flow analysis (Fig. 2.3B), we perform an additional smoothing step with a more extensive secondary smoothing kernel. The effect of different initial smoothing kernels is illustrated in Supplementary Fig. 2.10, the effect of increasing image noise in Supplementary Fig. 2.6D,E. Further, applying Horn-Schunck algorithm[30] requires setting a few parameters, particularly the regularization constant and the number of iterations. Here, we determined their values by trial-and-error from evaluating simulated as well as real Min protein pattern data and kept both constant from then on.

Depending on what kind of information is of interest, the obtained distribution of velocity vectors can be represented in different ways. A representation that combines information on the magnitude and directional preference is a 2D histogram such as the one shown in Fig. 2.3G for an example image stack of MinE data. If the magnitude of the wave propagation velocity is most important, the velocity magnitudes v can be plotted in a histogram to visualize their distribution and peak value, as shown in Fig. 2.3H. In other cases, the directional information may be of prime interest, for example, when studying the influence of an external bulk flow [26] or physical environmental parameters on the pattern.[22] For each vector component, an angle α can be calculated that corresponds to the wave crest point's direction of movement with respect to the direction of applied flow. The occurrence of different directions can then be plotted in a regular or polar histogram, as shown in Fig. 2.3I. As shown in Supplementary Fig. 2.11, the method can be applied to a wide range of image sizes. Decreasing the area on which analysis is performed generally leads to smaller standard deviation in velocity magnitude distribution, which is linked to a loss in directional information. The full local velocity pipeline is also presented in the Supplementary Notebook *DEMO_MinDE_local_analysis.ipynb* (please see section 2.5.2).

LOCAL MIND/MINE CREST SHIFT

When studying Min protein patterns, researchers routinely acquire data in two channels, for fluorescently-labelled MinD and MinE, respectively. Both these proteins exhibit a peak in their surface density, but these two peaks do not coincide in space and time (an example is given in Fig. 2.4A). To determine these differences, the analysis pipeline presented in section 2.3.2 for obtaining wave propagation velocity between sequential frames can be slightly adapted for measuring the difference in crest position between MinD and MinE waves. This can be achieved by first performing crest detection (analysis pipeline shown in Fig. 2.3A to D) for one stack, e.g. the MinD stack. The crest points attributed to the MinD stack can then be compared to the corresponding frame of the MinE stack, analogous to the comparison shown in Fig. 2.3E. The collected peak shifts d can be visualized in a histogram, such as shown in Fig. 2.4B for our example data.

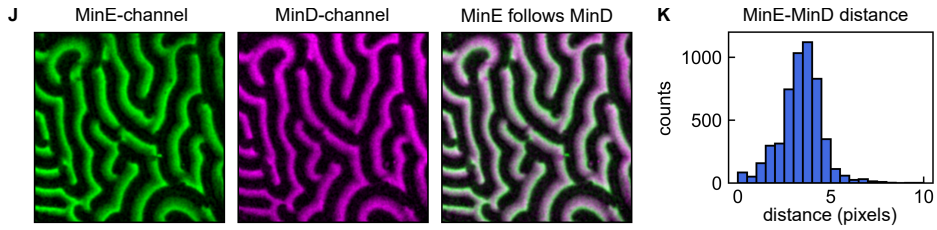


Figure 2.4: **Using the local analysis pipeline to determine local MinE-MinD crest positions shifts. A** MinD (magenta) and MinE (green) patterns. The pipeline for local analysis shown in panels A-F can be used to quantify other properties of the pattern, such as the MinE-MinD crest point distance in a simultaneous dual-channel acquisition. Here, crest point detection was performed for each frame of the MinD stack. Subsequently, the intensity traces at these positions were compared to those of the corresponding MinE frame. **B** Distribution of MinE-MinD crest point distances.

2.4. DISCUSSION

In this paper, we proposed protocols that can be applied to analyze data on *E. coli* Min protein surface patterns with respect to quantitative parameters such as the spatial wavelength, oscillation period, or wave crest propagation velocities. Our primary goal was to develop user-independent and largely automatized strategies for pattern analysis in order to (i) improve comparability of results obtained from different studies and research groups, and (ii) provide tools for quantification of experimental data for comparing results to theoretical studies. We presented global and local analysis methods which both can be valuable depending on what kind of pattern information is of interest. All of the routines that we suggested and described can be further modified to better fit the requirements posed by a particular research question – thus providing a framework that others can build upon.

The methodology we describe can be combined with many of the aspects and practices of Min pattern analysis which we did not cover here. For example, in studies investigating absolute or relative local concentrations or concentration gradients of MinD and MinE on the surface, fluorescence calibration can be important. Calibration allows to relate fluorescence intensity to the local membrane protein density.[19, 21, 12, 16] However, in many cases the patterns as such – their shapes, domains, wavelength, or dynamics – can be studied without this step, using the acquired fluorescence intensity data in arbitrary units, and this is what we focused on in this paper.

The global analysis that was presented here provides parameters averaged over entire image frames (spatial analysis) or slices along fixed spatial coordinates (temporal analysis). We found that for well-cleaned images, spatial autocorrelation robustly quantifies the main dominant wavelength within an image frame, as identified by the distance at which maximum self-correlation is present. This yielded results that are very comparable to those obtained by manual quantification, albeit with higher statistical reliability

(see Supplementary Fig. 2.5 for an example comparison of manual and automatic analysis). For temporal autocorrelation, we recommend re-orienting the image stack into slices of fixed x- or y-coordinates and calculating autocorrelation-maps along sets of kymographs, as described. We found this to be an efficient way to access large parts of the information provided within the image stack. Pixelwise analysis of intensity traces at distinct surface location, autocorrelation thereof and subsequent averaging is a more straightforward approach. However, we found that taking this detour via reslicing as presented in this paper reduces computational time by about two orders of magnitude, and hence, allows for easier processing of large amounts of data (cf. SI).

In many cases, parameters obtained from spatial and temporal analysis can be averaged for several frames/slices. However, whether this is justified depends on the time evolution of the pattern over the course of the acquisition. Supplementary Fig. 2.12 shows the temporal autocorrelation results for an example image stack which shows a decline in oscillation period over time. This is visible from the spreading of peaks in the resliced image (cf. Supplementary Fig. 2.12A) as well as in the variation in the shape of the $\Delta x = 0$ traces (cf. Supplementary Fig. 2.12B). In such a case, averaging is only justified over the part of the stack that shows a constant temporal periodicity. If required, the routines can be expanded to include peak analysis of single traces in the kymograph set and automatically determine up to which point averaging is permitted.

Local analysis, in contrast to global analysis, directly provides large-number distributions of parameters even when analysing only two consecutive images. Our approach to local analysis relies on the identification of wave crests and quantification of the positional shift thereof from one frame to the next. The first step can in principle be achieved by various strategies. For example, one could implement an algorithm that relies on thresholds of fluorescence intensity to identify peaks. Here, we presented a strategy that relies on established algorithms for optical flow analysis, as it offers certain advantages, such as direct access to the vector fields. We have already successfully used this local analysis methodology to examine and quantify the response of Min protein patterns to hydrodynamic bulk flow.[26] Numerous other applications can be imagined, in which a surface pattern is either exposed to an external stimulus and responds to it, or in which the time evolution of its characteristic properties is relevant. Using the local analysis pipeline presented here (or modifications thereof) allows to systematically quantify properties of interest with proper statistics rather than relying on qualitative description alone.

As our local analysis routine essentially offers a way to acquire a high number of intensity traces that are locally perpendicular to the wave fronts, it opens up possibilities for further in-depth analysis. Our brief illustration of a MinD-MinE crest distance detection is only one example of a parameter that can be extracted using an optical-flow-based routine. For example, it is imaginable to modify our local analysis pipeline such that it facilitates fast visualization of local fluorescence intensity profiles for both MinD and MinE waves. Upon fluorescence calibration, the fluorescence intensity can be converted to membrane protein density, and hence the relative peak heights can be connected to the protein ratio at the surface. Further, information obtained from local and global anal-

ysis can be combined, and local velocity analysis can provide an alternative to global methods if their requirements are not met. For example, while we found that a certain minimum number of entire oscillations is required for global temporal analysis to yield results (cf. Supplementary Fig. 2.8), local analysis can already be performed on only two consecutive frames, and can be combined with global spatial analysis to serve as an alternative route to determining the predominant oscillation period.

Finally, we note that the general strategies presented within this paper are not restricted to application to the analysis of *E. coli* Min protein surface patterns. Min protein patterns have some properties that are very specific to them – such as their quasi-periodic nature, dynamic oscillatory behavior, and their organization within domains – and our routines are designed for these specific properties. However, the routines presented here may very well be modifiable and applicable to quantify other types of semi-periodic surface patterns, biological or not, for example to the fascinating reaction-diffusion patterns of chemical systems like the BZ-AOT system[33]. We hope that our analysis toolbox will help to further disentangle the intriguing mechanisms that underlie pattern formation.

CODE AND DATA AVAILABILITY STATEMENT

The code created for this study as well as example data are openly available and can be found on GitHub at `https://github.com/M-Sabrina/MinDE_analysis_2022` and Zenodo at `https://zenodo.org/record/6724666` (second release). Please refer to Supplementary Material for further information.

2.5. SUPPLEMENTARY INFORMATION

2.5.1. METHODS

Plots were created using Python[23, 34] and assembled into figures using Inkscape[35]. A few panels were prepared with Fiji[36]. Example Min protein data was recorded using a spinning disc confocal microscope and processed as outlined in the main text. Unless specified otherwise, data for MinE is shown. Patterns are displayed in the colormap *viridis*, except for the dual-channel images shown in Fig. 4.

2.5.2. ONLINE CONTENT

The Python[23] code created for this study as well as example data can be found in open repositories on GitHub (`https://github.com`) and Zenodo (`https://zenodo.org`).
Find the GitHub repository at `https://github.com/M-Sabrina/MinDE_analysis_2022`.
Find the second release at Zenodo at: `https://zenodo.org/record/6724666`. The content of this paper refers to this second release.
Find the latest release at Zenodo at `https://doi.org/10.5281/zenodo.6500098`.

In the readme-file, we provide instructions on how to set up a Python environment "min_analysis", including a package "min_analysis_tools". The folder "min_analysis_scripts" contains scripts that use the tools to perform analysis on single stacks or batch processing of all stacks within a folder.

We provide several Jupyter notebooks, all of which can be immediately launched and viewed in a Jupyter binder, such as:
`https://mybinder.org/v2/gh/M-Sabrina/MinDE_analysis_2022/HEAD`.

The repository contains two Jupyter notebooks starting with "DEMO", one for global and one for local analysis:

- *DEMO_MinDE_global_analysis.ipynb* (snapshot as Appendix A on page 49)
- *DEMO_MinDE_local_analysis.ipynb* (snapshot as Appendix B on page 62)

These notebooks demonstrate in a step-by-step fashion how the analysis pipelines for autocorrelation analysis and local wave propagation detection work, using examples of simulated as well as real data. Snapshots of these Jupyter notebooks (for one out of several possible real examples) are provided as supplementary material in the appendix of this chapter (Appendix A and Appendix B). We recommend visiting the binder or installing the package for interactivity.

Further, the repository contains a notebook "Quickstart_Min_analysis.ipynb", which can directly be used to (remotely) perform analysis on a pre-cleaned single Min pattern data stack. Instructions are directly included in the notebooks.

Additionally, we provide a series of Supplementary notebooks, which can be used to repeat controls that we performed to test our analysis strategies:

- *Supplementary_crestpoint_bias.ipynb*: shows how accurately the originally determined crest points (from optical flow analysis) co-localize with local intensity maxima.
- *Supplementary_noise_sensitivity.ipynb*: shows effect of noise on accuracy of global methods and local velocity detection.
- *Supplementary_accuracy_global_spatial.ipynb*: shows effect of decreasing the image size on the accuracy of global autocorrelation analysis, with focus on the ratio of image size and spatial wavelength.
- *Supplementary_accuracy_global_temporal.ipynb*: shows effect of shortening the image stack along the temporal direction, with focus on the ratio of stack length and oscillation period.
- *Supplementary_accuracy_velocity.ipynb*: shows effect of decreasing the image size on the accuracy of local velocity analysis.
- *Supplementary_compare_temporal_autocorrelation_methods.ipynb*: shows a comparison of reslicing-based temporal autocorrelation analysis (as presented in the paper) and pixelwise autocorrelation. An analysis performed on the dataset represented in Fig. 1 run on the Jupyter binder [24-06-2022] returned comparable results for the oscillation period within 0.2 s for the reslicing method and 17.4 s for the pixelwise method.

2.5.3. SUPPLEMENTARY FIGURES

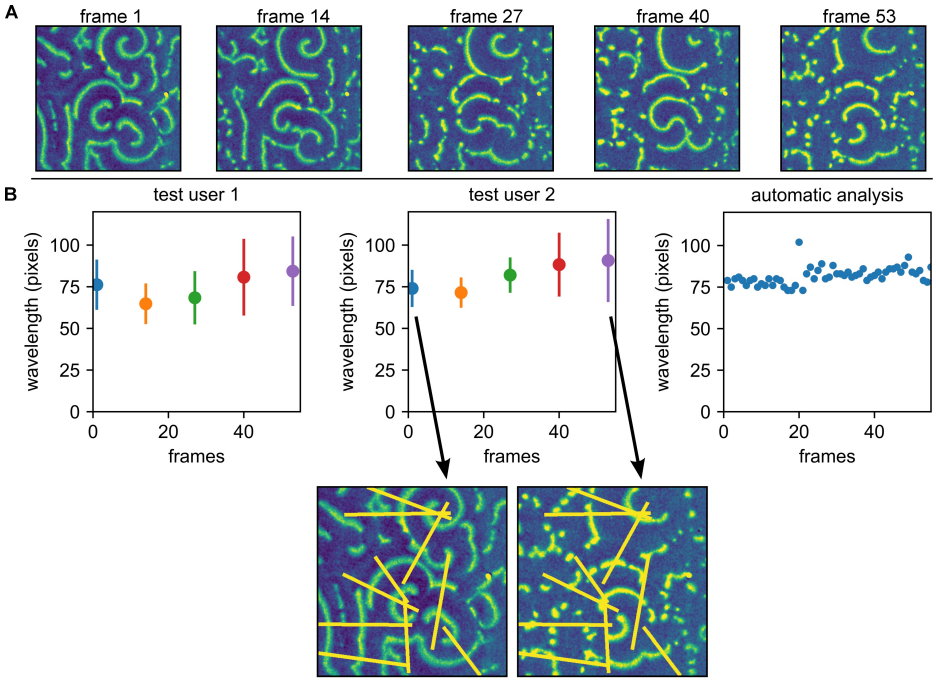


Figure 2.5: **A** Example frames from an image stack comprising 55 sequential frames of size 512 x 512 pixels). **B** For comparing the outcome of our automatized spatial autocorrelation routine to manual quantification, we asked two test persons to analyse the stack using Fiji[36] via the following procedure: Based upon the pattern presented in frame 1, pick ten cross-sections of line-width 10 pixels, which will be kept constant over the movie. For each cross-section, identify two peaks (if possible), then plot a line profile and identify the spacing of two consecutive peaks. This spacing is indicative of the wavelength. Perform this for frames 1, 14, 27, 40, and 53. Left and center panel: Manual results from test persons 1 and 2. Error bars denote standard deviations. Bottom panel shows the cross-sections selected by test user 2 for frames 1 and 53. Right panel: Results from the automated spatial correlation analysis.

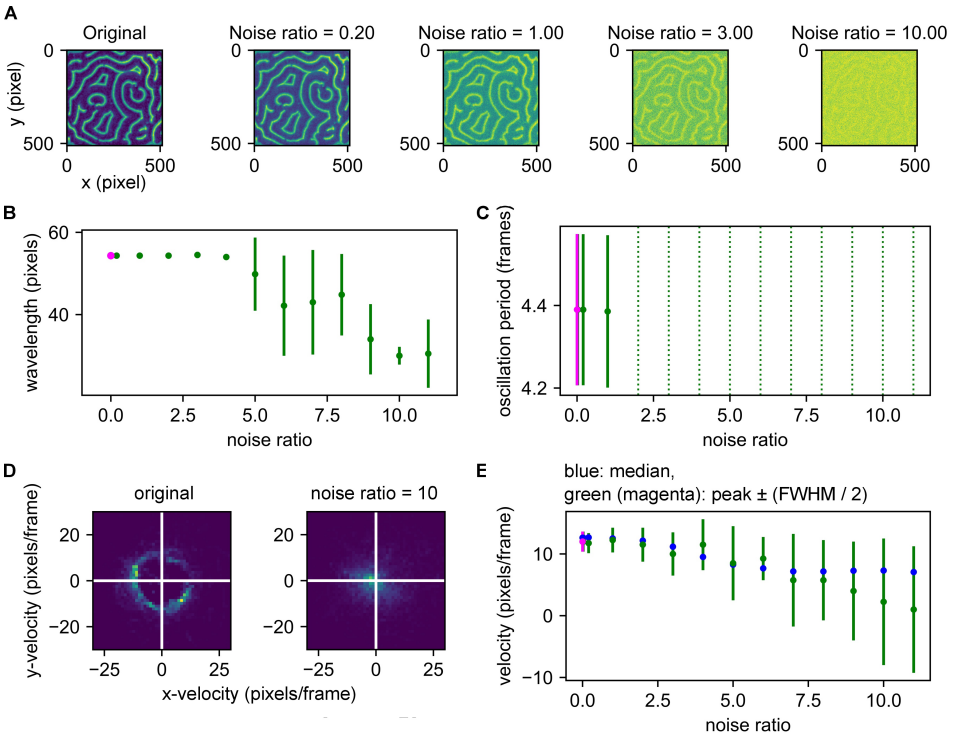


Figure 2.6: **A** Starting from a clean image stack comprising 20 sequential frames, we created a set of image stacks of decreasing quality by adding higher levels of Gaussian noise. Example frames of different noise ratios are shown here. Noise ratio refers to the standard deviation of added Gaussian noise with respect to the intrinsic image standard deviation. **B** Effect of noise on global spatial analysis, from analysis of first 6 frames. Resulting wavelength and standard deviation without noise in magenta, for increasing noise ratios in green. **C** Effect of noise on global temporal analysis from analysis on 20 frames, for 10 horizontal and vertical line traces each. Resulting period and standard deviation without noise in magenta, for increasing noise ratios in green. Green dashed lines indicated noise ratios for which our algorithm failed to return a result. **D** Example 2D histograms showing the effect of strong noise on local velocity analysis. **E** Results for local velocity analysis on first 6 frames. Resulting peak velocity magnitude and standard deviation (from FWHM of distribution) without noise in magenta, for increasing noise ratios in green. Median velocities in blue. *Also see notebook Supplementary_noise_sensitivity.ipynb*

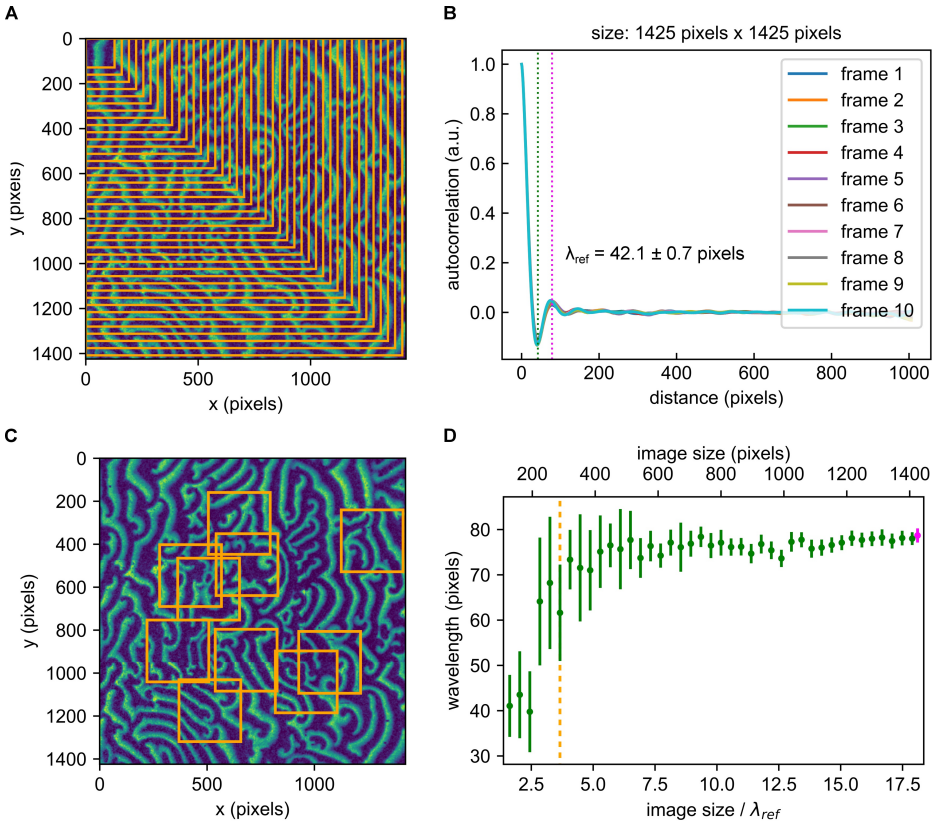


Figure 2.7: **A** Image stack comprising 10 consecutive frames, sequentially cropped to smaller sizes. **B** Spatial autocorrelation results for full-scale image stack. **C** For each cropping sizes, 10 random surface locations are chosen. **D** Spatial autocorrelation results for different cropping sizes, averaged from 10 randomly selected surface regions such as shown in C. Resulting wavelength and standard deviation for full in magenta (referred to as λ_{ref}), for cropped images in green. x-axis denotes both absolute image size (in pixels) as well as image size with respect to λ_{ref}. Image size for the example in C indicated by orange dashed line. *Also see notebook Supplementary_accuracy_global_spatial.ipynb*

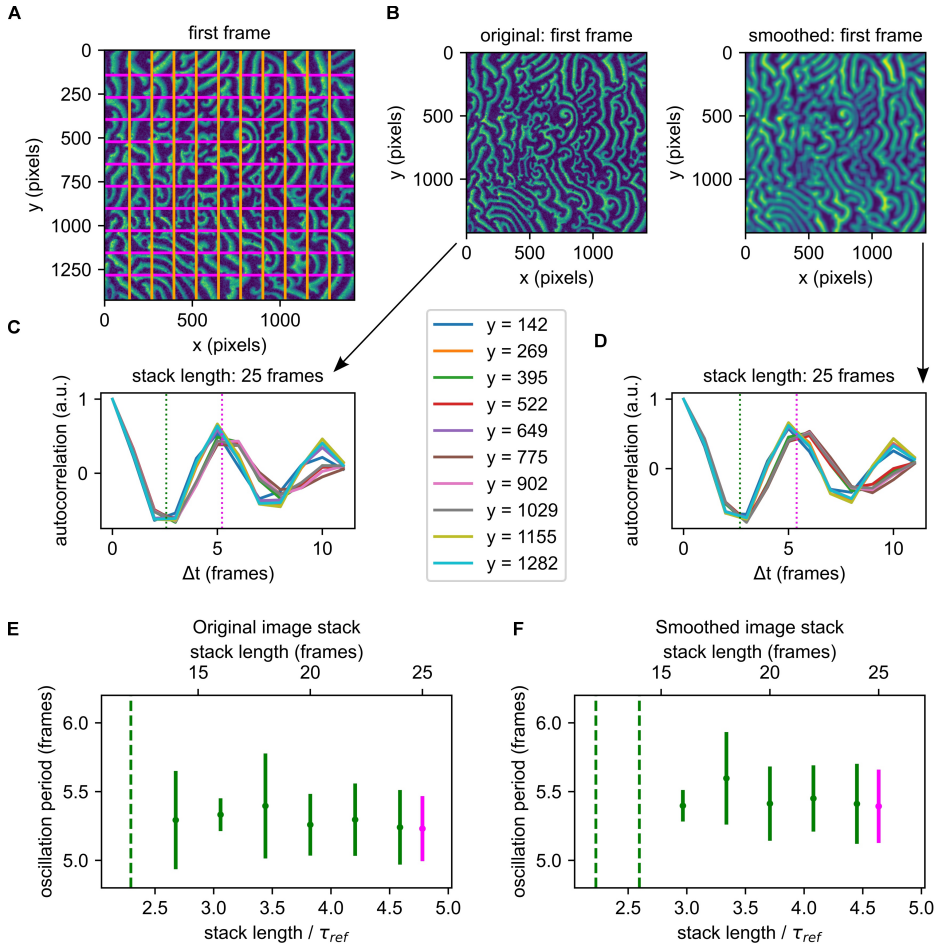
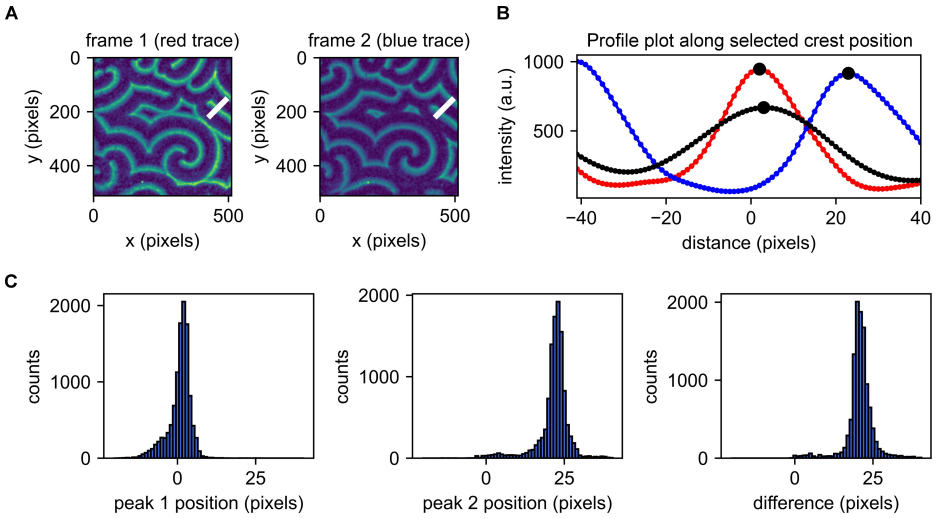


Figure 2.8: Starting from an image stack comprising 25 frames, we sequentially crop it in the temporal direction and study the effect of this shortening on both an unsmoothed and smoothed image. **A** Analysis is performed along the horizontal and vertical lines indicated. Each line (corresponding to one resliced image stack) provides a result from global temporal autocorrelation analysis. These results are collected to obtain a mean and standard deviation for the oscillation period. **B** Original (unsmoothed) and smoothed image stacks, first frame shown for each. **C** Full analysis (25 frames) for original image stack as shown in B, results providing the reference oscillation period τ_{ref}. **D** Full analysis (25 frames) on strongly smoothed image stack as shown in B, results providing the reference oscillation period τ_{ref}. **E** Results for original image stack shown as dependent on absolute stack length (in frames) and with respect to τ_{ref}. Resulting period and standard deviation for full stack in magenta (referred to as τ_{ref}), for cropped image stacks in green. Green dashed lines indicated stack lengths at which our algorithm failed to return a result. **F** Same as E for strongly smoothed stack. *Also see notebook Supplementary_accuracy_global_temporal.ipynb*



kernel	peak position 1	peak 1 FWHM	peak shift	peak shift FWHM
10	1.5	2	19.5	6
20	1.5	3	19.5	5
30	1.5	3	19.5	5
40	1.5	4	19.5	6
50	2.5	7	19.5	6
60	1.5	19	20.5	5

Figure 2.9: **A** Example frames of a sequential image series. **B** Example intensity traces of frames 1 (red), frame 2 (blue) and smoothed intensity trace of frame 1 (black, smoothing kernel 35 pixels) at the location indicated in A. **C** Histograms showing locations of peaks from frame 1 (peak 1 position) and frame 2 (peak 2 position) with respect to the originally assumed crest position as determined from optical flow analysis.**Table:** Position of peak 1 (pixels) from originally determined crest position as dependent on smoothing kernel used for optical flow analysis. *Also see notebook Supplementary_crestpoint_bias.ipynb*

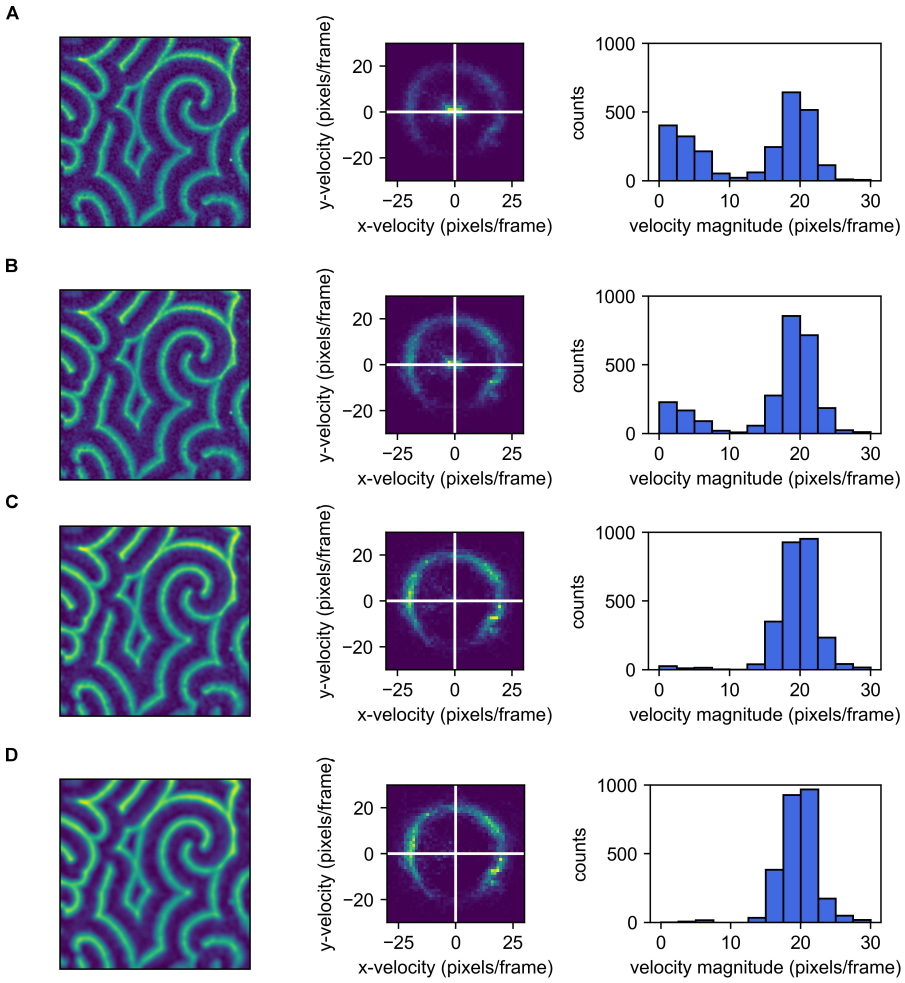


Figure 2.10: Effect of initial image smoothing on the quantification of local velocity (with for the optical flow analysis, a constant additional smoothing step with kernel of 35 pixels size). Quantification was performed over 10 consecutive frames of an example image stack, image size (512 x 512 pixels). **A** No smoothing. **B** Smoothing kernel of 5 pixels size. **C** Smoothing kernel of 10 pixels size. **D** Smoothing kernel of 15 pixels size.

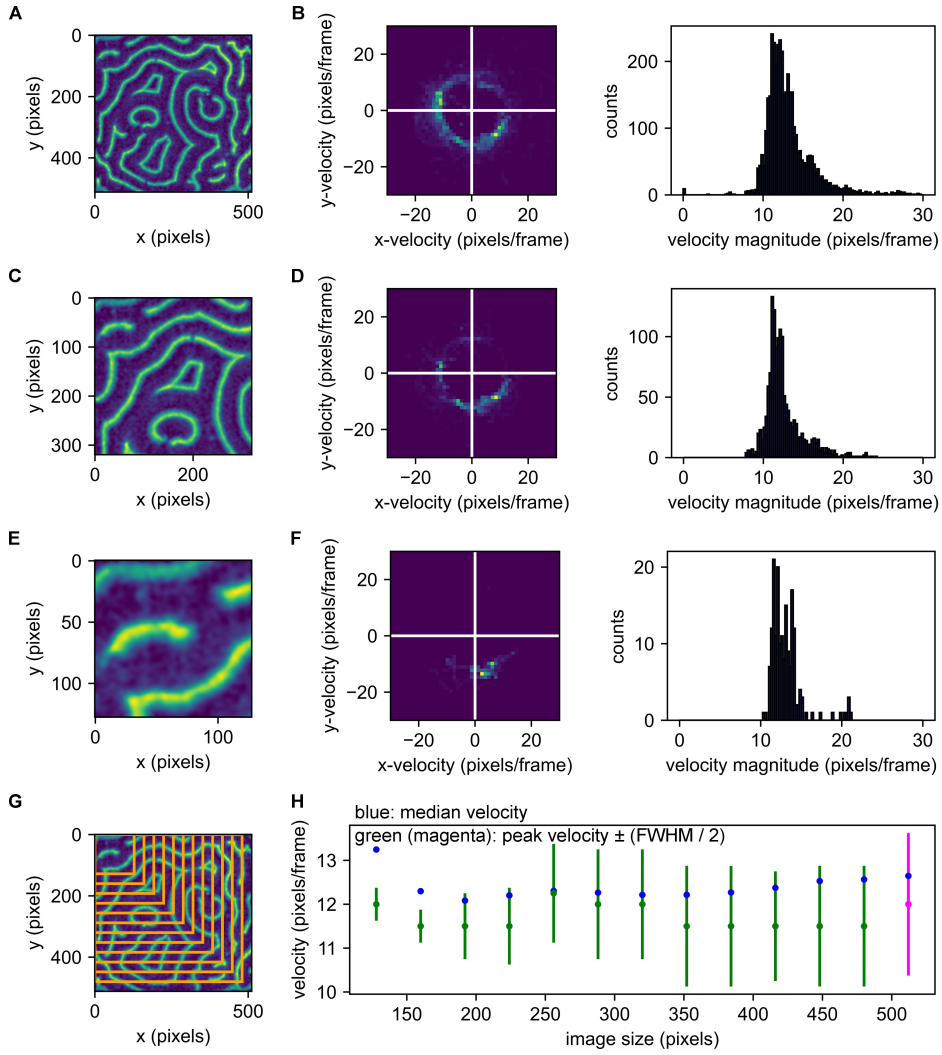


Figure 2.11: Effect of image size on local velocity analysis, as shown on an example image stack comprising 4 consecutive frames, sequentially cropped to smaller sizes. **A** Original image size, first frame. **B** Local velocity analysis results for original image size. **C** and **D** Same as A and B for cropped image size. **E** and **F** Same as A and B for further cropped image. **G** Illustration of all used cropping sizes. **H** Results for local velocity analysis on 4 frames for cropping sizes illustrated in G. Resulting peak velocity magnitude and standard deviation (from FWHM of distribution) for full image size in magenta, for cropped images in green. Median velocities in blue. *Also see notebook Supplementary_accuracy_velocity.ipynb*

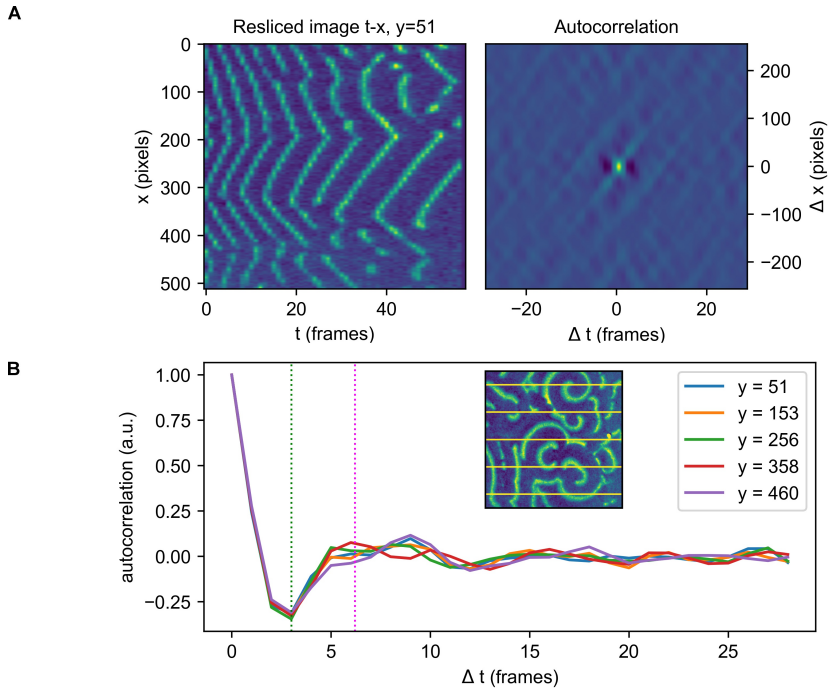


Figure 2.12: Temporal autocorrelation analysis performed for the image stack shown in Supplementary Fig. 2.5A. **A** Resliced image (set of kymographs) for fixed spatial y-coordinate (left) and autocorrelation map (right). **B** $\Delta x = 0$ traces for fixed y-coordinates. Inset shows fixed y-positions along which analysis was performed superimposed on frame 1. The magenta dashed line indicates the average position of the first maximum, which in this case yields an incorrect result for the oscillation period.

2.5.4. APPENDIX A: DEMO GLOBAL ANALYSIS

DEMO_MinDE_global_analysis

June 24, 2022

1 Wavelength and oscillation period of MinDE patterns

Jacob Kerssemakers, Sabrina Meindlhumer, Cees Dekker lab, 2022

The flowing, semi-periodic patterns of MinDE pose some challenges to quantification. Here, we illustrate a systematic approach to extract global parameters, in particular the global wavelength μ and global oscillation period τ.

READ-ME: Cells in this notebook need to be executed sequentially. Upon starting to explore this notebook, click the double-arrow symbol above (*Restart the kernel, then re-run the whole notebook*) and hit "Restart" to ensure all required packages are loaded. After that, the notebook will take a few moments to set up, and figures/plots will re-appear one by one. At distinct positions in the notebook, the user is invited to change numeric input. After doing so, the notebook needs to be executed anew at least from this point on for changes to be applied. The notebook can be re-run from any given point onwards by clicking *Run* in the menu-bar above, and selecting *Run Selected Cell and All Below*. Alternatively, the double-arrow symbol can be used again, which will re-run the notebook from the start. This will take a moment longer, but will have the same effect.

1.1 Setup

Import of standard modules and assisting custom-made modules. Needs to be executed at least once to ensure correction functionality (see instructions above).

[1]:
```
import numpy as np
from skimage import io
import matplotlib.pyplot as plt
from pathlib import Path

from min_analysis_tools import correlation_tools
from min_analysis_tools import get_data

# Reload modules automatically before executing code
%reload_ext autoreload
%autoreload 2

# Figure quality
import matplotlib as mpl
mpl.rcParams['figure.dpi'] = 300
```

1.2 Select example

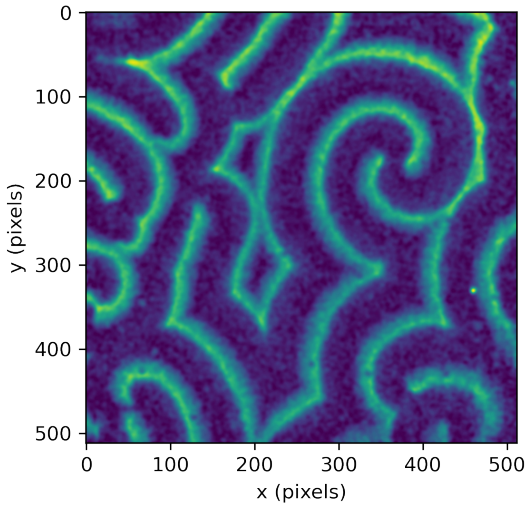
Choose an example from the provided stacks in the list below: (1) Simulated spiral (2) Min spiral (example data) (3) Min southeast-directed traveling waves (example data) (4) Min west-directed traveling waves (example data) (5) Min large stitched pattern (example data) (6) Min horizontally stitched pattern (example data) Choose the example by setting the variabel *selection* in the code-box below. The notebook needs to be re-run (at least from this point onwards) for changes to be applied.

[2]:
```
selection = 2  # set to 1 ... 6
```

[3]:
```
if selection not in np.arange(1, 7):
    print("Invalid selection. Set to selection 1 (Simulated spiral).")
    selection = 1
    MinDE_st = get_data.generate_pattern(
        lambda_t=20, lambda_x=1, size=512, N_frames=50, demo=False
    )
elif selection == 1:  # "Simulated spiral"
    MinDE_st = get_data.generate_pattern(
        lambda_t=20, lambda_x=1, size=512, N_frames=50, demo=False
    )
elif selection > 1:
    if selection == 2:  # "Min spiral (example data)"
        stack_path = Path().cwd() / "example_data" / "demo_spiral.tif"
    if selection == 3:  # "Min southeast-directed traveling waves (example data)"
        stack_path = Path().cwd() / "example_data" / "demo_southeast.tif"
    if selection == 4:  # "Min west-directed traveling waves (example data)"
        stack_path = Path().cwd() / "example_data" / "paper_west_E.tif"
    if selection == 5:  # "Min large stitched pattern (example data)"
        stack_path = Path().cwd() / "example_data" / "demo_square_stitch.tif"
    if selection == 6:  # "Min horizontally stitched pattern (example data)"
        stack_path = Path().cwd() / "example_data" / "demo_horizontal_stitch.tif"
    MinDE_st = io.imread(stack_path)
nt, ny, nx = np.shape(MinDE_st)

fig, ax = plt.subplots()
ax.imshow(MinDE_st[0, :, :])
ax.set_xlabel("x (pixels)")
ax.set_ylabel("y (pixels)")
plt.show()

print(f"Current selection: {selection}")
```




```
Current selection: 2
```

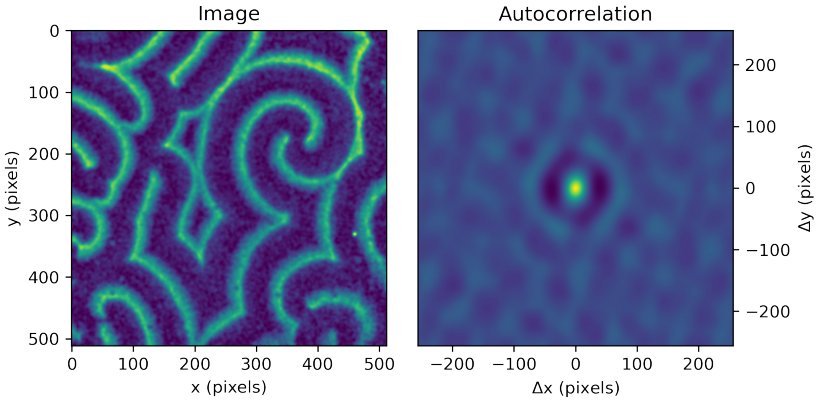
1.3 Spatial autocorrelation

Spatial autocorrelation analysis is performed on a set number of images per movie. For each autocorrelation output image, a radial profile is recorded starting from the main central correlation peak. The resulting spatial radial correlation curves are subjected to maxima analysis. The first maximum after radius $R = 0$ indicates the most predominant distance between wave edges, irrespective of propagation direction. This distance is identified as the pattern's global wavelength. First, we perform autocorrelation on a set number of frames of our loaded stack. For each analyzed frame, we obtain a correlation matrix such as the one below. You can change this number in the code-box below. The notebook needs to be re-run (at least from this point on) for changes to apply.

[4]:
```
frames_to_analyse = 10  # integer number, default: 10
```

[5]:
```
# calculate spatial autocorrelation maps for all analysed frames
(
    crmx_storage,
    fig,
    ax_corr,
    ax_orig,
) = correlation_tools.get_spatial_correlation_matrixes(
    MinDE_st, frames_to_analyse, demo=True
)
```

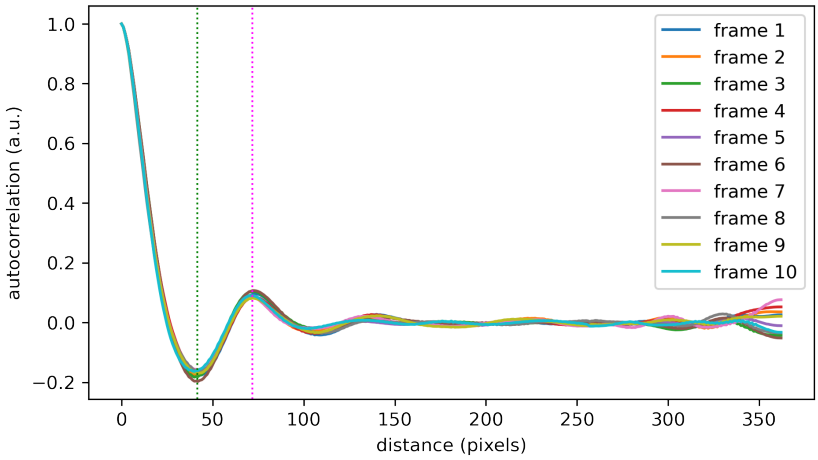
```
Analysing 10 frames
```



1.4 Radial profile traces

Next, we perform radial averaging starting from the center peak. Ideally, we obtain a curve showing a clear first peak, indicating high correlation. We interpret this peak as representing the pattern's predominant, "global" wavelength μ.

[6]:
```
# calculate radially averaged profile traces and analyze them with respect to␣
↪first min and max
(
    min_pos,
    min_val,
    max_pos,
    max_val,
    fig,
    ax,
) = correlation_tools.analyze_radial_profiles(crmx_storage, demo=True)
```



Wavelengths obtained from all analysed frames can be averaged:

[7]:
```
# output characteristic parameters
print(f"Mean position of first valley: {np.mean(min_pos):.02f}")
print(f"Mean position of first peak: {np.mean(max_pos):.02f} (wavelength in␣
 ↪pixels)")
```

```
Mean position of first valley: 41.60
Mean position of first peak: 71.90 (wavelength in pixels)
```

1.5 Temporal autocorrelation

For temporal correlation, we generate a set of t-x or t-y kymographs per movie, evenly distributed over a set middle fraction fraction of an image. For each set of kymographs, autocorrelation analysis is performed. The Δx=0 or Δy=0 line of the resulting autocorrelation maps then in effect represent a temporal correlation curve averaged over all the original image points on this line. In other words, they represent average temporal correlation signals sampled from all selected surface locations. Analogous to the spatial correlation analysis, the first maximum after $\Delta t = 0$ indicates a main oscillation period. We start by reslicing our images in x- or y-direction. Note that one frame in such a stack then corresponds to one horizontal or vertical cross-section in the original imaged region, meaning that the frames in our stack are comprised of kymographs of all points along this line.

[8]:
```
# reslice frames
MinDE_shift_tx = np.moveaxis(MinDE_st, 0, -1)  # creates t-x resliced frames
MinDE_shift_yt = np.moveaxis(MinDE_st, -1, 0)  # creates y-t resliced frames
```

```
# next transpose y-t slices to have t axis in 1st dimension
MinDE_shift_ty = np.empty((nx, ny, nt))
for frame in range(nx):
    MinDE_shift_ty[frame, :, :] = np.transpose(MinDE_shift_yt[frame, :, :])
```

Using these resliced stacks makes it easier to access the temporal information within our data. We will now perform autocorrelation for selected frames of our resliced stacks, corresponding to cross sections along the x- or y-axis along our original images as shown above. The x- and y-positions of these lines are determined by the two parameters *reps_per_kymostack* and *kymoband*. These input numbers can be changed in the code-box below. The notebook needs to be re-run (at least from this point on) for changes to apply.

[9]:
```
reps_per_kymostack = 5  # pick ... kymographs around middle (integer number, default: 5)
kymoband = 0.8  # analyse middle ... part of image (< 1, default: 0.8)
```

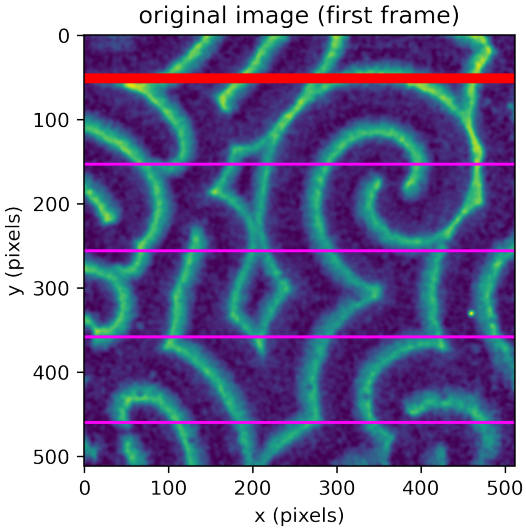
Below, the colored lines indicate all cross-sections for constant y along which autocorrelation is performed, each corresponding to one particular frame in the t-x resliced stack. The thick, red lines highlights the first horizontal cross-section at constant y, for which the exemplary t-x slice and its autocorrelation map are shown. Note that the slice is comprised of a series of kymographs for all x positions along that particular constant y.

[10]:
```
print(f"Current reps_per_kymostack: {reps_per_kymostack}")
print(f"Current kymoband: {kymoband}")

slices2analyze_x = ny * np.linspace(
    0.5 - kymoband / 2, 0.5 + kymoband / 2, reps_per_kymostack
)
slices2analyze_x = slices2analyze_x.astype(int)

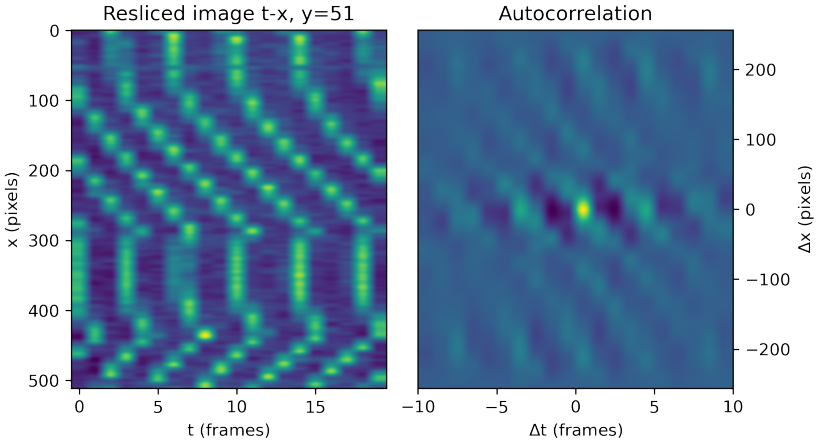
fig, ax = plt.subplots(1, 1)
ax.imshow(MinDE_st[0, :, :])
ax.set_xlabel("x (pixels)")
ax.set_ylabel("y (pixels)")
ax.set_title("original image (first frame)")
for num_y, y_axis in enumerate(slices2analyze_x):
    if num_y == 0:
        ax.axhline(y=y_axis, color="red", linewidth=5)
    else:
        ax.axhline(y=y_axis, color="magenta")
```

```
Current reps_per_kymostack: 5
Current kymoband: 0.8
```



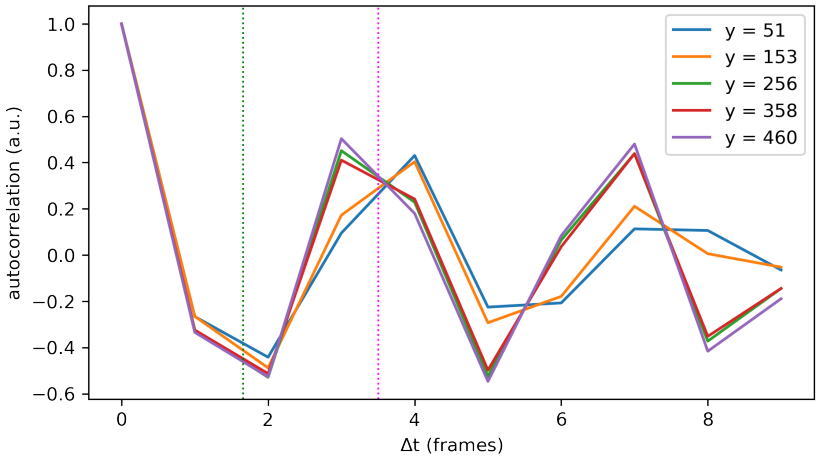
[11]:
```
selection_reslice_x = f"{selection}_x_resliced"
(
    crmx_storage_x,
    slices2analyze,
    fig,
    ax_corr,
    ax_orig,
) = correlation_tools.get_temporal_correlation_matrixes(
    MinDE_shift_tx,
    "x",
    kymoband,
    reps_per_kymostack,
    demo=True,
)
```

```
Analyzing t-x slices for y = [ 51 153 256 358 460]
```



The $\Delta x = 0$ line of these autocorrelation maps then in effect represents a temporal correlation curve averaged over all the original image points along this cross-section at constant y. Analogous to the spatial correlation analysis, the first maximum after $\Delta t = 0$ indicates a main oscillation period. As temporal autocorrelation curves will generally be more coarse as they are not obtained from radial averaging, we perform cubic spline fitting and determine the peak and valley from extreme point analysis.

[12]:
```
# analyse selected traces with respect to first min and max
(
    first_min_pos_x,
    first_min_val_x,
    first_max_pos_x,
    first_max_val_x,
    fig,
    ax,
) = correlation_tools.analyze_temporal_profiles(
    "x", crmx_storage_x, slices2analyze_x, demo=True
)
```



The same analysis pipeline can be performed for cross-sections at constant x. Below, the colored lines indicate all cross-sections for constant x along which autocorrelation is performed, each corresponding to one particular frame in the t-y resliced stack. The thick, red lines highlights the first horizontal cross-section at constant x, for which the exemplary t-y slice and its autocorrelation map are shown. Again, note that the slice is comprised of a series of kymographs for all y positions along that particular constant x.

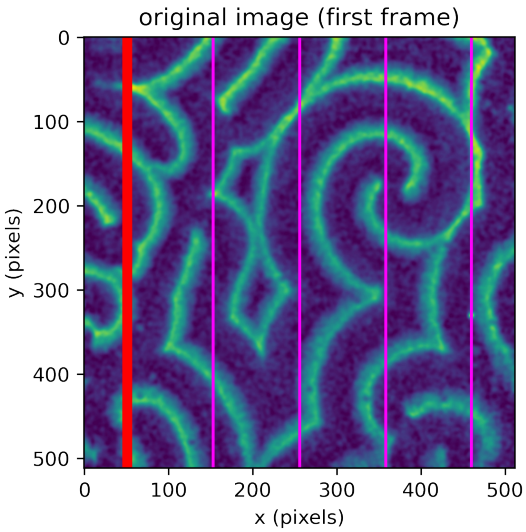
[13]:
```
print(f"Current reps_per_kymostack: {reps_per_kymostack}")
print(f"Current kymoband: {kymoband}")

slices2analyze_y = nx * np.linspace(
    0.5 - kymoband / 2, 0.5 + kymoband / 2, reps_per_kymostack
)
slices2analyze_y = slices2analyze_y.astype(int)

fig, ax = plt.subplots(1, 1)
ax.imshow(MinDE_st[0, :, :])
ax.set_xlabel("x (pixels)")
ax.set_ylabel("y (pixels)")
ax.set_title("original image (first frame)")
for num_x, x_axis in enumerate(slices2analyze_y):
    if num_x == 0:
        ax.axvline(x=x_axis, color="red", linewidth=5)
    else:
        ax.axvline(x=x_axis, color="magenta")
```

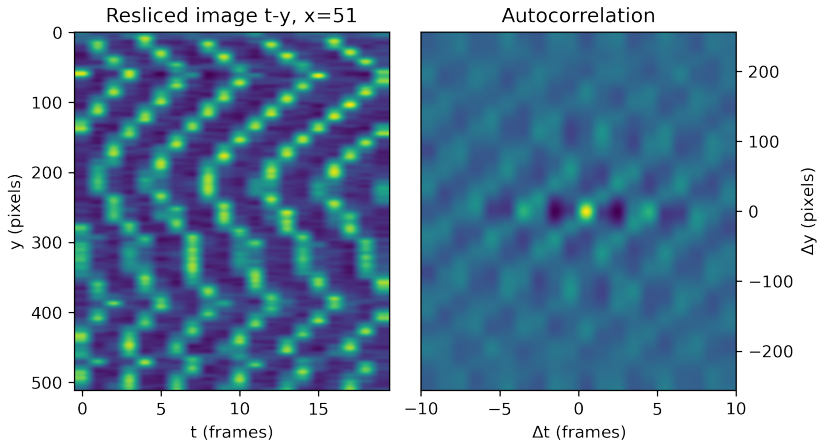
```
Current reps_per_kymostack: 5
```

```
Current kymoband: 0.8
```

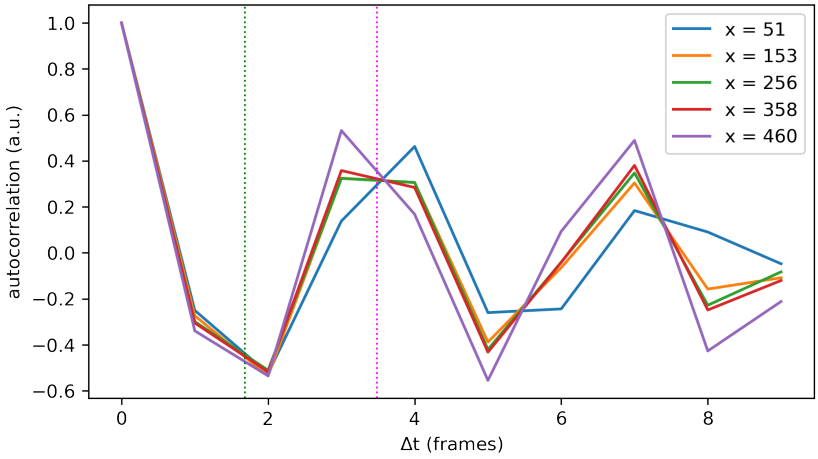


[14]:
```
selection_reslice_y = f"{selection}_y_resliced"
(
    crmx_storage_y,
    slices2analyze_y,
    fig,
    ax_corr,
    ax_orig,
) = correlation_tools.get_temporal_correlation_matrixes(
    MinDE_shift_ty,
    "y",
    kymoband,
    reps_per_kymostack,
    demo=True,
)
```

```
Analyzing t-y slices for x = [ 51 153 256 358 460]
```



[15]:
```
(
    first_min_pos_y,
    first_min_val_y,
    first_max_pos_y,
    first_max_val_y,
    fig,
    ax,
) = correlation_tools.analyze_temporal_profiles(
    "y", crmx_storage_y, slices2analyze_y, demo=True
)
```



Finally, the parameters collected from all used slices can be averaged to identify the predominant, "global" oscillation period τ of the pattern:

[16]:
```
# output characteristic parameters
print(
    f"Mean position of first valley: {np.mean(np.append(first_min_pos_x,␣
 ↪first_min_pos_y)):.02f}"
)
print(
    f"Mean position of first peak: {np.mean(np.append(first_max_pos_x,␣
 ↪first_max_pos_y)):.02f} (oscillation period in frames)"
)
```

```
Mean position of first valley: 1.67
Mean position of first peak: 3.49 (oscillation period in frames)
```

2.5.5. APPENDIX B: DEMO LOCAL ANALYSIS

DEMO_MinDE_local_analysis

June 24, 2022

1 Wave crest propagation speed of MinDE patterns

Jacob Kerssemakers, Sabrina Meindlhumer, Cees Dekker lab, 2022

The flowing, semi-periodic patterns of MinDE pose some challenges to quantification. Here, we illustrate a systematic approach to determine wave crest propagation velocities $\vec{v} = (v_x, v_y)$ for individual wave crest points. Our approach includes the identification of wave crests (using optical flow image analysis tools) and frame-wise comparison of crest positions to determine their local propagation speed. Unlike global analysis (compare our illustration for extraction of global parameters using autocorrelation methods), this approach has the potential to directly yield large distributions of parameters, associated with their (x, y) coordinates within the field-of-view.

READ-ME: Cells in this notebook need to be executed sequentially. Upon starting to explore this notebook, click the double-arrow symbol above (*Restart the kernel, then re-run the whole notebook*) and hit "Restart" to ensure all required packages are loaded. After that, the notebook will take a few moments to set up, and figures/plots will re-appear one by one. At distinct positions in the notebook, the user is invited to change numeric input. After doing so, the notebook needs to be executed anew at least from this point on for changes to be applied. The notebook can be re-run from any given point onwards by clicking *Run* in the menu-bar above, and selecting *Run Selected Cell and All Below*. Alternatively, the double-arrow symbol can be used again, which will re-run the notebook from the start. This will take a moment longer, but will have the same effect.

1.1 Setup

Import of standard modules, the used flow field analysis method (Horn-Schunck) and assisting custom-made modules. Needs to be executed at least once to ensure correct functionality (see instructions above).

[1]:
```
from pathlib import Path
import numpy as np
from skimage import io
import matplotlib.pyplot as plt
from cv2 import filter2D

from pyoptflow import HornSchunck
from min_analysis_tools.get_auto_halfspan import get_auto_halfspan
from min_analysis_tools import get_data, min_de_patterns_crests, peak_profile
from min_analysis_tools.local_velocity_analysis import local_velocity_analysis
```

```
# Reload modules automatically before executing code
%reload_ext autoreload
%autoreload 2

# Figure quality
import matplotlib as mpl
mpl.rcParams['figure.dpi'] = 300
```

1.2 Select example

Choose an example from the provided stacks in the list below: (1) Simulated spiral (2) Min spiral (example data) (3) Min southeast-directed traveling waves (example data) (4) Min west-directed traveling waves (example data) (5) Min large stitched pattern (example data) (6) Min horizontally stitched pattern (example data) Choose the example by setting the variable *selection* in the code-box below. The notebook needs to be re-run (at least from this point onwards) for changes to be applied.

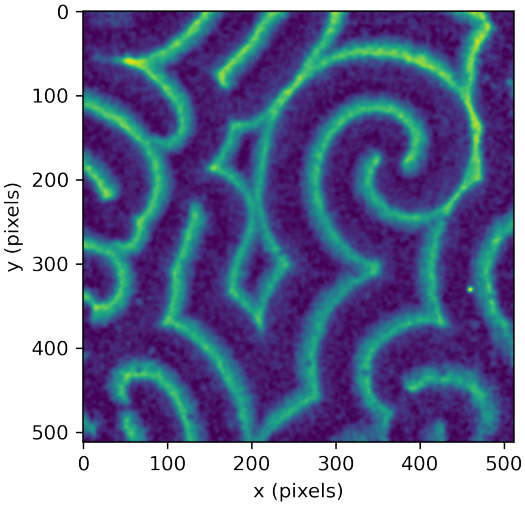
[2]:
```
selection = 2  # set to 1 ... 6
```

[3]:
```
if selection not in np.arange(1, 7):
    print("Invalid selection. Set to selection 1 (Simulated spiral).")
    selection = 1
    MinDE_st_original = get_data.generate_pattern(
        lambda_t=20, lambda_x=1, size=512, N_frames=50, demo=False
    )
    zm_lo = 45
    zm_hi = 70
elif selection == 1:  # "Simulated spiral"
    MinDE_st_original = get_data.generate_pattern(
        lambda_t=20, lambda_x=1, size=512, N_frames=50, demo=False
    )
    zm_lo = 45
    zm_hi = 70
elif selection > 1:
    if selection == 2:  # "Min spiral (example data)"
        stack_path = Path().cwd() / "example_data" / "demo_spiral.tif"
        zm_lo = 75
        zm_hi = 100
    if selection == 3:  # "Min southeast-directed traveling waves (example data)"
        stack_path = Path().cwd() / "example_data" / "demo_southeast.tif"
        zm_lo = 75
        zm_hi = 100
    if selection == 4:  # "Min west-directed traveling waves (example data)"
        stack_path = Path().cwd() / "example_data" / "paper_west_E.tif"
        zm_lo = 150
        zm_hi = 175
    if selection == 5:  # "Min large stitched pattern (example data)"
```

```
        stack_path = Path().cwd() / "example_data" / "demo_square_stitch.tif"
        zm_lo = 75
        zm_hi = 100
    if selection == 6:  # "Min horizontally stitched pattern (example data)"
        stack_path = Path().cwd() / "example_data" / "demo_horizontal_stitch.tif"
        zm_lo = 65
        zm_hi = 90
    MinDE_st_original = io.imread(stack_path)
nt, ny, nx = np.shape(MinDE_st_original)
auto_halfspan = get_auto_halfspan(
    MinDE_st_original, frames_to_analyse=10, verbose=False
)

fig, ax = plt.subplots()
ax.imshow(MinDE_st_original[0, :, :])
ax.set_xlabel("x (pixels)")
ax.set_ylabel("y (pixels)")
plt.show()

print(f"Current selection: {selection}")
```



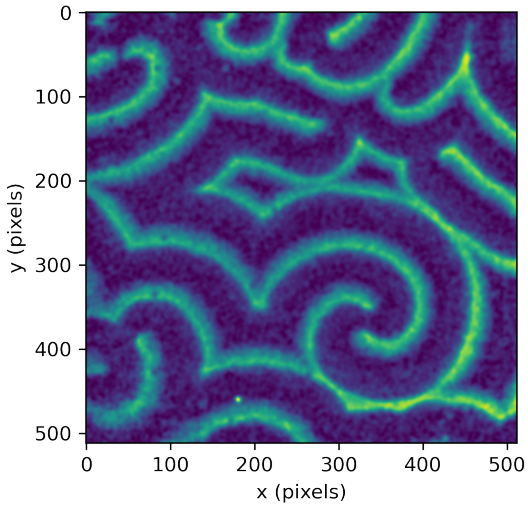

```
Current selection: 2
```

Note that depending on what environment we use, the orientation of x- or y-components does not always match what you see by eye when opening the image stack with an image viewer, such

as Fiji. When relying on the indexing used by NumPy and representation by Matplotlib, we can ensure that the final vector direction matches the apparent directionality by performing some simple transformations on the stack before starting.

[4]:
```
MinDE_st = min_de_patterns_crests.adjust_stack_orientation(MinDE_st_original)
```

[5]:
```
fig, ax = plt.subplots()
ax.imshow(MinDE_st[0, :, :])
ax.set_xlabel("x (pixels)")
ax.set_ylabel("y (pixels)")
plt.show()
```



An important parameter to define is *halfspan*, the meaning of which will be explained further below. As a rule of thumb, *halfspan* should be set to approximately half the global wavelength. This can be determined from global analysis or estimated from visual inspection of the pattern. For our demo, we suggest default values for *halfspan*, determined via spatial autocorrelation analysis in the code-box below the example selection. To try other values for *halfspan*, replace "auto_halfspan" by a numeric value (length in pixel). Choosing a value that strongly deviates from the recommended one can lead to erroneous results. Another parameter is *sampling_width*, will later on define the distance between sampling points when comparing crest point position between frames. These parameters can be set in the code-box below. The notebook needs to be re-run (at least from this point on) for changes to apply.

[6]:
```
halfspan = auto_halfspan  # default: auto_halfspan
sampling_width = 1  # default: 1
```

[7]:
```
print(f"Current halfspan: {halfspan} pixels")
print(f"Current sampling_width: {sampling_width} pixels")
```

```
Current halfspan: 41 pixels
Current sampling_width: 1 pixels
```

In the following, we work through the given image stack by performing optical-flow analysis on pairs of sequential images and using this information to identify wave crests.

1.3 Flow field analysis

We build two smoothed image stacks, first one with a finer smoothing kernel, then one with a rather large kernel. The strongly-smoothed stack (*_smz_flow*) is used only for flow analysis (Horn-Schunck), the lightly-smoothed stack (*_smz*) will later on be used for peak detection. The value for light and strong smoothing can be set in the code-box below. Changing these values will lead to results of different quality, and optimal values may differ from file to file. The notebook needs to be re-run (at least from this point on) for change to apply.

[8]:
```
kernel_size_general = 15  # for general (light) smoothing
kernel_size_flow = 35  # stronger smoothing for optical flow analysis
```

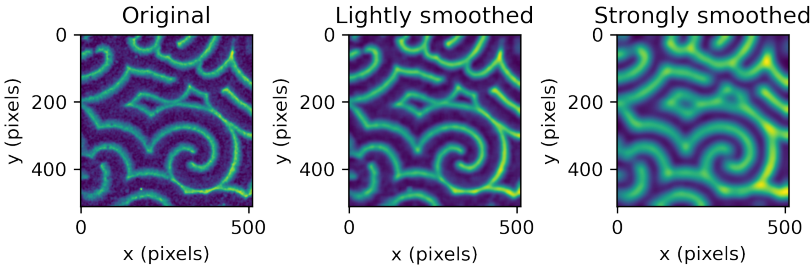
[9]:
```
# build kernel for first smoothing step (for processing)
general_kernel = np.ones((kernel_size_general, kernel_size_general), np.float32)␣
 ↪/ (
    kernel_size_general**2
)

# build kernel for obtaining flow pattern
flow_kernel = np.ones((kernel_size_flow, kernel_size_flow), np.float32) / (
    kernel_size_flow**2
)

# create lightly and strongly smoothed images
im0_raw = MinDE_st[0, :, :]
im1_raw = MinDE_st[1, :, :]
im0_smz = filter2D(im0_raw, -1, general_kernel)
im1_smz = filter2D(im1_raw, -1, general_kernel)
im0_smz_flow = filter2D(im0_smz, -1, flow_kernel)
im1_smz_flow = filter2D(im1_smz, -1, flow_kernel)

fig, (ax1, ax2, ax3) = plt.subplots(1, 3)
ax1.imshow(im0_raw)
ax1.set_title("Original")
ax1.set_xlabel("x (pixels)")
ax1.set_ylabel("y (pixels)")
ax2.imshow(im0_smz)
ax2.set_title("Lightly smoothed")
ax2.set_xlabel("x (pixels)")
```

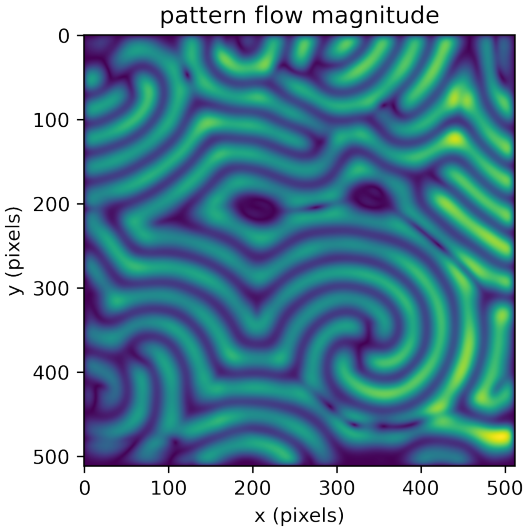
```
ax2.set_ylabel("y (pixels)")
ax3.imshow(im0_smz_flow)
ax3.set_title("Strongly smoothed")
ax3.set_xlabel("x (pixels)")
ax3.set_ylabel("y (pixels)")
fig.tight_layout()
plt.show()
```



For each sequential pair of images in our stack, we first perform flow analysis using Horn-Schunck algorithm, which gives us an estimate of the local mass flow of fluorescent intensity between subsequent image frames We obtain this information in the form of flow field vector maps describing the local flow components in x- and y-direction. Note that this is still local flow and not the actual wave propagation. In the map below, the magnitude of each position's corresponding flow vector is shown as image brightness.

[10]:
```
flow_x, flow_y = HornSchunck(im0_smz_flow, im1_smz_flow, alpha=100, Niter=100)
```

[11]:
```
# Show the optical flow magnitude
flow_mag = np.hypot(flow_x, flow_y)
fig, ax = plt.subplots()
ax.imshow(flow_mag)
ax.set_title("pattern flow magnitude")
ax.set_xlabel("x (pixels)")
ax.set_ylabel("y (pixels)")
plt.show()
```

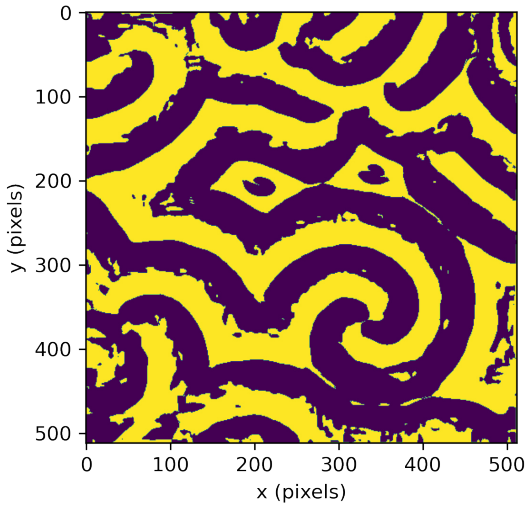


1.4 Crest detection

Next, we can use this optical flow analysis results to identify wave crests. We do this by starting from a given pixel position, using the corresponding vector obtained from optical flow analysis and comparing the pixel's intensity to the one at a position located a short distance along the direction of the flow vector. That allows us to divide the image in areas where fluorescent intensity is decreasing in the direction of flow (corresponding to the "front" of a wave) or increasing (its "wake"). This binary division can be represented as a wavesign-image, representing the front regions as bright and wake regions as dark areas.

[12]:
```
wavesign_im = min_de_patterns_crests.get_rise_or_fall(flow_x, flow_y, im0_smz)
```

[13]:
```
fig, ax = plt.subplots()
ax.imshow(wavesign_im)
ax.set_xlabel("x (pixels)")
ax.set_ylabel("y (pixels)")
plt.show()
```



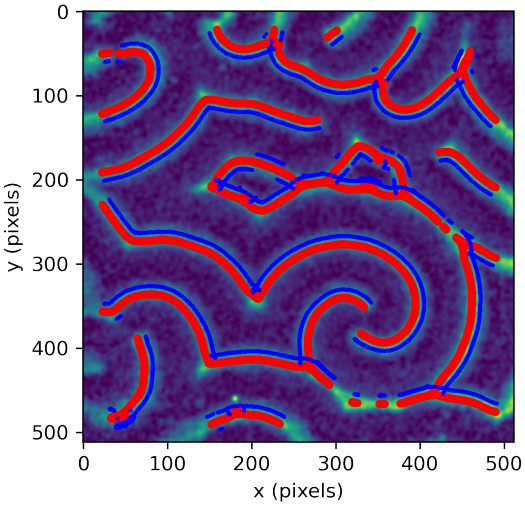
Using this image, we obtain the crests, defined as the points that lie between front or wake areas *and* where the intensity is above average (since otherwise, we would also get the "valleys"). Each crest point comes with (x, y) coordinates and a unit vector (w_x, w_y) perpendicular to the local crest line, in the direction of wave propagation.

[14]:
```
(
    crests_x,
    crests_y,
    forward_wavevector_x,  # w_x
    forward_wavevector_y,  # w_y
) = min_de_patterns_crests.get_crests(wavesign_im, im0_smz, halfspan / 2)
```

In the representation below, the identified wave crests are shown in red, and their direction of propagation is indicated in blue. Crest points close the edges of the frame are discarded to avoid edge-effects.

[15]:
```
fig, ax = plt.subplots()
span = 10
cx2 = crests_x + span * forward_wavevector_x
cy2 = crests_y + span * forward_wavevector_y
ax.imshow(im0_raw)
ax.plot(crests_x, crests_y, "ro", markersize=3)
ax.plot(cx2, cy2, "bo", markersize=1)
ax.set_xlabel("x (pixels)")
ax.set_ylabel("y (pixels)")
```

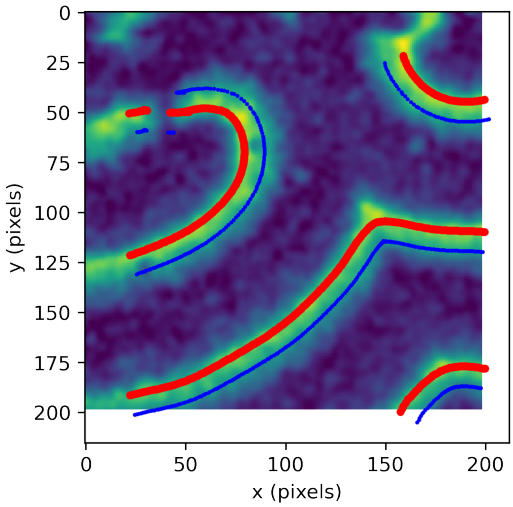
```
plt.show()
```



1.5 Profile mapping

We can use the wave vectors at the identified crest positions to estimate the local propagation of the pattern. For illustration, we plot a corner of the pattern. Again, the detected crest points are shown in red, an indication of local propagation direction in blue.

[16]:
```
fig, ax = plt.subplots()
zm = 200
Le = len(crests_x)
span = 10
cx1 = crests_x
cy1 = crests_y
cx2 = cx1 + span * forward_wavevector_x
cy2 = cy1 + span * forward_wavevector_y
zm_ix = np.argwhere((cx1 < zm) & (cy1 < zm))
ax.imshow(im0_raw[0 : zm - 1, 0 : zm - 1])
ax.plot(cx1[zm_ix], cy1[zm_ix], "ro", markersize=3)
ax.plot(cx2[zm_ix], cy2[zm_ix], "bo", markersize=1)
ax.set_xlabel("x (pixels)")
ax.set_ylabel("y (pixels)")
plt.show()
```



For each crest point and its accompanying wave vector, we can now obtain a cross-section profile by two-dimensional interpolation. For efficiency, this is done as a grid-style 2D interpolation for all the crest points together. Left panel: For clarity, we show a zoomed-in section of the pattern and the overlaying crests (red) and cross-section samplings (black). Right panel: The corresponding sampling map.

[17]:
```
(profile_map1, xxgrid, yygrid) = min_de_patterns_crests.sample_crests(
    im0_smz,
    crests_x,
    crests_y,
    forward_wavevector_x,
    forward_wavevector_y,
    halfspan,
    sampling_width,
)
```

[18]:
```
# Show a zoom-in of the result, specified by the variables zm_lo and zm_hi
# zm_lo and zm_hi are defined in the code-box below the selection above

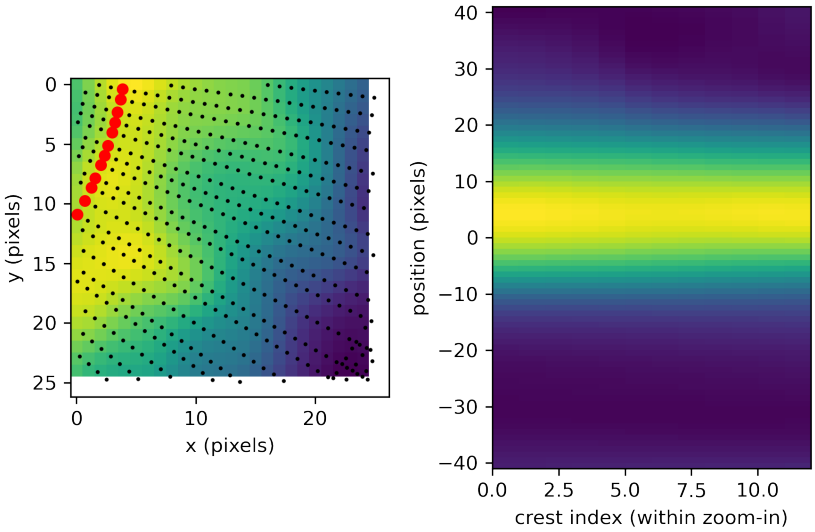
rr, cc = np.shape(im0_raw)
zm_ix1 = np.argwhere(
    (crests_x > zm_lo) & (crests_y > zm_lo) & (crests_x < zm_hi) & (crests_y <␣
 ↪zm_hi)
)
zm_ix2 = np.argwhere(
```

```
    (xxgrid.ravel() > zm_lo)
    & (yygrid.ravel() > zm_lo)
    & (xxgrid.ravel() < zm_hi)
    & (yygrid.ravel() < zm_hi)
)
fig, (ax_1, ax_2) = plt.subplots(1, 2)

ax_1.imshow(im0_raw[zm_lo:zm_hi, zm_lo:zm_hi])
ax_1.plot(
    xxgrid.ravel()[zm_ix2] - zm_lo,
    yygrid.ravel()[zm_ix2] - zm_lo,
    "ko",
    markersize=1,
)
ax_1.plot(
    crests_x[zm_ix1] - zm_lo,
    crests_y[zm_ix1] - zm_lo,
    "ro",
    markersize=5,
)
ax_1.set_xlabel("x (pixels)")
ax_1.set_ylabel("y (pixels)")

ax_2.imshow(
    profile_map1.T[:, zm_ix1],
    aspect="auto",
    origin="lower",
    extent=[0, crests_x[zm_ix1].size, -halfspan, halfspan],
)
ax_2.set_xlabel("crest index (within zoom-in)")
ax_2.set_ylabel("position (pixels)")

fig.tight_layout()
plt.show()
```



The same sampling grid is now used for the next image frame. As can be seen in the second sampling map, the (upwards) shift of all profile maxima reflects the motion of the crests from one frame to the next. Note that the parameter *halfspan* defines the distance (plus/minus) starting from the crest position of the first frame, within which intensities are sampled (at density *sampling_width*). If there is no shifted intensity profile visible in the sampling map below, it could be that a higher value for *halfspan* has to be chosen.

[19]:
```
(profile_map2, xxgrid, yygrid) = min_de_patterns_crests.sample_crests(
    im1_smz,
    crests_x,
    crests_y,
    forward_wavevector_x,
    forward_wavevector_y,
    halfspan,
    sampling_width,
)
```

[20]:
```
# Show a zoom-in of the result, specified by the variables zm_lo and zm_hi
# zm_lo and zm_hi are defined in the code-box below the selection above

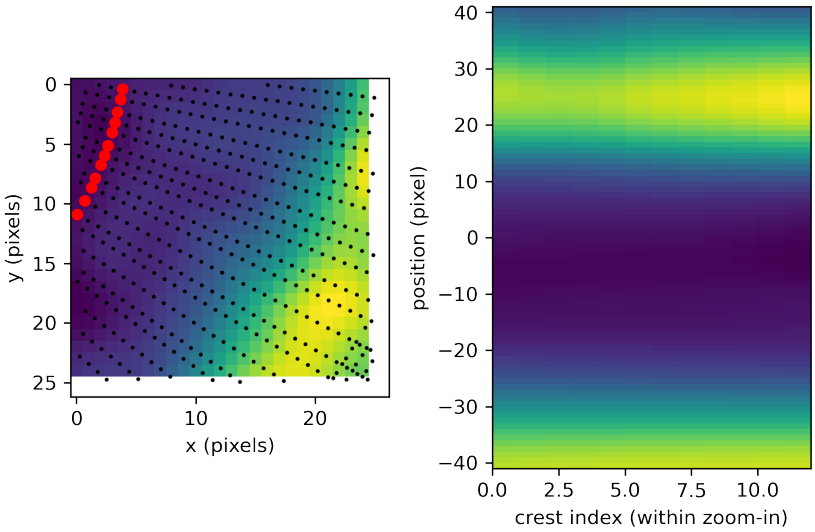
rr, cc = np.shape(im1_raw)
zm_ix1 = np.argwhere(
    (crests_x > zm_lo) & (crests_y > zm_lo) & (crests_x < zm_hi) & (crests_y <␣
 ↪zm_hi)
```

```
)
zm_ix2 = np.argwhere(
    (xxgrid.ravel() > zm_lo)
    & (yygrid.ravel() > zm_lo)
    & (xxgrid.ravel() < zm_hi)
    & (yygrid.ravel() < zm_hi)
)
fig, (ax_1, ax_2) = plt.subplots(1, 2)

ax_1.imshow(im1_raw[zm_lo:zm_hi, zm_lo:zm_hi])
ax_1.plot(
    xxgrid.ravel()[zm_ix2] - zm_lo,
    yygrid.ravel()[zm_ix2] - zm_lo,
    "ko",
    markersize=1,
)
ax_1.plot(
    crests_x[zm_ix1] - zm_lo,
    crests_y[zm_ix1] - zm_lo,
    "ro",
    markersize=5,
)
ax_1.set_xlabel("x (pixels)")
ax_1.set_ylabel("y (pixels)")

ax_2.imshow(
    profile_map2.T[:, zm_ix1],
    aspect="auto",
    origin="lower",
    extent=[0, crests_x[zm_ix1].size, -halfspan, halfspan],
)
ax_2.set_xlabel("crest index (within zoom-in)")
ax_2.set_ylabel("position (pixel)")

fig.tight_layout()
plt.show()
```



1.6 Velocity tracking

The two maps offer two profiles per crest position, one for the current frame (frame 1) and one for the next (frame 2). For each profile, a sub-unit maximum position is determined by a multi-point parabolic fit around the maximum. Since the cross-section was taken perpendicular to the wave crest, the shift between the two maxima reflects the shift of the crest peak position perpendicular to the local wave orientation. Thus, this shift equals a crest velocity in pixels per frame. The translocation distance d (in distance units) from peak to peak divided the time Δt that passed between the acquisition (in time units) on sequential frames then yields the velocity magnitude: $v = \frac{d}{\Delta t}$ Combined with the direction of the normalized flow vectors (w_x, w_y), this yields a vector $\vec{v}$ for each individual crest position (x, y). The parameter $look_ahead = 1$ defines that we are considering peaks located in front of the current one, that is, in propagation direction (as determined from optical flow analysis). If no local maximum can be determined in the direction of interest, the crest point is discarded. In other applications of the local analysis pipeline (like DE distance detection, when looking for the position of a MinE wave running behind a MinD wave), it can make sense to look towards the other direction.

[21]:
```
velocities = min_de_patterns_crests.compare_crestmaps(
    profile_map1, profile_map2, sampling_width, look_ahead=1
)
```

[22]:
```
print(f"Determined velocities for {np.size(velocities)} crest points.")
bad_count = 0
bad_indices = []
```

```
for ind, vel in enumerate(velocities):
    if not vel >= 0:
        bad_indices.append(int(ind))
        bad_count = bad_count + 1
velocities = np.delete(velocities, bad_indices, 0)
profile_map1 = np.delete(profile_map1, bad_indices, 0)
profile_map2 = np.delete(profile_map2, bad_indices, 0)
xxgrid = np.delete(xxgrid, bad_indices, 0)
yygrid = np.delete(yygrid, bad_indices, 0)
print(f"Discarded {bad_count} peaks due to failed peak detection.")
```

```
Determined velocities for 3441 crest points.
Discarded 390 peaks due to failed peak detection.
```

Below, the profile along the highlighted line will be shown in red for frame 1 and in blue for frame 2. The maximum identified will be shown as black dot. The crest index to be shown can be set below (notebook needs to be re-run from this point on for changes to apply).

[23]:
```
length = np.shape(profile_map1)[0]
print(
    f"Considered wave crest points: {length} (set crest index to integer number␣
 ↪from 0 to {length-1})"
)
```

```
Considered wave crest points: 3051 (set crest index to integer number from 0 to
3050)
```

[24]:
```
crest_index = 1000  # crest index for viewing, can be changed here
```

[25]:
```
# show position of profile to be displayed on the image
fig, (ax1, ax2) = plt.subplots(1, 2)
ax1.imshow(im0_raw)
ax1.plot(xxgrid[crest_index], yygrid[crest_index], color="white", linewidth=3)
ax1.set_title("frame 1 (red trace)")
ax1.set_xlabel("x (pixels)")
ax1.set_ylabel("y (pixels)")
ax2.set_title("frame 2 (blue trace)")
ax2.imshow(im1_raw)
ax2.plot(xxgrid[crest_index], yygrid[crest_index], color="white", linewidth=3)
ax2.set_xlabel("x (pixels)")
ax2.set_ylabel("y (pixels)")
fig.tight_layout()

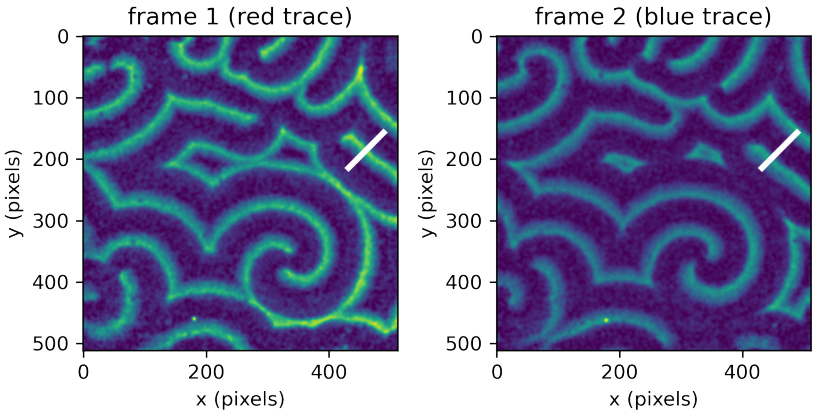
# identify peak positions for this particular crest location
prf1 = profile_map1[crest_index, :]
prf2 = profile_map2[crest_index, :]
peak_shift, x1, y1, x2, y2 = min_de_patterns_crests.compare_profiles(
    prf1, prf2, sampling_width, look_ahead=1, return_peaks=True
```

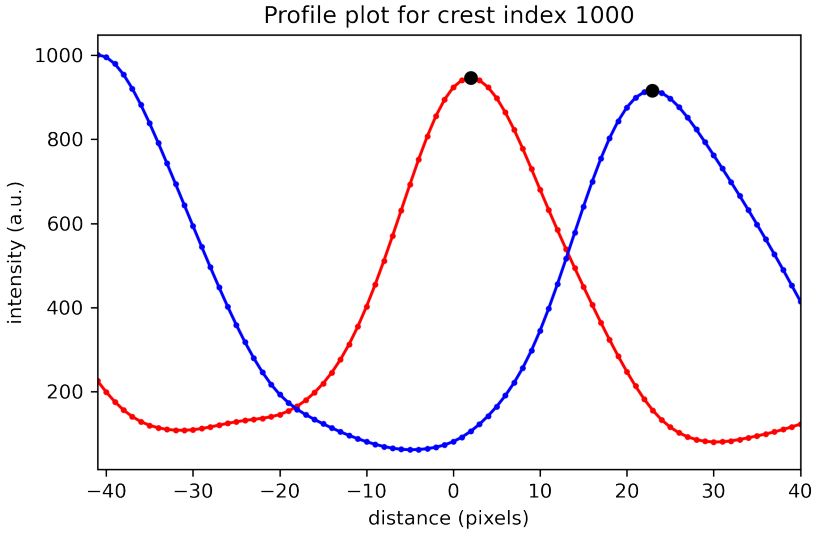
```
)
print(len(prf1))

# create shifted axis to have first peak close to center and plot
x_axis_shift = np.arange(-halfspan, halfspan, sampling_width)

# plot example profile
fig, ax = plt.subplots()
ax.set_title(f"Profile plot for crest index {crest_index}")
ax.plot(x_axis_shift, prf1, "ro-", markersize=2)
ax.plot(x_axis_shift, prf2, "bo-", markersize=2)
ax.plot(x1 * sampling_width - halfspan, y1, "ko", markersize=6)
ax.plot(x2 * sampling_width - halfspan, y2, "ko", markersize=6)
ax.set_xlabel("distance (pixels)")
ax.set_ylabel("intensity (a.u.)")
ax.set_xlim([-halfspan, halfspan - sampling_width])
fig.tight_layout()
plt.show()
```

82





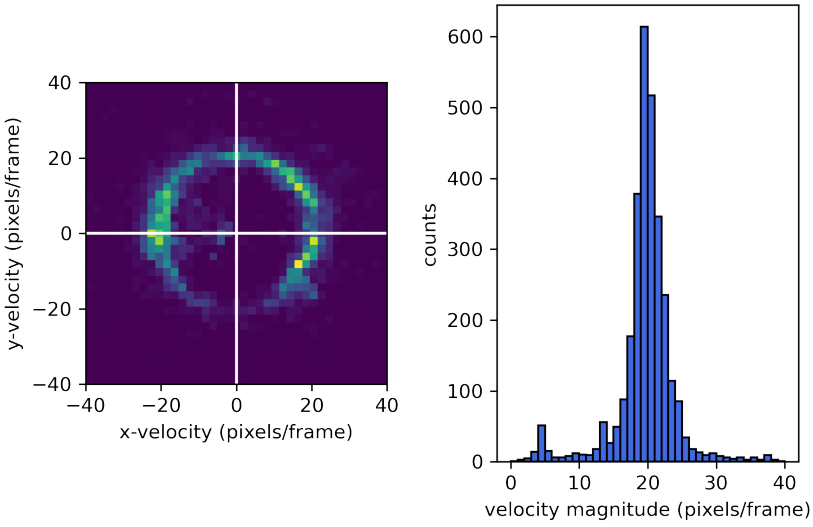
1.7 Velocity distribution

The analysis routine presented so far can be performed for all pairs of frames within a given image stack. Collecting these results yields a distribution of velocity vectors, which can be represented in different ways, depending on what information (magnitude, directionality) is of interest.

[26]:
```
(
    velocities,  # velocity magnitude
    forward_wavevector_x,  # unit vector w_x
    forward_wavevector_y,  # unit vector w_y
    all_wheels,  # data generated for velocity wheel (2D histogram)
    crests_x,
    crests_y,
    framenr,
    max_x1,
    max_y1,
    max_x2,
    max_y2,
    fig,
    ax_wheel,
    ax_sum,
) = local_velocity_analysis(
    MinDE_st_original,
    frames_to_analyse=5,  # use first ... frames
```

```
    halfspan=halfspan,
    sampling_width=sampling_width,
    edge=40,  # width of velocity wheel (2D histogram) and max of magnitude␣
↪histogram
    bins_wheel=40,  # number of bins (horizontal/vertical) for velocity wheel␣
↪(2D histogram)
    binwidth_sum=1,  # binwidth for velocity mangitude histogram
    kernel_size_general=kernel_size_general,  # kernel for first smoothing step
    kernel_size_flow=kernel_size_flow,  # kernel for additional smoothing step
    look_ahead=1,  # 1 -> look in propagation direction, -1 -> against it
    demo=True,  # True -> return figure handles
)
plt.show()
```

```
Analysing 5 frames
Working frame 0 to 1
Working frame 1 to 2
Working frame 2 to 3
Working frame 3 to 4
peak velocity magnitude: 19.00 pixels/frame
FWHM velocity magnitude: 5.00 pixels/frame
Median velocity magnitude: 19.90 pixels/frame
```



REFERENCES

[1] Alan Turing. "The chemical basis of morphogenesis". In: *Philosophical Transactions of the Royal Society of London. Series B, Biological Sciences* 237.641 (Aug. 14, 1952), pp. 37–72. ISSN: 2054-0280. DOI: 10.1098/rstb.1952.0012. URL: http://www.royalsocietypublishing.org/doi/10.1098/rstb.1952.0012 (visited on 11/22/2019).

[2] Justin S. Bois, Frank Jülicher, and Stephan W. Grill. "Pattern Formation in Active Fluids". In: *Physical Review Letters* 106.2 (Jan. 13, 2011), p. 028103. ISSN: 0031-9007, 1079-7114. DOI: 10.1103/PhysRevLett.106.028103. URL: https://link.aps.org/doi/10.1103/PhysRevLett.106.028103 (visited on 12/23/2021).

[3] Shigeru Kondo and Takashi Miura. "Reaction-Diffusion Model as a Framework for Understanding Biological Pattern Formation". In: *Science* 329.5999 (Sept. 24, 2010), pp. 1616–1620. ISSN: 0036-8075, 1095-9203. DOI: 10.1126/science.1179047. URL: https://www.science.org/doi/10.1126/science.1179047 (visited on 04/07/2022).

[4] J. Halatek, F. Brauns, and E. Frey. "Self-organization principles of intracellular pattern formation". In: *Philosophical Transactions of the Royal Society B: Biological Sciences* 373.1747 (May 26, 2018), p. 20170107. ISSN: 0962-8436, 1471-2970. DOI: 10.1098/rstb.2017.0107. URL: https://royalsocietypublishing.org/doi/10.1098/rstb.2017.0107 (visited on 11/22/2019).

[5] François Schweisguth and Francis Corson. "Self-Organization in Pattern Formation". In: *Developmental Cell* 49.5 (June 2019), pp. 659–677. ISSN: 15345807. DOI: 10.1016/j.devcel.2019.05.019. URL: https://linkinghub.elsevier.com/retrieve/pii/S1534580719303910 (visited on 01/08/2020).

[6] Max Rietkerk and Johan van de Koppel. "Regular pattern formation in real ecosystems". In: *Trends in Ecology & Evolution* 23.3 (Mar. 2008), pp. 169–175. ISSN: 01695347. DOI: 10.1016/j.tree.2007.10.013. URL: https://linkinghub.elsevier.com/retrieve/pii/S0169534708000281 (visited on 04/07/2022).

[7] Beatrice Ramm, Tamara Heermann, and Petra Schwille. "The E. coli MinCDE system in the regulation of protein patterns and gradients". In: *Cellular and Molecular Life Sciences* 76.21 (Nov. 2019), pp. 4245–4273. ISSN: 1420-682X, 1420-9071. DOI: 10.1007/s00018-019-03218-x. URL: http://link.springer.com/10.1007/s00018-019-03218-x (visited on 11/22/2019).

[8] Simon Kretschmer and Petra Schwille. "Pattern formation on membranes and its role in bacterial cell division". In: *Current Opinion in Cell Biology* 38 (Feb. 2016), pp. 52–59. ISSN: 09550674. DOI: 10.1016/j.ceb.2016.02.005. URL: https://linkinghub.elsevier.com/retrieve/pii/S0955067416300126 (visited on 11/22/2019).

[9] Kiyoshi Mizuuchi and Anthony G Vecchiarelli. "Mechanistic insights of the Min oscillator via cell-free reconstitution and imaging". In: *Physical Biology* 15.3 (Mar. 1, 2018), p. 031001. ISSN: 1478-3975. DOI: 10.1088/1478-3975/aa9e5e. URL: http:

//stacks.iop.org/1478-3975/15/i=3/a=031001?key=crossref.18bf29cccb7b7223b142cdbecfc43d0d (visited on 11/22/2019).

[10] Lukas Wettmann and Karsten Kruse. "The Min-protein oscillations in *Escherichia coli*: an example of self-organized cellular protein waves". In: *Philosophical Transactions of the Royal Society B: Biological Sciences* 373.1747 (May 26, 2018), p. 20170111. ISSN: 0962-8436, 1471-2970. DOI: 10.1098/rstb.2017.0111. URL: https://royalsocietypublishing.org/doi/10.1098/rstb.2017.0111 (visited on 12/01/2021).

[11] Erwin Frey et al. "Protein Pattern Formation". In: *Physics of Biological Membranes*. Ed. by Patricia Bassereau and Pierre Sens. Cham: Springer International Publishing, 2018, pp. 229–260. ISBN: 978-3-030-00628-0 978-3-030-00630-3. DOI: 10.1007/978-3-030-00630-3_10. URL: http://link.springer.com/10.1007/978-3-030-00630-3_10 (visited on 10/14/2021).

[12] Anthony G. Vecchiarelli et al. "Differential affinities of MinD and MinE to anionic phospholipid influence Min patterning dynamics *in vitro*: Flow and lipid composition effects on Min patterning". In: *Molecular Microbiology* 93.3 (Aug. 2014), pp. 453–463. ISSN: 0950382X. DOI: 10.1111/mmi.12669. URL: http://doi.wiley.com/10.1111/mmi.12669 (visited on 11/29/2019).

[13] Tamara Heermann et al. "Mass-sensitive particle tracking to elucidate the membrane-associated MinDE reaction cycle". In: *Nature Methods* 18.10 (Oct. 2021), pp. 1239–1246. ISSN: 1548-7091, 1548-7105. DOI: 10.1038/s41592-021-01260-x. URL: https://www.nature.com/articles/s41592-021-01260-x (visited on 10/15/2021).

[14] H. Meinhardt and P. A. J. de Boer. "Pattern formation in Escherichia coli: A model for the pole-to-pole oscillations of Min proteins and the localization of the division site". In: *Proceedings of the National Academy of Sciences* 98.25 (Dec. 4, 2001), pp. 14202–14207. ISSN: 0027-8424, 1091-6490. DOI: 10.1073/pnas.251216598. URL: http://www.pnas.org/cgi/doi/10.1073/pnas.251216598 (visited on 11/22/2021).

[15] Karsten Kruse, Martin Howard, and William Margolin. "An experimentalist's guide to computational modelling of the Min system". In: *Molecular Microbiology* 63.5 (Mar. 2007), pp. 1279–1284. ISSN: 0950-382X, 1365-2958. DOI: 10.1111/j.1365-2958.2007.05607.x. URL: https://onlinelibrary.wiley.com/doi/10.1111/j.1365-2958.2007.05607.x (visited on 10/14/2021).

[16] Anthony G. Vecchiarelli et al. "Membrane-bound MinDE complex acts as a toggle switch that drives Min oscillation coupled to cytoplasmic depletion of MinD". In: *Proceedings of the National Academy of Sciences* 113.11 (Mar. 15, 2016), E1479–E1488. ISSN: 0027-8424, 1091-6490. DOI: 10.1073/pnas.1600644113. URL: http://www.pnas.org/lookup/doi/10.1073/pnas.1600644113 (visited on 11/22/2019).

[17] Jonas Denk et al. “MinE conformational switching confers robustness on self-organized Min protein patterns”. In: *Proceedings of the National Academy of Sciences* 115.18 (May 1, 2018), pp. 4553–4558. ISSN: 0027-8424, 1091-6490. DOI: 10.1073/pnas.1719801115. URL: http://www.pnas.org/lookup/doi/10.1073/pnas.1719801115 (visited on 07/28/2020).

[18] Fridtjof Brauns et al. “Bulk-surface coupling identifies the mechanistic connection between Min-protein patterns in vivo and in vitro”. In: *Nature Communications* 12.1 (Dec. 2021), p. 3312. ISSN: 2041-1723. DOI: 10.1038/s41467-021-23412-5. URL: http://www.nature.com/articles/s41467-021-23412-5 (visited on 06/03/2021).

[19] V. Ivanov and K. Mizuuchi. “Multiple modes of interconverting dynamic pattern formation by bacterial cell division proteins”. In: *Proceedings of the National Academy of Sciences* 107.18 (May 4, 2010), pp. 8071–8078. ISSN: 0027-8424, 1091-6490. DOI: 10.1073/pnas.0911036107. URL: http://www.pnas.org/cgi/doi/10.1073/pnas.0911036107 (visited on 11/29/2019).

[20] Beatrice Ramm et al. “The MinDE system is a generic spatial cue for membrane protein distribution in vitro”. In: *Nature Communications* 9.1 (Dec. 2018), p. 3942. ISSN: 2041-1723. DOI: 10.1038/s41467-018-06310-1. URL: http://www.nature.com/articles/s41467-018-06310-1 (visited on 01/17/2020).

[21] Martin Loose et al. “Min protein patterns emerge from rapid rebinding and membrane interaction of MinE”. In: *Nature Structural & Molecular Biology* 18.5 (May 2011), pp. 577–583. ISSN: 1545-9993, 1545-9985. DOI: 10.1038/nsmb.2037. URL: http://www.nature.com/articles/nsmb.2037 (visited on 11/22/2019).

[22] Katja Zieske, Jakob Schweizer, and Petra Schwille. “Surface topology assisted alignment of Min protein waves”. In: *FEBS Letters* 588.15 (Aug. 1, 2014), pp. 2545–2549. ISSN: 00145793. DOI: 10.1016/j.febslet.2014.06.026. URL: http://doi.wiley.com/10.1016/j.febslet.2014.06.026 (visited on 01/14/2020).

[23] Guido Van Rossum and Fred L. Drake. *Python 3 Reference Manual*. Scotts Valley, CA: CreateSpace, 2009. ISBN: 1441412697.

[24] Anthony G. Vecchiarelli et al. *MinE recruits, stabilizes, releases, and inhibits MinD interactions with membrane to drive oscillation*. preprint. Microbiology, Feb. 17, 2017. DOI: 10.1101/109637. URL: http://biorxiv.org/lookup/doi/10.1101/109637 (visited on 11/22/2019).

[25] Beatrice Ramm et al. “A diffusiophoretic mechanism for ATP-driven transport without motor proteins”. In: *Nature Physics* 17.7 (July 2021), pp. 850–858. ISSN: 1745-2473, 1745-2481. DOI: 10.1038/s41567-021-01213-3. URL: http://www.nature.com/articles/s41567-021-01213-3 (visited on 10/05/2021).

[26] Sabrina Meindlhumer et al. “Directing Min protein patterns with advective bulk flow”. In: *Nature Communications* 14.1 (Jan. 27, 2023), p. 450. ISSN: 2041-1723. DOI: 10.1038/s41467-023-35997-0. URL: https://www.nature.com/articles/s41467-023-35997-0 (visited on 03/25/2023).

[27] Yaron Caspi and Cees Dekker. “Mapping out Min protein patterns in fully confined fluidic chambers”. In: *eLife* 5 (Nov. 25, 2016), e19271. ISSN: 2050-084X. DOI: 10.7554/eLife.19271. URL: https://elifesciences.org/articles/19271 (visited on 11/22/2019).

[28] Laeschkir Würthner et al. “Bridging scales in a multiscale pattern-forming system”. In: *Proceedings of the National Academy of Sciences* 119.33 (Aug. 16, 2022), e2206888119. ISSN: 0027-8424, 1091-6490. DOI: 10.1073/pnas.2206888119. URL: https://pnas.org/doi/full/10.1073/pnas.2206888119 (visited on 11/02/2022).

[29] Claire Robertson. “Theory and practical recommendations for autocorrelation-based image correlation spectroscopy”. In: *Journal of Biomedical Optics* 17.8 (Aug. 8, 2012), p. 080801. ISSN: 1083-3668. DOI: 10.1117/1.JBO.17.8.080801. URL: http://biomedicaloptics.spiedigitallibrary.org/article.aspx?doi=10.1117/1.JBO.17.8.080801 (visited on 03/10/2022).

[30] Berthold K. P. Horn and Brian G. Schunck. “Determining optical flow”. In: *Artificial Intelligence* 17.1 (1981), pp. 185–203. ISSN: 0004-3702. DOI: https://doi.org/10.1016/0004-3702(81)90024-2. URL: https://www.sciencedirect.com/science/article/pii/0004370281900242.

[31] M. Mesbah. “Gradient-based optical flow: a critical review”. In: *ISSPA ’99. Proceedings of the Fifth International Symposium on Signal Processing and its Applications (IEEE Cat. No.99EX359)*. Fifth International Symposium on Signal Processing and its Applications. Vol. 1. Brisbane, Qld., Australia: Queensland Univ. Technol, 1999, pp. 467–470. ISBN: 978-1-86435-451-5. DOI: 10.1109/ISSPA.1999.818213. URL: http://ieeexplore.ieee.org/document/818213/ (visited on 03/10/2022).

[32] Michael and Ilya. *scivision/pyoptflow: update implementation, compare 3 implementations*. Version v1.4.0. Oct. 2021. DOI: 10.5281/zenodo.5574844. URL: https://doi.org/10.5281/zenodo.5574844.

[33] Vladimir K. Vanag and Irving R. Epstein. “Pattern formation mechanisms in reaction-diffusion systems”. In: *The International Journal of Developmental Biology* 53.5 (2009), pp. 673–681. ISSN: 0214-6282. DOI: 10.1387/ijdb.072484vv. URL: http://www.intjdevbiol.com/paper.php?doi=072484vv (visited on 04/12/2022).

[34] John D Hunter. “Matplotlib: A 2D graphics environment”. In: *Computing in science & engineering* 9.3 (2007), pp. 90–95.

[35] Inkscape Project. “Inkscape”. Version 1.1. In: *https://inkscape.org* (2021).

[36] Johannes Schindelin et al. “Fiji: an open-source platform for biological-image analysis”. In: *Nature Methods* 9.7 (July 2012), pp. 676–682. ISSN: 1548-7091, 1548-7105. DOI: 10.1038/nmeth.2019. URL: http://www.nature.com/articles/nmeth.2019 (visited on 11/19/2021).

3

DIRECTING MIN PROTEIN PATTERNS WITH ADVECTIVE BULK FLOW

The Min proteins constitute the best-studied model system for pattern formation in cell biology. We theoretically predict and experimentally show that the propagation direction of in vitro *Min protein patterns can be controlled by a hydrodynamic flow of the bulk solution. We find downstream propagation of Min wave patterns for low MinE:MinD concentration ratios, upstream propagation for large ratios, but multistability of both propagation directions in between. Whereas downstream propagation can be described by a minimal model that disregards MinE conformational switching, upstream propagation can be reproduced by a reduced switch model, where increased MinD bulk concentrations on the upstream side promote protein attachment. Our study demonstrates that a differential flow, where bulk flow advects protein concentrations in the bulk, but not on the surface, can control surface-pattern propagation. This suggests that flow can be used to probe these features and to constrain mathematical models for pattern-forming systems.*

This chapter has been published in Nature Communications **14**, 450 (2023) by Sabrina MEINDLHUMER, Fridtjof BRAUNS, Jernej Rudi FINŽGAR, Jacob KERSSEMAKERS, Cees DEKKER and Erwin FREY.
Please also consider the Author's Correction (2024) in Sec. 3.10 starting on page 153, published in Nature Communications **15**, 6522 (2024).

3.1. INTRODUCTION

Pattern formation is a phenomenon observed in widely different contexts from physics to biology. In cell biology and embryology, it has been studied across species in intracellular[1, 2, 3] as well as multicellular systems[4, 5, 6]. The term broadly refers to the self-organization of molecules based on physicochemical principles, realized by the interplay of complex reaction networks, transport mechanisms, and guiding cues.[1, 2, 4, 7, 8, 9, 10, 11] Intracellular pattern formation is known to play important roles in the positioning of protein assemblies, particularly during cell division.[1, 2, 3, 7, 8, 12, 13, 14, 15]

The Min protein system from *E. coli* bacteria is the best studied model system for intracellular pattern formation. While rich in complexity with all its known and possible interactions within a cell and its biological role prior to Z-ring formation,[13, 16] it is at the same time intriguingly simple as its core pattern-forming mechanism essentially comes down to the interaction of only two proteins, MinD and MinE. The interaction of these proteins is widely considered the textbook example for a mass-conserving reaction diffusion system and has become the subject of numerous theoretical and experimental studies.[17, 19, 20, 21, 22, 23, 24, 25, 26, 18] *In vitro* reconstitution is well-established and relies on imaging of fluorescently labeled purified Min protein on supported lipid bilayers.[3, 21]

MinD is an ATPase, which binds ATP in the bulk solution and subsequently, binds the lipid membrane. Once membrane-bound, it recruits more MinD-ATP, leading to a positive feedback loop with an enhanced binding of MinD-ATP in its vicinity. This process is constantly counteracted by MinE, an ATPase-activating protein that also gets recruited by membrane-bound MinD-ATP. Membrane-bound MinE triggers MinD to hydrolyze its ATP and to detach from the membrane. Back in the bulk, MinD exchanges ADP for ATP and starts the cycle anew.[1, 7, 13] This simplified description (see Fig. 3.1C) is complemented and modified by countless details within the process, such as multimerization,[25] the local MinE:MinD stoichiometry,[26, 27] the formation of a depletion zone,[27] bulk-surface coupling,[19] and (particularly notable for our study) the so-called MinE switch[23]. The latter describes the ability of MinE to temporarily adopt a latent, non-reactive state upon membrane detachment. Non-switching mutants of MinE that cannot access this latent state were found to still be capable of pattern formation, albeit only within an extremely reduced concentration range. The presence of the MinE switch thus increases the robustness of the Min system to concentration fluctuations.[23] Numerous strategies have been employed to study, manipulate, and take advantage of the properties of Min patterns.[28] Examples include changing the membrane or buffer composition[24], crafting surface topology[29], microfabrication of sample chambers[30], variation of sample chamber geometry[19, 18], exploration of cargo molecule transport[31], integration with photoswitchable compounds[32], liposome encapsulation[33], and de novo synthesis within liposomes[34].

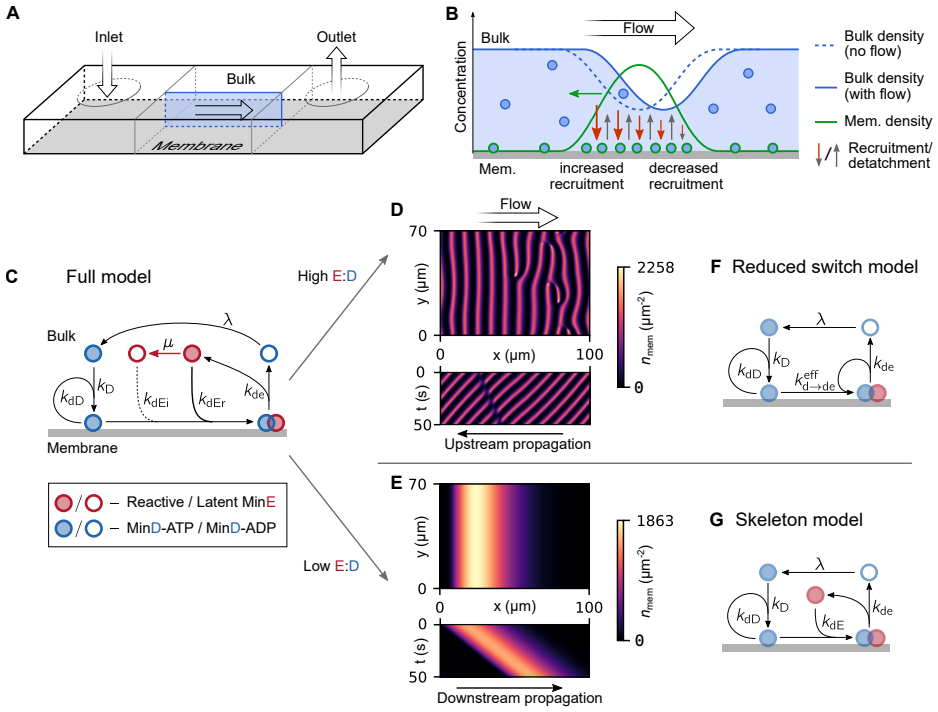


Figure 3.1: **Min models and simulation results.** **A** Basic illustration of setup used for simulations as well as experiments. **B** Illustration of the effect of bulk flow on pattern formation. MinD advection in the bulk shifts its concentration profile in the bulk relative to the membrane pattern, leading to an increase in the bulk concentration on the upstream side of wave crests relative to the downstream side. This enhances the recruitment rate (green arrows) on the upstream side relative to the downstream side and thus, results in a movement of the membrane pattern (but not the individual proteins) in the upstream direction. **C** Diagram depicting the interactions in the full switch model. This model includes the MinE switch. MinD-ATP binds the membrane, recruiting more MinD-ATP as well as reactive MinE. After MinE stimulates ATP-hydrolysis, MinD-ADP and MinE detach from the membrane. MinD needs to ADP for ATP in the bulk. MinE temporarily assumes a latent state before rebinding to the membrane. **D, E** Typical spatial pattern (snapshots) and kymograph of the membrane protein density found in the full switch model at high E:D ratios (**D**) and at low E:D ratio (**E**). **F** For high E:D ratios the full switch model can be simplified into the reduced switch model. MinE bulk gradients become negligible. **G** At low E:D ratios, the behavior of the Min system is captured well by the skeleton model. This model does not include the MinE switch.

In an *in vitro* study by Vecchiarelli et al,[24] external hydrodynamic flow was shown to influence Min protein patterns. More specifically, Min protein patterns were observed to propagate *upstream* under fast bulk flow, meaning that they formed waves that were

traveling against the direction of the hydrodynamic flow. The authors hypothesized that the cause of this upstream propagation was advective transport of reactive MinE in the vicinity of the membrane – a hypothesis which, to the best of our knowledge, has not been tested to date. More generally, an important implication of this finding is that bulk flow, a macroscopic perturbation, can be used to indirectly probe molecular mechanisms. This motivated us to systematically study the effect of bulk flow on pattern formation in the Min protein system. While it does not appear to fulfill a known biological function in the Min pattern forming process of *E. coli*, fluid flow was indeed found to be essential for asymmetry and pattern formation in several other organisms.[35] A prominent example is the establishment of the posterior-anterior axis within the monocellular *C. elegans* zygote, in which actomyosin cortical flows were found to transport regulatory PAR proteins[36, 37, 38] and to be associated with cytosolic streaming[39]. A generic consequence of advective flows is the directed transport of proteins. To investigate the effect of such advective transport on intracellular pattern formation in a controlled setting, we here focus on a system that allows for *in vitro* reconstitution and controlled manipulation of system parameters.

In the investigations presented here, we combine numerical simulations of theoretical models and *in vitro* experimental analysis to study the influence of bulk fluid flow on Min protein patterns. We find that in response to applied flow, Min protein surface patterns tend to align in mostly planar wave fronts which propagate in the direction of the bulk flow. Furthermore, we noticed that observables such as their preferred direction of propagation can be linked to underlying molecular mechanisms. In this paper, we aim to demonstrate that advective bulk flow can serve as a tool which helps to indirectly probe and reveal these mechanisms. Mathematical models play a key role in this approach as they help to link the molecular mechanisms to the macroscopic observations (e.g. response of protein pattern to bulk flow).

3.2. RESULTS

3.2.1. MINE-TO-MIND CONCENTRATION RATIO DETERMINES THE PROPAGATION DIRECTION

Our primary goal is to study the qualitative response of Min patterns to external fluid flow. For simplicity, we consider uniform laminar flow and use a previously established, parsimonious model[40, 17, 23, 8, 19] for the Min reaction kinetics as depicted in Fig. 3.1C. This model describes the basic interactions between MinD and MinE using mass-action law kinetics. MinD binds to the membrane, with a rate that is enhanced by MinD already on the membrane (self-recruitment). Membrane-bound MinD then recruits MinE to the membrane, forming a MinDE complex. In this complex, MinE catalyzes MinD hydrolysis, leading to the dissociation of the complex from the membrane, releasing both constituents into the bulk. In the bulk, MinD undergoes nucleotide exchange before it can bind to the membrane again. The interplay between these basic reactions and diffusive transport gives rise to a rich variety of concentration patterns that form on the membrane, where diffusion is much slower than in the bulk.[8, 17, 19] Here, we extend

this model by accounting for advective transport in the bulk. Membrane-bound proteins are not affected by the flow (see Supplementary Information in section 3.5). Moreover, since a previous experimental study hypothesized that switching of MinE between reactive and latent states in the bulk is responsible for the upstream propagation of Min patterns,[24] we explicitly include this conformational switching of MinE in our model, which we accordingly refer to as the *full (switch) model*.[23] The model equations are provided in the Materials and Methods section with further details in the SI (section 3.5).

We performed finite element simulations in a rectangular area representing the lipid bilayer membrane and the bulk solution above it, choosing periodic boundary conditions in the lateral directions to reduce finite-size effects. The dimension orthogonal to the membrane was integrated out (and explicitly accounting for this dimension does not change the qualitative findings, see SI (section 3.5). We performed simulations for different E:D ratios because previous studies did show that the total concentrations of MinD and MinE, and in particular their E:D ratio, are essential control parameters for Min protein pattern formation.[27]

As illustrated in Fig. 3.1D and Fig. 3.1E, our simulations show that uniform flow has two main effects: (i) Wave fronts align perpendicular to flow direction and (ii) the wave propagation direction aligns upstream (against the flow) or downstream (with the flow), depending on the E:D ratio. While upstream propagation occurs for high E:D ratios (Movie 1), downstream propagation is found for low E:D ratios (Movie 2). Notably, we predict downstream propagation in regimes that would not allow for pattern formation in the absence of flow. We refer to this phenomenon as a *flow-driven instability*.[41, 42] (Please see SI Sec. 3.5.10.) Moreover, we observed that downstream propagating patterns slowly increase in wavelength, in a process reminiscent of coarsening dynamics in phase-separating systems. Eventually, only a single propagating soliton-like pulse remained in the simulation domain, as shown in Fig. 3.1E.

To test our theoretical predictions, we performed experiments with purified Min proteins in flow channels that were coated with a lipid bilayer. To reliably determine the patterns' response to flow, we developed automatized tools that allowed us to quantify the propagation speed and direction of wave crests.[43] Fig. 3.2 shows exemplary images along with the results from this wave crest velocity analysis visualized as 2D histograms. Data were collected from multiple comparably sized imaging regions within one flow cell. We experimentally found that an applied advective flow had multiple effects on the Min patterns. We observed a clear decrease in the occurrence of spiral patterns, as patterns tended to transition into traveling waves with wave fronts aligned orthogonal to the flow direction. Importantly, the traveling waves that formed during an applied flow, exhibited *upstream* propagation for high E:D ratio (E:D=10, Fig. 3.2A and Movie 3), but *downstream* propagation for low E:D ratio (E:D=2, Fig. 3.2B and Movie 4). Notably, in a control experiment we reversed the flow rate and found that the pattern's propagation direction also reversed after several minutes (see Fig. 3.21 and Movie 3).

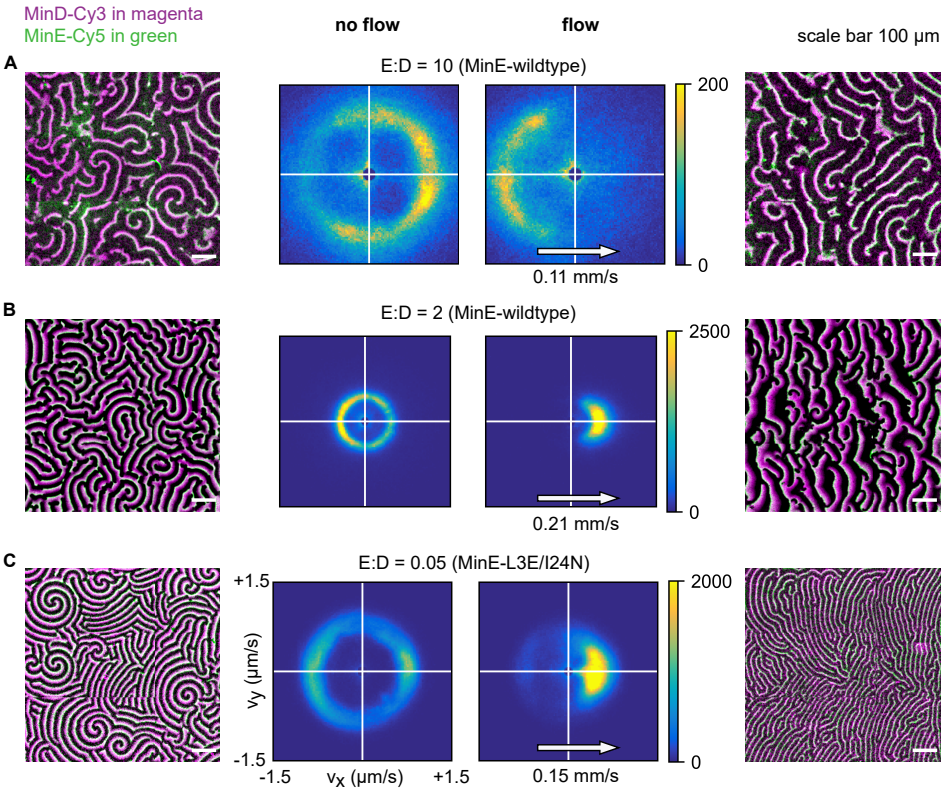


Figure 3.2: **Experimental data showing how patterns respond to flow at different E:D ratios.** Data are for MinE-wildtype (**A, B**) and MinE-L3E/I24N (**C**), with bulk flow directed left-to-right. Min patterns (outer left and outer right columns) show MinDCy3 in magenta and MinE-Cy5 in green. All scale bars are 100 μm. The results of wave-propagation analysis calculated for MinD-Cy3 data are represented as 2D histograms (center columns) with binning size (25 nm/s) × (25 nm/s), showing counts for directionality (v_x, v_y). Left half of the figures displays an exemplary image as well as wave-propagation analysis for the no-flow case. Right half of the figures displays an exemplary image as well as wave-propagation analysis with flow. Images were stitched from 3 × 3 fields of view. **A** Upstream propagation was observed in experiments for high E:D ratio (initial 10). **B** Downstream propagation observed for low E:D ratio (initial 2, corrected 1.3). **C** Downstream propagation observed for the MinE-L3E/I24N mutant at E:D = 0.05.* *__Important note: The data shown in panel C was later found to be unsuitable for the velocity analysis performed here, as specified in an Author's Correction (2024), given in section 3.10__.

All these experimental observations are in good qualitative agreement with the simulation results. Most importantly, we predicted from our simulations that the relative concentration of MinE with respect to MinD would lead to different outcomes with respect to the patterns' directionality relative to the external flow. There are, however, also notable differences, both qualitative and quantitative. An example of the former is that downstream waves are experimentally observed for E:D ratios that also exhibit pattern formation without any applied flow. This finding stands in contrast to our simulations, where downstream propagation only appears in regimes which would not allow for pattern formation in the absence of flow. Further, we do not observe the predicted coarsening (i.e., a strong increase of wavelength) for downstream propagating waves in our experiments (see Fig. 3.23).

A quantitative difference is the value for the E:D ratio above which upstream propagation can be observed. In experiments, we had to go to much higher E:D ratios (>2) than in the simulations to get upstream propagation, where we observed it starting from E:D ratios of 0.1 (Fig. 3.3).

3.2.2. MODEL REDUCTIONS AND MECHANISTIC EXPLANATION OF UPSTREAM PROPAGATION

Reducing a model to the key features dominating within a given parameter regime is a strategy that can provide important insights into the mechanisms underlying the entire process described by the model. To gain intuition about the origin of the E:D dependence of a pattern's response to bulk flow, we studied two reduced models that reproduce the results of the full model in the limits of high and low E:D ratio, respectively.

In the limit of large MinE concentration and fast switching of MinE between the reactive and latent conformations, the MinE switching dynamics can be eliminated using a quasi-steady state approximation (see SI (section 3.5)). The resulting *reduced switch model*, visualized by the network cartoon in Fig. 3.1F, exclusively exhibits upstream propagation in response to flow (Fig. 3.7). This is consistent with the numerical simulations of the full model in the regime of large E:D ratio (see Fig. 3.3). In the limit where the reduced switch model is valid, bulk concentration gradients of MinE are negligible such that MinE bulk concentrations no longer appear explicitly as dynamic variables. This in turn implies that advective transport of MinE has no effect on the dynamics. As an additional test, we performed simulations of the full model where MinE is not advected by the flow. Consistent with our expectation from the theoretical analysis, we found upstream propagation. Taking the above results together, we conclude that – contrary to an earlier hypothesis[24] – upstream propagation of Min-protein patterns is not due to downstream transport of (reactive) MinE.

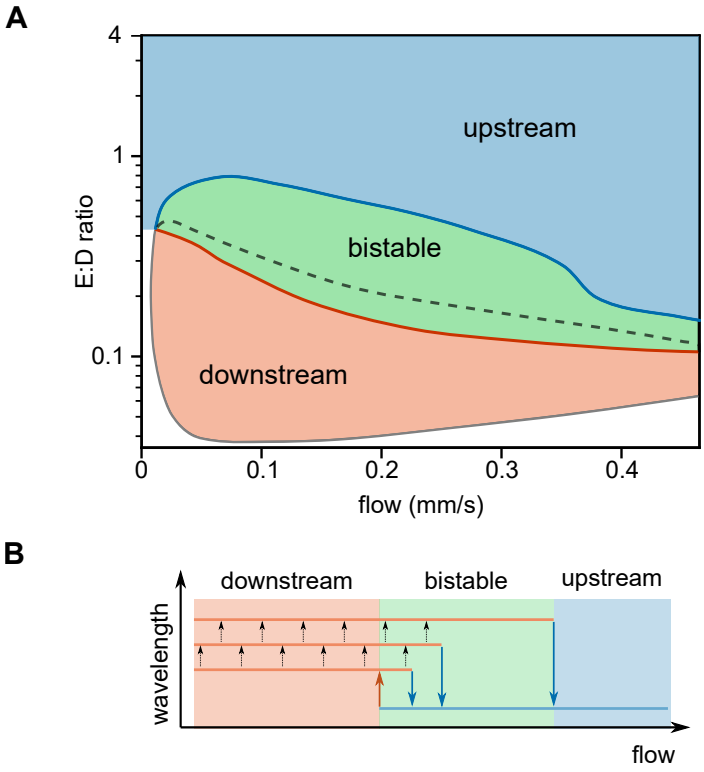


Figure 3.3: **Phase diagram displaying the predicted direction of pattern propagation.** **A** Phase diagram displaying the predicted direction of pattern propagation. Red and blue regions indicate the parts of the parameter space where exclusively downstream or upstream patterns are observed, respectively. Green region indicates the multistability regime, where the propagation direction depends on the initial conditions. If simulations are initiated from the homogeneous steady state, the observed propagation direction is downstream below the black dashed line, and upstream above it. Details on the adiabatic parameter sweeps and the data points underlying the phase diagram are provided in SI Sec. 3.5.8 and Fig. 3.10. **B** Schematic visualizing that the transition flow velocity depends on the wavelength of the pattern. Upon increasing the flow velocity, larger wavelength patterns reverse the propagation direction at a higher flow velocity.

This naturally raises the question of what the actual cause of upstream propagation is. To understand this, we consider an incipient accumulation zone of MinD on the membrane. Recruitment of MinD to the membrane acts as a sink, such that the neighboring bulk region becomes depleted of MinD (see Fig. 3.1B and Fig. 3.8). This depletion zone is replenished by diffusion, and at the same time transported downstream by the bulk flow. This downstream transport accelerates the replenishment on the upstream side of the accumulation zone and thus, allows faster recruitment of MinD there. Vice versa, re-

cruitment on the downstream side is reduced. As a net effect, one obtains an upstream movement of the accumulation zone (while the individual proteins do not move laterally). This differential flow-induced propagation has been theoretically studied for two-component mass-conserving reaction diffusion models.[44] There, it was shown that flow drives the upstream propagation of patterns that are stationary in the absence of flow.

Let us now turn to the regime of low E:D concentration ratio in which we observe *downstream* propagation of the membrane-bound protein waves. Previous studies showed that conformational switching of MinE can be neglected in this regime.[19] This is because the majority of MinE (within the penetration depth of bulk gradients orthogonal to the membrane) is in the reactive form and rapidly cycles between membrane and bulk. Indeed, in simulations of a reduced *skeleton model* that does not include MinE conformational switching, we exclusively found downstream propagating waves, consistent with the notion that the model captures the relevant dynamics in the low E:D regime (see Fig. 3.9). To experimentally test this rationale, we replaced MinE with a non-switching mutant MinE-L3E/I24N[23] and indeed found downstream propagating waves only, as shown in Fig. 3.2C and Movie 5. Notably, we find that pattern formation with this MinE mutant requires sufficiently low E:D ratios in agreement with previous experiments and theory.[23]

Next, we tried to decipher the mechanism of downstream propagation. Here, the situation is much more convoluted than in the regime of high E:D, because here bulk gradients of both MinD and MinE are significant. While MinD recruits itself to the membrane, MinE recruited by MinD drives MinD detachment by catalyzing MinD hydrolysis. Intuitively, one might think that the above reasoning for flow-induced upstream propagation might be applied to explain downstream propagation based on MinE advection and the MinE-driven MinD detachment. The reasoning would be that MinE is replenished faster and therefore, recruited faster on the upstream side of the MinD-accumulation zone. This would result in faster MinD detachment there, compared to the downstream side, resulting in a downstream propagation of the MinD-accumulation zone. To test this intuition, we performed simulations in which MinE was not advected by the flow. Strikingly, we *still* observe downstream propagating waves (see Fig. 3.12). This indicates that an intricate interplay of advective MinD transport and diffusive MinE transport is responsible for downstream propagation, whereas MinE advection is not crucial. Disentangling this interplay remains an open challenge for future research.

3.2.3. HYSTERESIS AND TRANSITION TO UPSTREAM PROPAGATION BY INCREASING FLOW RATE

Next, we turned to two closely connected questions: First, how does the propagation direction transition from upstream to downstream (Movie 6) at intermediate E:D ratios? Second, how does the flow speed impact the dynamics?

To address these questions, we mapped out a two-dimensional phase diagram employing finite-element simulations using the flow speed and the E:D ratio as control parame-

ters. The resulting phase diagram is shown in Fig. 3.3A. A striking feature of this phase diagram is that increasing the flow rate can drive a *reversal* from downstream propagation to upstream propagation for intermediate E:D ratios. Importantly, we find that this transition shows hysteresis, meaning that the point on which the transition occurs depends on whether one increases or decreases the flow rate or the E:D ratio. Consequently, there is a regime in which propagation in either direction is possible as the propagation direction sensitively depends on the initial conditions and history. For the downstream to upstream transition, we also observed a correlation with the pattern wavelength (see Fig. 3.10). Downstream propagating patterns were found to slowly coarsen (increase their wavelength) in our simulations. We observed that the downstream-to-upstream transition occurred at higher flow rates for longer wavelength patterns (see Fig. 3.3B).

In a linear stability analysis of the homogeneous steady state, we find two distinct instabilities in the multistable region: One at short wavelengths, corresponding to upstream propagating waves (as indicated by the imaginary part of the growth rate, see SI (section 3.5)), and another one at long wavelengths, corresponding to downstream propagating waves. We find that the onset of the first instability (at short wavelengths) precisely coincides with the transition from upstream to downstream propagating waves in simulations with adiabatically decreasing flow velocities. This suggests that upstream propagating waves emerge from this instability. In contrast, we did not find a characteristic feature in the linear stability properties (encoded in the dispersion relation) that corresponds to the transition from downstream to upstream propagation upon increasing flow rate.

We next tested the predicted hysteresis and multistability of the Min patterns experimentally. Taking advantage of our closed-circle experimental setup, we could incrementally increase the flow rate and acquire protein patterns at distinct points (flow rate, E:D ratio) in the parameter space. Note however, that for practical reasons (such as long incubation/equilibration times), the experimental approach is not identical to the one followed in the simulations depicted in Fig. 3.3A. In the simulation, we started from a homogeneous steady state at a certain E:D ratio and directly applied a given flow rate. In the experiment, we first established patterns in the absence of flow, and then incrementally went through a sequence of flow rates, with an associated waiting time (15-30 minutes) at each point.

An example image series of Min patterns at the same location within the flow channel, yet at different bulk flow rates is displayed in Fig. 3.4A. Analysis of the crest propagation directions as dependent on the bulk flow rate is provided in Fig. 3.4B to 3.4E for different E:D ratios in the intermediate regime. Both upstream and downstream propagating patterns were observed. Fig. 3.4F shows an overview on the peak velocities obtained for different E:D ratios and flow rates. The full crest velocity analysis of all experiments can be found in the SI (section 3.8).

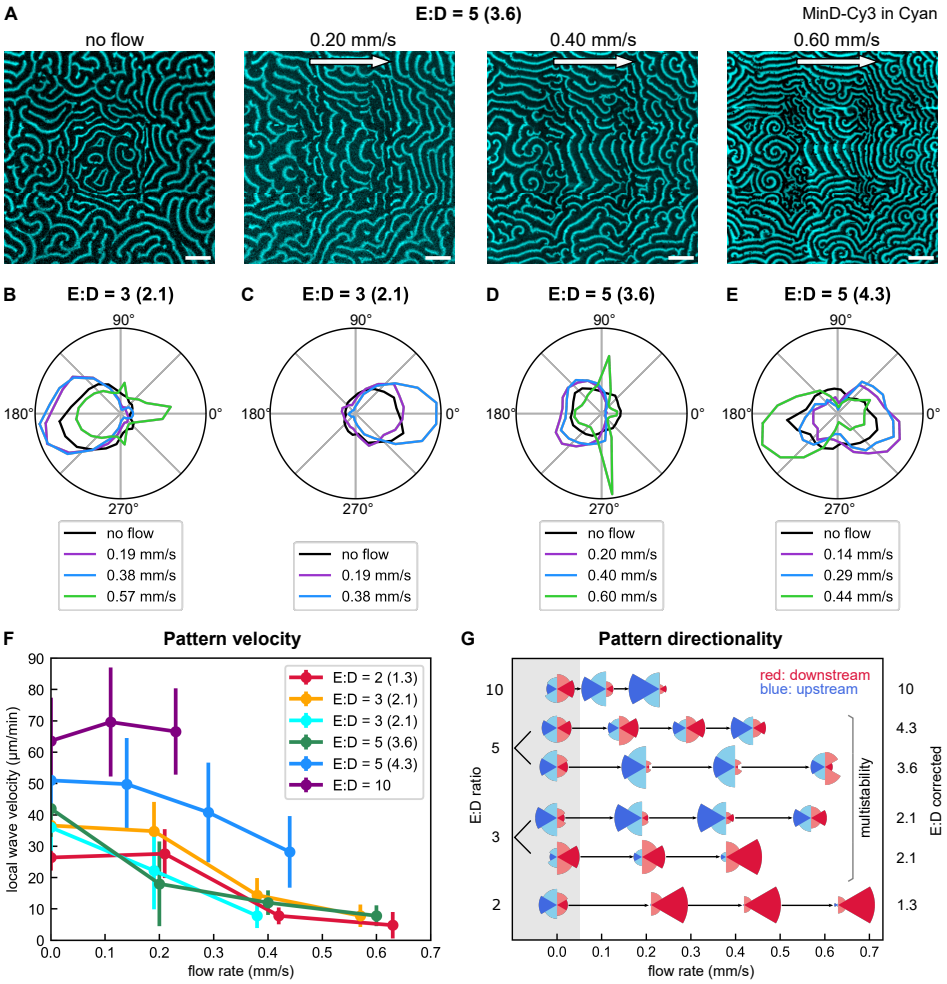


Figure 3.4: **Experimental data showing how Min patterns respond to a sequence of flow rates.** **A** Min patterns for different flow velocities at initial ratio E:D = 5 (corrected 3.6) sampled at the same location within the flow channel. Channel MinD-Cy3 in cyan, scale bars 100 μm. Images stitched from 3 × 3 fields of view. **B** Polar histogram showing counts per angular segment for initial ratio E:D = 3 (corrected 2.1). **C** Idem for initial ratio E:D = 3 (corrected 2.1). **D** Idem for initial ratio E:D = 5 (corrected 3.6). **E** Idem for initial ratio E:D = 5 (corrected 4.3). **F** Peak velocity magnitude ± FWHM/2 (calculated from histogram with binning size 10 nm/s) shown as function of flow rate for different E:D ratios. **G** Overview of experiments done for wildtype MinE. Downstream and upstream fractions are obtained from histogram counts per angular segment, with one series (horizontal line) representing one experiment. Size of fraction is given by the segment's radius. Red indicates downstream flowing patterns, blue indicates upstream patterns. Source data are provided as a Source Data file. Full experimental analysis is shown in the SI (section 3.5).

To obtain a quick overview on a pattern's response to flow, we calculated angles from the vectoral components obtained from our wave propagation analysis, binned them in segments of 15^o and plotted their normalized occurrence for different flow rates, as shown Fig. 3.4B to 3.4E. This can be understood as a summation over counts found in a certain angular segment from a 2D histogram plot of (v_x, v_y) such as those shown in Fig. 3.2. In Fig. 3.4G, we show overviews on results obtained from all experiments done with wildtype MinE. Defining the -30^o to +30^o segment as "downstream" (shaded red in Fig. 3.4B to 3.4E) and 150^o to 210^o as "upstream" (shaded blue in Fig. 3.4B to 3.4E), we show the downstream and upstream fractions as red and blue segments respectively, with the symbol radius proportional to the occurrence. Fig. 3.17 provides an overview on the visual representations. At the lowest E:D ratio, downstream propagation was clearly favored upon exposing a pattern to flow, while at the highest E:D ratio, upstream propagation was dominant. For intermediate E:D ratios, the outcome was less clear. Here, we found that the propagation direction sensitively depended on the initial condition, i.e. on the initial propagation direction in the absence of flow.

For most E:D ratios, we observed that waves tended to slow down upon increasing the flow rate (see Fig. 3.4F and Fig. 3.22). We were able to confirm that the observed slowing down is indeed induced by the flow and not merely a consequence of the experiment's duration. In a control experiment, the Min pattern in a sample channel was not exposed to flow yet observed over the same time period as a flow-experiment that was run in parallel in a separate flow channel (at an initial E:D ratio of 3). The results of both the regular and control experiment are shown in Fig. 3.19 and Fig. 3.20. Analysis showed that while the control's pattern did change over time, it did not show the distinctive directional features of the pattern exposed to bulk flow. Slowing down of the wave crest was observed, yet much less pronounced than for the flow experiment. In simulations, we find that waves generally speed up under faster flow, while a slowdown is only observed in a small regime of slow flow speeds (Fig. 3.13).

3.3. DISCUSSION

In our study, we performed simulations as well as *in vitro* experiments designed to investigate the influence of advective bulk flow on membrane-bound protein patterns. We theoretically predicted and experimentally showed that Min protein patterns respond differently to hydrodynamic flow depending on the E:D ratio and flow rate. The transition from upstream propagation (high E:D) to downstream propagation (low E:D) is qualitatively captured by a parsimonious model that explicitly accounts for conformational switching of MinE. For intermediate E:D ratios, our model predicts multistability of waves propagating in either direction, resulting in hysteresis. This imparts a strong dependence of the dynamics on the initial state, which we indeed observed in our experiments for intermediate E:D ratios (Fig. 3.4G). Our analysis shows that different pattern-forming mechanisms operate in low and high E:D conditions, with the role of MinE bulk gradients being the key difference between these mechanisms. For large E:D ratios, we found MinE bulk gradients along the membrane to be negligible. In this way, we were able to reduce the full model to a simplified, effective model for MinD dynamics that al-

lowed us to understand the mechanism of upstream propagation. In particular, we have shown that upstream propagation is not caused by MinE advection, but by a difference in MinD bulk gradients which promote attachment on the upstream side. At low E:D ratios, MinE conformational switching can be neglected, as we showed both by numerical simulations and experiments using a non-switching MinE mutant. Although much has been elucidated about the role of bulk flow on pattern formation, it remains an open question at this point how downstream propagation emerges at low E:D ratios.

The key feature of our studied system is *differential* flow, i.e. the advection of different components (protein concentrations) with different velocities.[41] Bulk flow leads to advection of the proteins in solution, but not those on the membrane where the observed pattern forms. Therefore, bulk flow affects the patterns only indirectly, through the bulk-surface coupling[19] related to the attachment and detachment of proteins at the membrane surface. As a result of this indirect coupling between the protein pattern and the hydrodynamic flow, the patterns can propagate both upstream and downstream relative to the flow direction, depending sensitively on various molecular aspects of the reaction kinetics such as the attachment–detachment dynamics. The patterns' response to flow can therefore be used as a robust, qualitative observable that allows one to identify regimes where different pattern-forming mechanisms operate. Bulk-surface coupling is a general feature of protein-based pattern formation.[1] Differential flow will generally occur when bulk flows (e.g. cytoplasmic streaming) are present in such systems.[45] On a larger scale, bulk-surface coupling is important for morphogenesis, where epithelial sheets surround fluid-filled lumens.[46, 47] Signaling molecules released to the lumen will be subjected to advective flows therein. By contrast, molecules that diffuse directly from cell to cell, e.g., through gap junctions, are not subject to such flows. Here, secretion and receptor-binding are the analogs to detachment and attachment in the Min system.

From a broader perspective, advective flow is a perturbation that breaks a symmetry of the system by imposing a preferred spatial direction. Pattern formation is innately connected to symmetry breaking, to the point where the terms are sometimes even used interchangeably.[48, 49] In the absence of spatial cues, symmetry breaking happens spontaneously due to the amplification of small random fluctuations or small heterogeneities within the system. As exemplified by Min patterns in the absence of flow or other cues, the propagation direction of waves is random and there is no predominant direction on average. Advective bulk flow breaks this symmetry, causing the wave patterns to align in a particular direction, either with or against the flow (as we showed). Thus, the bulk flow can be thought of as an analogue to an external magnetic field applied to a ferromagnetic material. Using such symmetry-breaking perturbations to probe these materials has provided valuable insights into the underlying physics. Here, we demonstrated that a related approach can be applied to a complex pattern-forming system that operates far from equilibrium.

Taking the experimentally observed responses to flow into account puts constraints on theoretical models. We tested two other Min models from the literature (developed by Bonny et al[50] and Loose et al[51]) for their propensity to produce both upstream and downstream propagating patterns (see SI (section 3.5), Fig. 3.15). We found that for the

previously published kinetic rates, these models produced only downstream propagating patterns over the entire range of E:D ratios where patterns occur, even upon expanding them to include MinE-conformational switching. Thus, while our model predicted a transition between upstream and downstream propagation in qualitative agreement with experiments, we found that the other tested Min models did not. Although our simulations and *in vitro* experiments yielded a very similar qualitative behavior of the influence of advective bulk flow on membrane-bound Min protein patterns, shortcomings of our own model became apparent upon making quantitative comparisons to experiments. For instance, we were unable to quantitatively predict the critical E:D ratio at which the transition from downstream to upstream propagation occurs. Moreover, the dependence of wavelength and wave speed on flow speed disagree between model and experiment (compare Fig. 3.1E vs Fig. 3.23, and Fig. 3.13 vs Fig. 3.22). However, note that for the experiments, we indicate the average flow rate across the channel. The flow rate in the vicinity of the membrane (within the gradient penetration depths of a few micrometers) is significantly slower due to the Poiseuille flow profile in the channel.

The influence of advective flow on biological pattern formation has rarely been studied, both experimentally and theoretically, and remains an active topic of research.[24, 42, 10, 52, 53, 54] Our findings on the Min protein system's response to flow suggest that additional molecular features of the protein reaction network, not yet accounted for by the current Min models, are necessary to quantitatively explain the observed phenomena. Identifying these still unknown features and including them in theoretical models remains an open issue and active topic of research. Insight into the detailed biochemical mechanisms of the MinD-MinE interactions (such as cooperative MinD self-recruitment, dimerization of MinD and MinE, MinE membrane binding, etc.) is likely needed to make progress and to allow for an accurate quantitative fit of the spatiotemporal dynamics of the Min system.

To conclude, the application of hydrodynamic flow exposed the limitations of the current models and yielded additional data that can be used to constrain models in future studies. Microfluidic applications may take advantage of Min patterns where bulk flow can be used to orient membrane-bound protein patterns and adjusting the E:D ratio allows one to decide whether one wants the protein waves to go with or against the flow. Combined with the Min system's capacity for cargo transport,[31] this could offer a platform for directed transport of other membrane-associated proteins.

3.4. METHODS

Please find theoretical methods as well as extended experimental methods in the SI (section 3.6).

3.4.1. MATHEMATICAL MODEL

We adopt a previously established model for the Min-protein dynamics based in mass-action-law kinetics on a membrane and the adjacent bulk solution. Below, we describe

the model in the simplified two-dimensional setting where the vertical dimension of the bulk has been integrated out (see SI Sec. 3.5.12). This model describes the concentrations of the following conformational states of MinD and MinE: Membrane-bound MinD (m_d); membrane-bound MinDE complex (m_{de}); cytosolic MinD-ADP (c_{DT}); cytosolic MinD-ATP (c_{DT}); cytosolic reactive (switch open) MinE (c_{Er}); cytosolic inactive (switch closed) MinE (c_{Ei}). The dynamics of the membrane-bound components are governed by

$$\partial_t m_d(x,t) = D_m \nabla^2 m_d + f_d, \quad (1)$$

$$\partial_t m_{de}(x,t) = D_m \nabla^2 m_{de} + f_{de}. \quad (2)$$

And the dynamics in the bulk, including advective flow, read

$$\partial_t c_{DD}(x,t) + v_f \nabla c_{DD} = D_c \nabla^2 c_{DD} + f_D - \lambda c_{DD} \quad (3)$$

$$\partial_t c_{DT}(x,t) + v_f \nabla c_{DT} = D_c \nabla^2 c_{DT} + f_{DT} + \lambda c_{DD} \quad (4)$$

$$\partial_t c_{Er}(x,t) + v_f \nabla c_{Er} = D_c \nabla^2 c_{Er} + f_{Er} - \mu c_{Er} \quad (5)$$

$$\partial_t c_{Ei}(x,t) + v_f \nabla c_{Ei} = D_c \nabla^2 c_{Ei} + f_{Ei} + \mu c_{Er} \quad (6)$$

The reaction terms f_i describing the attachment, detachment and interconversion of species at the membrane as illustrated in Fig. 3.1C are given by

$$f_d = (k_D + k_{dD} m_d) c_D - k_{dEr} m_d c_{Er} - k_{dEi} m_d c_{Ei} \quad (7)$$

$$f_{de} = k_{dEr} m_d c_{Er} + k_{dEi} m_d c_{Ei} - k_{de} m_{de} \quad (8)$$

$$f_{DD} = k_{de} m_{de} \quad (9)$$

$$f_{DT} = -(k_D + k_{dD} m_d) c_{DT} \quad (10)$$

$$f_{Er} = -k_{dEr} m_d c_{Er} + k_{de} m_{de} \quad (11)$$

$$f_{Ei} = -k_{dEi} m_d c_{Ei}. \quad (12)$$

The above dynamics conserve the total density of MinD and MinE

$$\underline{n}_D = dx^2 \; m_d + m_{de} + c_{DD} + c_{DT} \; , \quad (13)$$

$$\underline{n}_E = dx^2 \; m_{de} + c_{Er} + c_{Ei} \; . \quad (14)$$

Together with the diffusion constants, the flow velocity and the kinetic rates, these densities are important control parameters of the dynamics. The parameter values used

throughout this study are adapted from Denk et al (2018)[23] and summarized in Tab. 3.1. The derivation of the reduced switch model, corresponding to the interaction network cartoon in Fig. 3.1F, is described in SI Sec. 3.5.3. Parameters and equations for the full model, skeleton model and reduced switch model are given in SI Sec. 3.5.4. Further, we provide details on the hysteresis sweep (SI Sec. 3.5.7), simulations with disabled MinE advection (SI Sec. 3.5.9), linear stability analysis (SI Sec. 3.5.10) as well as results obtained using other Min models (SI Sec. 3.5.11).

3.4.2. SAMPLE PREPARATION

Chemicals were bought from Sigma Aldrich unless specified otherwise. Flow cells were assembled using cover and microscope slides cleaned by sonication and acid Piranha, using Parafilm as a spacer, and sealed by melting the Parafilm on a hotplate. Flow channels were about 25 mm long, 3 mm wide and 200 μm high, i.e. well above the threshold of tens of micrometers, below which coupling between upper and lower surfaces were observed.[19] Exact channel heights and widths for individual experiments are given in Tab. S3. Sample channels were coated with lipid bilayers composed of DOPC:DOPG in a molar ratio 67:33 substituted with 0.01–0.02 % mol TopFluor Cardiolipin, where the latter allowed us to confirm full bilayer formation before the experiment. SUVs for lipid bilayer formation were prepared via swelling followed by stepwise extrusion with final pore size of 40 nm. Before the experiment, chambers were filled with SUV solution, incubated for 1 h at 37^o C, then rinsed thoroughly with Min buffer (150 mM KCl, 25 mM TRIS pH 7.45, 5 mM MgCl[2]). Next, the chamber (as well as the tubing for closed-circle experiments) were filled with Min protein solution comprising 1 μM MinD and MinE at a concentration in μM equal to that of the E:D ratio indicated (both including labeled fraction). The protein solution was supplemented with 5 mM ATP (Thermo Fisher) as well as 5 mM Phosphoenolpyruvic acid (Alfa Aesar) and 0.01 mg/mL pyruvate kinase for ATP regeneration. In order to study a wide range of flow rates, experiments with wildtype MinE were done in closed-circle systems (see Fig. 3.16). Here, the tubing was inserted into the pump, filled with the protein solution and then connected to the pre-filled flow channel via two ports at its end. This allowed repeated recycling of the protein within the closed system. To check whether protein concentrations changed due to sticking to the comparably large internal surfaces of the tubing, we collected a portion of the original solution as well as the sample extracted from the closed-circle system at the end of every experiment and ran them side-by-side on a gel (see Fig. 3.18) to calculate an estimate for the loss, which typically was ~30% for MinD and ~50 % for MinE. In the experiments described, the corrected ratios are given along with the initial ratios. Experiments with MinE-L3E/I24N were performed with an open system, with the channel's outlet connected to the pump via tubing and its inlet connected to a reservoir of protein solution, in order to minimize loss of protein due to sticking. Laminar hydrodynamic flow was created using a pressure-driven pump (Ismatec, model IPC).

3.4.3. IMAGE ACQUISITION

Images were acquired using an Olympus IX-81 inverted microscope equipped with an Andor Revolution XD spinning disk system and a 20x objective (Olympus PlanN 20x / 0.4 NA). For excitation of MinD-Cy3 and MinE-Cy5, laser lines 561 nm and 640 nm were used. Images were acquired at multiple positions in grid geometries with some overlap between adjacent fields of view (as shown in Fig. 3.16) at 15 s intervals (4 frames per minute). Up to three comparably sized regions per sample were imaged (example given in Fig. 3.24), obtaining total covered areas of up to 2 mm^2. Regions were located in the central third of the channel to avoid possible turbulence close to the inlet and outlet. Following 1 hour of incubation at room temperature, images were first recorded without flow at the selected positions in order to get a reference for comparing subsequential acquisitions to. The flow rate was then set and increased incrementally as indicated. The average cross-sectional flow rate (in mm/s) was calculated from the flow channel's width and height as well as the pump's set flow rate (in volume/time). Images at the chosen flow rates and positions were recorded following at least 15 min of incubation, as we empirically found this to be about the time the pattern needed to respond to the new flow rate.

3.4.4. IMAGE ANALYSIS

Image cleaning, stitching as well as wave crest detection and propagation analysis were done using custom-built MatLab and Python scripts using the methodology outlined in Meindlhumer et al (2022)[43]. More details are also given in the SI (section 3.7). In brief, we identified wave crests in each frame within a stack using phase images, then compared sequential images to obtain the translation of each crestpoint frame to frame. The result of our analysis is a collective list of vectors (v_x, v_y) found at positions (x, y) of individual frames, collected from up to three comparable imaging regions. These vectors were analyzed with respect to their magnitude and directionality. Very low propagation velocities were cropped to eliminate the influence of static objects (protein aggregates) that would otherwise show in the results. Velocity vectors were excluded if they had a magnitude below 10% of the median. Analysis shown in the paper was performed on the patterns acquired for MinD-Cy3 unless noted otherwise. The full pattern direction analysis results for all experiments performed can be found in the SI (section 3.8).

CODE AND DATA AVAILABILITY

The code used in this study is available upon request to the corresponding author. The simulation and experimental data created for this study are freely available on Zenodo at https://doi.org/10.5281/zenodo.7339803. Source data are provided with the online version of the paper: `https://doi.org/10.1038/s41467-023-35997-0`

3.5. SUPPLEMENTARY THEORETICAL METHODS

In the following, we summarize the theoretical methods used in this paper. The structure is as follows: In Sec. 3.5.1 we present the theoretical model of the experimental setup – this amounts to extending the *switch model* introduced in Ref. [23] to account for advective bulk flow. As numerical simulations of the full system are costly, we justify and implement several simplifications of the full geometry (Sec. 3.5.2). Next, we show in Sec. 3.5.7 how in the limit of high MinE:MinD ratio, the reaction kinetics of the switch model can be simplified, arriving at the *reduced switch model*. We then state the equations of motion and parameters for the switch model (Sec. 3.5.4), the reduced switch model (Sec. 3.5.5), and the *skeleton model* (Sec. 3.5.6), which does not include conformational switching of MinE. We then describe how the effects of advective flow on the presented models are analysed by means of finite element simulations and a linear stability analysis. Finally, in Sec. 3.5.12 we present three other theoretical models from the literature [23, 50, 51], and extend them to include molecular switching of MinE. We conclude by summarizing the findings of a preliminary analysis of the effects of flow on these models.

3.5.1. SETUP

In order to simulate the full experimental system, one would have to perform Finite Element Method (FEM) simulations in a 2+3D box geometry, with 2-dimensional membranes at the top and bottom encapsulating a 3-dimensional box of cytosol (see panel A in Fig. 3.5). Since we are predominantly interested in phenomena that occur in the direction of flow, we consider as a starting point a 1+2D slice of the full 2+3D geometry, where the direction of "slicing" is parallel to the direction of advective flow.

The slice geometry (panel B in Fig. 3.5) is a rectangle $[0, L] \times [0, H]$, where L is the length of the slice and H is the height of the bulk. The membrane is located at $z = 0$. In this geometry, the switch model can be formulated as follows, starting with the membrane species:

$$\partial_t m_{\mathrm{d}}(x,t) = D_m \partial_x^2 m_{\mathrm{d}} + f_d \tag{3.1a}$$

$$\partial_t m_{\mathrm{de}}(x,t) = D_m \partial_x^2 m_{\mathrm{de}} + f_{\mathrm{de}}, \tag{3.1b}$$

where m_{d} and m_{de} describe the concentrations of membrane bound MinD and MinDE complexes, respectively. The dynamics of the cytosolic components read:

$$\partial_t c_{\mathrm{DD}}(x,z,t) + \mathbf{v}_f \cdot \nabla c_{\mathrm{DD}} = D_c \nabla^2 c_{\mathrm{DD}} - \lambda c_{\mathrm{DD}} \tag{3.2a}$$

$$\partial_t c_{\mathrm{DT}}(x,z,t) + \mathbf{v}_f \cdot \nabla c_{\mathrm{DT}} = D_c \nabla^2 c_{\mathrm{DT}} + \lambda c_{\mathrm{DD}} \tag{3.2b}$$

$$\partial_t c_{\mathrm{Er}}(x,z,t) + \mathbf{v}_f \cdot \nabla c_{\mathrm{Er}} = D_c \nabla^2 c_{\mathrm{Er}} - \mu c_{\mathrm{Er}} \tag{3.2c}$$

$$\partial_t c_{\mathrm{Ei}}(x,z,t) + \mathbf{v}_f \cdot \nabla c_{\mathrm{Ei}} = D_c \nabla^2 c_{\mathrm{Ei}} + \mu c_{\mathrm{Er}} \tag{3.2d}$$

Here, c_{DD} and c_{DT} denote the cytosolic concentrations of MinD-ADP and MinD-ATP, respectively. c_{Er} and c_{Ei} correspond to the concentrations of reactive and latent MinE.

The section "Supplementary Theoretical Methods" was written by Fridtjof Brauns and Jernej Rudi Finžgar.

Moreover, we used a parabolic flow profile

$$\mathbf{v}_f = \left[v_{\mathrm{f}}^{\max}(h-z)(h+z)/h^2, 0\right] \tag{3.3}$$

where $v_{\mathrm{f}}^{\max}$ is the flow velocity in the middle of the channel (at $z = 0$).

We are interested in the dynamics far (compared to the wavelength) from the inlet. Therefore, we employ periodic boundary conditions both for the membrane species ($u_m \in \{m_{\mathrm{d}}, m_{\mathrm{de}}\}$)

$$u_m(0,t) = u_m(L,t) \tag{3.4a}$$
$$\partial_x u_m(0,t) = \partial_x u_m(L,t), \tag{3.4b}$$

and likewise for the cytosolic species ($u_c \in \{c_{\mathrm{DD}}, c_{\mathrm{DT}}, c_{\mathrm{Er}}, c_{\mathrm{Ei}}\}$):

$$u_c(0,z,t) = u_c(L,z,t) \tag{3.5a}$$
$$\partial u_c(0,z,t) = \partial_x u_c(L,z,t). \tag{3.5b}$$

These boundary conditions allow us to study periodic phenomena such as traveling waves on a relatively small domain.

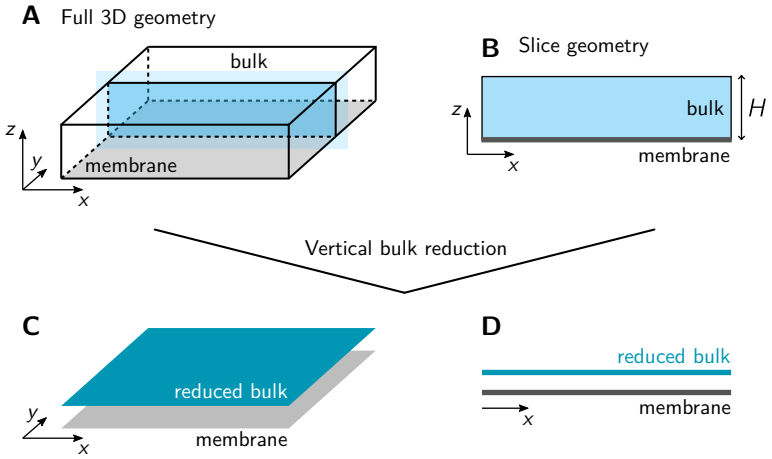


Figure 3.5: **A** Bottom half of the full 3D geometry. Blue shaded area corresponds marks the slice visualized in panel B. **B** A 1+2D slice of the full 2+3D geometry. **C** The 2D geometry obtained from the full 3D geometry by eliminating the vertical bulk dimension. **D** The line geometry obtained from the slice geometry by eliminating the vertical bulk dimension.

The attachment to and detachment from the membrane are included in the reactive

boundary conditions, which couple the membrane and the cytosol:

$$-D_c \partial_z c_{\mathrm{DD}}|_{z=0} = f_{\mathrm{DD}}|_{z=0} \tag{3.6a}$$
$$-D_c \partial_z c_{\mathrm{DT}}|_{z=0} = f_{\mathrm{DT}}|_{z=0} \tag{3.6b}$$
$$-D_c \partial_z c_{\mathrm{Er}}|_{z=0} = f_{\mathrm{Er}}|_{z=0} \tag{3.6c}$$
$$-D_c \partial_z c_{\mathrm{Ei}}|_{z=0} = f_{\mathrm{Ei}}|_{z=0}. \tag{3.6d}$$

Whereas at $z = H$, we impose a no-flux boundary condition $\partial_z c_i|_{z=H} = 0$ where $i = \mathrm{DD}, \mathrm{DT}, \mathrm{Er}, \mathrm{Ei}$.

The reaction terms, corresponding to the schematic in main text Fig. 1B are:

$$f_{\mathrm{d}} = (k_{\mathrm{D}} + k_{\mathrm{dD}} m_{\mathrm{d}}) c_{\mathrm{DT}} - (k_{\mathrm{dEr}} c_{\mathrm{Er}} + k_{\mathrm{dEi}} c_{\mathrm{Ei}}) m_{\mathrm{d}} \tag{3.7a}$$
$$f_{\mathrm{de}} = (k_{\mathrm{dEr}} c_{\mathrm{Er}} + k_{\mathrm{dEi}} c_{\mathrm{Ei}}) m_{\mathrm{d}} - k_{\mathrm{de}} m_{\mathrm{de}} \tag{3.7b}$$
$$f_{\mathrm{DT}} = -(k_{\mathrm{D}} + k_{\mathrm{dD}} m_{\mathrm{d}}) c_{\mathrm{DT}} \tag{3.7c}$$
$$f_{\mathrm{DD}} = k_{\mathrm{de}} m_{\mathrm{de}} \tag{3.7d}$$
$$f_{\mathrm{Er}} = k_{\mathrm{de}} m_{\mathrm{de}} - k_{\mathrm{dEr}} m_{\mathrm{d}} c_{\mathrm{Er}} \tag{3.7e}$$
$$f_{\mathrm{Ei}} = -k_{\mathrm{dEi}} m_{\mathrm{d}} c_{\mathrm{Ei}}, \tag{3.7f}$$

where the cytosolic components are to be evaluated at the membrane, i.e. at $z = 0$.

Note that the above dynamics conserve the total numbers of MinD and MinE

$$\bar{n}_{\mathrm{D}} V_{\mathrm{bulk}} = \int_{\mathrm{mem}} \mathrm{d}x\, (m_{\mathrm{d}} + m_{\mathrm{de}}) + \int_{\mathrm{bulk}} \mathrm{d}x^2\, (c_{\mathrm{DD}} + c_{\mathrm{DT}}), \tag{3.8}$$
$$\bar{n}_{\mathrm{E}} V_{\mathrm{bulk}} = \int_{\mathrm{mem}} \mathrm{d}x\, m_{\mathrm{de}} + \int_{\mathrm{bulk}} \mathrm{d}x^2\, (c_{\mathrm{Ei}} + c_{\mathrm{Er}}). \tag{3.9}$$

Therefore, the average total densities $\bar{n}_{\mathrm{D}}$ and $\bar{n}_{\mathrm{E}}$ are important control parameters of the system.

3.5.2. ELIMINATING THE VERTICAL BULK DIMENSION

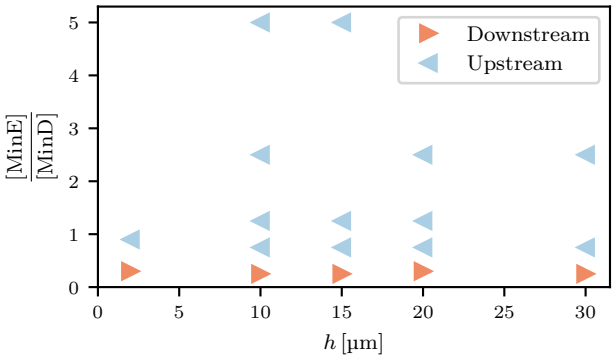


Figure 3.6: Results of a parameter sweep of the switch model, where the bulk height h was varied along with the E:D ratio (other parameters can be found in Table 3.1). Red/blue markers indicate simulations where downstream/upstream propagation was observed.

Performing simulations in this 2-dimensional slice geometry reveals that bulk height does not significantly affect the wave propagation direction in response to flow (see Fig. 3.6). Specifically, we find that the E:D ratio where the propagation direction changes from downstream to upstream propagation does not sensitively depend on the the bulk height. This suggests that vertical bulk gradients are not important for the effect of (lateral) advective flow on the wave patterns. We therefore eliminate the vertical bulk dimension by "integrating out" the vertical concentration profiles. This reduces the model to a one-dimensional geometry (see panel D in Fig. 3.5), which significantly speeds up numerical simulations. A more detailed discussion of this model reduction is given at the end of this section.

To eliminate the vertical bulk dimension, and thus reduce the model to a one-dimensional (line) geometry, we vertically average the cytosolic concentrations

$$\bar{u}_c(x,t) := H^{-1} \int_0^H \mathrm{d}z\, u_c(x,z,t), \tag{3.10}$$

for each $u_c \in \{c_{\mathrm{DD}}, c_{\mathrm{DT}}, c_{\mathrm{Ei}}, c_{\mathrm{Er}}\}$. Recall the bulk dynamics

$$\partial_t u_c + v_{\mathrm{f}}(z)\nabla_x u_c = D_c \nabla^2 u_c + \gamma_{u_c}(u_c), \tag{3.11}$$

where $\gamma_{u_c}(u_c)$ are linear functions of the cytosolic concentrations u_c, cf. Eq. (3.2). We can integrate this equation over the vertical dimension, and divide it by H, obtaining

$$\partial_t \bar{u}_c + \bar{v}_f \nabla_x \bar{u}_c = D_c \left[\nabla_x^2 \bar{u}_c + H^{-1}\, \nabla_z u_c|_0^H\right] + \gamma_{u_c}(\bar{u}_c). \tag{3.12}$$

Here, $\bar{v}_f$ is the average flow velocity in the cytosol. Using the reactive boundary conditions at $z = 0$ (cf. Eq. 3.6) and the zero-flux boundary condition at $z = H$ yields

$$\partial_t \bar{u}_c + \bar{v}_f \partial_x \bar{u}_c = D_c \partial_x^2 \bar{u}_c + H^{-1} f_{u_c}\left(u_m, u_c|_{z=0}\right) + \gamma_{u_c}(\bar{u}_c). \tag{3.13}$$

To obtain a closed set of equations, we approximate the cytosolic concentrations at the membranes with the vertically averaged concentration as $u_c|_{z=0} \approx \bar{u}_c$ in both the membrane and cytosolic dynamics:

$$\partial_t u_m + \bar{v}_f \partial_x \bar{u}_c = D_m \partial_x^2 u_m + f_{u_m}(u_m, \bar{u}_c) \tag{3.14a}$$

$$\partial_t \bar{u}_c = D_c \partial_x^2 \bar{u}_c + H^{-1} f_{u_c}(u_m, \bar{u}_c) + \gamma_{u_c}(\bar{u}_c). \tag{3.14b}$$

By this approximation, we are neglecting vertical concentration gradients in the bulk. This becomes precise if the bulk height is small enough that the bulk diffusion mixes it well on the timescale of the reactions at the membrane. This is not the case in the Min system, unless the bulk height is smaller than about 5 µm (see Brauns, et al.[19]). Indeed, vertical gradients have been shown to play an important role for several characteristics of the Min-protein dynamics in vitro[8, 19]. However, as we discussed above, simulations in a domain with vertically extended bulk show no significant effect of the bulk height on the wave propagation direction. Therefore, this *qualitative* effect of bulk flow can be studied in a one-dimensional domain where the bulk is integrated out, as described above. Thus, we study the switch model in a line geometry, with the dynamical equations as in Sec. 3.5.4. This significantly speeds up the simulations and allows us to map out the phase diagram in the parameter plane of flow velocity and E:D ratio. It also allows us to run long simulations and thus perform adiabatic parameter sweeps to demonstrate hysteresis.

3.5.3. SUMMARY OF MODELS AND PARAMETERS USED

As a consequence of the arguments outlined in Sec. 3.5.2 and the gained computational simplicity, the simulations presented in this work were performed on a line geometry (see Fig. 3.5, panel D), namely on an interval of length $L = 500\,\mu\text{m}$, with periodic boundary conditions. Across all simulations, the parameters stated in Tab. 3.1 were shared. In the following we will use $u(x, t) \equiv u$, i.e. omit explicitly stating the dependencies of the concentrations on the position and time.

We here state the equations of motion for the switch model, and two simplified versions of it; the reduced switch model, which does not include the cytosolic MinE components, and the skeleton model, where conformational switching of MinE is disabled. For a visualization of the reaction kinetics, refer to main text Fig. 1.

Parameter	Value	Description
D_c	$60\,\mu m^2\,s^{-1}$	Cytosolic diffusion constant
D_m	$0.013\,\mu m^2\,s^{-1}$	Membrane diffusion constant
λ	$6\,s^{-1}$	MinD-ADP to MinD-ATP transition rate
μ	$100\,s^{-1}$	MinE switching rate
k_D	$0.1\,s^{-1}$	MinD membrane attachment rate
k_{dD}	$0.1\,\mu m\,s^{-1}$	MinD membrane recruitment rate
k_{de}	$0.5\,s^{-1}$	MinDE membrane detachment rate
k_{dEr}	$2\,\mu m\,s^{-1}$	Reactive MinE recruitment rate
k_{dEi}	$10^{-3}\,\mu m\,s^{-1}$	Latent MinE recruitment rate
k_{dE}	$2\,\mu m\,s^{-1}$	MinE recruitment rate (skeleton model)
L	$500\,\mu m$	Size of simulation domain
$\bar{n}_D$	$638\,\mu m^{-1}$	Average MinD density
$\bar{n}_E$	varied	Average MinE density
v_f	varied	Flow velocity

Table 3.1: Parameters used for finite element simulations and linear stability analysis in a line geometry, adopted from Ref. [23]. The rates μ, k_{dEr} and k_{dEi} only apply to the full model with conformational switching of MinE, while the rate k_{dE} describes MinE recruitment in the 'skeleton model'. $\bar{n}_D$ and $\bar{n}_D$ are the spatial averages of total MinD and MinE densities, respectively.

3.5.4. SWITCH MODEL

The switch model dynamics in 1D (as obtained in Sec. 3.5.2) read

$$\partial_t m_d = D_m \partial_x^2 m_d + \bar{f}_d \tag{3.15a}$$
$$\partial_t m_{de} = D_m \partial_x^2 m_{de} + \bar{f}_{de} \tag{3.15b}$$
$$\partial_t c_{DD} + v_f \partial_x c_{DD} = D_c \partial_x^2 c_{DD} + \bar{f}_{DD} \tag{3.15c}$$
$$\partial_t c_{DT} + v_f \partial_x c_{DT} = D_c \partial_x^2 c_{DT} + \bar{f}_{DT} \tag{3.15d}$$
$$\partial_t c_{Er} + v_f \partial_x c_{Er} = D_c \partial_x^2 c_{Er} + \bar{f}_{Er} \tag{3.15e}$$
$$\partial_t c_{Ei} + v_f \partial_x c_{Ei} = D_c \partial_x^2 c_{Ei} + \bar{f}_{Ei}, \tag{3.15f}$$

with the reaction terms:

$$\bar{f}_d = (k_D + k_{dD} m_d) c_{DT} - (k_{dEr} c_{Er} + k_{dEi} c_{Ei}) m_d \tag{3.16a}$$
$$\bar{f}_{de} = (k_{dEr} c_{Er} + k_{dEi} c_{Ei}) m_d - k_{de} m_{de} \tag{3.16b}$$
$$\bar{f}_{DT} = -(k_D + k_{dD} m_d) c_{DT} + \lambda c_{DD} \tag{3.16c}$$
$$\bar{f}_{DD} = k_{de} m_{de} - \lambda c_{DD} \tag{3.16d}$$
$$\bar{f}_{Er} = k_{de} m_{de} - k_{dEr} m_d c_{Er} - \mu c_{Er} \tag{3.16e}$$
$$\bar{f}_{Ei} = -k_{dEi} m_d c_{Ei} + \mu c_{Er}, \tag{3.16f}$$

which correspond to the schematic in Fig. 1B in the main text. In addition to the parameters found in Table 3.1, $k_{dEr} = 2\,\mu m\,s^{-1}$ and $k_{dEi} = 0.001\,\mu m\,s^{-1}$ were used.

In a line geometry, the conservation laws Eq. (3.8) and Eq. (3.9) read:

$$\bar{n}_\mathrm{D} L = \int_0^L \mathrm{d}x\,(m_\mathrm{d} + m_\mathrm{de} + c_\mathrm{DD} + c_\mathrm{DT}) \tag{3.17}$$

$$\bar{n}_\mathrm{E} L = \int_0^L \mathrm{d}x (m_\mathrm{de} + c_\mathrm{Ei} + c_\mathrm{Er}). \tag{3.18}$$

3.5.5. REDUCED SWITCH MODEL

In the limit of a fast switching rate μ and slow recruitment rate of inactive MinE k_dEi, the switch model can be reduced by a quasi-steady state elimination of MinE's switching dynamics. A detailed description of the model reduction is given in Sec. 3.5.7 below. The dynamics of this reduced switch model are as follows:

$$\partial_t m_\mathrm{d} = D_m \partial_x^2 m_\mathrm{d} + \bar{r}_\mathrm{d} \tag{3.19a}$$

$$\partial_t m_\mathrm{de} = D_m \partial_x^2 m_\mathrm{de} + \bar{r}_\mathrm{de} \tag{3.19b}$$

$$\partial_t c_\mathrm{DD} = D_c \partial_x^2 c_\mathrm{DD} - v_\mathrm{f} \partial_x c_\mathrm{DD} + \bar{r}_\mathrm{DD} \tag{3.19c}$$

$$\partial_t c_\mathrm{DT} = D_c \partial_x^2 c_\mathrm{DT} - v_\mathrm{f} \partial_x c_\mathrm{DT} + \bar{r}_\mathrm{DT}. \tag{3.19d}$$

Reducing the switch model yields the reaction network displayed in Fig. 1E, stated mathematically:

$$\bar{r}_\mathrm{d} = (k_\mathrm{D} + k_\mathrm{dD} m_\mathrm{d}) c_\mathrm{D} - \left[k_\mathrm{dEi}^\mathrm{eff} + \frac{k_\mathrm{de} m_\mathrm{de}}{\sqrt{\mu D_c}/k_\mathrm{dEr} + m_\mathrm{d}} \right] m_\mathrm{d} \tag{3.20a}$$

$$\bar{r}_\mathrm{de} = \left[k_\mathrm{dEi}^\mathrm{eff} + \frac{k_\mathrm{de} m_\mathrm{de}}{\sqrt{\mu D_c}/k_\mathrm{dEr} + m_\mathrm{d}} \right] m_\mathrm{d} - k_\mathrm{de} m_\mathrm{de} \tag{3.20b}$$

$$\bar{r}_\mathrm{DT} = -(k_\mathrm{D} + k_\mathrm{dD} m_\mathrm{d}) c_\mathrm{DT} + \lambda c_\mathrm{DD} \tag{3.20c}$$

$$\bar{r}_\mathrm{DD} = k_\mathrm{de} m_\mathrm{de} - \lambda c_\mathrm{DD}, \tag{3.20d}$$

with the effective kinetic rate $k_\mathrm{dEi}^\mathrm{eff} = k_\mathrm{dEi} n_\mathrm{E}$.

In the reduced switch model only the total number of MinD proteins

$$\bar{n}_\mathrm{D} L = \int_0^L \mathrm{d}x\,(m_\mathrm{d} + m_\mathrm{de} + c_\mathrm{DD} + c_\mathrm{DT}) \tag{3.21}$$

is a conserved quantity. The total density of MinE only appears via the effective MinE-recruitment rate $k_\mathrm{dEi}^\mathrm{eff}$.

In contrast to the full switch model, the reduced switch model exhibits only upstream propagation of wave patterns (see Fig. 3.7B).

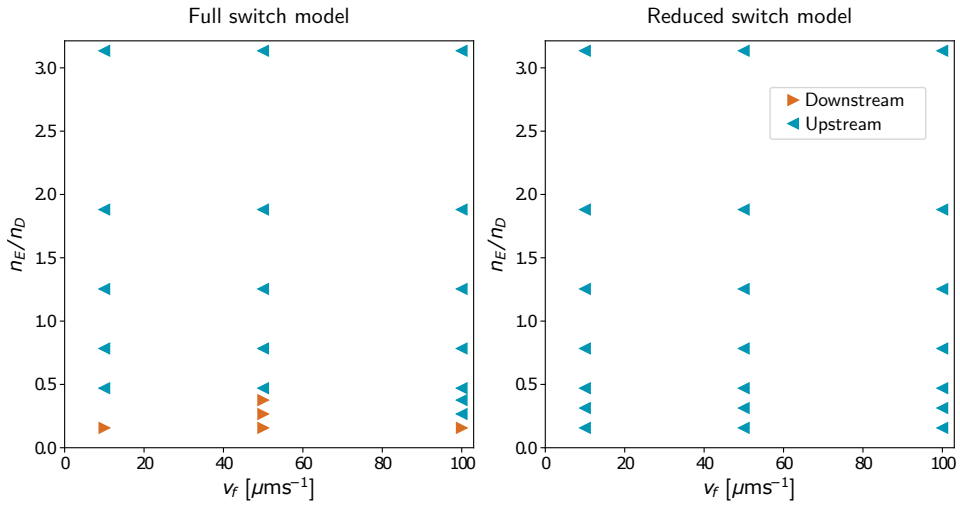


Figure 3.7: Parameter sweeps in the $(v_f, n_E/n_D)$ parameter plane for the full switch model and the reduced switch model. **A**. The full switch model exhibits both downstream propagation for low E/D ratios and upstream propagation for high E/D ratios. **B**. The reduced switch model exhibits only upstream propagation.

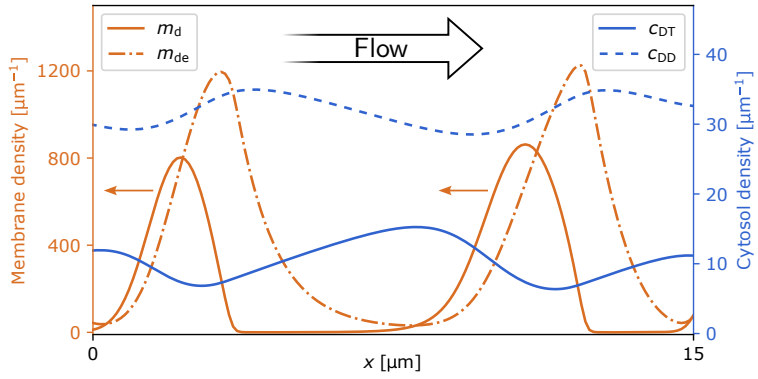


Figure 3.8: Concentration profiles of the membrane and bulk components of the reduced switch model. The bulk flow is from left to right while the membrane-bound pattern travels from right to left. Note that the MinD-ATP bulk concentration (c_T) is higher on the upstream flank than of the membrane-concentration peak than on the downstream flank. This facilitates faster recruitment of MinD-ATP to the membrane in the upstream flank which drives the upstream propagation of the membrane-bound pattern (see Fig. 1B).

3.5.6. SKELETON MODEL

The equations for the skeleton model (Fig. 1F) are:

$$\partial_t m_\mathrm{d} = D_m \partial_x^2 m_\mathrm{d} + \bar{g}_\mathrm{d} \tag{3.22a}$$
$$\partial_t m_\mathrm{de} = D_m \partial_x^2 m_\mathrm{de} + \bar{g}_\mathrm{de} \tag{3.22b}$$
$$\partial_t c_\mathrm{DD} = D_c \partial_x^2 c_\mathrm{DD} - v_\mathrm{f} \partial_x c_\mathrm{DD} + \bar{g}_\mathrm{DD} \tag{3.22c}$$
$$\partial_t c_\mathrm{DT} = D_c \partial_x^2 c_\mathrm{DT} - v_\mathrm{f} \partial_x c_\mathrm{DT} + \bar{g}_\mathrm{DT} \tag{3.22d}$$
$$\partial_t c_\mathrm{E} = D_c \partial_x^2 c_\mathrm{E} - v_\mathrm{f} \partial_x c_\mathrm{E} + \bar{g}_\mathrm{E}, \tag{3.22e}$$

with the reaction terms

$$\bar{g}_\mathrm{d} = (k_\mathrm{D} + k_\mathrm{dD} m_\mathrm{d}) c_\mathrm{DT} - k_\mathrm{dE} m_\mathrm{d} c_\mathrm{E} \tag{3.23a}$$
$$\bar{g}_\mathrm{de} = k_\mathrm{dE} m_\mathrm{d} c_\mathrm{E} - k_\mathrm{de} m_\mathrm{de} \tag{3.23b}$$
$$\bar{g}_\mathrm{DT} = -(k_\mathrm{D} + k_\mathrm{dD} m_\mathrm{d}) c_\mathrm{DT} + \lambda c_\mathrm{DD} \tag{3.23c}$$
$$\bar{g}_\mathrm{DD} = k_\mathrm{de} m_\mathrm{de} - \lambda c_\mathrm{DD} \tag{3.23d}$$
$$\bar{g}_\mathrm{E} = k_\mathrm{de} m_\mathrm{de} - k_\mathrm{dE} m_\mathrm{d} c_\mathrm{E}. \tag{3.23e}$$

Analogously to the switch model, the total MinD and MinE densities

$$\bar{n}_\mathrm{D} L = \int_0^L \mathrm{d}x \, (m_\mathrm{d} + m_\mathrm{de} + c_\mathrm{DD} + c_\mathrm{DT}) \tag{3.24}$$
$$\bar{n}_\mathrm{E} L = \int_0^L \mathrm{d}x \, (m_\mathrm{de} + c_\mathrm{E}) \tag{3.25}$$

are conserved by the above dynamics. Extensive parameter sweeps show that the skeleton model exhibits only downstream propagating patterns; see Fig. 3.9.

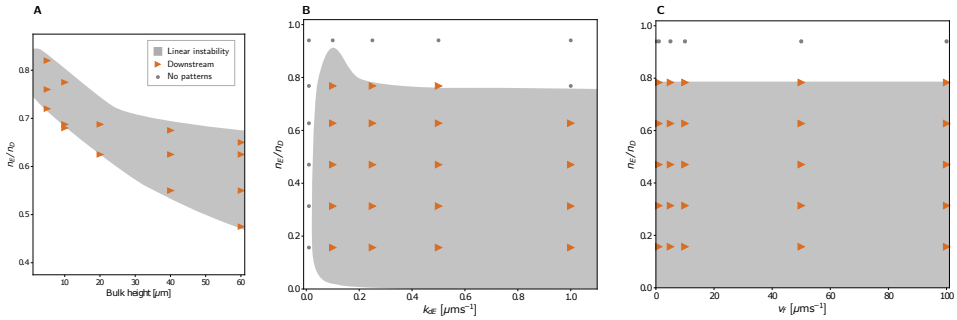


Figure 3.9: Parameter sweeps performed for the Skeleton model show only downstream propagation. **A** For the skeleton model with explicit extended bulk [8, 19], the bulk height has no effect on the wave propagation direction. **B** and **C**: Simulations in the simplified line geometry show only downstream propagation when kinetic rates and flow speed are varied.

3.5.7. MAPPING THE FULL SWITCH MODEL TO THE REDUCED SWITCH MODEL

For simplicity, the model reduction is performed for a one-dimensional domain. At the end of this section we briefly discuss how the calculation can be generalized to take into account the extended bulk dimension.

Starting from the one-dimensional dynamics for the switch model as given in Sec. 3.5.4, we take two limits to arrive at the reduced switch model. First, we consider the simultaneous limits of high total MinE density ($n_E \to \infty$) and slow recruitment of latent MinE to the membrane ($k_{dEi} \to 0$), such that their product $k_{dEi}^{eff} = k_{dEi} \cdot n_E$ is kept constant. Second, in the limit where conformational switching between reactive and latent MinE is fast ($\mu \to \infty$), the majority of cytosolic MinE is in its latent conformation, forming an effective reservoir. This means we can eliminate the latent cytosolic conformation of MinE c_{Ei} and replace the terms describing its membrane binding by $k_{dEi} m_d c_{Ei} \to k_{dEi}^{eff} m_d$. Because switching and membrane recruitment "compete" for reactive MinE, taking the limit of fast switching ($\mu \to \infty$) requires that recruitment of reactive MinE is fast such that the ratio μ / k_{dEr} remains constant. In this double limit, both processes involving reactive MinE are fast compared to other processes in the system. Therefore, reactive MinE will rapidly approach a steady state where the reaction term (see Eq. (3.16f) below) vanishes. This means we can make a quasi-steady state approximation (QSSA) solving for the quasi-steady state concentration of the reactive MinE:

$$c_{Er}^{*} \approx \frac{k_{de} m_{de}}{k_{dEr} m_d + \mu} \tag{3.26}$$

The effective transition rate between membrane bound MinD and MinDE complexes

then reads:

$$k'_{\mathrm{d}\to\mathrm{de}} \approx \left[k^{\mathrm{eff}}_{\mathrm{dEi}} + \frac{k_{\mathrm{de}} m_{\mathrm{de}}}{\mu / k_{\mathrm{dEr}} + m_{\mathrm{d}}} \right] m_{\mathrm{d}}. \tag{3.27}$$

The numerator in the second term implies that the formation of MinDE complexes is essentially autocatalytic, since the production term is proportional to m_{de} itself. The intuitive explanation lies in the fact that MinDE complexes detaching from the membrane are the only source of reactive MinE in the cytosol, which is then quickly recruited back to the membrane by MinD. Omitting this intermediate recruitment step in the limit of rapid membrane recruitment ($k_{\mathrm{dEr}} \to \infty$) then yields the autocatalytic behaviour in Eq. (3.28).

In the above derivation, we implicitly assumed that the cytosolic concentrations are well-mixed in the direction orthogonal to the membrane. However, this assumption is in conflict with taking the limit of fast MinE deactivation, which results in a sharp gradient of reactive MinE in the vicinity of the membrane.[1] We can account for this by averaging the bulk flux of reactive MinE at the membrane not over the entire domain height h but only over the penetration depth $l_p = \sqrt{D_c/\mu}$. Thus, when averaging the bulk dynamics of reactive MinE, the factor l_p^{-1} replaces the factor h^{-1}, since reactions predominantly occur in a thin layer of order l_p in the vicinity of the membrane. Taking this into account yields the corrected transition rate between membrane MinD and MinDE complexes as:

$$k_{\mathrm{d}\to\mathrm{de}} \approx \left[k^{\mathrm{eff}}_{\mathrm{dEi}} + \frac{k_{\mathrm{de}} m_{\mathrm{de}}}{\sqrt{D_c \mu} / k_{\mathrm{dEr}} + m_{\mathrm{d}}} \right] m_{\mathrm{d}}. \tag{3.28}$$

This corrected QSSA is valid if we hold the ratio $\sqrt{D_c\mu}/k_{\mathrm{dEr}}$ constant when taking the limits $\mu \to \infty$ and $k_{\mathrm{dEr}} \to \infty$. Indeed, a model reduction in the 2+1D domain where vertical bulk gradients are accounted for yields the same expression for the effective rate $k_{\mathrm{d}\to\mathrm{de}}$.

In essence, we completely eliminated both cytosolic MinE components from the dynamics, arriving at a simplified model of the Min system which we refer to as the *reduced switch model*. The full set of equations that constitute the reduced model is stated in Sec. 3.5.5.

3.5.8. DETAILS OF HYSTERESIS SWEEPS

To probe the transition between upstream and downstream propagation in the phase diagram in Fig. 3.3, we performed sweeps where the flow velocity v_{f} was varied adiabatically over the course of the simulation.

[1] In a (2+1) dimensional geometry as presented in Sec. 3.5.1 the bulk concentration profile of reactive MinE in a laterally uniform steady state is given by $c_{\mathrm{Er}}(z) \propto \cosh\left(\sqrt{\mu/D_c}\, z\right)$.

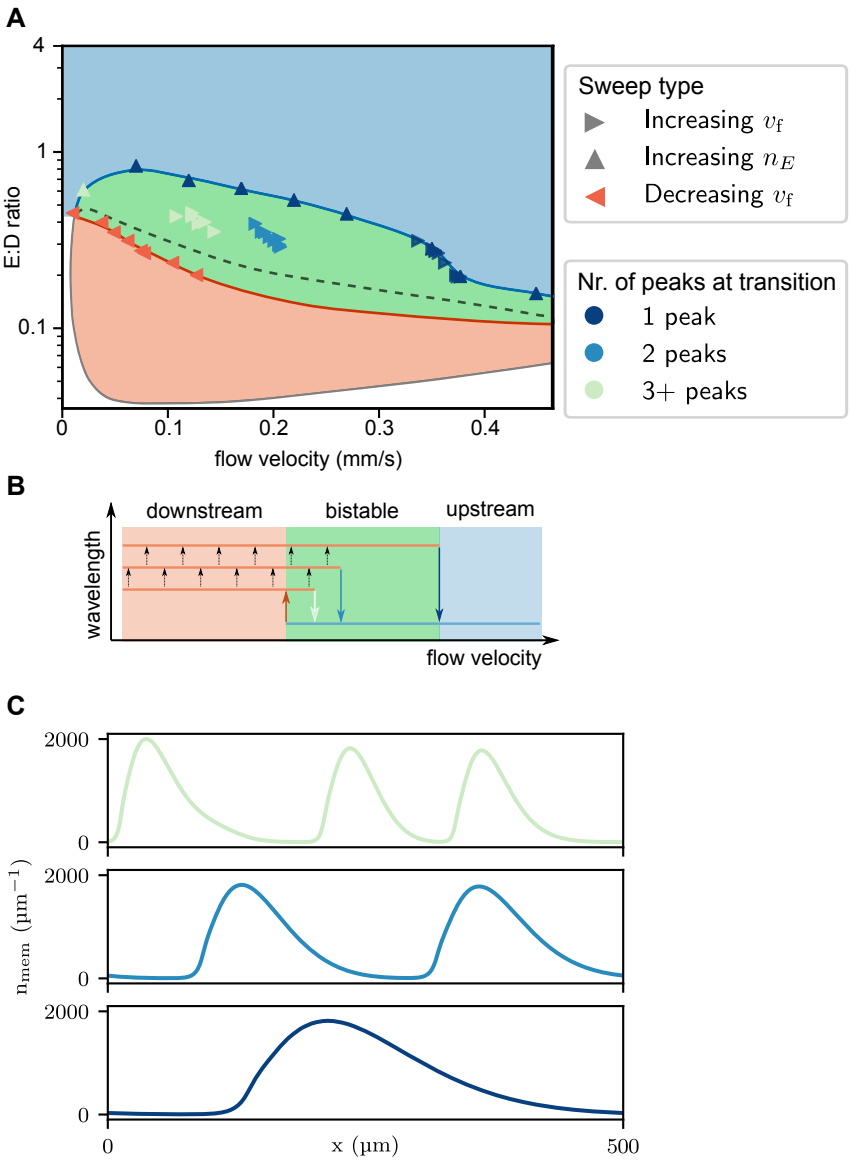


Figure 3.10: **A** Phase diagram of the full model, where the shadings correspond to the downstream, bistable and upstream regime, for red, green and blue, respectively (same as in Fig. 3.3A). The dashed line marks the E:D ratios above which upstream propagating modes are unstable in a Linear Stability Analysis (see also the corresponding dashed line and caption in Fig. 3.14, panel A). The markers correspond to where reversals of the propagation direction happened in sweeps, where a parameter was varied adiabatically (see SI Sec. 3.5.8). For increasing v_f and increasing n_E the transition was from downstream to upstream, while the decreasing v_f correspond to upstream to downstream transitions. The downstream to upstream markers are color coded to display the wavelength of the pattern at the transition point – we quantify that by the number of peaks (see panel C). **B** Similar to main text Fig. 3.3B, but with the transition arrows color coded in agreement with panels A and C. **C** Different wavelength pattern profiles of the downstream propagating patterns shortly before the transition point.

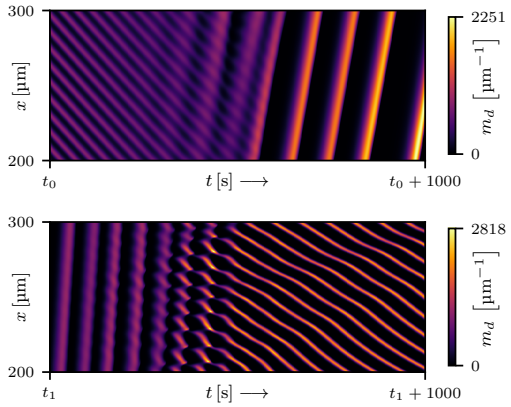


Figure 3.11: Typical kymographs of the upstream to downstream (above) and downstream to upstream transition (below). Advective flow runs in the positive x-direction.

To study the downstream to upstream transition, we initiated patterns at a flow velocity where patterns propagate downstream, if the simulation is initiated from an initially homogeneous state. After the patterns have stabilized in the typical downstream propagating shape, we linearly increased the flow velocity, with a slope that did not exceed $\mathrm{d}v_\mathrm{f}/\mathrm{d}t < 0.03\,\mu\mathrm{m\,s}^{-2}$.

Analogously, we studied the upstream to downstream transition starting from an upstream propagating pattern, and decreasing the velocity linearly with a slope smaller (in absolute value) than $|\mathrm{d}v_\mathrm{f}/\mathrm{d}t| < 0.03\,\mu\mathrm{m\,s}^{-2}$.

To completely map out the bistability regime, we also performed simulations where the pattern was initiated at a point in parameter space which exhibits exclusively downstream propagation and then increased the total MinE density, by uniformly supplying it across the entire domain. The transitions from downstream to upstream propagation obtained in this manner are indicated by upright triangles in panel A of Fig. 3.10. The rate at which the density was changed was $\mathrm{d}n_\mathrm{E}/\mathrm{d}t < 0.5\,\mu\mathrm{m}^{-1}\,\mathrm{s}^{-1}$.

3.5.9. DETAILS OF SIMULATIONS WITH DISABLED MINE ADVECTION

To unravel the mechanism behind downstream propagation at low E:D ratios, we performed simulations where we prohibited advection of the cytosolic MinE species by setting $v_f = 0$ in the equations of motion for the species c_{Er} and c_{Ei}. Strikingly, the patterns still propagated downstream – for typical profile shapes, side by side with typical profile shapes where all species advect normally see Fig. 3.12.

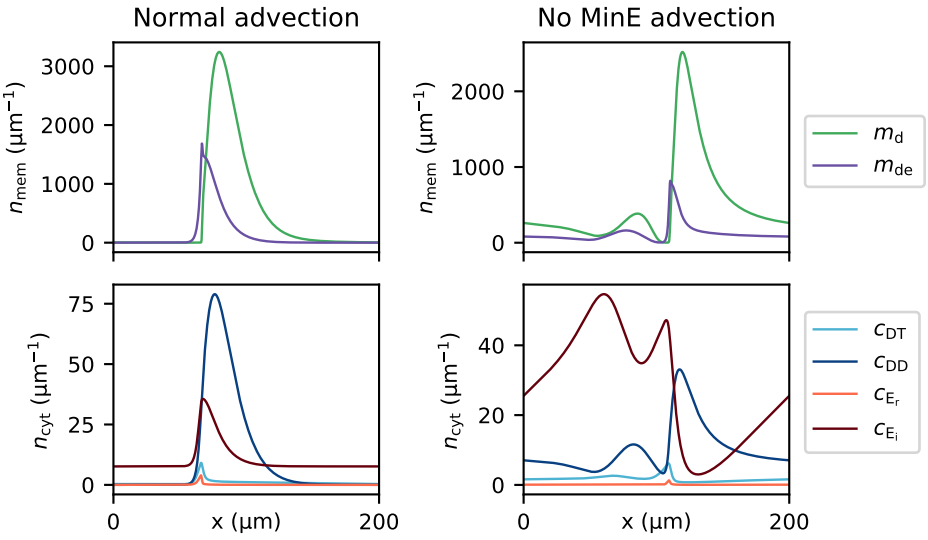


Figure 3.12: Typical profile shapes of the downstream propagating patterns, in the case of all cytosolic species being fully advected (left panel), and when exclusively cytosolic MinD is advected (right panel).

3.5.10. WAVE SPEED VS FLOW SPEED

In experiments, we have observed a slow down of the surface-bound protein waves with increasing bulk-flow speed. To test whether our model can reproduce this observation, we ran simulations for a range of flow speeds and recorded the wave speed (see Fig. 3.13). We find that the wave initially speed decreases for increasing flow speed. However, for larger flow speeds, this dependence reverses, and wave speed approximately increases linearly with flow speed. This discrepancy, in addition to other quantitative discrepancies between theory and experiment, indicate that the current models are missing molecular details.

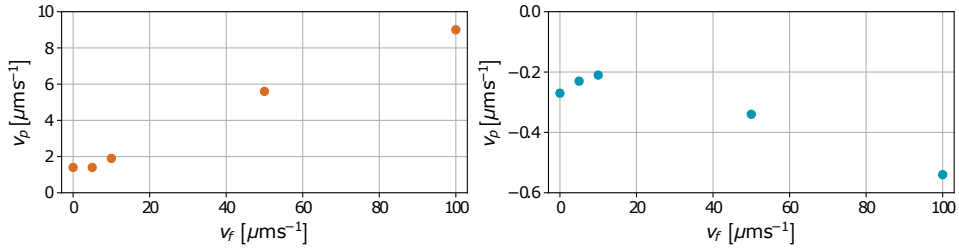


Figure 3.13: Wave propagation velocity (v_p) as a function of flow speed (v_f) for the skeleton model/low E:D regime (left) and the reduced switch model/high E:D regime (right). Note that the wave velocity in the latter case is negative, indicating upstream propagation. Except for small flow speeds, the magnitude of the wave speed increases as a function of the flow speed.

3.5.11. LINEAR STABILITY ANALYSIS

To study the dynamics in the vicinity of the homogeneous steady state, we performed linear stability analysis (LSA). Collecting the concentrations into a vector $\mathbf{u}(x,t) = [u_1(x,t),...,u_n(x,t)]^T$, we can write a general Reaction-Diffusion-Advection equation as

$$\partial_t \mathbf{u} = \underline{\underline{D}}\partial_x^2 \mathbf{u} - \underline{\underline{V}}\partial_x \mathbf{u} + \mathbf{f}(\mathbf{u}), \tag{3.29}$$

where $\underline{\underline{D}} = \mathrm{diag}(D_1,...,D_n)$ contains the diffusion constants.
The velocity matrix $\underline{\underline{V}} = \mathrm{diag}(v_\mathrm{f}, 0, ..., v_\mathrm{f})$ determines whether or not a certain component is advected or not (i.e. it is set to zero for membrane concentrations and v_f for cytosolic components). The vector of nonlinear functions $\mathbf{f} = \left[f_1(\mathbf{u}),...,f_n(\mathbf{u})\right]^T$ encodes the reaction kinetics.

We consider the dynamics of small perturbations $\delta\mathbf{u}$ to the homogeneous steady state $\mathbf{u}^*$, for which $\mathbf{f}(\mathbf{u}^*) = \mathbf{0}$. Inserting $\mathbf{u} = \mathbf{u}^* + \delta\mathbf{u}$ into Eq. (3.29) and linearizing the reaction kinetics, we obtain:

$$\partial_t \delta\mathbf{u} = \underline{\underline{D}}\partial_x^2 \delta\mathbf{u} - \underline{\underline{V}}\partial_x \delta\mathbf{u} + \underline{\underline{J}}\delta\mathbf{u}, \tag{3.30}$$

where $\left(\underline{\underline{J}}\right)_{ij} = \frac{\partial f_i}{\partial u_j}|_{\mathbf{u}^*}$.

Using the ansatz

$$\delta\mathbf{u}^{(q)}(x,t) = e^{\sigma t + iqx}\mathbf{e}^{(q)} \tag{3.31}$$

Eq. (3.30) turns into an eigenvalue problem

$$-q^2\underline{\underline{D}}\mathbf{e}^{(q)} - iq\underline{\underline{V}}\mathbf{e}^{(q)} + \underline{\underline{J}}\mathbf{e}^{(q)} = \sigma(q)\mathbf{e}^{(q)}, \tag{3.32}$$

with $\mathrm{Re}\left[\sigma(q)\right]$ representing the growth rate of a perturbation with a wavenumber q. In addition, due to the travelling wave form of the ansatz in Eq. (3.31), we recognize in $-\mathrm{Im}\left[\sigma(q)\right]$ the angular frequency $\omega(q)$, which allows us to extract the LSA expression for the phase velocity[44] as

$$v_p(q) = \frac{-\mathrm{Im}\left[\sigma(q)\right]}{q}. \tag{3.33}$$

As $\mathrm{Im}\left[\sigma(q)\right]$ typically changes sign within the band of the unstable modes q, it is a priori unclear which (if any) of the wavenumbers q would be relevant to determine the propagation direction.

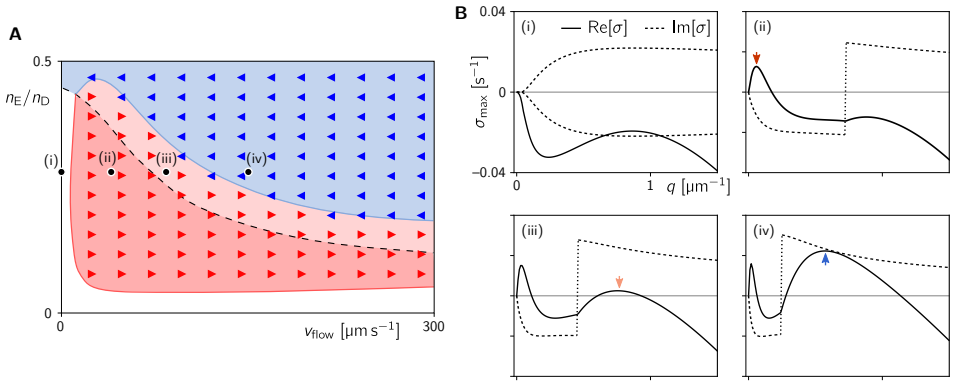


Figure 3.14: **A** Stability diagram obtained from linear stability analysis (background shading) and numerical simulations (triangle markers) of the full model in 1D. The shading is based on the signs of the imaginary part at the fastest growing mode $q_{\max}$ and at the right edge of the band of unstable modes q_+ (see representative dispersion relations in B and text for details). Blue and red markers indicate upstream and downstream propagation observed in numerical simulations initiated at the homogeneous steady state. **B** Dispersion relations corresponding to the points marked in the phase diagram (A). In the absence of flow [panel (i)], the eigenvalues come in pairs of complex conjugates, such that there are two branches with equal real part (solid line) and opposite imaginary parts (dashed lines). This reflects the left-right symmetry of the system. This symmetry, and thus the degeneracy of the real parts is broken by flow. In panels (ii–iv), only the eigenvalue with the largest real part is plotted causing the jumps in the imaginary part.

It turns out that in general, the sign of the imaginary part across the band of the unstable nodes is not a good proxy for the actual propagation direction observed in numerical simulations. For the parameter set used throughout this manuscript however, we obtain good agreement between the LSA prediction and the direction of propagation (see panel A in Fig. 3.14). We believe that this is a consequence of the separation of the typical length scales of the mechanisms underlying the downstream and upstream propagating instabilities – see the bimodal structure of the dispersion relations in panel B of Fig. 3.14. This bimodal structure of the dispersion relations further corroborates the bistability observed in numerical simulations and experiments.

3.5.12. OTHER MODELS OF MIN PROTEIN DYNAMICS

We performed a preliminary analysis of how flow influences pattern formation in some of the other models for the Min protein dynamics in the literature. In the following, we provide the modified part of the dynamics for each of the models we considered, state the parameters used and summarize the observations.

3.5.13. PERSISTENT MINE MEMBRANE BINDING

We extended the switch model by persistent MinE membrane binding introduced by Denk, et al.[23] to test whether this has an effect on the propagation direction of waves. The model is essentially an extension of the Switch model, that includes the possibility of MinE persisting on the membrane without being bound in a MinDE complex. We denote this density of membrane bound MinE proteins as m_e. The equations of motion are then as for the switch model (see Sec. 3.5.4), with the additional equation governing the dynamics of membrane bound MinE:

$$\partial_t m_e = D_m \partial_x^2 m_e + f_e \tag{3.34}$$

and the following reaction terms modified or added:

$$f_d = (k_\mathrm{D} + k_\mathrm{dD} m_\mathrm{d}) c_\mathrm{D} - (k_\mathrm{dEr} c_\mathrm{Er} + k_\mathrm{dEi} c_\mathrm{Ei} + k_\mathrm{ed} m_e) m_\mathrm{d} \tag{3.35a}$$

$$f_{de} = (k_\mathrm{dEr} c_\mathrm{Er} + k_\mathrm{dEi} c_\mathrm{Ei} + k_{ed} m_e) m_\mathrm{d} - k_{de} m_\mathrm{de} \tag{3.35b}$$

$$f_e = k_{de} m_\mathrm{de} - k_{ed} m_e m_\mathrm{d} - k_e m_e \tag{3.35c}$$

$$f_{Er} = k_e m_e - k_\mathrm{dEr} m_\mathrm{d} c_\mathrm{Er}. \tag{3.35d}$$

For the parameter range studied in Ref.[23], we found no qualitative change compared to the model without MinE membrane binding, i.e. what we here refer to as the switch model.

3.5.14. LOOSE, ET AL. MODEL

Next, we performed simulations of the model introduced by Loose, et al.[51] extended to include the MinE conformational switch. This amounts to modifying the reactions given in the original reference as:

$$\begin{aligned} f_d &= (\omega_D + \omega_{dD} m_\mathrm{d}) c_\mathrm{D} - m_\mathrm{d}\big[c_\mathrm{Ei}(\omega_{Ei} + \omega_{eEi} m_\mathrm{de}^2) \\ &\quad + c_\mathrm{Er}(\omega_{Er} + \omega_{eEr} m_\mathrm{de}^2)\big] && \text{(3.36a)} \\ f_{de} &= m_\mathrm{d}\left[c_\mathrm{Ei}(\omega_{Ei} + \omega_{eEi} m_\mathrm{de}^2) + c_\mathrm{Er}(\omega_{Er} + \omega_{eEr} m_\mathrm{de}^2)\right] - \omega_{de} m_\mathrm{de} && \text{(3.36b)} \\ f_D &= \omega_{de} m_\mathrm{de} - (\omega_D + \omega_{dD} m_\mathrm{d}) c_\mathrm{D} && \text{(3.36c)} \\ f_{Ei} &= -c_\mathrm{Ei} m_\mathrm{d}(\omega_{Ei} + \omega_{eEi} m_\mathrm{de}^2) + \mu c_\mathrm{Er} && \text{(3.36d)} \\ f_{Er} &= \omega_{de} m_\mathrm{de} - c_\mathrm{Er} m_\mathrm{d}(\omega_{Er} + \omega_{eEr} m_\mathrm{de}^2) - \mu c_\mathrm{Er}. && \text{(3.36e)} \end{aligned}$$

All of the reaction rates and diffusion constants were taken from the original publication[51], supplemented with $\mu = 100\,\mathrm{s}^{-1}$, $\omega_{eEi} = 1{\cdot}10^{-20}\,\mu\mathrm{m}^2\,\mathrm{s}^{-1}$, $\omega_{eEr} = 2.1{\cdot}10^{-18}\,\mu\mathrm{m}^2\,\mathrm{s}^{-1}$, $\omega_{Ei} = 9.5{\cdot}10^{-11}\,\mu\mathrm{m\,s}^{-1}$, $\omega_{Er} = 1.9{\cdot}10^{-8}\,\mu\mathrm{m\,s}^{-1}$.

We simulated this model on an interval of length $L = 500\,\mu\mathrm{m}$, and observed exclusively downstream propagation both with and without MinE molecular switching, for several densities in the range $n_E = 2.5{\cdot}10^6 - 1.9{\cdot}10^7\,\mu\mathrm{m}^{-2}$ (see Fig. 3.15A). We did however notice that the regime pattern formation is extended to higher E:D ratios upon the introduction of the MinE conformational switch, similarly to how the pattern forming range of the switch model is increased relative to that of the skeleton model.

3.5.15. BONNY, ET AL. MODEL

Finally, we performed a preliminary analysis of the effects of flow on the model introduced by Bonny, et al.[50]. As this model was introduced in the 2+1D slice geometry as introduced in Sec. 3.5.1, we reuse that framework with the following reaction kinetics, which constitute our extension of the reaction kinetics given in the original reference:

$$\begin{aligned} f_d &= (\omega_D + \omega_{dD} m_\mathrm{d}) c_\mathrm{D} (c_\mathrm{max} - m_\mathrm{d} - m_\mathrm{de})/c_\mathrm{max} \\ &\quad - (\omega_{Er} c_\mathrm{Er} + \omega_{Ei} c_\mathrm{Ei} + \omega_{ed} m_e) m_\mathrm{d} && \text{(3.37a)} \\ f_{de} &= (\omega_{Er} c_\mathrm{Er} + \omega_{Ei} c_\mathrm{Ei} + \omega_{ed} m_e) m_\mathrm{d} - (\omega_{de,m} + \omega_{de,c}) m_\mathrm{de} && \text{(3.37b)} \\ f_e &= \omega_{de,m} m_\mathrm{de} - \omega_{ed} m_e m_\mathrm{d} - \omega_e m_e && \text{(3.37c)} \\ f_D &= -(\omega_D + \omega_{dD} m_\mathrm{d}) c_\mathrm{D} (c_\mathrm{max} - m_\mathrm{d} - m_\mathrm{de})/c_\mathrm{max} \\ &\quad + (\omega_{de,m} + \omega_{de,c}) m_\mathrm{de} && \text{(3.37d)} \\ f_{Er} &= \omega_e m_e + \omega_{de,c} m_\mathrm{de} - \omega_{Er} m_\mathrm{d} c_\mathrm{Er} && \text{(3.37e)} \\ f_{Ei} &= -\omega_{Ei} m_\mathrm{d} c_\mathrm{Ei}. && \text{(3.37f)} \end{aligned}$$

We note here explicitly, that the switching of MinE from its reactive to its latent conformation was modelled in the same way as in the switch model, using a linear process with a rate $\mu = 100\,\mathrm{s}^{-1}$. However, the Bonny model does not include the binding of ATP to MinD explicitly, i.e. there is only a single MinD species in their model.

Another addition to the switch model discussed in Sec. 3.5.4 is the inclusion of membrane bound MinE, which is governed by Eq. (3.34) with D_m replaced by the original D_e. All parameters were set to the values used in the original paper, with the exception of $\omega_{Ei} = 1.36 \cdot 10^{-5}\,\mu\mathrm{m}^2\,\mathrm{s}^{-1}$, $\omega_{Er} = 1.36 \cdot 10^{-1}\,\mu\mathrm{m}\,\mathrm{s}^{-1}$ and the total MinE density which was varied in the range $627\,\mu\mathrm{m}^{-1} - 2527\,\mu\mathrm{m}^{-1}$. (Outside this range, the model does not exhibit patters.) A parabolic flow profile as in Eq. (3.3) was used, with $v_\mathrm{f}^\mathrm{max} = 50\,\mu\mathrm{m}\,\mathrm{s}^{-1}$ and a bulk height $h = 15$.

Upon introducing MinE molecular switching in this manner, we observed that the range of pattern formation was extended to higher E:D ratios. However, the propagation direction was downstream both with and without MinE switching, in the entirety of the pattern forming range (see Fig. 3.15B).

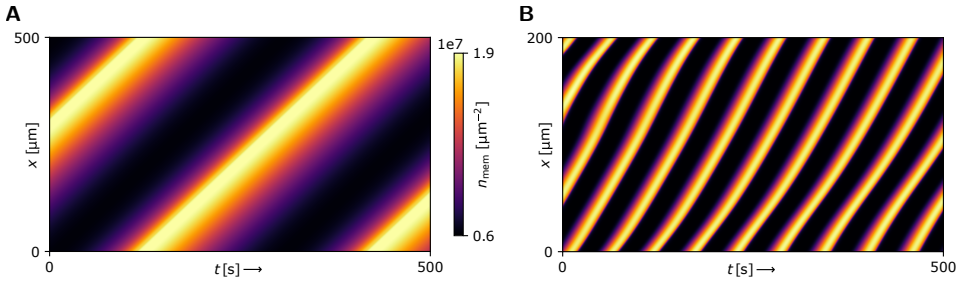


Figure 3.15: Kymographs showing typical wave patterns of the Loose et al. (A) and Bonny et al. (B) models. Bulk flow in the positive x-direction.

3.6. SUPPLEMENTARY EXPERIMENTAL METHODS

3.6.1. CHEMICALS

Unless indicated otherwise, chemicals were bought from Sigma Aldrich. For buffer and solvent preparation, we exclusively used deionized water (Merck Mili-Q®). An overview on important reagents and their storage conditions is given in Tab. 3.2.

Table 3.2: Overview on important reagents and their storage conditions

Product name	**Abbreviation**	**Provider**	**Article number**	**Storage**
18:1 (Δ9-Cis) PC	DOPC	Avanti Polar Lipids	850375C-25mg	chloroform, −20 °C
18:1 (Δ9-Cis) PG	DOPG	Avanti Polar Lipids	840475C-25mg	chloroform, −20 °C
TopFluor® Cardiolipin	-	Avanti Polar Lipids	810286C-100ug	chloroform, −20 °C
Adenosine triphosphate	ATP	Thermo Fisher	10304340	−20 °C
Pyruvate kinase	PK	Merck Sigma	P7768-1KU	stock at 4 °C, aliquots at −20 °C
Phosphoenolpyruvic acid monopotassium salt, 99 %	PEP	Alfa Aesar	B20358.06	dissolved in water and pH adjusted with KOH to ~7.4, stored at −20 °C

3.6.2. PREPARATION AND HANDLING OF SUVS

Chloroform-suspended lipids (DOPG:DOPC in a ratio 33:67, with 0.01–0.02 % mol TopFluor Cardiolipin) were mixed in a glass vial, then dried with a nitrogen gun and further left to dry in a desiccator for 15 minutes. Next, they were resuspended in SUV buffer (150 mol L^{-1} KCl, 25 mol L^{-1} TRIS pH 7.4-7.5 at room temperature) at a concentration of 5 mg mL^{-1} and left to swell at room temperature for at least 1 h. After swelling, they were vortexed for about 20 s and sonicated for 30 min. Avanti Mini-Extruder (Avanti Polar Lipids) was used to produce SUVs. The extruder was pre-warmed on a hotplate set to 45 °C and remained there throughout the procedure. The lipid solution was extruded through a filter membrane of pore size 100 nm for 21 times, followed by another round of extrusion using filters with a pore size of 40 nm. The uneven number of filtering counts ensured that the lipid solution ended up in the originally empty one of the two syringes, so as to avoid taking along aggregates that might accumulate in the first syringe. The resulting SUV solution was aliquoted and stored at 4 °C for up to 10 days.

Before the experiment, an aliquot of SUV solution (stored at 5 mg mL^{-1} at 4 °C) was diluted to a concentration of 1 mg mL^{-1} in 150 mmol L^{-1} KCl, 25 mmol L^{-1} TRIS (pH 7.4-7.5) and 4 mmol L^{-1} $MgCl_2$, then sonicated for 15 min. Next, the solution was injected into the flow cell and incubated at 37 °C for 1 h. The flow cell was then rinsed with Min buffer (150 mmol L^{-1} KCl, 25 mmol L^{-1} TRIS pH 7.4-7.5 and 5 mmol L^{-1} $MgCl_2$) using at least 10 times the volume of the flow cell to ensure removal of residual SUVs.

3.6.3. PROTEIN PURIFICATION AND LABELING

Min protein were purified and labeled as described previously (see Caspi & Dekker[30]) and stored in Min storage buffer (containing 50 mmol L^{-1} Hepes pH 7.25 at 4 °C, 150 mmol L^{-1} KCl, 10 % V/V glycerol, 0.1 mmol L^{-1} EDTA pH 7.4 and for MinD additionally 80 mmol L^{-1} ADP) at −80 °C. labeled protein had labeling efficiencies of about 88 % for Cy3:MinD-Lysine and 45 % for Cy5:MinE-Cysteine.
MinE-L3E/I24N (see Denk et al.[23]) was overexpressed, purified and labeled with Cy5-maleimide (Cytiva PA15131) as described previously (see Caspi & Dekker[30]) with the following modifications: Affinity purified proteins were concentrated using a Vivaspin 10 kDa ultrafiltration device before application to a Superdex S200 gel filtration column. The labeling efficiency was about 58 %.

3.6.4. FLOW CELL PREPARATION AND ASSEMBLY

To create inlets and outlets, holes were drilled in cover slides. Microscope slides and cover slides were then placed in Teflon containers and pre-cleaned by sequential sonication in deionized water for 5 min, Acetone for 15 min, KOH (1 mol L^{-1}) for 1 h and Ethanol for 1 h. Between sonication steps, the containers were rinsed with deionized water several times to remove the preceding solution. Next, the slides were cleaned with acid Piranha (H_2SO_4 and H_2O_2 in a ratio 5:1) and after rinsing with plenty of deionized water, stored in fresh Ethanol.
To assemble a flow cell, a set of up to four channels was cut into a double layer of Parafilm® using a cutting mold. Microscope and cover slides were dried with a nitrogen gun, then additionally plasma-cleaned (at about 50 W for 1 min) before assembly. Cover slide, parafilm and microscope slide were stacked on top of each other, then the flow cell was sealed by placing it on a hotplate at 95 °C for a few minutes and gently pressing the channels' edges down with a cotton swab. The flow cells were then stored at room temperature and used either on the same day, or a maximum of two days after assembly. The resulting channels would have heights of 180–230 µm, which were measured on the microscope from the height difference between the top and bottom bilayer. Their cross-sectional widths would be roughly 3 mm and also measured directly on the microscope stage for each individual flow channel. Measurements are given in Tab. 3.3. As found previously by Brauns et al., coupling of patterns on the upper and lower glass slide can be expected for bulk heights up to 30 µm [19]. To avoid possible complications, it was made sure that all used flow cells considerably exceeded this height.
Cut pipette tips were used to connect the flow channel's inlet and outlet to the tubing,

and fixed in position using 5-Minute Epoxy (Thorlabs). For closed-circle experiments, both the channel and the tubing were filled with protein solution prior to connecting and sealing off them with 5-Minute Epoxy. The tubing would go through a dispensing pump (model IPC, Ismatec®), allowing for cycling of the protein solution within a closed system (compare Fig. 3.16). This system was used for all shown experiments performed with MinE-wiltype.
Due to protein sticking and resulting change in concentration, the closed-circle system was found unsuitable for experiments with the less robust mutant MinE-L3E/I24N. For experiments with this variant, we used an open system. Here, only the outlet was connected to the pump, while the inlet's tubing led to a reservoir of Min protein solution, from which it could be sucked into the channel.

3.6.5. MIN PATTERN ACQUISITION

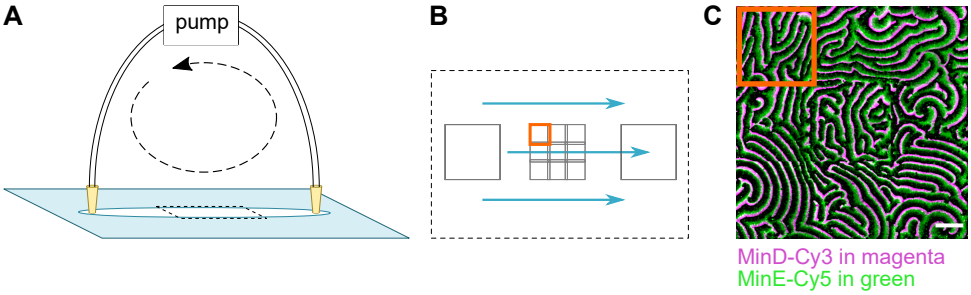


Figure 3.16: **A** Closed-circle flow cell setup (schematic). **B** Stitching of up to three 3x3 regions, reaching areas of about 0.8 mm x 0.8 mm in size. Dashed rectangle corresponds to region indicated in A. **C** Exemplary stitched image frame, stitched from nine frames of originally 512x512 pixel. Scale bar 100 µm. Single FOV highlighted in orange, corresponding to the equally highlighted region in **B**.

Unless stated otherwise, Min protein at the indicated concentrations (with 10–20 % labeled protein, not accounting for labeling efficiency) were supplemented with 0.01 mg mL^{-1} PK and 5 mol L^{-1} PEP and mixed in Min buffer. The volume of all reagents was accounted for to achieve a total concentration of 150 mmol L^{-1} KCl due to its strong influence on Min pattern formation, as found by Vecchiarelli et al.[24]. The exact final concentration of all buffer components (taking the storage buffer into account) would then amount to 150 mmol L^{-1} KCl, 5 mmol L^{-1} $MgCl_2$, 19–23 mmol L^{-1} TRIS pH 7.4-7.5 (21 °C) and 5–11 mmol L^{-1} Hepes pH 7.25 (4 °C), plus small amounts of glycerol, EDTA and ADP. Pipetting and mixing of Min protein was done using low-binding tubes and pipette tips (Eppendorf™) to reduce the loss of protein while transferring.

Min patterns were incubated with 2.5 mmol L^{-1} ATP for at least 1 h at room temperature before imaging. All images were captured on an Olympus IX-81 inverted microscope with an Andor Revolution XD spinning disk system and FRAPPA, EM-CCD Andor iXon

X3 DU897 camera, Andor Revolution and Yokogawa CSU X1 system for illumination and detection, a z-piezo stage and motorized x-y stage, using a 20× objective (Olympus PlanN 20x / 0.4 NA). For excitation of MinD-Cy3 and MinE-Cy5, laser lines 561 nm (617/73 nm filter) and 640 nm (685/40 nm filter) were used. Images were acquired in the central third of the channel (dashed rectangle in Fig. 3.16) in multiple positions at 15 s intervals (4 frames per minute). For 3x3 stitching of images (see Fig. 3.16, acquisition time was set to 400 ms, laser power was adjusted individually depending on the protein concentration.

3.7. SUPPLEMENTARY IMAGE AND DATA ANALYSIS

3.7.1. GENERAL INFORMATION

Min image stack data were pre-processed using home-built MatLab scripts (The Math Works, Inc. MATLAB. Version 2018b, The Math Works, Inc., 2020. `www.mathworks.com`; scripts available upon request) and analysed using home-built Python[55] scripts following the methodology described in a separate publication[43]. Schematics and figures were arranged using Inkscape (Inkscape Project, 2020. `https://inkscape.org`).
In the following, we present an outline of the analysis performed for this paper.

3.7.2. IMAGE PROCESSING AND REPRESENTATION

The images for this paper were acquired using a spinning disc confocal microscope. The associated relative high background signal could vary considerably for different E:D ratios (with the concentration of MinE-Cy5 at 45 % labeling efficiency ranging from 0.4–1 μmol L^{-1}). In addition, patterns did bleach under prolonged imaging, illumination was typically inhomogeneous and pattern diagnostics per field of view (FOV) could be cumbersome as the length scale of wave patterns is typically large compared to the FOV.
Finally, the closed-circle flow cell setup posed additional challenges in the form of objects entering and passing through the FOV, as well as adhering to the surface. As Min proteins might form aggregates over time, more and more of these artefacts would emerge as well as occasionally detach from the surface. To minimize the effects of these experimental limitations, prior to wave pattern analysis we prepared the images as follows: As we acquired images in (mostly 3x3) grids, we first split movies into (e.g. 9) individual tif-stacks for both channels. In our experimental setup, in these images the flow goes from right to left. Hence, we flipped all images horizontally so as to change the flow direction from left to right. This does not change any quantitative or qualitative statements of this paper, as it merely corresponds to changing one's perspective onto the sample from a downwards to an upwards view. First, standard cleaning steps were performed for individual movies:

- Fluorescence bleaching was corrected by normalizing each frame on its mean intensity value.
- An illumination correction map I_{illum} was made by strongly smoothing and averaging all movie images, then normalizing the result to its maximum.

- In addition, a 'static background'-image I_{stat} was made by averaging out all moving (wave pattern) features of the movie stack, leaving only static fluorescent features such as specks, holes and scratches.
- Each movie image was then corrected via the following image operation: $I_{cor} = (I_{movie} - I_{stat})/I_{illum}$.
- Occasionally remaining bright or dark artefacts were removed by outlier cropping.
- Images were smoothed to diminish the effect of remaining sharp edges and artefacts from the cropping.

The cleaned movies were then re-assembled into stitched 3x3 frames. Overlaps between adjoining images were cropped out and residual average intensity levels between individual FOVs were corrected for.
This way, all individual movie stacks were assembled into one movie showing a large area pattern with an optimally visible pattern. For closed-circle experiments, these areas were roughly 0.8 mm x 0.8 mm in size. An overview on the used areas is given in Sec. 3.8.7.

3.7.3. IMAGE REPRESENTATION

The microscope images shown in the paper were additionally prepared using Fiji[56]. As acquisitions from different experiments were done at different concentrations, they varied in intensity of background and local spikes. Depending on the quality of the individual files, images shown in the figures were additionally processed with background subtraction and/or de-noise methods (outlier removal) in Fiji.
Notably, the different treatment of images for purely graphical representation does not affect the quantitative analysis as described below in Sec. 3.7.4, as the latter is performed independently on image data pre-processed solely in MatLab as described in Sec. 3.7.2.

3.7.4. LOCAL WAVE CREST PROPAGATION ANALYSIS

As described in Ref. [43], we analyzed local wave speed by performing two steps: 1) identification of wave crests for each frame in a stack, and 2) frame-by-frame comparison of points along these wave crests. To achieve this, we estimate an optical flow vector field using Horn-Schunck algorithm.[57] From such vector fields, we obtain a phase image for each frame, with phases defined by the wave intensity either going up ('front'), or going down ('wake'). Wave 'crests' were then defined as positions between front and wake, in areas of the upper half of the wave intensity (the latter step excludes analogous wave 'valleys'). For every crest position, we determined the velocity by measurement of the perpendicular crest translation. This translation was obtained by sampling a cross-sectional profile at subpixel resolution (stretching over the crest position plus/minus half the wavelength) in the current and the former image, and measuring the shift in crest peak position.
This procedure yielded a list of vectors with components (v_x, v_y) at frame n in position (x,y). Velocity vectors with magnitudes lower than 10 % of the mean magnitude were discarded, as they may result from noise or non-pattern features not fully removed dur-

ing the cleaning procedure. From the vector components, an angle α was calculated, which corresponds to the wave crest point's direction of movement with respect to the direction of applied flow (defined as 0°, left to right in processed images). The collected vector components and resulting angles from all frames (n = 2...20) were further subjected to statistical analysis.

Notably, the quantitative outcome of local analysis as described in Ref. [43] depends on adequate pre-processing of the images. In addition to image stitching and cleaning (Sec. 3.7.2), two smoothing steps (Gaussian smoothing, covering a certain range of pixels) need to be performed as part of the local analysis pipeline. The first smoothing step is performed at the very start of local analysis and essentially reduces spatial noise. Hence, its range is determined by image quality. The second smoothing step is solely used for optical flow field analysis (Horn-Schunck), and should not surpass the range of the pattern's wavelength to avoid information loss. To minimize the number of different settings for these two smoothing parameters, but make sure to be in a suitable regime, we performed parameter screening for smoothing parameters varying between 10 and 50 pixels (6 µm to 30 µm) each, considering the first 5 frames for at least one stitched regions from each experiment. The results of this parameter screening (with the chosen set of parameters highlighted) can be found as supplementary panels on the associated online repository (Zenodo).

3.7.5. ANALYSIS AND VISUALIZATION OF LOCAL WAVE CREST ANALYSIS RESULTS

Throughout this paper's main text and supplementary material, we use a few types of graphical representations to visualize the results of local wave propagation analysis. An overview on the types of representation and how they connect to each other shown in Fig. 3.17.

Local wave propagation analysis as described in Sec. 3.7.4 essentially provides a list of vectors with components (v_x, v_y) at the identified wave crest positions of each frame within the image stack. The collected velocities can be collected and represented in a 2D histogram, with brightness indicating the number of counts within a given bin (corresponding to a particular crest velocity). Going from there, analysis can be performed according to the quantity of interest.

For analysing the wave propagation speed, the relevant quantity is each velocity vector's magnitude. Magnitudes can be calculated for all given vectors (v_x, v_y) and represented in a histogram as shown in Fig. 3.17 (box: "magnitude component").

For analysing the direction of wave propagation, the magnitude can be disregarded and the number of counts within a given direction (i.e. within a given angular segment) was determined. Practically, this was done by calculating the angles α for each vector and binning. The results can again be represented in a histogram, denoting the counts per direction. Aiming for a better intuitive understanding, these bins can also be plotted in a radial histogram, with the number of normalized counts represented by the radial distance. Both the regular and radial histogram offer the advantage of allowing to overlay results for different conditions (here, flow rates) and hence, to compare directional preferences of the Min waves for these conditions.

For the "experimental phase diagram" in Fig. 3.4G, we chose a slightly different graphical representation, again aiming for better visualization and comparability to the phase diagram shown in Fig. 3. These radial histograms corresponds to the introduced radial histogram plots, just with a wider binning size (60°). Again, the radial distance from the center denotes the number of counts within this segment. The different types of representation are shown in Fig. 3.17 in the box "directional component".

3.7.6. SPATIAL AUTOCORRELATION ANALYSIS

Complementary to the local wave crest analysis, we also obtained global, image-averaged parameters like spatial wavelength. Spatial autocorrelation analysis was performed on 10 individual images per movie. For each autocorrelation output image, a radial average was recorded, starting from the main central correlation peak. The resulting spatial radial correlation curve was subjected to maxima analysis. The first maximum after radius $R = 0$ indicated the most predominant distance between wave edges, irrespective of propagation direction. This distance was identified as a representative wavelength λ for this movie.

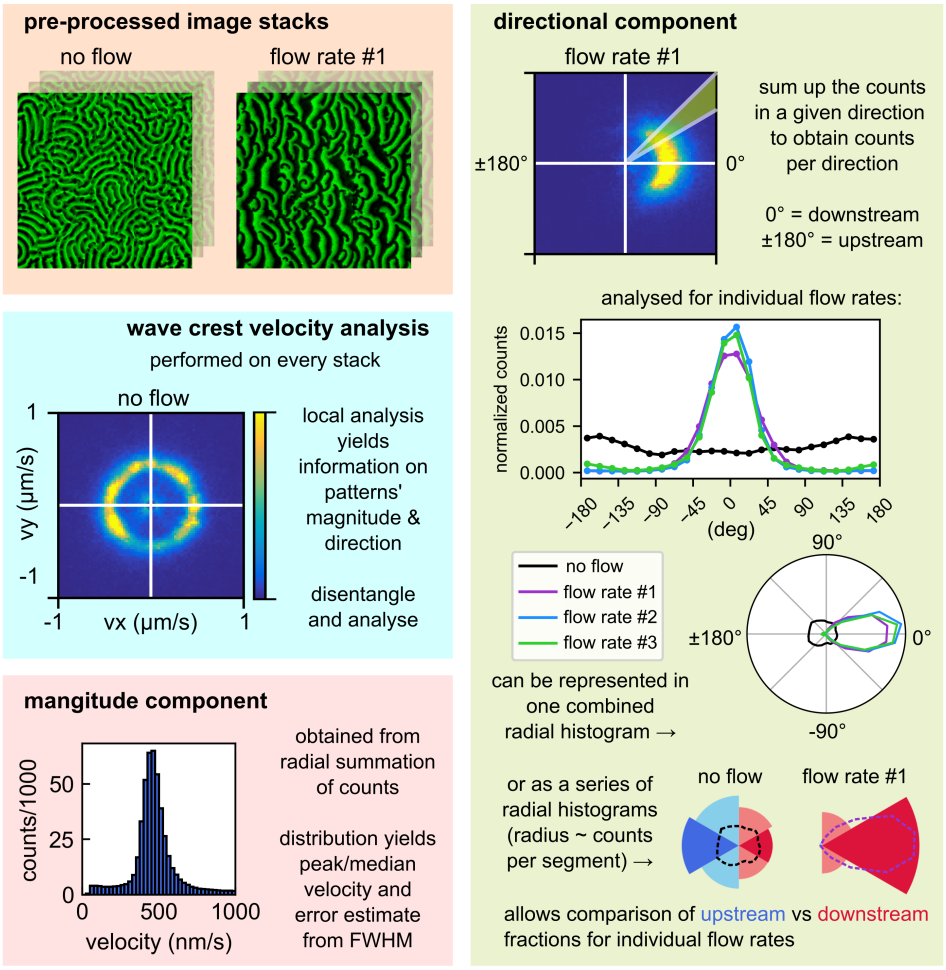


Figure 3.17: An overview on the different types of representation used for local analysis results within the main text as well as the SI.

3.8. SUPPLEMENTARY DATA

3.8.1. CONCENTRATION/RATIO CHANGE IN CLOSED-CIRCLE SETTINGS

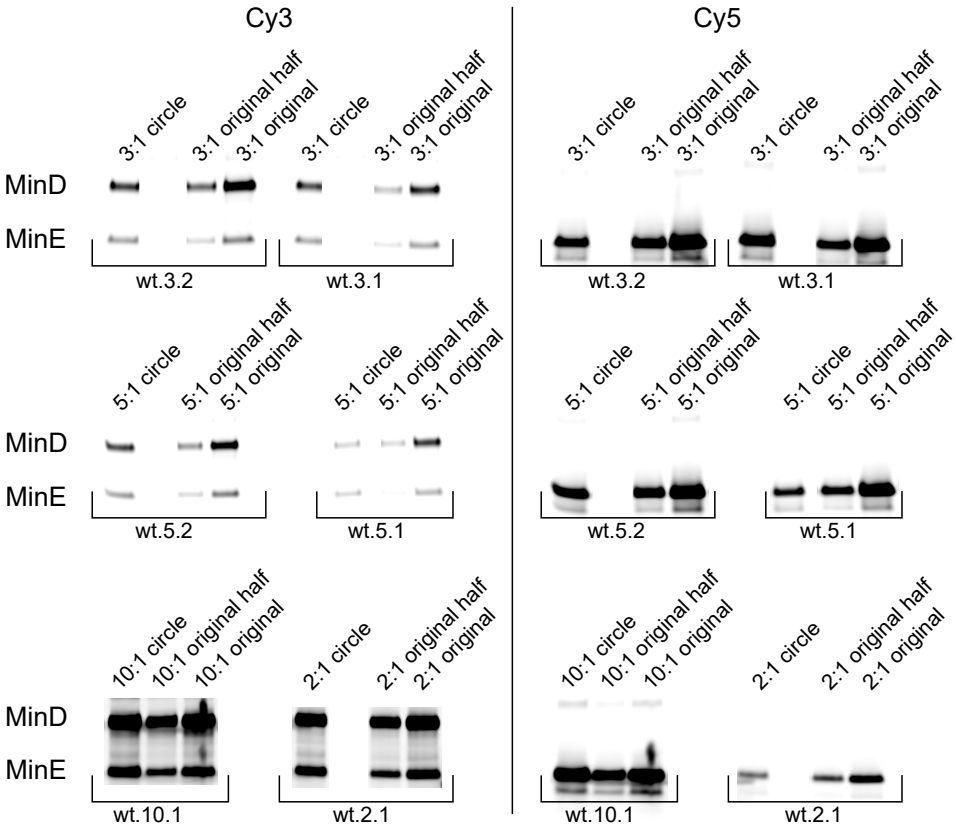


Figure 3.18: Results of protein gels run with samples from the experiment IDs indicated, referring to the experiments listed in Tab. 3.3. For each experiment, a portion of the original sample (*original*), the original sample diluted 1:1 in buffer (*original half*) and the sample extracted from the closed-circle system after the experiment (*circle*) were compared. The remaining fractions of protein were calculated by comparing the intensities of the bands to those of the original sample. The results are summarized in Tab. 3.3.

Closed-circle experiments (repeated circulation of a fixed amount of Min protein solution thorough a flow channel, led back from the outlet to the inlet via a tubing pump) allows for multiple hours of experimentation without consuming high amounts of protein. However, it can be expected that the concentration of Min protein injected into the flow cell and the tubing differs from the actual concentration in the experimental set-

ting due to sticking of the protein to the inner side of the tubing as well as components of the flow cell not covered by lipid bilayers (e.g. the edge of the parafilm). To estimate this concentration change, the protein solution was ejected from the flow channel and tubing after the experiment and run on a protein gel (NuPAGE™ 4–12 % Bis-Tris-Gel by Initrogen™, in MES buffer) side by side with a portion of the original Min protein solution injected into the channel/tubing. The concentration change was then estimated by comparing the fluorescence signal (Cy3 for MinD, Cy5 for MinE) from both the used and original solution (measured using Amersham Typhoon™, GE Healthcare). The remaining fractions were calculated by interpolation between fluorescence signal of the original solution and the original solution diluted 1:1 in buffer. The gels are shown in Fig. 3.18, the corrected ratios are shown alongside the initial ones in Tab. 3.3.
For the sample with initial ratio E:D=10 (*wt.10.1* in Tab. 3.3), a higher fluorescence was measured for the experiment sample than for the original sample. This was most likely caused by evaporation or aggregation. Therefore, no correction factor could be calculated for this sample. However, due to the high protein concentration, we assume that the real ratio is close to 10.

3.8.2. FLOW-INDEPENDENT TIME EVOLUTION OF WAVE PROPAGATION VELOCITY

As revealed by analysing the wave propagation speed for different flow rates (see Fig. 3.22), the average propagation speed was found to be lower with flow as compared to without flow. However, due to incubation and acquisition times, a few hours can pass between recording images with and without flow. Therefore, the option has to be considered that the lower propagation speed might be caused by other factors, such as ATP depletion over time. To test this option, two parallel flow channels were filled with Min protein solution (3 µmol L^{-1} MinE, 1 µmol L^{-1} MinD). One was connected to tubing in a closed-circle setup, while the other one was left as it was and checked regularly. The results for the closed-circle experiment are shown in Fig. 3.19, the results for the control in Fig. 3.20. On a side note: Some images such as the one shown in Fig. 3.19D exhibit heavy bleaching, as can be seen particularly well from dark regions where single microscope images meet. To make sure shortcomings in image quality do not affect quantitative results, such data sets were excluded from analysis based on visual inspection.

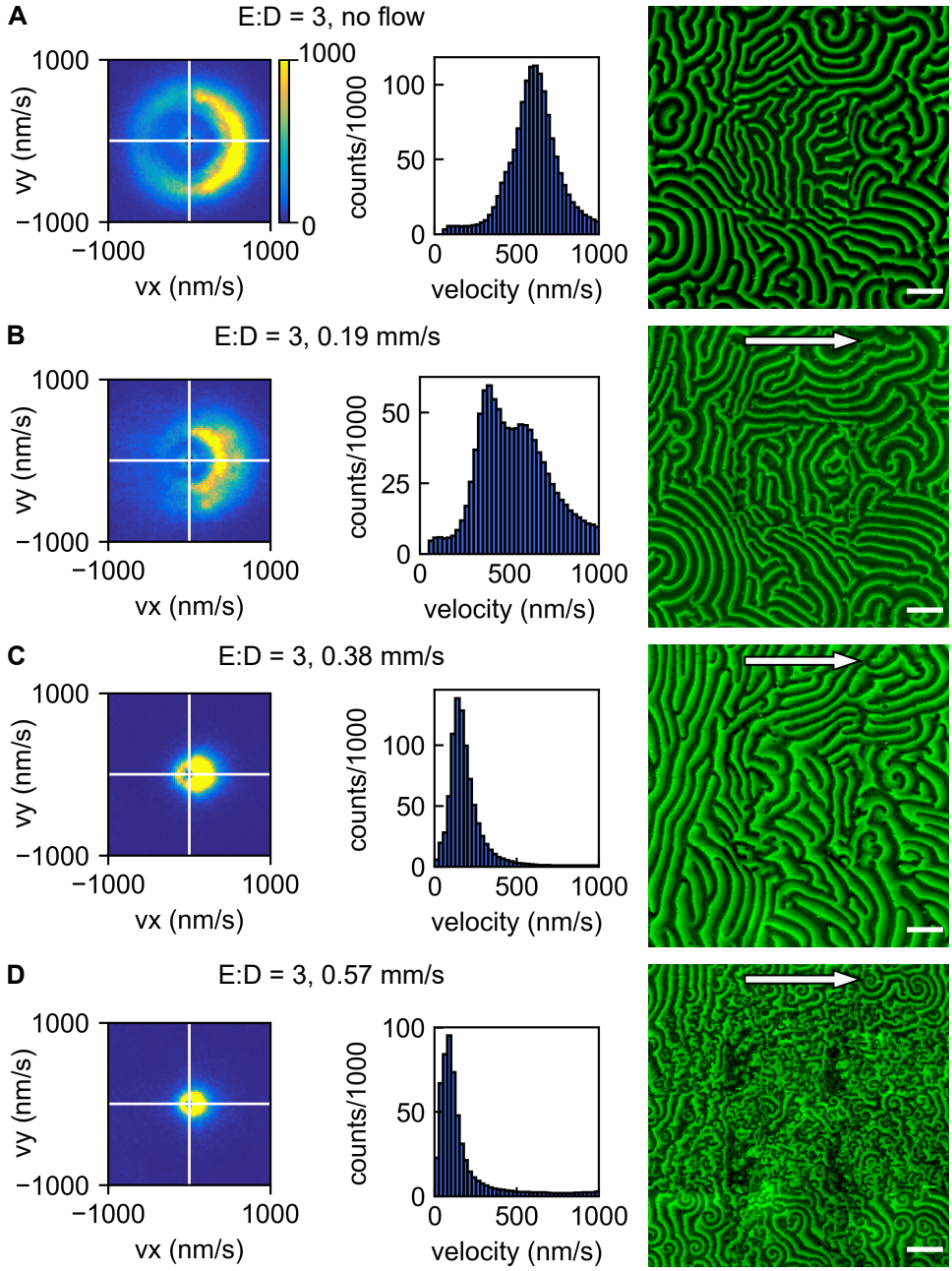


Figure 3.19: Initial E:D = 3 (corrected 2.1), wave front propagation analysis performed for MinD-Cy3. Total covered area of 2.01 mm^2 (one out of 3 regions shown for illustration). Data cropped below 10 % of mean velocity. 2D histogram for segments of 25x25 nm/s. 1D histograms with bin-size of 25 $nm\,s^{-1}$. Exemplary stitched images for MinE-Cy5 given, scale bars 100 µm. **A** Wave propagation analysis and exemplary image without flow. **B** Wave propagation analysis and exemplary image at 0.19 $mm\,s^{-1}$. **C** Wave propagation analysis and exemplary image at 0.38 $mm\,s^{-1}$. **D** Wave propagation analysis and exemplary image at 0.57 $mm\,s^{-1}$.

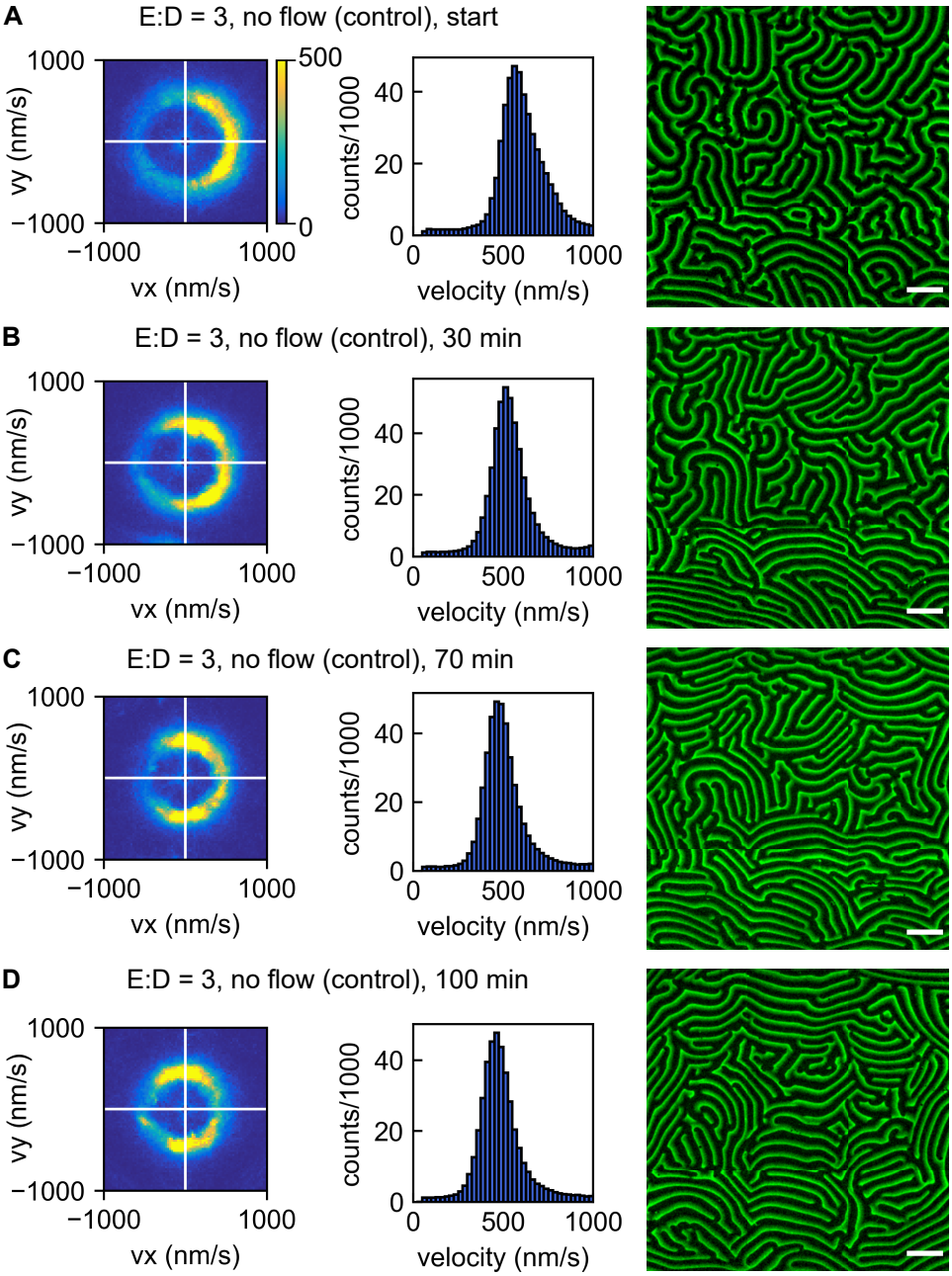


Figure 3.20: Initial E:D = 3, wave front propagation analysis performed for MinD-Cy3. Total covered area of 0.69 mm^2 (0.83 mm x 0.83 mm). Data cropped below 10 % of mean velocity. 2D histogram for segments of 25x25 nm/s. 1D histograms with bin-size of 25 $nm\,s^{-1}$. Stitched images for MinE-Cy5 given, scale bars 100 µm. **A** Wave propagation analysis and image at start of experiment. **B** Wave propagation analysis and image about 30 min after start of experiment. **C** Wave propagation analysis and image about 70 min after start of experiment. **D** Wave propagation analysis and image about 100 min after start of experiment.

3.8.3. EFFECT OF FLOW REVERSAL

Reversing the flow direction was found to reverse the patterns preferential direction of wave propagation. This was demonstrated during an experiment with 10 µmol L^{-1} MinE, 1 µmol L^{-1} MinD, where the direction of flow was reversed at a flow rate of 0.23 mm s^{-1}. See Fig. 3.21A and Fig. 3.21B for the results of wave propagation analysis in the initial situations without flow and with flow in the standard direction (left to right). The final patterns shown in in Fig. 3.21C were acquired about 15 min after flow reversal.

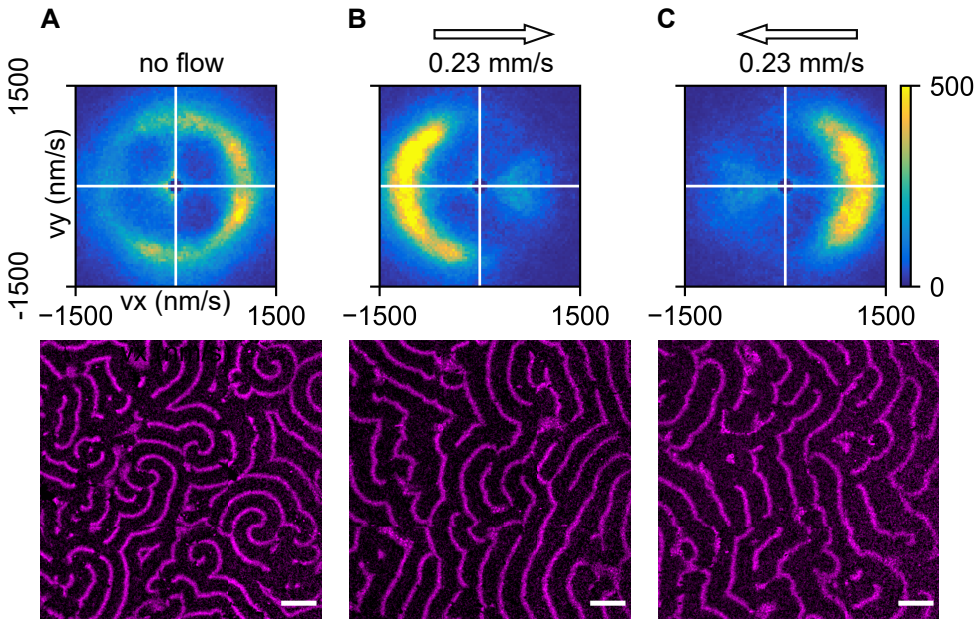


Figure 3.21: Initial E:D = 10, wave front propagation analysis performed for MinD-Cy3. The parameter v_x refers to velocity in x (perpendicular to flow), v_y to velocity in y direction (parallel to flow). Shown range of (v_x, v_y) extends from −1500 to 1500 nm s^{-1}. Data cropped below 10 % of mean velocity. 2D histogram for segments of 25x25 nm/s. Exemplary image shown for MinD-Cy3 channel, scale bar 100 µm. **A** Without flow. **B** With 0.23 mm s^{-1} flow, left to right. **C** With 0.23 mm s^{-1} flow, right to left.

3.8.4. WAVE-CREST VELOCITY DEPENDENCE ON FLOW

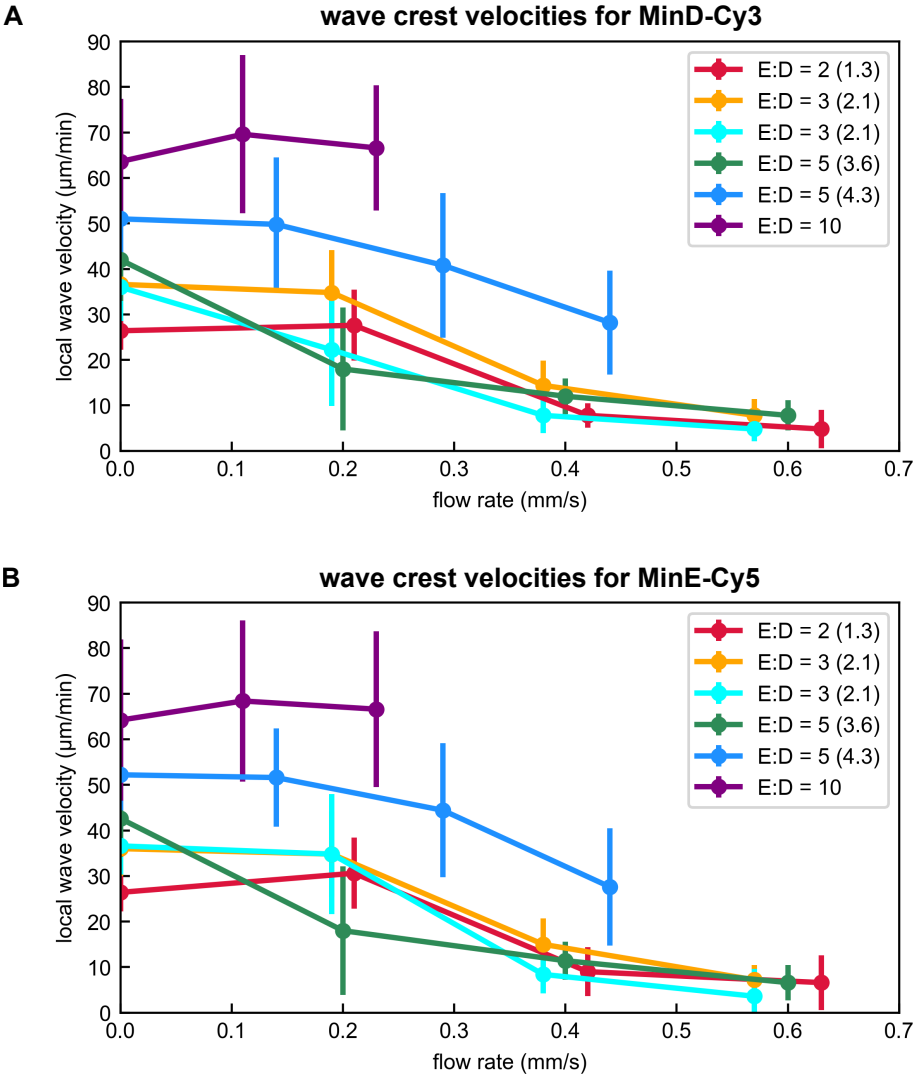


Figure 3.22: **A** Dependence of local wave velocity for MinD-Cy3 on flow rate and E:D ratio. **B** Dependence of wavelength for MinE-Cy5 on flow rate and E:D ratio. For both **A** and **B**, the wave-crest velocities from all imaged regions within one experiment (see Tab. 3.3) were collected and their magnitude's histogram distribution was calculated with a binning width of $10\,\mathrm{nm\,s^{-1}}$. The peak of this histogram distribution was identified as predominant wave velocity and plotted as a function of the E:D ratio and the flow rate, along with the velocity distribution's FWHM as error bars (peak velocity ± FWHM/2).

3.8.5. WAVELENGTH DEPENDENCE ON FLOW

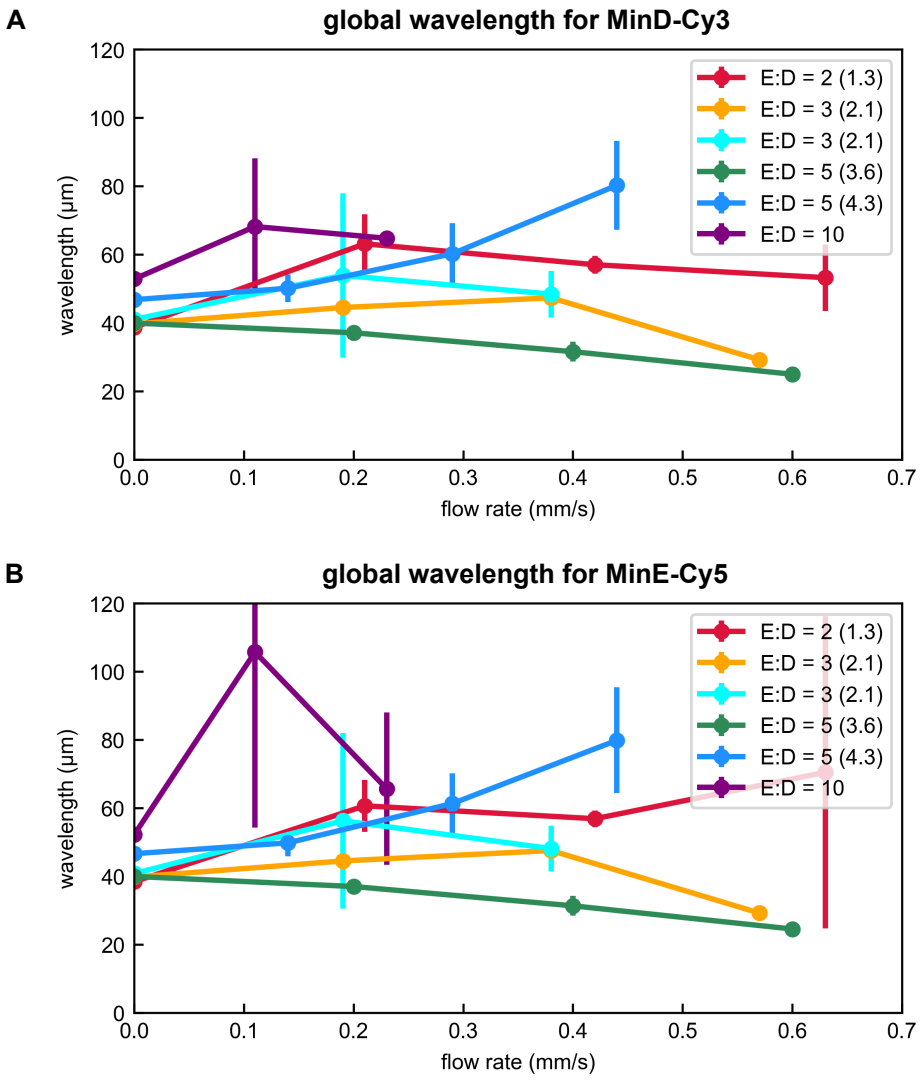


Figure 3.23: **A** Dependence of global wavelength for MinD-Cy3 on flow rate and E:D ratio. **B** Dependence of wavelength for MinE-Cy5 on flow rate and E:D ratio. For both **A** and **B**, the wavelengths from all imaged regions within one experiment (see Tab. 3.3) were averaged and their standard deviation was calculated to obtain error bars. Large errors could be attributed to issues with image quality, such as bleaching.

3.8.6. POSITIONAL DEPENDENCE

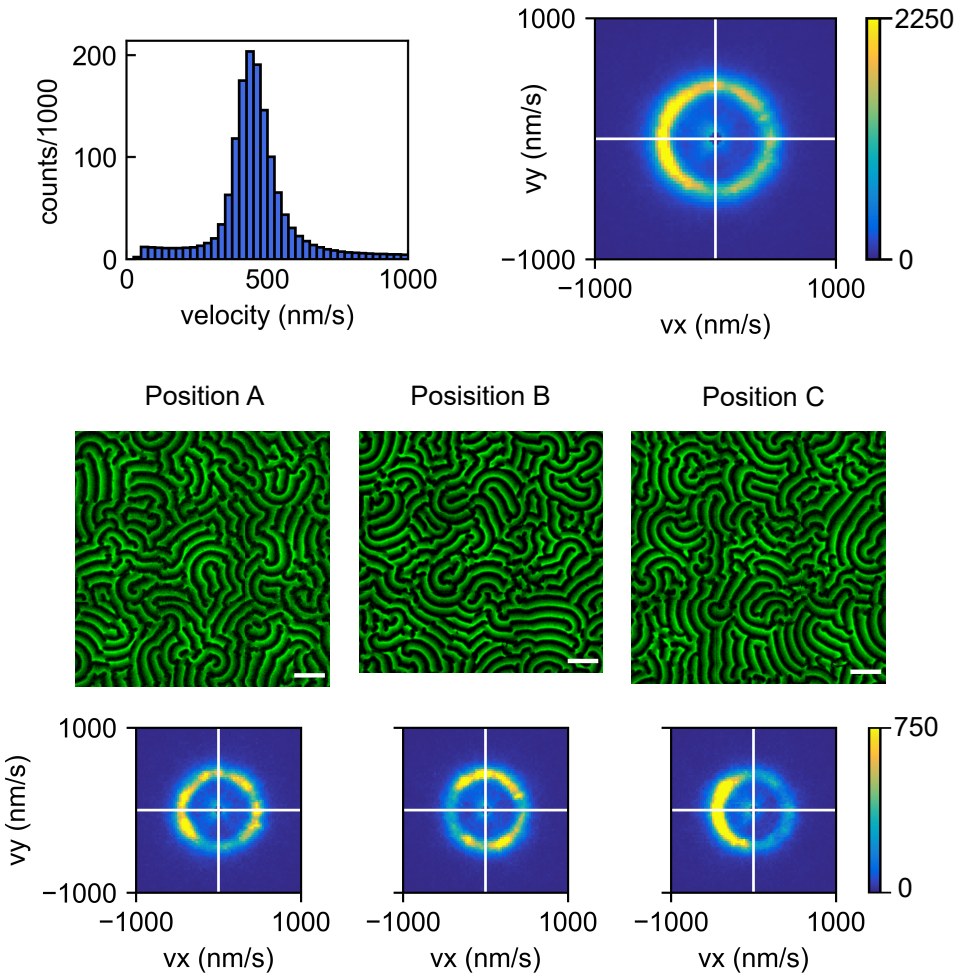


Figure 3.24: The wave-crest velocity data for one E:D ratio is obtained from up to three comparable imaging regions within the same flow channel. Here, we show individual analyses of the MinD-Cy3 channel for the three regions imaged at an E:D ratio of 2 (1.3), as fully shown in Fig. 3.25. Exemplary images shown in green from MinE-Cy5 channel. Scale bars are 100 µm, areas of the three imaging regions are given in Sec. 3.8.7. The velocity vectors are collected and evaluated with respect to their magnitude and direction. They can be visualized in color-coded 2D histograms (top right and bottom row, in bins of 25x25 nm/s). Their magnitudes can be represented in histogram form (top left, in bins of 25 nm s^{-1}).

3.8.7. OVERVIEW ON CLOSED-CIRCLE EXPERIMENTS

Tab. 3.3 on page 138 shows an overview on all image stacks used to compose main text figure 4. These image stacks are processed as tif files (separate for MinD-Cy3 and MinE-Cy5). An overview on local analysis results is given below in section 3.8.8.
The flow rate v (always referring to the average cross-sectional flow rate) was calculated from the flow channel's dimensions (height h and width w) and the set flow rate $V\,t^{-1}$, set on the pump in $\mu L\,min^{-1}$, as

$$v = \frac{V\,t^{-1}}{w \cdot h}$$

The parameters v, h and w allow to calculate the flow channel's Reynolds number. As we obtain low Reynolds numbers for all channels and flow rates, we assume laminar flow for all experiments.
To estimate the standard deviation (error) of the flow rate, the following values were assumed:

- $(V\,t^{-1})_{std}$ = 5% of set value of pump
- w_{std} = 100 µm
- h_{std} = 10 µm

Position 4 of the experiment ID indicates the total area covered by the experiment's type of stitching pattern. The respective values are:

- A: 0.69 mm^2 (0.83 mm x 0.84 mm)
- B: 0.63 mm^2 (0.80 mm x 0.79 mm)
- C: 0.68 mm^2 (0.83 mm x 0.82 mm)
- alt: other (1 pixel = 594 nm in tif files)

Unless indicated otherwise, one frame was recorded every 15 s.
As the imaged areas are comprised of individual FOVs, some stitching artifacts can be visible where adjacent areas meet, resulting in small discontinuities.

For every experiment, the original Min protein mix injected into the flow channel would contain 1 $\mu mol\,L^{-1}$ MinD. Therefore, a certain initial ratio corresponds to the same initial concentration of MinE in $\mu mol\,L^{-1}$.
Both MinD and MinE would partially stick to the channel/tubing. Based on the gels shown in Fig. 3.18, a corrected ratio was calculated where applicable. Each experiment was performed with a fraction of labeled protein, ranging from 10–20 %, as indicated in Tab. 3.3. MinD-Cy3 was found to have a labeling efficiency of 88 %, MinE-Cy5 of 45 % (compare Caspi & Dekker[30]).

Table 3.3: Overview on closed-circle experiments

experiment ID	image stack ID	initial ratio	corrected ratio	imaged area (mm^2)	MinD-Cy3 (%)	MinE-Cy5 (%)	width (μm)	height (μm)	flow (mm/s)	flow error (mm/s)
wt.2.1	wt.2.1.[A/B/C].00	2	1.29	2.01	20	20	2953	183.26	0.00	0.00
	wt.2.1.[A/B/C].01	2	1.29	2.01	20	20	2953	183.26	0.21	0.02
	wt.2.1.[A/B/C].02	2	1.29	2.01	20	20	2953	183.26	0.42	0.04
	wt.2.1.[A/B/C].03	2	1.29	2.01	20	20	2953	183.26	0.63	0.06
wt.3.1	wt.3.1.[A/B/C].00	3	2.05	2.01	20	20	2937	203.39	0.00	0.00
	wt.3.1.[A/B/C].01	3	2.05	2.01	20	20	2937	203.39	0.19	0.02
	wt.3.1.[A/B/C].02	3	2.05	2.01	20	20	2937	203.39	0.38	0.04
	wt.3.1.[A/B/C].03	3	2.05	2.01	20	20	2937	203.39	0.57	0.06
wt.3.2	wt.3.2.[A/B/C].00	3	2.06	2.01	20	20	2865	208.86	0.00	0.00
	wt.3.2.[A/B/C].01	3	2.06	2.01	20	20	2865	208.86	0.19	0.02
	wt.3.2.[A/B/C].02	3	2.06	2.01	20	20	2865	208.86	0.38	0.04
wt.5.1	wt.5.1.[A/B/C].00	5	4.29	2.01	10	10	3561	229.76	0.00	0.00
	wt.5.1.[A/B/C].01	5	4.29	2.01	10	10	3561	229.76	0.14	0.01
	wt.5.1.[A/B/C].02	5	4.29	2.01	10	10	3561	229.76	0.29	0.03
	wt.5.1.[A/B/C].03	5	4.29	2.01	10	10	3561	229.76	0.44	0.04
wt.5.2	wt.5.2.[A/B/C].00	5	3.63	2.01	20	20	2874	198.40	0.00	0.00
	wt.5.2.[A/B/C].01	5	3.63	2.01	20	20	2874	198.40	0.20	0.02
	wt.5.2.[A/B/C].02	5	3.63	2.01	20	20	2874	198.40	0.40	0.04
	wt.5.2.[A/B/C].03	5	3.63	2.01	20	20	2874	198.40	0.60	0.06
wt.10.1	wt.10.1.[A/B].00	10	-	1.32	10	10	4347	230.30	0.00	0.00
	wt.10.1.[A/B].01	10	-	1.32	10	10	4347	230.30	0.11	0.01
	wt.10.1.[A/B].02	10	-	1.32	10	10	4347	230.30	0.23	0.02

3.8.8. LOCAL VELOCITY ANALYSIS: CLOSED-CIRCLE EXPERIMENTS

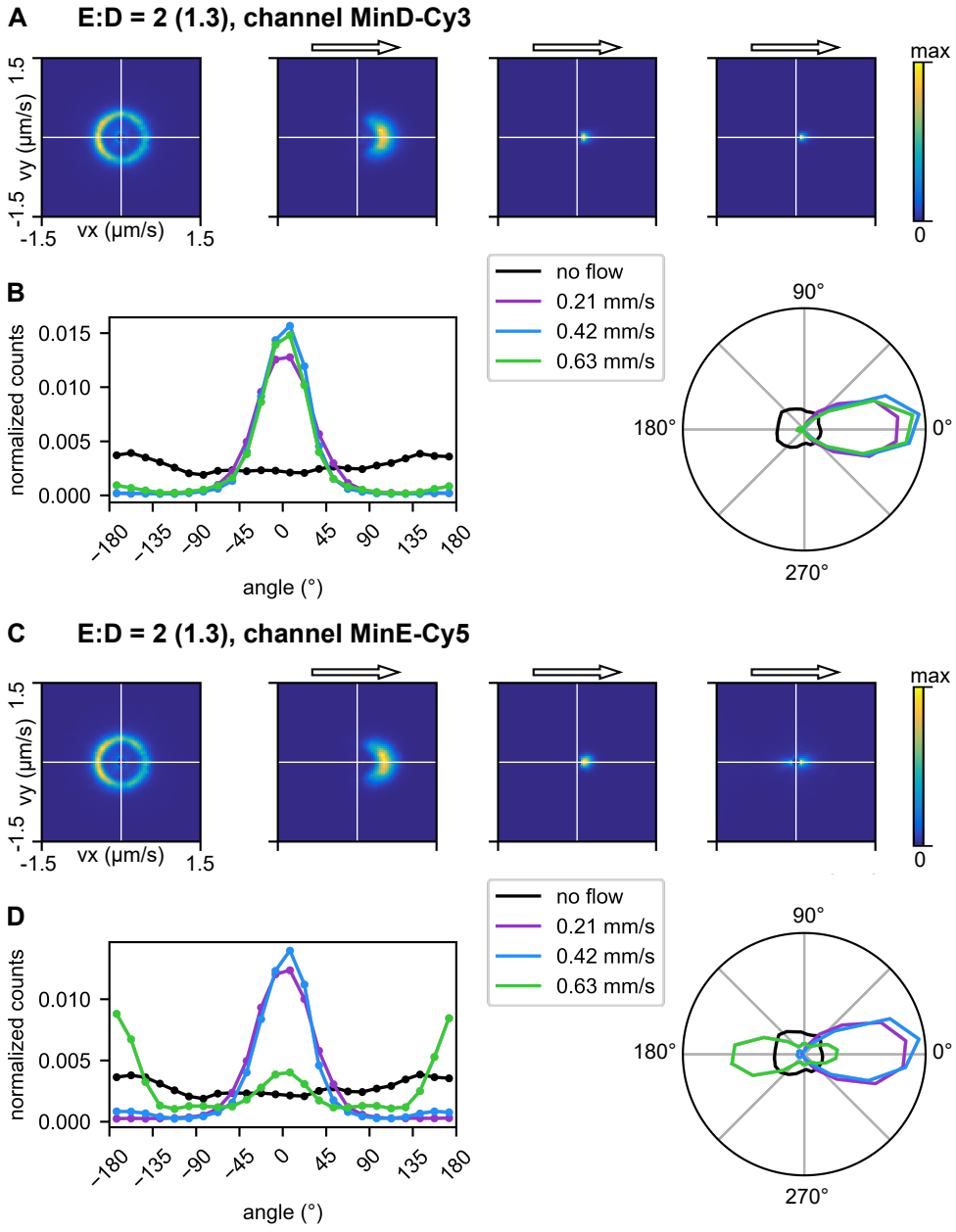


Figure 3.25: Analysis for E:D=2 (corrected 1.3, closed-circle), *wt.2.1*, performed with tools presented in Ref.[43] using general smoothing kernel 12 µm (20 pixels) and flow smoothing kernel 30 µm (50 pixels). Velocity data cropped below 10 % of mean magnitude. **A**, **C** Vector counts per segment for no-flow setting and sequentially applied flow rates as given in the box in **B**, represented as 2D histograms (80 bins in x-/y-direction each), counts per box indicated by color, maximum (yellow) corresponds to maximum bin count for each individual 2D histogram. **B**, **D** 1D histogram and polar histogram representation of counts per direction in bins of 15° for different flow rates.

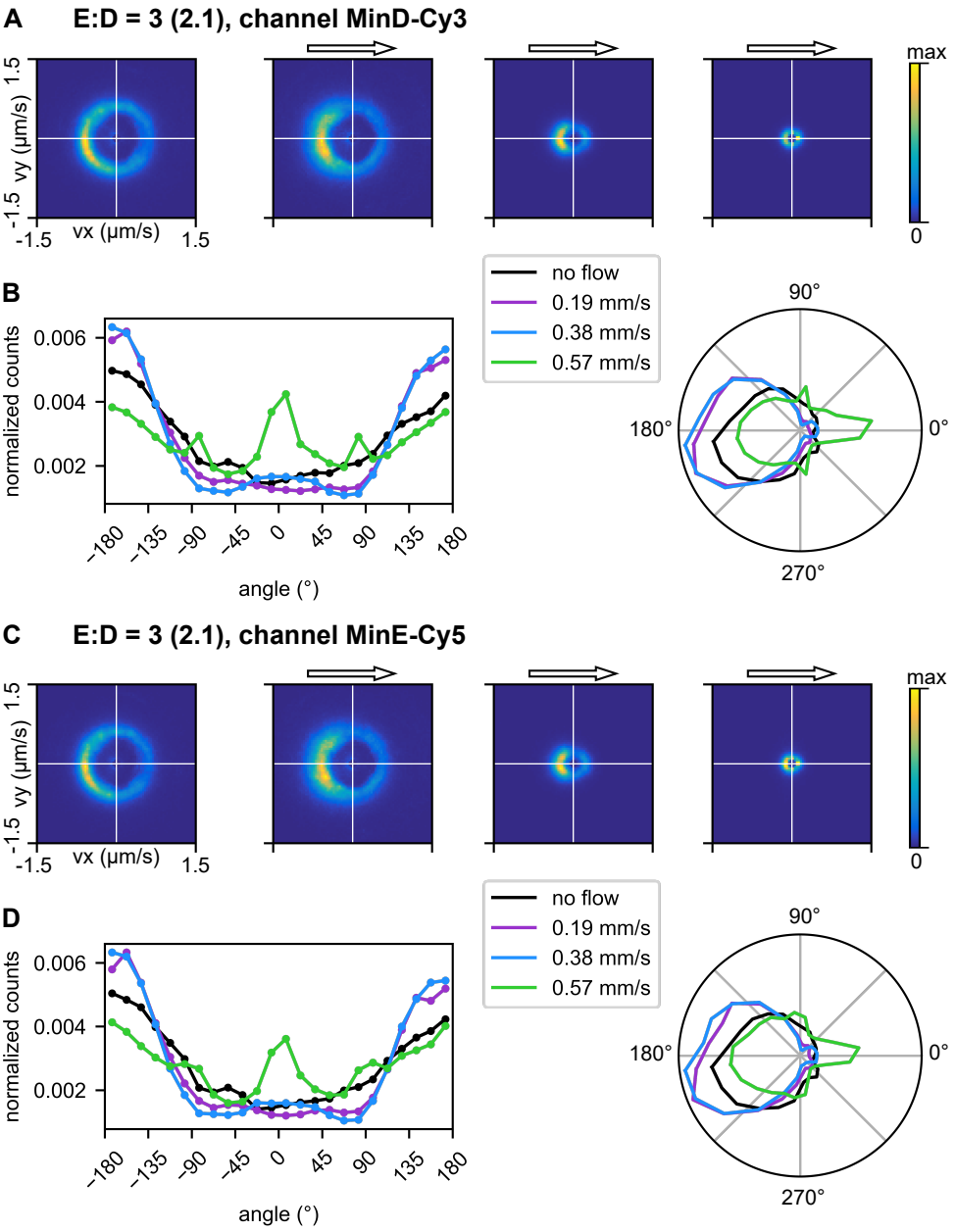


Figure 3.26: Analysis for E:D=3 (corrected 2.1, closed-circle), *wt.3.1*, performed with tools presented in Ref.[43] using general smoothing kernel 12 µm (20 pixels) and flow smoothing kernel 30 µm (50 pixels). Velocity data cropped below 10 % of mean magnitude. **A**, **C** Vector counts per segment for no-flow setting and sequentially applied flow rates as given in the box in **B**, represented as 2D histograms (80 bins in x-/y-direction each), counts per box indicated by color, maximum (yellow) corresponds to maximum bin count for each individual 2D histogram. **B**, **D** 1D histogram and polar histogram representation of counts per direction in bins of 15° for different flow rates.

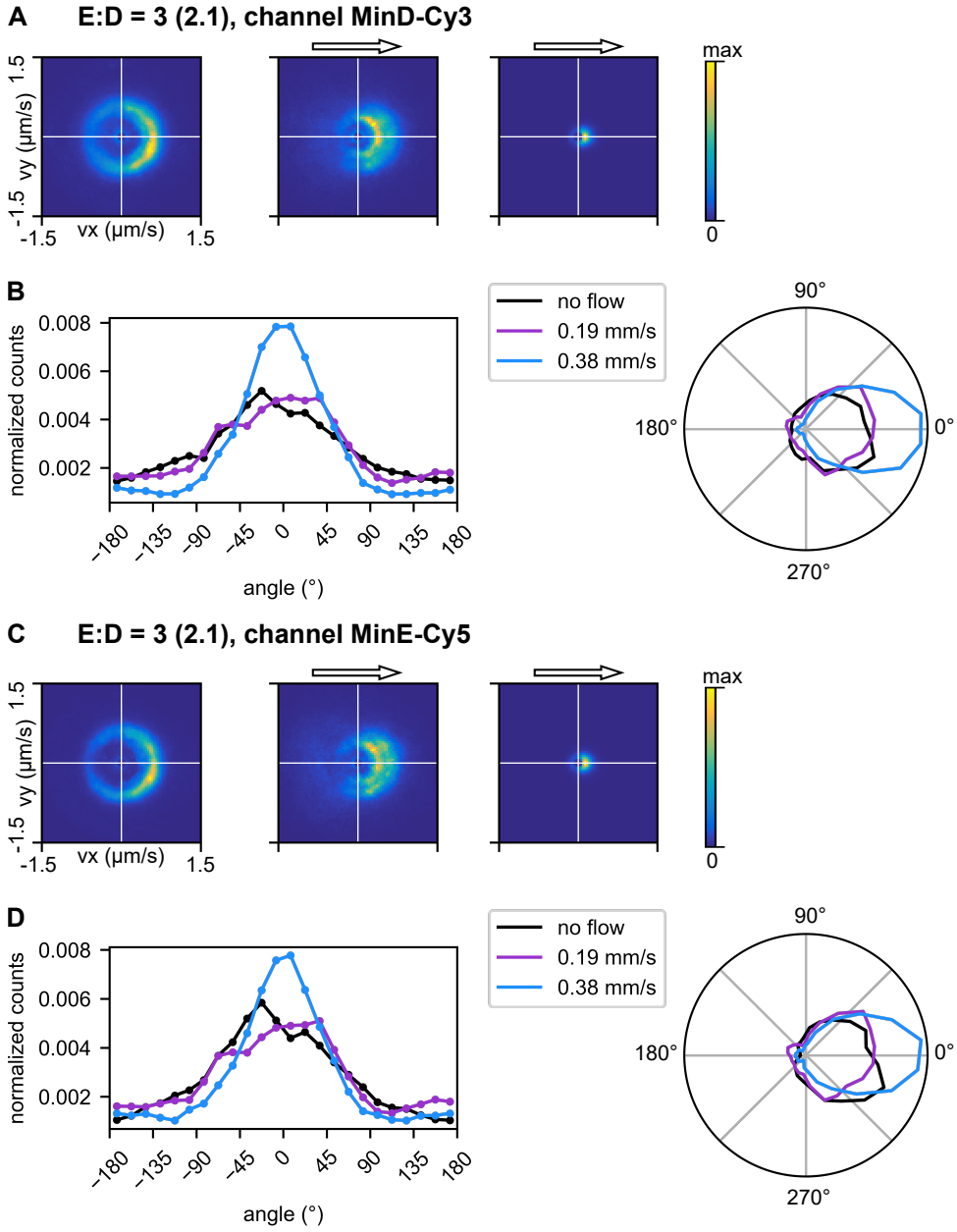


Figure 3.27: Analysis for E:D=3 (corrected 2.1, closed-circle), *wt.3.2*, performed with tools presented in Ref.[43] using general smoothing kernel 12 µm (20 pixels) and flow smoothing kernel 30 µm (50 pixels). Velocity data cropped below 10 % of mean magnitude. **A**, **C** Vector counts per segment for no-flow setting and sequentially applied flow rates as given in the box in **B**, represented as 2D histograms (80 bins in x-/y-direction each), counts per box indicated by color, maximum (yellow) corresponds to maximum bin count for each individual 2D histogram. **B**, **D** 1D histogram and polar histogram representation of counts per direction in bins of 15° for different flow rates.

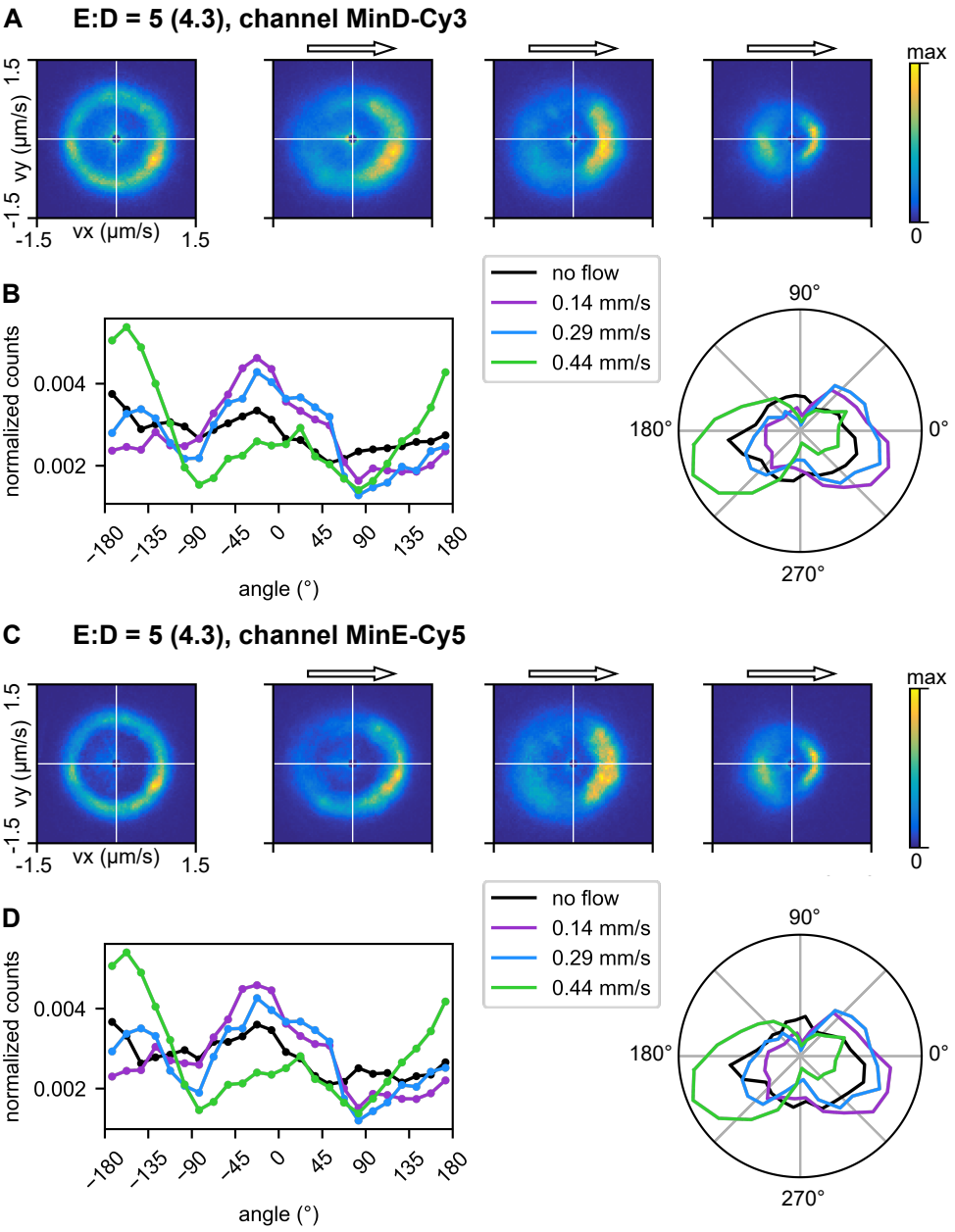


Figure 3.28: Analysis for E:D=5 (corrected 4.3, closed-circle), *wt.5.1*, performed with tools presented in Ref.[43] using general smoothing kernel 12 µm (20 pixels) and flow smoothing kernel 30 µm (50 pixels). Velocity data cropped below 10 % of mean magnitude. **A**, **C** Vector counts per segment for no-flow setting and sequentially applied flow rates as given in the box in **B**, represented as 2D histograms (80 bins in x-/y-direction each), counts per box indicated by color, maximum (yellow) corresponds to maximum bin count for each individual 2D histogram. **B**, **D** 1D histogram and polar histogram representation of counts per direction in bins of 15° for different flow rates.

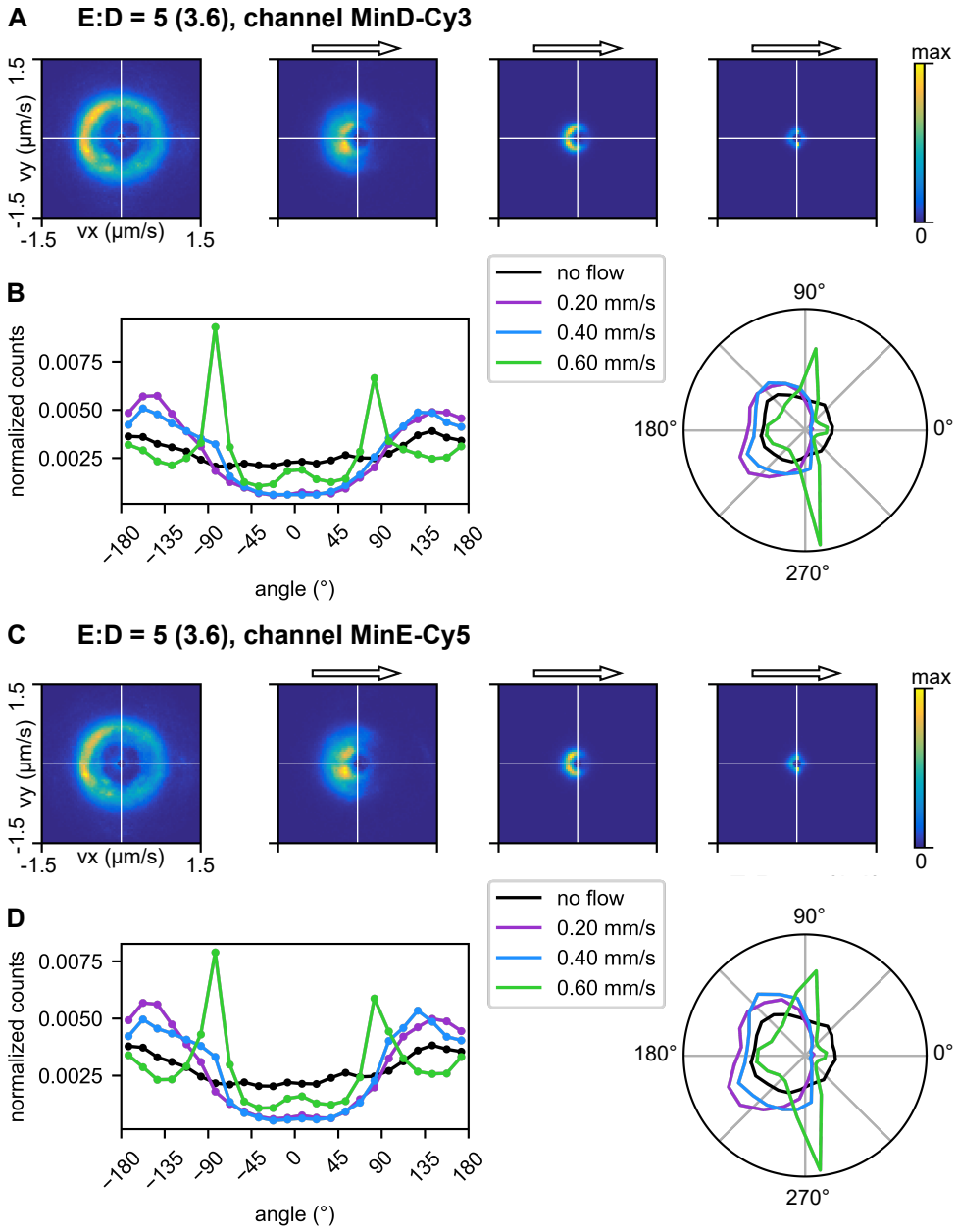


Figure 3.29: Analysis for E:D=5 (corrected 3.6, closed-circle), *wt.5.2*, performed with tools presented in Ref.[43] using general smoothing kernel 12 µm (20 pixels) and flow smoothing kernel 30 µm (50 pixels). Velocity data cropped below 10 % of mean magnitude. **A**, **C** Vector counts per segment for no-flow setting and sequentially applied flow rates as given in the box in **B**, represented as 2D histograms (80 bins in x-/y-direction each), counts per box indicated by color, maximum (yellow) corresponds to maximum bin count for each individual 2D histogram. **B**, **D** 1D histogram and polar histogram representation of counts per direction in bins of 15° for different flow rates.

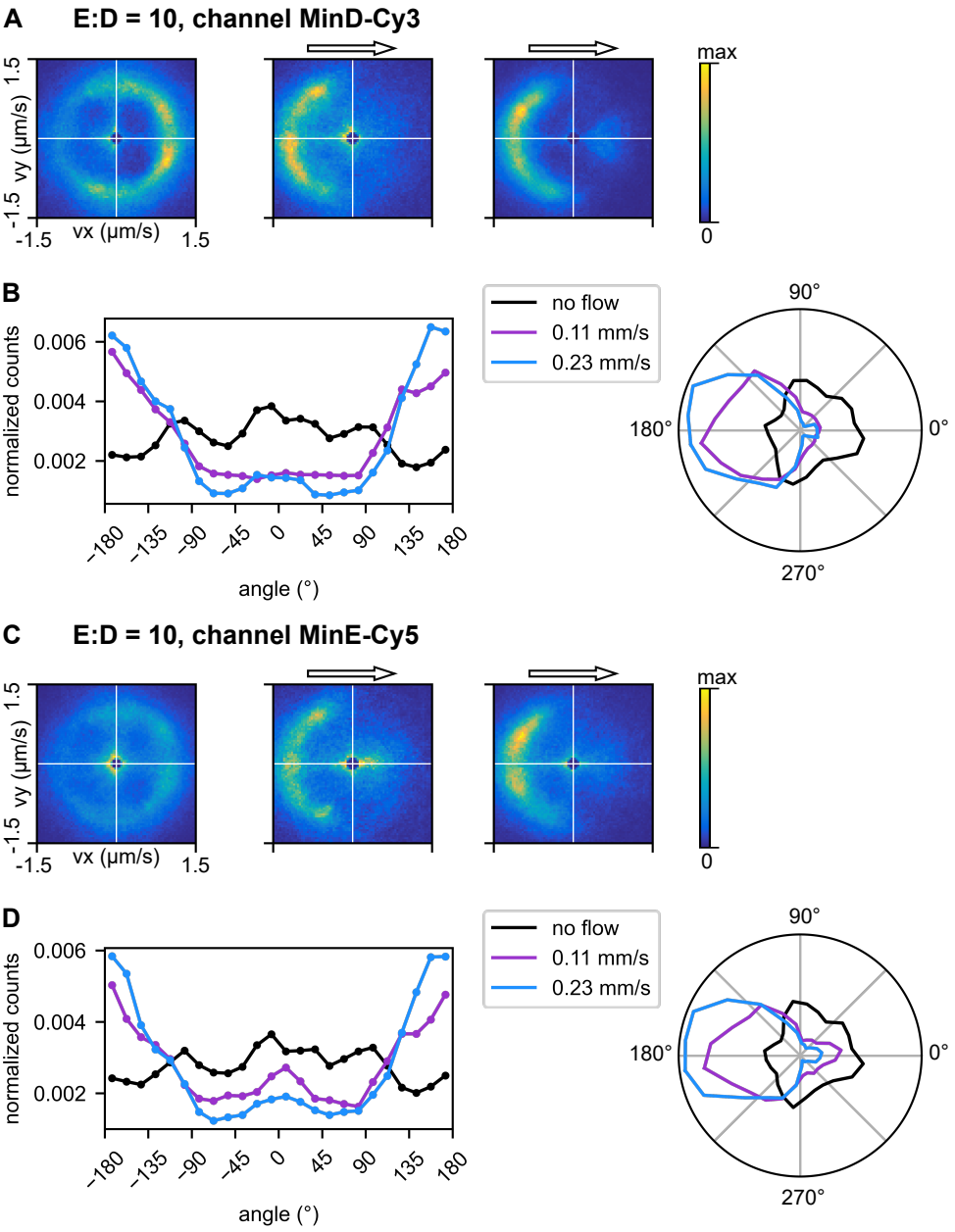


Figure 3.30: Analysis for E:D=10 (closed-circle), *wt.10.1*, performed with tools presented in Ref.[43] using general smoothing kernel 24 µm (40 pixels) and flow smoothing kernel 30 µm (50 pixels). Velocity data cropped below 10 % of mean magnitude. **A**, **C** Vector counts per segment for no-flow setting and sequentially applied flow rates as given in the box in **B**, represented as 2D histograms (80 bins in x-/y-direction each), counts per box indicated by color, maximum (yellow) corresponds to maximum bin count for each individual 2D histogram. **B**, **D** 1D histogram and polar histogram representation of counts per direction in bins of 15° for different flow rates.

3.8.9. OVERVIEW ON ADDITIONAL/CONTROL EXPERIMENTS

In table 3.4, an overview on the additional/control experiments performed for this study is shown. An overview on local analysis results not shown elsewhere is given below in section 3.8.10.
The results of *wt.3.3.alt* and *wt.10.1.[A/B].03* are given in Figs. 3.20 and 3.21, respectively.

Image IDs starting with "wt" indicate the use of MinE wildtype, IDs starting with "l3" indicate the use of the L3E/I24N mutant [23]. Experiment *l3.p05.1* (shown in main text Fig. 2C) was performed in an open flow channel, as closed-circle experiments were found to be unsuitable for the L3E/I24N mutant due to its strong concentration dependence (also compare Ref. [23]).
Unless indicated otherwise, one frame was recorded every 15 s.
The image stack *l3.p05.2* was recorded at 6 s intervals to confirm the suitability of the sampling rate for the narrower patterns produced by the L3E/I24N mutant. It was performed with MinD-Cy3 protein from an alternative batch and using exclusively labelled MinE-L3E/I24N-Cy5.
Experiment *wt.2.2* was performed for an initial ratio E:D=2 in a closed-circle system. Here, the tubing was passivated with Bovine Serum Albumin (BSA) and rinsed with Min buffer before it was filled with protein solution. Protein gels (compare Sec. 3.8.1, data not shown) indicated a reduced loss of protein concentration. However, we decided against this method to avoid potential complications arriving from an additional components.
Experiments *wt.1p5.1* and *wt.5.3* were performed in slightly deviating experimental settings (open systems, alternative flow cell design) in 150 mmol L^{-1} KCl, 5 mmol L^{-1} $MgCl_2$, 19–23 mmol L^{-1} and TRIS pH 7.4-7.5 (21 °C) (all components ±10%), plus small amounts of Hepes pH 7.25, glycerol, EDTA and ADP.

Table 3.4: Overview on additional experiments

experiment ID	image stack ID	initial ratio	corrected ratio	imaged area (mm^2)	MinD-Cy3 (%)	MinE-Cy5 (%)	width (μm)	height (μm)	flow (mm/s)	flow error (mm/s)
l3.p05.1	l3.p05.1.[B/C].00	0.05	-	1.31	20	10	3296	218.64	0.00	0.00
	l3.p05.1.[B/C].01	0.05	-	1.31	20	10	3296	218.64	0.15	0.02
wt.10.1	wt.10.1.[A/B].03	10	-	1.32	10	10	4347	230.30	-0.23	0.02
wt.3.3	wt.3.3.alt.00	3	-	0.69	20	20	-	-	0.00	0.00
	wt.3.3.alt.01	3	-	0.69	20	20	-	-	0.00	0.00
	wt.3.3.alt.02	3	-	0.69	20	20	-	-	0.00	0.00
	wt.3.3.alt.03	3	-	0.69	20	20	-	-	0.00	0.00
wt.2.2	wt.2.2.alt.00	2	-	0.72	20	20	4596	111.34	0.00	0.00
	wt.2.2.alt.01	2	-	0.72	20	20	4596	111.34	0.21	0.02
	wt.2.2.alt.02	2	-	0.72	20	20	4596	111.34	0.43	0.04
	wt.2.2.alt.03	2	-	0.72	20	20	4596	111.34	0.64	0.06
wt.1p5.1	wt.1p5.1.alt.00	1.5	-	0.5	10 - 20	10 - 20	3777	103.81	0.00	0.00
	wt.1p5.1.alt.01	1.5	-	0.5	10 - 20	10 - 20	3777	103.81	0.43	0.04
wt.5.3	wt.5.3.alt.00	5	-	0.57	10 - 20	10 - 20	3582	103.86	0.00	0.00
	wt.5.3.alt.01	5	-	0.57	10 - 20	10 - 20	3582	103.86	0.29	0.03
l3.p05.2	l3.p05.2.alt.01	0.05	-	0.28	10 - 20	100	3360	242	0.14	0.01

3.8.10. LOCAL VELOCITY ANALYSIS: ADDITIONAL/CONTROL DATA

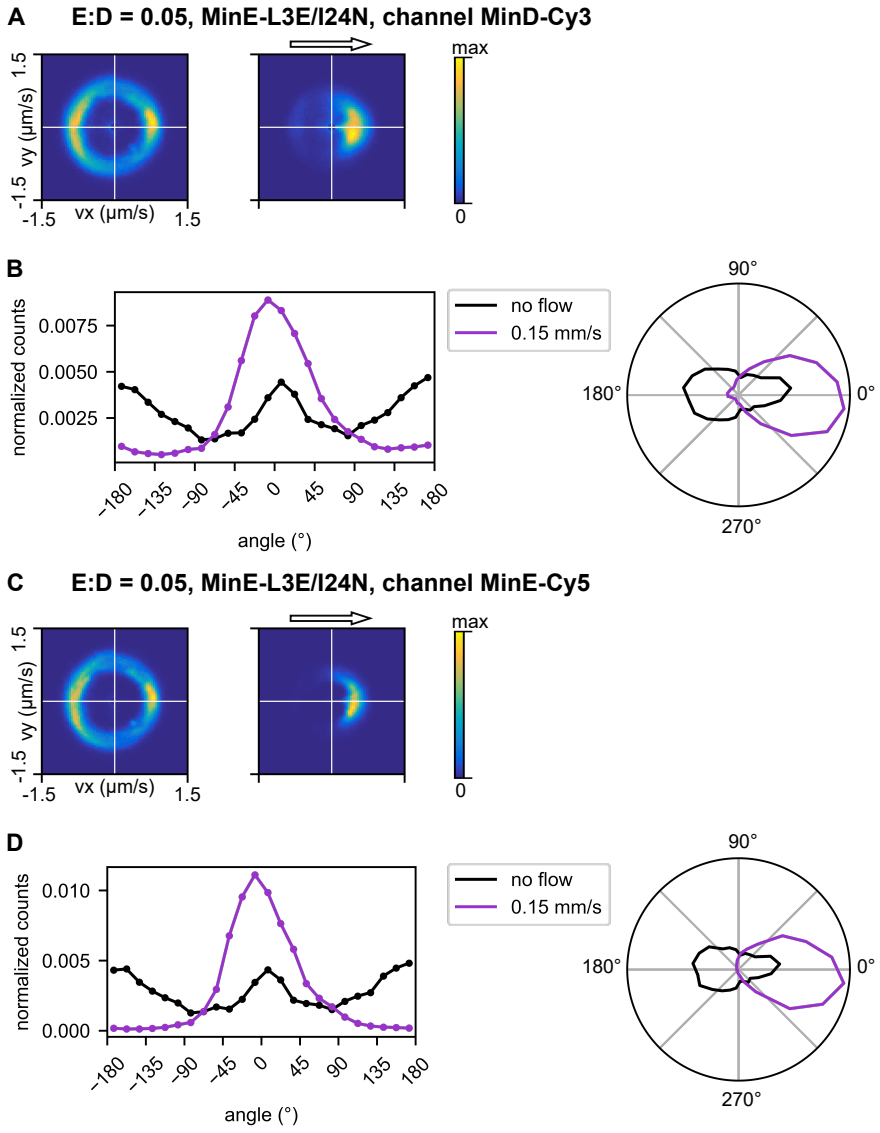


Figure 3.31: Analysis for E:D=0.05, MinE-L3E/I24N, *l3.p05.1* (open flow channel), performed with tools presented in Ref.[43] using general smoothing kernel 12 µm (20 pixels) and flow smoothing kernel 12 µm (20 pixels). Velocity data cropped below 10 % of mean magnitude. **A**, **C** Vector counts per segment for no-flow setting and sequentially applied flow rates as given in the box in **B**, represented as 2D histograms (80 bins in x-/y-direction each), counts per box indicated by color, maximum (yellow) corresponds to maximum bin count for each individual 2D histogram. **B**, **D** 1D histogram and polar histogram representation of counts per direction in bins of 15° for different flow rates. **Important note**: This data was later found to be unsuitable for the velocity analysis performed here, as specified in an Author's Correction (2024), given in section 3.10.

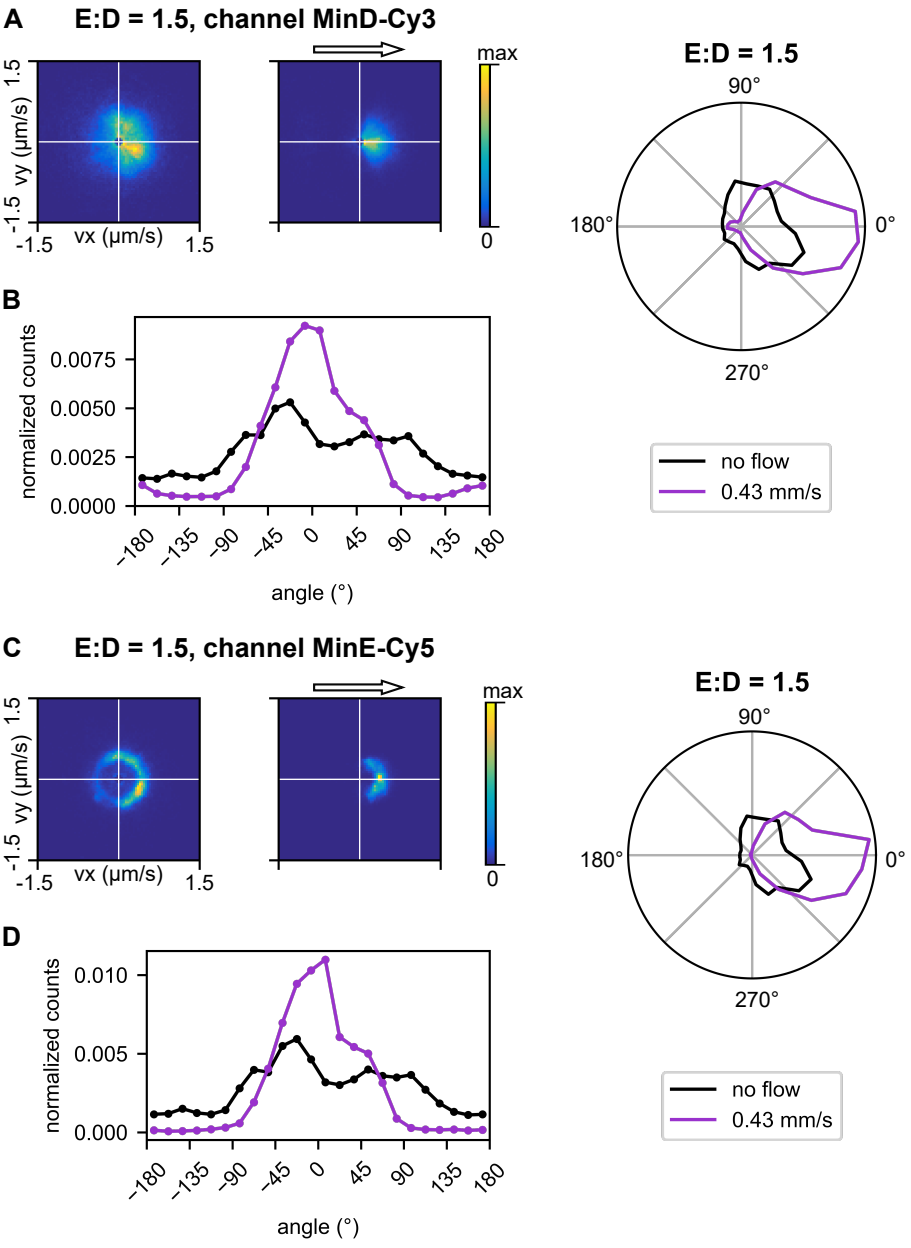


Figure 3.32: Analysis for E:D=1.5, *wt.1p5.1.alt* (open flow channel), performed with tools presented in Ref.[43] using general smoothing kernel 12 µm (20 pixels) and flow smoothing kernel 30 µm (50 pixels). Velocity data cropped below 10 % of mean magnitude. **A**, **C** Vector counts per segment for no-flow setting and sequentially applied flow rates as given in the box in **B**, represented as 2D histograms (80 bins in x-/y-direction each), counts per box indicated by color, maximum (yellow) corresponds to maximum bin count for each individual 2D histogram. **B**, **D** 1D histogram and polar histogram representation of counts per direction in bins of 15° for different flow rates.

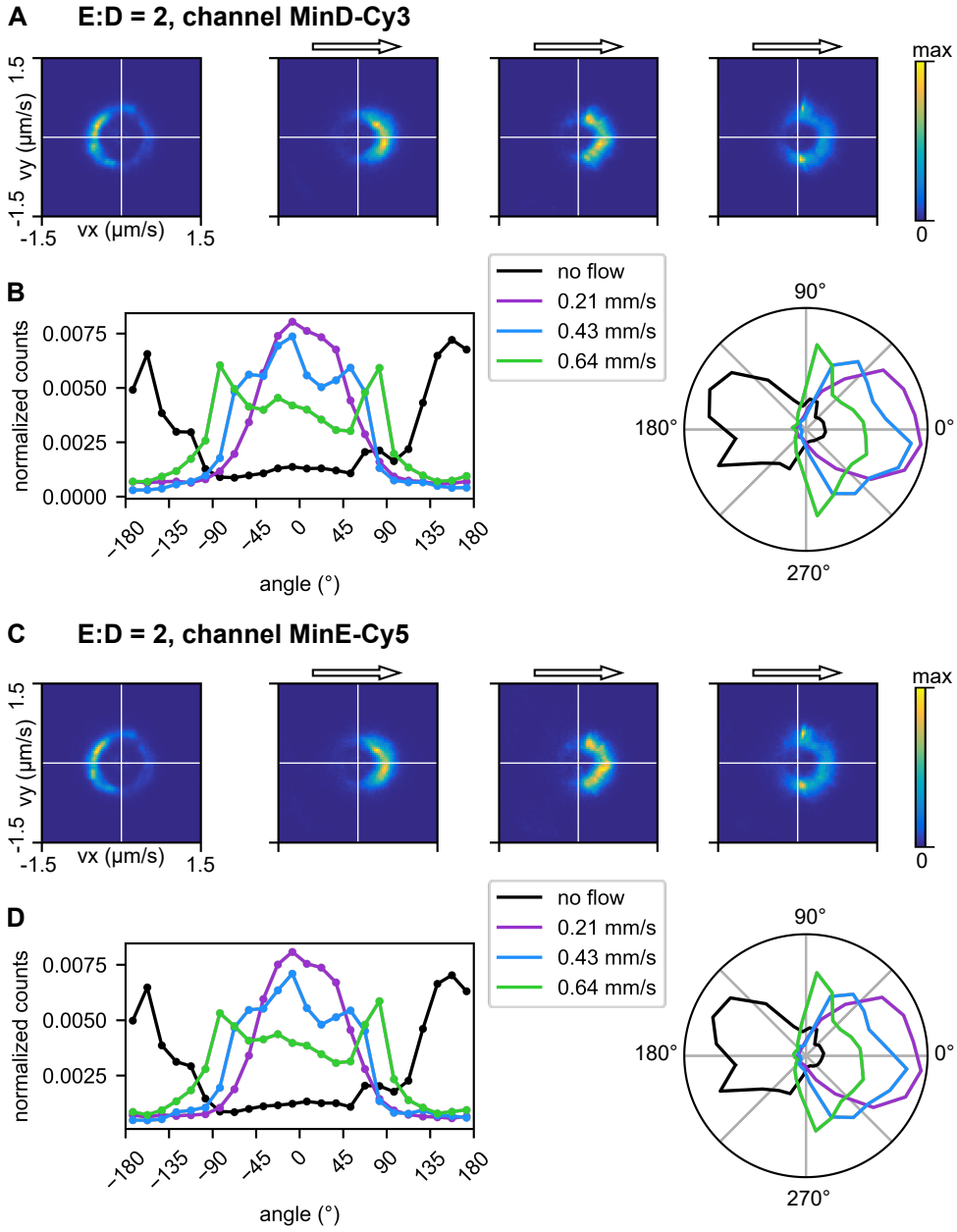


Figure 3.33: Analysis for E:D=2, *wt.2.2.alt* (closed-circle, tubing passivated with 1 mg mL^{-1} Bovine Serum Albumin and rinsed with Min buffer), performed with tools presented in Ref.[43] using general smoothing kernel 12 µm (20 pixels) and flow smoothing kernel 30 µm (50 pixels). Velocity data cropped below 10 % of mean magnitude. **A**, **C** Vector counts per segment for no-flow setting and sequentially applied flow rates as given in the box in **B**, represented as 2D histograms (80 bins in x-/y-direction each), counts per box indicated by color, maximum (yellow) corresponds to maximum bin count for each individual 2D histogram. **B**, **D** 1D histogram and polar histogram representation of counts per direction in bins of 15° for different flow rates.

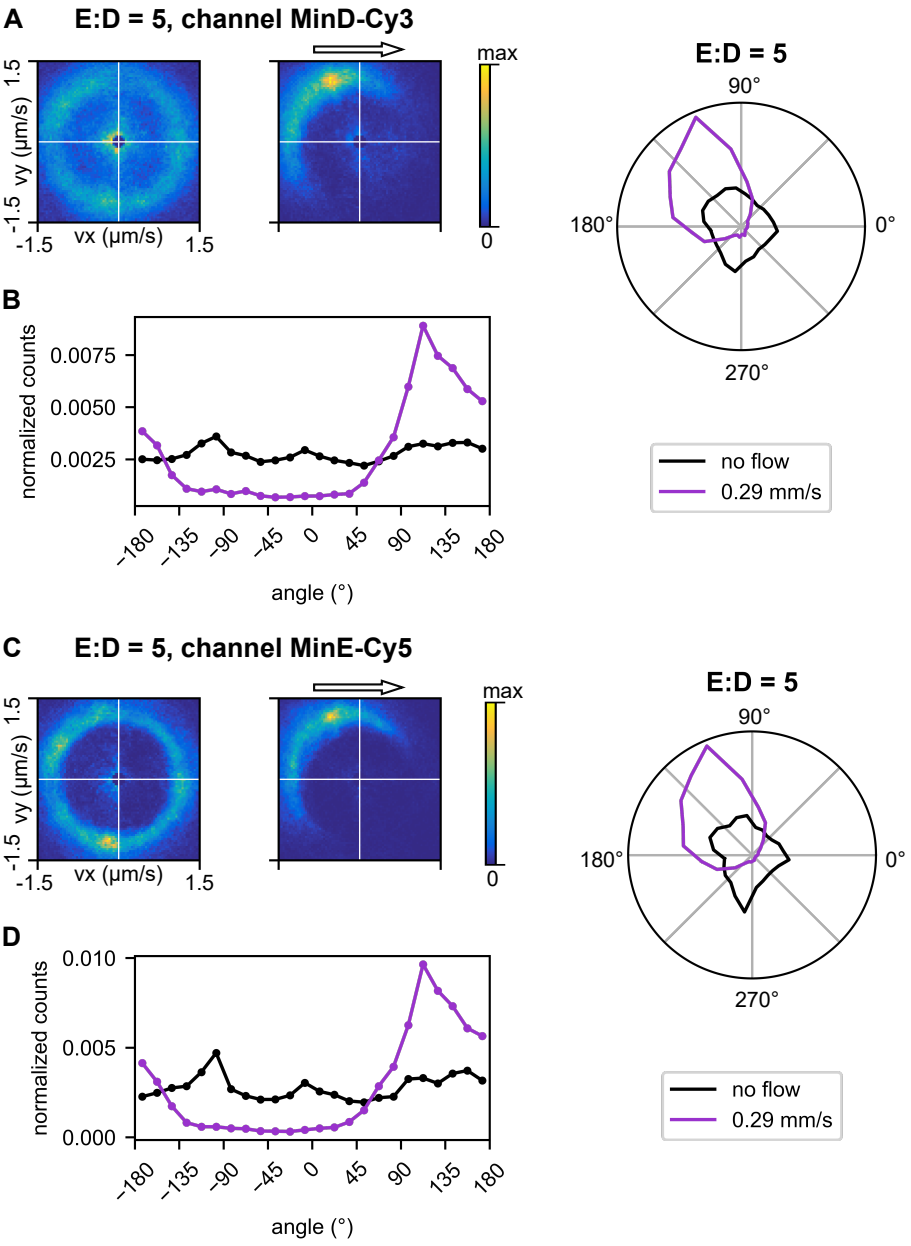


Figure 3.34: Analysis for E:D=5, *wt.5.3.alt* (open flow channel), performed with tools presented in Ref.[43] using general smoothing kernel 24 µm (40 pixels) and flow smoothing kernel 30 µm (50 pixels). Velocity data cropped below 10 % of mean magnitude. **A**, **C** Vector counts per segment for no-flow setting and sequentially applied flow rates as given in the box in **B**, represented as 2D histograms (80 bins in x-/y-direction each), counts per box indicated by color, maximum (yellow) corresponds to maximum bin count for each individual 2D histogram. **B**, **D** 1D histogram and polar histogram representation of counts per direction in bins of 15° for different flow rates.

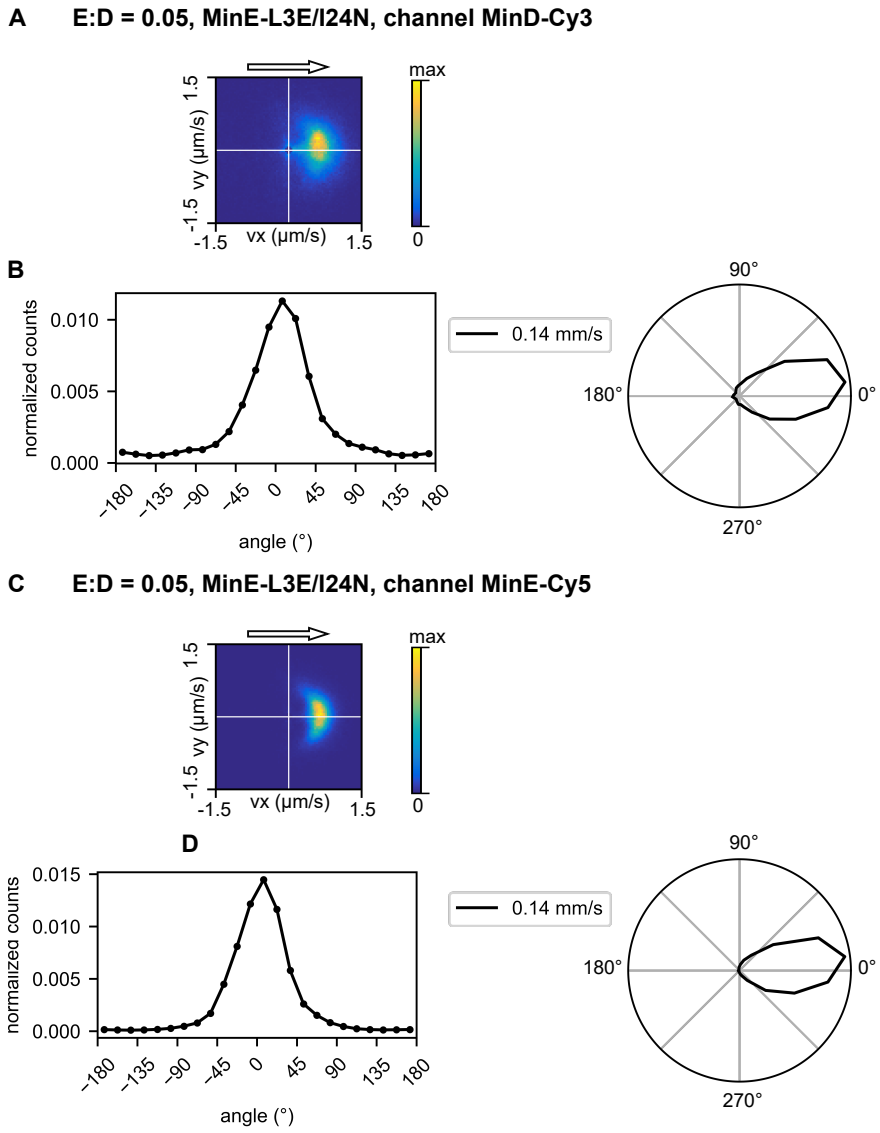


Figure 3.35: Analysis for E:D=0.05, MinE-L3E/I24N, *l3.p05.2* (open flow channel), performed with tools presented in Ref.[43] using general smoothing kernel 12 µm (20 pixels) and flow smoothing kernel 12 µm (20 pixels). One frame recorded every 6 s. Velocity data cropped below 10 % of mean magnitude. **A**, **C** Vector counts per segment for no-flow setting and sequentially applied flow rates as given in the box in **B**, represented as 2D histograms (80 bins in x-/y-direction each), counts per box indicated by color, maximum (yellow) corresponds to maximum bin count for each individual 2D histogram. **B**, **D** 1D histogram and polar histogram representation of counts per direction in bins of 15° for different flow rates. **Important note**: This data was later found to be unsuitable for the velocity analysis performed here, as specified in an Author's Correction (2024), given in section 3.10.

3.9. SUPPLEMENTARY MOVIE CAPTIONS

Six movies are provided along with the main text of the paper. Three of them (movie 1, movie 2, movie 6) contain simulation results, the other three (movie 3, movie 4, movie 5) show exemplary experimental results from the list of acquisitions given in tables 3.3 and 3.4. Movies are provided as mp4 files. The provided movies are:

Supplementary Movie 1 (movie_2.mp4): Simulation result showing upstream propagation, duration 50 s, n_E=1000 µm^2, v_f=50 µm s^{-1}.

Supplementary Movie 2 (movie_1.mp4): Simulation result showing downstream propagation, duration 50 s, n_E=150 µm^2, v_f=50 µm s^{-1}

Supplementary Movie 3 (movie_3.mp4): Experimental results for E:D=10, MinE wildtype, without flow, 0.11 mm s^{-1}, 0.23 mm s^{-1} and 0.23 mm s^{-1} reversed.

Supplementary Movie 4 (movie_4.mp4): Experimental results for E:D=2 (corrected 1.3), MinE wildtype, without flow, 0.21 mm s^{-1}, 0.42 mm s^{-1} and 0.63 mm s^{-1}.

Supplementary Movie 5 (movie_5.mp4): Experimental results for E:D=0.05, MinE L3E/I24N, without flow and 0.15 mm s^{-1}.

Supplementary Movie 6 (movie_6.mp4): Simulation result showing upstream to downstream transition, duration 600 s, n_E=191.4 µm^2. Flow velocity v_f decreases linearly from v_f = 100 µm s^{-1} at t = 0 s, to v_f = 50 µm s^{-1} at t = 100 s, remaining at that value until the end of the simulation.

For numerical simulations, unless specified otherwise, parameters given in Table 3.1 were used, with the units appropriately extended to account for the fact that protein densities have units µm^{-2} in 2D compared to µm^{-1} in a line geometry.

3.10. AUTHOR'S CORRECTION

While the main message of our published paper[58] – that the propagation direction of in vitro Min protein patterns can be controlled by a hydrodynamic flow of the bulk solution – remains unchanged, we discovered that the data of Fig. 3.2C in the paper cannot be used to support this point, due to an undersampling issue in the optical imaging.

When we performed the majority of experiments on how Min protein patterns react to bulk flow, we set an imaging rate of 1 frame per 15 seconds in order to minimize the risk of photodamage from repeatedly imaging the same areas over hours of experimentation. This seemed a reasonable choice, as it captured the features of interest in preliminary experiments performed with MinE-wildtype, and it seemed adequate for the published (0.1 – 0.6 µm/s)[13] and observed (up to 1.5 μm/s) values for the propagation speeds of Min protein patterns. For experiments with MinE-L3E/I24N[23], we obtained velocities which seemed consistent with the results for MinE-wildtype, as shown in Fig. 3.2.

After publication of the work, however, we repeated our experiments with MinE-L3E/I24N at higher sampling rates. These new data showed that the formerly chosen sampling rate under-sampled the speed of the patterns formed by this mutant. Fig. 3.36 shows examples of patterns acquired in new experiments with 1 μM MinD and 0.05 μM MinE-L3E/I24N. Images were now acquired at 1 frame per second. We find that the patterns travel over the length of one wavelength within roughly 20 seconds, meaning that the originally chosen imaging setting (1 frame per 15 seconds) was insufficient. Consequently, the original data for MinE-L3E/I24N in a flow, i.e. Fig. 3.2C and SI Figs. 3.31 and 3.35, were not suitable for reliably extracting the patterns' propagation velocity.

By contrast, the originally chosen frame rate *was* sufficient to capture the propagation velocity of the patterns for the MinE-wildtype. Fig. 3.37 shows examples of patterns acquired in new experiments with 1 μM MinD and 5 μM MinE, now acquired at 1 frame per second. The data show the same result (a decreasing pattern velocity with flow) as in the published Fig. 3.4. To ensure this holds true for other MinE:MinD ratios as well, we performed new experiments for MinE-wildtype and performed a velocity analysis on them, as shown in Fig. 3.38. Based on this newly acquired data, we conclude that the sampling rate chosen for the original data was adequate to capture the features of interest for patterns formed by MinE-wildtype, and the data shown in the publication's Fig. 3.4 (as well as associated SI figures) are not affected.

Fig. 3.39 shows analysis results for additional experiments with MinE-L3E/I24N. Unfortunately, our report that MinE-L3E/I24N patterns only propagate downstream is not supported by these new data, though the initial directional trends already present in the absence of flow hampers an unambiguous interpretation of the automatized analysis. These new findings have implications for the modelling, as they indicate that the original data of Fig. 3.2C cannot be used to support the skeleton model.

In contrast to the statement made in the discussion of the manuscript, conformational

This addendum has been published in Nature Communications **15**, 6522 (2024) by Sabrina MEINDLHUMER, Fridtjof BRAUNS, Jernej Rudi FINŽGAR, Jacob KERSSEMAKERS, Cees DEKKER and Erwin FREY.

switching still appears to be relevant even at low E:D ratios in the experiments. While there are possible candidates for molecular mechanisms not accounted for by the skeleton model that could be responsible for this discrepancy between theory and experiments, a conclusive answer has to await further experimental and theoretical studies.

The data associated with this correction can be found on:
https://zenodo.org/records/11108536 (DOI 10.5281/zenodo.11108536)

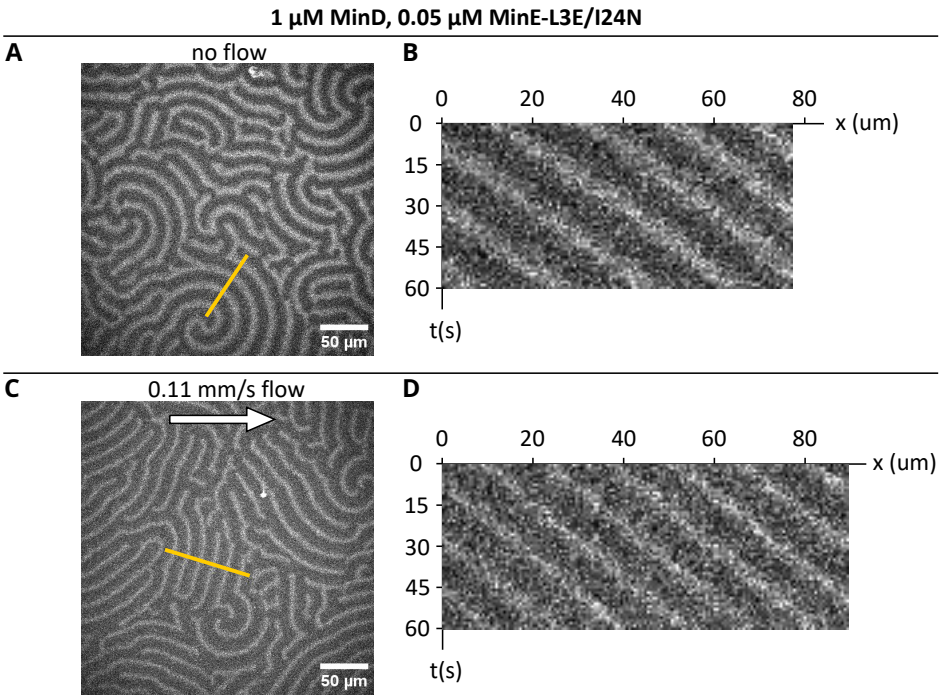


Figure 3.36: Min patterns for 1 μM MinD + 0.05 μM MinE-L3E/I24N. Left shows a single frame; right shows kymographs that were taken at the yellow line indicated at left. **A** Snapshot of pattern without flow. **B** Kymograph of designated line trace without flow. **C** Snapshot of pattern with 0.11 mm/s bulk flow. **D** Kymograph of designated line trace with 0.11 mm/s bulk flow. Flow was applied via use of a syringe pump. Acquisition was started after a waiting time of at least 15 minutes.

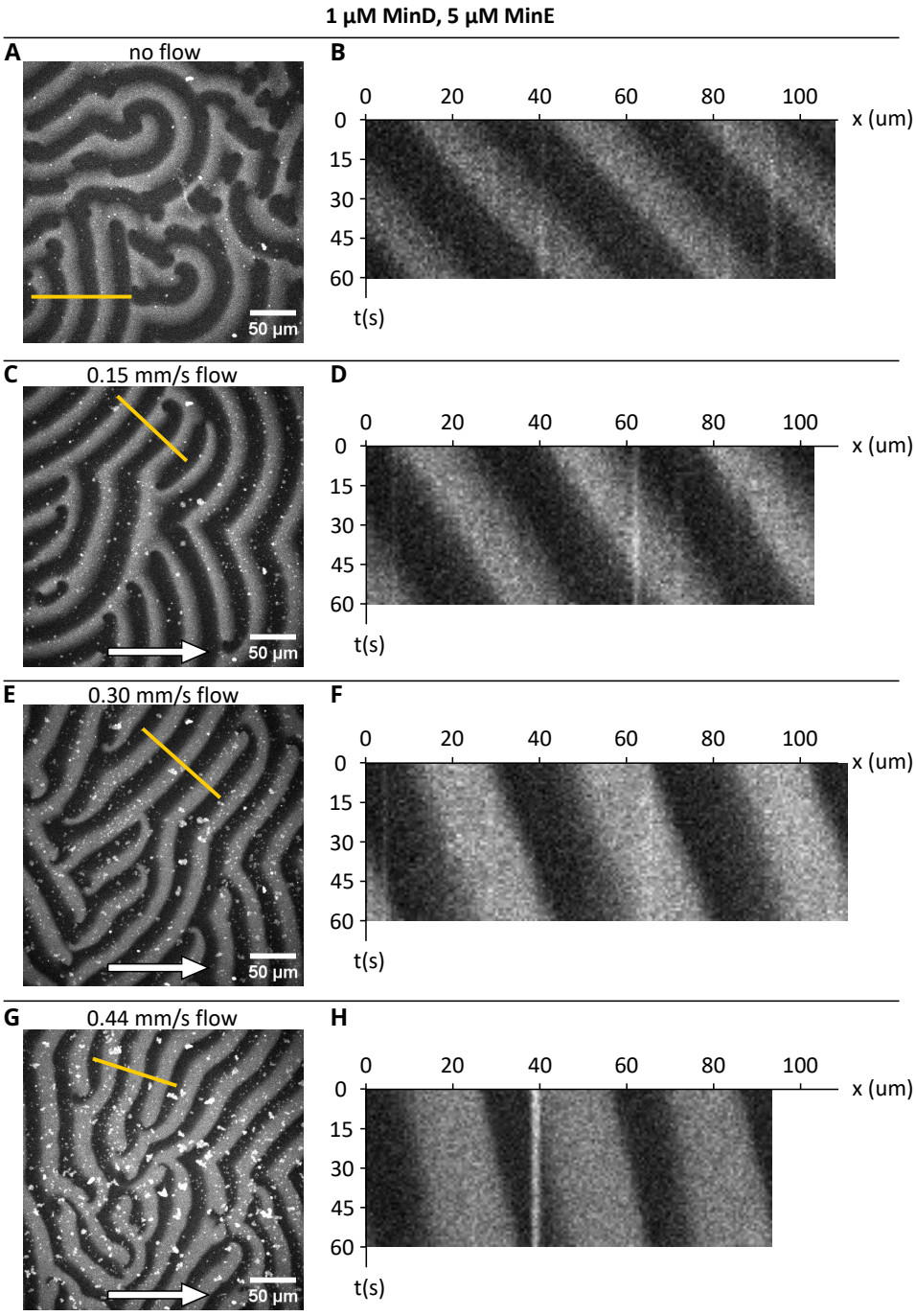


Figure 3.37: Min patterns for 1 μM MinD + 5 μM MinE. From top to bottom: Snapshots of pattern with **A** no flow, followed by increasing flow rates **C** 0.15 mm/s, **E** 0.30 mm/s, **G** 0.44 mm/s. Panels **B**, **D**, **F** and **H** show a kymograph at the line trace indicated in the corresponding image frame on the left. Flow was applied via a peristaltic pump through a closed-circle system. Acquisition was started after a waiting time of at least 15 minutes after changing the flow rate.

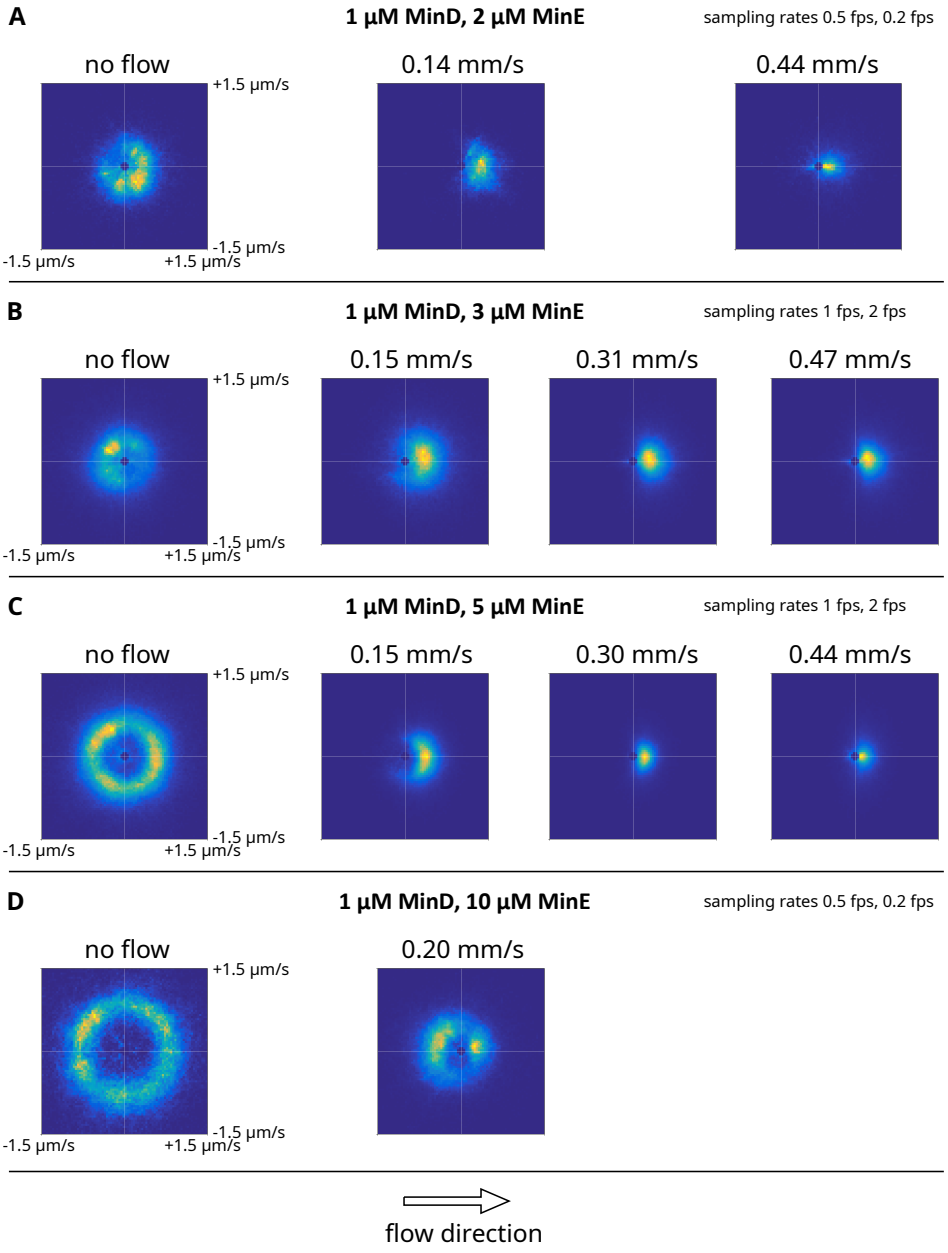


Figure 3.38: Repetition of experiments for MinE-wildtype with 1 μM MinD. **A** Data for 2 μM MinE. **B** Idem 3 μM MinE. **C** Idem 5 μM MinE. **D** Idem 10 μM MinE. Data shown are velocity analyses based on averaging over multiple individual field-of-views within the sample channel. Analysis was based on image data for MinD-Cy3.

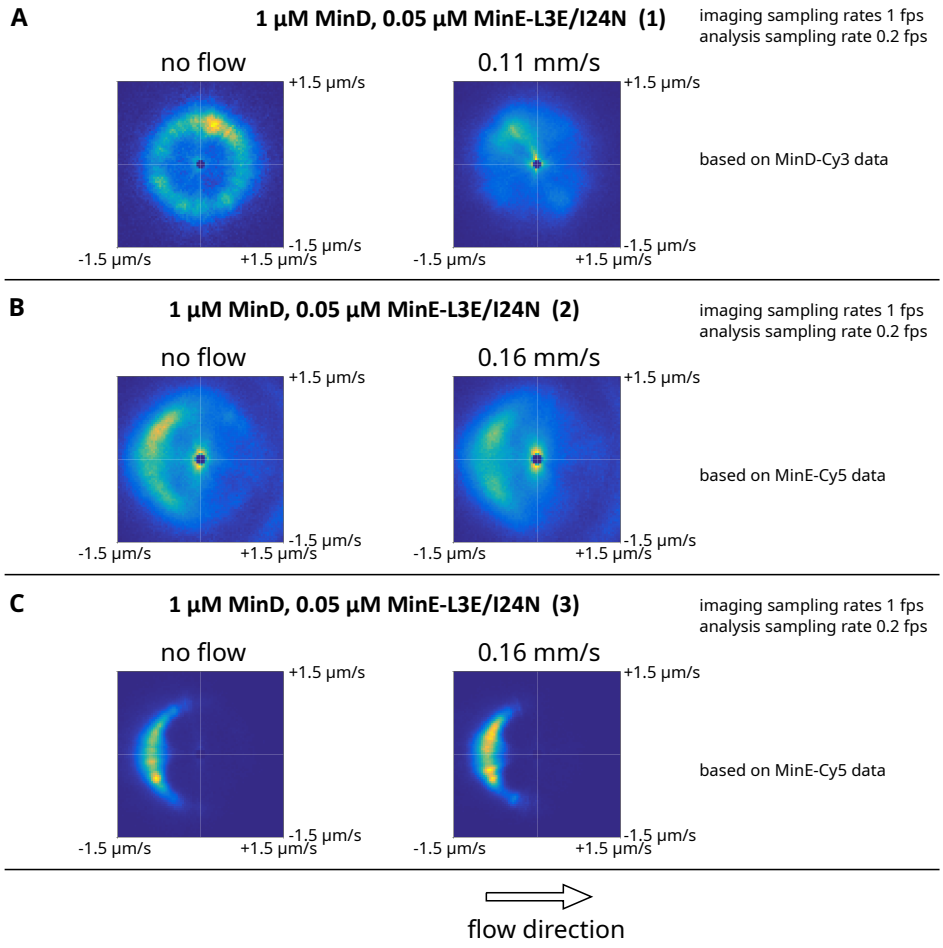


Figure 3.39: Repetition of individual experiments for MinE-L3E/I24N and associated velocity analysis, averaged over multiple individual field-of-views within the sample channel. **A**, **B**, and **C** are three independent experiments.

REFERENCES

[1] J. Halatek, F. Brauns, and E. Frey. "Self-organization principles of intracellular pattern formation". In: *Philosophical Transactions of the Royal Society B: Biological Sciences* 373.1747 (May 26, 2018), p. 20170107. ISSN: 0962-8436, 1471-2970. DOI: 10.1098/rstb.2017.0107. URL: https://royalsocietypublishing.org/doi/10.1098/rstb.2017.0107 (visited on 11/22/2019).

[2] Simon Kretschmer and Petra Schwille. "Pattern formation on membranes and its role in bacterial cell division". In: *Current Opinion in Cell Biology* 38 (Feb. 2016), pp. 52–59. ISSN: 09550674. DOI: 10.1016/j.ceb.2016.02.005. URL: https://linkinghub.elsevier.com/retrieve/pii/S0955067416300126 (visited on 11/22/2019).

[3] Lukas Wettmann and Karsten Kruse. "The Min-protein oscillations in *Escherichia coli*: an example of self-organized cellular protein waves". In: *Philosophical Transactions of the Royal Society B: Biological Sciences* 373.1747 (May 26, 2018), p. 20170111. ISSN: 0962-8436, 1471-2970. DOI: 10.1098/rstb.2017.0111. URL: https://royalsocietypublishing.org/doi/10.1098/rstb.2017.0111 (visited on 12/01/2021).

[4] François Schweisguth and Francis Corson. "Self-Organization in Pattern Formation". In: *Developmental Cell* 49.5 (June 2019), pp. 659–677. ISSN: 15345807. DOI: 10.1016/j.devcel.2019.05.019. URL: https://linkinghub.elsevier.com/retrieve/pii/S1534580719303910 (visited on 01/08/2020).

[5] Shigeru Kondo, Masakatsu Watanabe, and Seita Miyazawa. "Studies of Turing pattern formation in zebrafish skin". In: *Philosophical Transactions of the Royal Society A: Mathematical, Physical and Engineering Sciences* 379.2213 (Dec. 27, 2021), p. 20200274. ISSN: 1364-503X, 1471-2962. DOI: 10.1098/rsta.2020.0274. URL: https://royalsocietypublishing.org/doi/10.1098/rsta.2020.0274 (visited on 12/09/2021).

[6] Victor Hatini and Stephen DiNardo. "Divide and conquer: pattern formation in Drosophila embryonic epidermis". In: *Trends in Genetics* 17.10 (Oct. 2001), pp. 574–579. ISSN: 01689525. DOI: 10.1016/S0168-9525(01)02448-9. URL: https://linkinghub.elsevier.com/retrieve/pii/S0168952501024489 (visited on 12/09/2021).

[7] Erwin Frey et al. "Protein Pattern Formation". In: *Physics of Biological Membranes*. Ed. by Patricia Bassereau and Pierre Sens. Cham: Springer International Publishing, 2018, pp. 229–260. ISBN: 978-3-030-00628-0 978-3-030-00630-3. DOI: 10.1007/978-3-030-00630-3_10. URL: http://link.springer.com/10.1007/978-3-030-00630-3_10 (visited on 10/14/2021).

[8] J. Halatek and E. Frey. "Rethinking pattern formation in reaction–diffusion systems". In: *Nature Physics* 14.5 (May 2018), pp. 507–514. ISSN: 1745-2473, 1745-2481. DOI: 10.1038/s41567-017-0040-5. URL: http://www.nature.com/articles/s41567-017-0040-5 (visited on 11/27/2019).

[9] Jaime Agudo-Canalejo, Pierre Illien, and Ramin Golestanian. “Cooperatively enhanced reactivity and “stabilitaxis” of dissociating oligomeric proteins”. In: *Proceedings of the National Academy of Sciences* 117.22 (June 2, 2020), pp. 11894–11900. ISSN: 0027-8424, 1091-6490. DOI: 10.1073/pnas.1919635117. URL: http://www.pnas.org/lookup/doi/10.1073/pnas.1919635117 (visited on 12/23/2021).

[10] Manon C. Wigbers et al. “Flow Induced Symmetry Breaking in a Conceptual Polarity Model”. In: *Cells* 9.6 (June 23, 2020), p. 1524. ISSN: 2073-4409. DOI: 10.3390/cells9061524. URL: https://www.mdpi.com/2073-4409/9/6/1524 (visited on 11/17/2021).

[11] Tom Burkart et al. “Control of protein-based pattern formation via guiding cues”. In: *Nature Reviews Physics* (May 16, 2022). ISSN: 2522-5820. DOI: 10.1038/s42254-022-00461-3. URL: https://www.nature.com/articles/s42254-022-00461-3 (visited on 05/25/2022).

[12] Dominik Thalmeier, Jacob Halatek, and Erwin Frey. “Geometry-induced protein pattern formation”. In: *Proceedings of the National Academy of Sciences* 113.3 (Jan. 19, 2016), pp. 548–553. ISSN: 0027-8424, 1091-6490. DOI: 10.1073/pnas.1515191113. URL: http://www.pnas.org/lookup/doi/10.1073/pnas.1515191113 (visited on 01/08/2020).

[13] Beatrice Ramm, Tamara Heermann, and Petra Schwille. “The E. coli MinCDE system in the regulation of protein patterns and gradients”. In: *Cellular and Molecular Life Sciences* 76.21 (Nov. 2019), pp. 4245–4273. ISSN: 1420-682X, 1420-9071. DOI: 10.1007/s00018-019-03218-x. URL: http://link.springer.com/10.1007/s00018-019-03218-x (visited on 11/22/2019).

[14] Phillip Nußbaum et al. “An Oscillating MinD Protein Determines the Cellular Positioning of the Motility Machinery in Archaea”. In: *Current Biology* (Oct. 2020), S0960982220314433. ISSN: 09609822. DOI: 10.1016/j.cub.2020.09.073. URL: https://linkinghub.elsevier.com/retrieve/pii/S0960982220314433 (visited on 11/12/2020).

[15] Simon Kretschmer et al. “Synthetic cell division via membrane-transforming molecular assemblies”. In: *BMC Biology* 17.1 (Dec. 2019), p. 43. ISSN: 1741-7007. DOI: 10.1186/s12915-019-0665-1. URL: https://bmcbiol.biomedcentral.com/articles/10.1186/s12915-019-0665-1 (visited on 11/22/2019).

[16] Paola Bisicchia et al. “MinC, MinD, and MinE Drive Counter-oscillation of Early-Cell-Division Proteins Prior to Escherichia coli Septum Formation”. In: *mBio* 4.6 (Dec. 31, 2013). Ed. by Susan Gottesman. ISSN: 2161-2129, 2150-7511. DOI: 10.1128/mBio.00856-13. URL: https://journals.asm.org/doi/10.1128/mBio.00856-13 (visited on 10/15/2021).

[17] Jacob Halatek and Erwin Frey. “Highly Canalized MinD Transfer and MinE Sequestration Explain the Origin of Robust MinCDE-Protein Dynamics”. In: *Cell Reports* 1.6 (June 2012), pp. 741–752. ISSN: 22111247. DOI: 10.1016/j.celrep.2012.04.005. URL: https://linkinghub.elsevier.com/retrieve/pii/S2211124712001180 (visited on 10/15/2021).

[18] Laeschkir Würthner et al. “Bridging scales in a multiscale pattern-forming system”. In: *Proceedings of the National Academy of Sciences* 119.33 (Aug. 16, 2022), e2206888119. ISSN: 0027-8424, 1091-6490. DOI: 10.1073/pnas.2206888119. URL: https://pnas.org/doi/full/10.1073/pnas.2206888119 (visited on 11/02/2022).

[19] Fridtjof Brauns et al. “Bulk-surface coupling identifies the mechanistic connection between Min-protein patterns in vivo and in vitro”. In: *Nature Communications* 12.1 (Dec. 2021), p. 3312. ISSN: 2041-1723. DOI: 10.1038/s41467-021-23412-5. URL: http://www.nature.com/articles/s41467-021-23412-5 (visited on 06/03/2021).

[20] V. Ivanov and K. Mizuuchi. “Multiple modes of interconverting dynamic pattern formation by bacterial cell division proteins”. In: *Proceedings of the National Academy of Sciences* 107.18 (May 4, 2010), pp. 8071–8078. ISSN: 0027-8424, 1091-6490. DOI: 10.1073/pnas.0911036107. URL: http://www.pnas.org/cgi/doi/10.1073/pnas.0911036107 (visited on 11/29/2019).

[21] Kiyoshi Mizuuchi and Anthony G Vecchiarelli. “Mechanistic insights of the Min oscillator via cell-free reconstitution and imaging”. In: *Physical Biology* 15.3 (Mar. 1, 2018), p. 031001. ISSN: 1478-3975. DOI: 10.1088/1478-3975/aa9e5e. URL: http://stacks.iop.org/1478-3975/15/i=3/a=031001?key=crossref.18bf29cccb7b7223b142cdbecfc43d0d (visited on 11/22/2019).

[22] Martin Loose et al. “Min protein patterns emerge from rapid rebinding and membrane interaction of MinE”. In: *Nature Structural & Molecular Biology* 18.5 (May 2011), pp. 577–583. ISSN: 1545-9993, 1545-9985. DOI: 10.1038/nsmb.2037. URL: http://www.nature.com/articles/nsmb.2037 (visited on 11/22/2019).

[23] Jonas Denk et al. “MinE conformational switching confers robustness on self-organized Min protein patterns”. In: *Proceedings of the National Academy of Sciences* 115.18 (May 1, 2018), pp. 4553–4558. ISSN: 0027-8424, 1091-6490. DOI: 10.1073/pnas.1719801115. URL: http://www.pnas.org/lookup/doi/10.1073/pnas.1719801115 (visited on 07/28/2020).

[24] Anthony G. Vecchiarelli et al. “Differential affinities of MinD and MinE to anionic phospholipid influence Min patterning dynamics *in vitro*: Flow and lipid composition effects on Min patterning”. In: *Molecular Microbiology* 93.3 (Aug. 2014), pp. 453–463. ISSN: 0950382X. DOI: 10.1111/mmi.12669. URL: http://doi.wiley.com/10.1111/mmi.12669 (visited on 11/29/2019).

[25] Tamara Heermann et al. “Local Self-Enhancement of MinD Membrane Binding in Min Protein Pattern Formation”. In: *Journal of Molecular Biology* 432.10 (May 2020), pp. 3191–3204. ISSN: 00222836. DOI: 10.1016/j.jmb.2020.03.012. URL: https://linkinghub.elsevier.com/retrieve/pii/S0022283620302333 (visited on 10/14/2021).

[26] Tamara Heermann et al. “Mass-sensitive particle tracking to elucidate the membrane-associated MinDE reaction cycle”. In: *Nature Methods* 18.10 (Oct. 2021), pp. 1239–1246. ISSN: 1548-7091, 1548-7105. DOI: 10.1038/s41592-021-01260-x. URL:

https://www.nature.com/articles/s41592-021-01260-x (visited on 10/15/2021).

[27] Anthony G. Vecchiarelli et al. "Membrane-bound MinDE complex acts as a toggle switch that drives Min oscillation coupled to cytoplasmic depletion of MinD". In: *Proceedings of the National Academy of Sciences* 113.11 (Mar. 15, 2016), E1479–E1488. ISSN: 0027-8424, 1091-6490. DOI: 10.1073/pnas.1600644113. URL: http://www.pnas.org/lookup/doi/10.1073/pnas.1600644113 (visited on 11/22/2019).

[28] Philipp Glock and Petra Schwille. "Switching protein patterns on membranes". In: *Current Opinion in Colloid & Interface Science* 38 (Nov. 2018), pp. 100–107. ISSN: 13590294. DOI: 10.1016/j.cocis.2018.10.004. URL: https://linkinghub.elsevier.com/retrieve/pii/S135902941830044X (visited on 11/22/2019).

[29] Katja Zieske, Jakob Schweizer, and Petra Schwille. "Surface topology assisted alignment of Min protein waves". In: *FEBS Letters* 588.15 (Aug. 1, 2014), pp. 2545–2549. ISSN: 00145793. DOI: 10.1016/j.febslet.2014.06.026. URL: http://doi.wiley.com/10.1016/j.febslet.2014.06.026 (visited on 01/14/2020).

[30] Yaron Caspi and Cees Dekker. "Mapping out Min protein patterns in fully confined fluidic chambers". In: *eLife* 5 (Nov. 25, 2016), e19271. ISSN: 2050-084X. DOI: 10.7554/eLife.19271. URL: https://elifesciences.org/articles/19271 (visited on 11/22/2019).

[31] Beatrice Ramm et al. "A diffusiophoretic mechanism for ATP-driven transport without motor proteins". In: *Nature Physics* 17.7 (July 2021), pp. 850–858. ISSN: 1745-2473, 1745-2481. DOI: 10.1038/s41567-021-01213-3. URL: http://www.nature.com/articles/s41567-021-01213-3 (visited on 10/05/2021).

[32] Philipp Glock et al. "Optical Control of a Biological Reaction-Diffusion System". In: *Angewandte Chemie* 130.9 (Feb. 23, 2018), pp. 2386–2390. ISSN: 00448249. DOI: 10.1002/ange.201712002. URL: http://doi.wiley.com/10.1002/ange.201712002 (visited on 11/22/2019).

[33] Thomas Litschel et al. "Beating Vesicles: Encapsulated Protein Oscillations Cause Dynamic Membrane Deformations". In: *Angewandte Chemie International Edition* 57.50 (Dec. 10, 2018), pp. 16286–16290. ISSN: 14337851. DOI: 10.1002/anie.201808750. URL: http://doi.wiley.com/10.1002/anie.201808750 (visited on 11/22/2019).

[34] Elisa Godino et al. "De novo synthesized Min proteins drive oscillatory liposome deformation and regulate FtsA-FtsZ cytoskeletal patterns". In: *Nature Communications* 10.1 (Dec. 2019), p. 4969. ISSN: 2041-1723. DOI: 10.1038/s41467-019-12932-w. URL: http://www.nature.com/articles/s41467-019-12932-w (visited on 09/28/2020).

[35] Rukshala Illukkumbura, Tom Bland, and Nathan W. Goehring. "Patterning and polarization of cells by intracellular flows". In: *Current Opinion in Cell Biology* 62 (Feb. 2020), pp. 123–134. ISSN: 09550674. DOI: 10.1016/j.ceb.2019.10.005. URL: https://linkinghub.elsevier.com/retrieve/pii/S0955067419300924 (visited on 10/15/2021).

[36] Edwin Munro, Jeremy Nance, and James R. Priess. "Cortical Flows Powered by Asymmetrical Contraction Transport PAR Proteins to Establish and Maintain Anterior-Posterior Polarity in the Early C. elegans Embryo". In: *Developmental Cell* 7.3 (Sept. 2004), pp. 413–424. ISSN: 15345807. DOI: 10.1016/j.devcel.2004.08.001. URL: https://linkinghub.elsevier.com/retrieve/pii/S153458070400276X (visited on 10/17/2021).

[37] Nathan W. Goehring et al. "Polarization of PAR Proteins by Advective Triggering of a Pattern-Forming System". In: *Science* 334.6059 (Nov. 25, 2011), pp. 1137–1141. ISSN: 0036-8075, 1095-9203. DOI: 10.1126/science.1208619. URL: https://www.science.org/doi/10.1126/science.1208619 (visited on 12/23/2021).

[38] Peter Gross et al. "Guiding self-organized pattern formation in cell polarity establishment". In: *Nature Physics* 15.3 (Mar. 2019), pp. 293–300. ISSN: 1745-2473, 1745-2481. DOI: 10.1038/s41567-018-0358-7. URL: http://www.nature.com/articles/s41567-018-0358-7 (visited on 10/17/2021).

[39] R. Niwayama, K. Shinohara, and A. Kimura. "Hydrodynamic property of the cytoplasm is sufficient to mediate cytoplasmic streaming in the Caenorhabiditis elegans embryo". In: *Proceedings of the National Academy of Sciences* 108.29 (July 19, 2011), pp. 11900–11905. ISSN: 0027-8424, 1091-6490. DOI: 10.1073/pnas.1101853108. URL: http://www.pnas.org/cgi/doi/10.1073/pnas.1101853108 (visited on 10/17/2021).

[40] Kerwyn Casey Huang, Yigal Meir, and Ned S. Wingreen. "Dynamic structures in *Escherichia coli* : Spontaneous formation of MinE rings and MinD polar zones". In: *Proceedings of the National Academy of Sciences* 100.22 (Oct. 28, 2003), pp. 12724–12728. ISSN: 0027-8424, 1091-6490. DOI: 10.1073/pnas.2135445100. URL: https://pnas.org/doi/full/10.1073/pnas.2135445100 (visited on 05/20/2022).

[41] Arkady B. Rovinsky and Michael Menzinger. "Chemical instability induced by a differential flow". In: *Physical Review Letters* 69.8 (Aug. 24, 1992), pp. 1193–1196. ISSN: 0031-9007. DOI: 10.1103/PhysRevLett.69.1193. URL: https://link.aps.org/doi/10.1103/PhysRevLett.69.1193 (visited on 10/15/2021).

[42] A Gholami et al. "Flow-driven instabilities during pattern formation of *Dictyostelium discoideum*". In: *New Journal of Physics* 17.6 (June 8, 2015), p. 063007. ISSN: 1367-2630. DOI: 10.1088/1367-2630/17/6/063007. URL: https://iopscience.iop.org/article/10.1088/1367-2630/17/6/063007 (visited on 12/23/2021).

[43] Sabrina Meindlhumer, Jacob Kerssemakers, and Cees Dekker. "Quantitative analysis of surface wave patterns of Min proteins". In: *Frontiers in Physics* 10 (Aug. 3, 2022), p. 930811. ISSN: 2296-424X. DOI: 10.3389/fphy.2022.930811. URL: https://www.frontiersin.org/articles/10.3389/fphy.2022.930811/full (visited on 09/19/2022).

[44] Manon C. Wigbers et al. "Pattern localization to a domain edge". In: *Physical Review E* 101.2 (Feb. 18, 2020), p. 022414. ISSN: 2470-0045, 2470-0053. DOI: 10.1103/PhysRevE.101.022414. URL: https://link.aps.org/doi/10.1103/PhysRevE.101.022414 (visited on 11/17/2021).

[45] R. E. Goldstein, I. Tuval, and J.-W. van de Meent. “Microfluidics of cytoplasmic streaming and its implications for intracellular transport”. In: *Proceedings of the National Academy of Sciences* 105.10 (Mar. 11, 2008), pp. 3663–3667. ISSN: 0027-8424, 1091-6490. DOI: 10.1073/pnas.0707223105. URL: http://www.pnas.org/cgi/doi/10.1073/pnas.0707223105 (visited on 12/11/2021).

[46] Esteban Hoijman et al. “Mitotic cell rounding and epithelial thinning regulate lumen growth and shape”. In: *Nature Communications* 6.1 (Nov. 2015), p. 7355. ISSN: 2041-1723. DOI: 10.1038/ncomms8355. URL: http://www.nature.com/articles/ncomms8355 (visited on 12/11/2021).

[47] Agnik Dasgupta et al. “Cell volume changes contribute to epithelial morphogenesis in zebrafish Kupffer’s vesicle”. In: *eLife* 7 (Jan. 29, 2018), e30963. ISSN: 2050-084X. DOI: 10.7554/eLife.30963. URL: https://elifesciences.org/articles/30963 (visited on 12/11/2021).

[48] Andrew B. Goryachev and Marcin Leda. “Many roads to symmetry breaking: molecular mechanisms and theoretical models of yeast cell polarity”. In: *Molecular Biology of the Cell* 28.3 (Feb. 2017). Ed. by William Bement, pp. 370–380. ISSN: 1059-1524, 1939-4586. DOI: 10.1091/mbc.e16-10-0739. URL: https://www.molbiolcell.org/doi/10.1091/mbc.e16-10-0739 (visited on 10/19/2021).

[49] Andrew B. Goryachev and Marcin Leda. “Compete or Coexist? Why the Same Mechanisms of Symmetry Breaking Can Yield Distinct Outcomes”. In: *Cells* 9.9 (Sept. 1, 2020), p. 2011. ISSN: 2073-4409. DOI: 10.3390/cells9092011. URL: https://www.mdpi.com/2073-4409/9/9/2011 (visited on 10/19/2021).

[50] Mike Bonny et al. “Membrane Binding of MinE Allows for a Comprehensive Description of Min-Protein Pattern Formation”. In: *PLoS Computational Biology* 9.12 (Dec. 5, 2013). Ed. by Lawrence Rothfield, e1003347. ISSN: 1553-7358. DOI: 10.1371/journal.pcbi.1003347. URL: https://dx.plos.org/10.1371/journal.pcbi.1003347 (visited on 11/17/2021).

[51] Martin Loose et al. “Spatial Regulators for Bacterial Cell Division Self-Organize into Surface Waves in Vitro”. In: *Science* 320.5877 (May 9, 2008), pp. 789–792. ISSN: 0036-8075, 1095-9203. DOI: 10.1126/science.1154413. URL: https://www.science.org/doi/10.1126/science.1154413 (visited on 11/17/2021).

[52] Justin S. Bois, Frank Jülicher, and Stephan W. Grill. “Pattern Formation in Active Fluids”. In: *Physical Review Letters* 106.2 (Jan. 13, 2011), p. 028103. ISSN: 0031-9007, 1079-7114. DOI: 10.1103/PhysRevLett.106.028103. URL: https://link.aps.org/doi/10.1103/PhysRevLett.106.028103 (visited on 12/23/2021).

[53] Torsten Eckstein et al. “Influence of fast advective flows on pattern formation of Dictyostelium discoideum”. In: *PLOS ONE* 13.3 (Mar. 28, 2018). Ed. by Jun Ma, e0194859. ISSN: 1932-6203. DOI: 10.1371/journal.pone.0194859. URL: https://dx.plos.org/10.1371/journal.pone.0194859 (visited on 12/23/2021).

[54] Torsten Eckstein, Estefania Vidal-Henriquez, and Azam Gholami. "Experimental observation of boundary-driven oscillations in a reaction–diffusion–advection system". In: *Soft Matter* 16.17 (2020), pp. 4243–4255. ISSN: 1744-683X, 1744-6848. DOI: 10.1039/C9SM02291K. URL: http://xlink.rsc.org/?DOI=C9SM02291K (visited on 12/23/2021).

[55] Guido Van Rossum and Fred L. Drake. *Python 3 Reference Manual*. Scotts Valley, CA: CreateSpace, 2009. ISBN: 1441412697.

[56] Johannes Schindelin et al. "Fiji: an open-source platform for biological-image analysis". In: *Nature Methods* 9.7 (July 2012), pp. 676–682. ISSN: 1548-7091, 1548-7105. DOI: 10.1038/nmeth.2019. URL: http://www.nature.com/articles/nmeth.2019 (visited on 11/19/2021).

[57] Berthold K. P. Horn and Brian G. Schunck. "Determining optical flow". In: *Artificial Intelligence* 17.1 (1981), pp. 185–203. ISSN: 0004-3702. DOI: https://doi.org/10.1016/0004-3702(81)90024-2. URL: https://www.sciencedirect.com/science/article/pii/0004370281900242.

[58] Sabrina Meindlhumer et al. "Directing Min protein patterns with advective bulk flow". In: *Nature Communications* 14.1 (Jan. 27, 2023), p. 450. ISSN: 2041-1723. DOI: 10.1038/s41467-023-35997-0. URL: https://www.nature.com/articles/s41467-023-35997-0 (visited on 03/25/2023).

4

QUANTIFYING THE EFFECT OF MINE MEMBRANE BINDING ON PATTERN FORMATION

Though the Min system is routinely referred to as the best-studied system for intracellular pattern formation, its inner working mechanism still poses fundamental questions. Strikingly, there still is a significant quantitative mismatch between simulation results and in vitro experimental measurements, in particular when it comes to the characteristic length of the pattern. This signals a lack of full understanding of the inner mechanism that drives Min patterns. Recent findings suggest that the inclusion and investigation of persistent membrane binding of MinE might be the critical element in finally achieving congruence between predicted and observed patterns. This membrane binding potentially occurs with different probabilities in vivo and in vitro, making it crucial to reconciling observations from these two settings within a single model.

Here, we summarize the current status of an ongoing project to investigate this. This project is carried out in collaboration with the theoretical biophysics group of Erwin Frey. This chapter focuses on the experimental aspects of the project, as we present new data on Min patterns formed by wildtype MinE and by a mutant MinE with diminished membrane-binding capabilities.

This chapter contains contributions from Sabrina MEINDLHUMER, Jacob KERSSEMAKERS, Henrik WEYER, Mingqi YAN, Erwin FREY and Cees DEKKER.

4.1. INTRODUCTION

4.1.1. BACKGROUND & MOTIVATION

Intracellular pattern formation is known to fulfill a range of vital tasks in eukaryotic and prokaryotic cells alike.[1] The Min protein system of *E. coli* is often referred to as the best-studied system in the field of intracellular pattern formation, and for a good reason: After the first observation of *E. coli* "minicells" – resulting from deletion of what would later be called "Min" proteins – in 1967 by Adler et al.[2], studies on Min gained momentum since around the year 2000. This led to a series of longstanding and fruitful collaborations between experimental and theoretical groups, who shared an interest in elucidating the mechanisms underlying the intriguing pole-to-pole-oscillations observed in live cells.[3, 4] Following the first reconstitution of Min proteins on planar lipid bilayers in 2008 by Loose et al.[5], Min research was greatly enriched by the option of directly comparing *in vitro* experiments to their corresponding *in silico* simulation outcomes.[6, 7]

This research effort was enabled by the beneficial fact that the Min protein system presents itself as rather minimalistic, requiring the action of only two proteins MinD and MinE plus ATP (see Fig. 4.1A for an illustration of its core principles). This minimalism becomes particularly apparent when the Min system is compared to other intracellular pattern forming systems, such as the Cdc42 system from *S. cerevisiae*, which requires the action of seven proteins (including regulatory and scaffolding proteins), all of which need to be successfully purified for a comprehensive reconstitution.[1, 8]

The Min system with its two essential components (MinD and MinE) is therefore particularly appealing from both the theoretical and experimental point of view. Thanks to the combined efforts of theoretical and experimental science, we now have a fairly good understanding of how Min proteins interact with each other to form these mesmerizing, semi-periodic patterns that one can observe on a lipid bilayer. Relating experimental data to models and incrementally improving them helped us to learn a lot about the molecular details and mechanistic processes underlying the interaction of MinD and MinE.[6, 7].

However, despite significant efforts over more than two decades, a surprisingly large number of open questions on the Min system remain to this day. One aspect that turned out to be particularly puzzling is the lack of congruence between simulation and *in vitro* experimental results when it comes to *quantitative* properties of Min patterns. Quite consistently, simulation results indicate that patterns occur on a scale of a few micrometers, while experimentally observed patterns typically exhibit wavelengths of 50 micrometers and higher.[9, 10] The ongoing search for means to resolve this discrepancy was a main motivation for the experiments presented in this chapter.

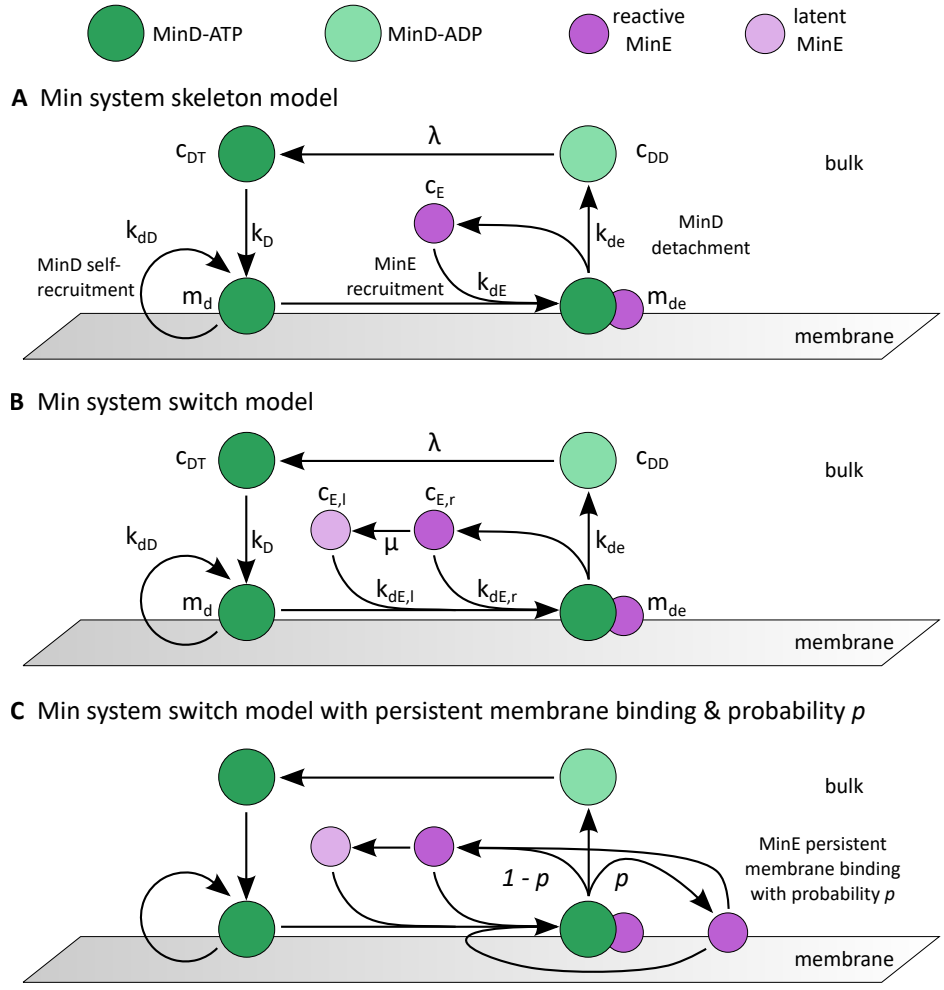


Figure 4.1: **Min models.** **A** The skeleton model describes a cycle of membrane attachment and detachment for MinD, with the latter stimulated by MinE. MinD cooperatively recruits more MinD to the membrane in its immediate vicinity, creating a feedback loop that enables surface pattern formation. Subscripts d and e denote parameters referring to membrane-bound MinD and MinE respectively, while D and E refer to MinD and MinE in bulk. Accordingly, m_d and m_{de} denote the membrane densities of MinD and complexed MinD-MinE, while c_E denotes MinE in bulk. For MinD, a distinction is made between MinD-ADP (c_{DD}) and MinD-ATP (c_{DT}), connected by an ATP-exchange rate λ. Kinetic rates k describe how proteins transition from one state to another: MinD initially binds to the membrane at a rate k_D, after which membrane-bound MinD recruits MinD from the bulk at a rate k_{dD}. MinE is recruited by membrane-bound MinD at a rate k_{dE}, then stimulates ATP-hydrolysis, upon which it detaches from the membrane along with MinD-ADP at a rate k_{de}. *Caption continues on next page.*

Figure 4.1: **B** The switch model extends the skeleton model by the introduction of a latent state of MinE in bulk, which it assumes shortly after membrane-release. The model from A is therefore extended by MinE in bulk undergoing a conformational switch from the reactive state $c_{E,r}$ to the latent state $c_{E,l}$ at a rate μ. Reactive and latent MinE are recruited to the membrane at different rates, $k_{dE,r}$ and $k_{dE,l}$ respectively, with $k_{dE,r} > k_{dE,l}$. **C** An extension of the switch model which permits persistent membrane binding of MinE occurring with probability p. Notably, this parameter p may assume different values *in vivo* and *in vitro*. The parameters from B still apply, yet are not explicitly denoted for simplicity.

4.1.2. RECENT ADVANCES

One of the more recent developments in modeling the mechanism underlying Min protein pattern formation is the discovery of the so-called "MinE switch", which led to the development of what was called the "Switch model".[11] This term refers to the capacity of MinE to undergo a conformational change while in bulk, switching from a highly reactive state into a latent state shortly after detaching from the membrane, as illustrated in Fig. 4.1B. In this latent state, MinE's affinity for re-attaching is reduced, effectively leading to slower reaction kinetics for the next cycle of MinE associating with membrane-bound MinD.[11]

This finding expanded the equations describing the MinD-MinE reaction cycle, as it introduced latent MinE as a species separate from reactive MinE, with its own set of kinetic parameters. It was shown experimentally and theoretically that the existence of the MinE switch vastly broadens the parameter regime (MinD/MinE ratio) in which pattern formation is possible.[11] Introducing an I24N mutation in MinE, which locks it in its reactive state, allowed for pattern formation only within a very constricted range of MinD/MinE ratios. This indicates that the MinE switch provides the overall system with robustness towards parameter changes. Therefore, the MinE switch likely presents an evolutionary benefit, allowing bacteria to split evenly, even if variations in the intracellular MinD/MinE ratio occur.[11]

The most given example of Min patterns is the "Min spiral", a dynamic pattern which is composed of traveling wave fronts that are circling as a spiral around an anchoring point. Dynamic patterns – such as spirals and linear traveling waves – captured the interest of researchers early on,[5] not only due to their intriguing aesthetics, but because their variation in properties allowed for systematic studies.[12, 13] The concentrations of MinD and MinE (and notably, their ratio) determine observables such as the wavelength and propagation speed. However, while these Min patterns having been studied over a large range of parameters, traveling waves only constitute one of many types of patterns that Min proteins are able to form. For very high protein concentrations, static patterns referred to as "amoebas" were found, whereas dynamic "mushrooms" and "bursts" were reported at low protein concentrations.[14, 6]

Another important finding of recent years was the influence of hitherto disregarded purification artifacts on *in vitro* Min pattern formation – most notably, the positioning of His-tags that are routinely inserted in MinE, as required for intermediate steps during the purification procedure – as first reported by Glock et al. in 2019[15]. Unexpectedly, the addition of a His-tag at MinE's N-terminus was found to influence MinE's capacity for stimulating MinD's ATPase activity and the related membrane detachment, effectively rendering it hyperactive. Upon moving this His-tag to MinE's C-terminus instead, static patterns – such as spot, mesh, and labyrinth patterns – were observed *in vitro* for a broad range of MinD/MinE ratios in which so far, only traveling waves and spirals had been reported. This finding was important as these static patterns were a new addition to the repertoire of patterns that Min proteins are able to create, and hence opened up new possibilities to explore this system for both theorists and experimentalists.[15]

In a recent collaboration between the groups of Jun and Frey,[16] it was found that the Switch model successfully captures the features of Min oscillations *in vivo*. In this study, *E. coli* bacteria were subjected to genetic engineering, which allowed for separate control of the intracellular MinD and MinE concentrations, as well as for treatment with cephalexin, which led to growth into elongated filamentous cell shapes. Depending on cell size as well as MinD/MinE ratio, different outcomes were observed: Pole-pole oscillations in normal-sized cells, standing waves in elongated cells, and travelling waves in strongly elongated filamentous cells. Modeling Min patterns within these geometries using the Switch model successfully reproduced essential features of the *in vivo* results. This allowed for the creation of a phase diagram (i.e. a map of what patterns occurred depending on MinD/MinE concentrations) which closely resembled the experimental counterpart.[16]

4.2. RESULTS

4.2.1. AIM OF THIS PROJECT

The challenge remains to go one step further and successfully create a phase diagram for the *in vitro* setting, plus to relate this *quantitatively* to the corresponding simulation results. Doing so would confirm that we have indeed finally acquired a profound understanding of the inner workings of Min proteins that can accurately and quantitatively predict the pattern observed *in vitro* for a given parameter setting.

A promising hypothesis currently pursued by the Frey group suggests that a more detailed consideration of MinE's membrane binding might provide the so-far missing link for understanding differences of Min pattern formation *in vivo* versus *in vitro*. Loose et al. (2011) coined the term "persistent membrane binding" for the observed property of MinE to remain attached to the lipid membrane for a short period of time after stimulating ATP-hydrolysis and membrane-detachment of MinD.[17] However, models of the Min system differ in how and whether they take this into account.

Extending the Switch Model[11] by an environment-dependent capacity for persistent membrane binding, MinE can either remain membrane-bound with a probability p or detach from the membrane with a probability $1-p$. This introduces an additional parameter into the reaction network, as illustrated in Fig. 4.1C. In the *in vivo* situation, Min proteins bind to the inner membrane of a bacterium, which is both heavily crowded and mechanically different from the plain planar bilayer routinely used for *in vitro* experiments. The current hypothesis is that p takes on rather small values *in vivo*, but becomes non-negligible *in vitro*.

With the aim to compare data to a theoretical phase diagram later on, we performed a series of *in vitro* experiments using both MinE-wildtype and a truncated mutant MinE-ΔMTS. This mutant lacks the N-terminal membrane-targeting sequence (MTS) of MinE and hence, cannot linger on the membrane upon detachment of associated MinD, effectively setting p to zero. Experiments were performed for both versions for different MinD/MinE ratios in large sample chambers, using Min proteins with all His-tags removed by the action of a SUMO-protease.

Using previously developed tools[18], we furthermore aim to provide a quantitative analysis of observed patterns, which brings our study also beyond mere reproducing the experimental phase diagram reported by Glock et al. (2019)[15]. In particular, we quantify the pattern's characteristic length scale (via 2D autocorrelation analysis). For dynamic patterns, we additionally determine the pattern's characteristic velocity (via detection of wave-crests and framewise comparison). In collecting and analyzing image data at various MinD/MinE ratios for both MinE-wildtype and MinE-ΔMTS, we aim to provide the experimental foundation for testing the hypothesis of environmentally-dependent membrane binding by MinE.

4.2.2. LARGE-SCALE ACQUISITIONS OF PATTERNS

We performed experiments studying Min pattern formation *in vitro* for MinD-wildtype in combination with either MinE-wildtype or the truncated mutant MinE-ΔMTS in glass-based, 3D closed sample chambers of roughly 2 cm length, 3 mm width, and 65 μm height. Supplementary Fig. 4.6 (on page 185) provides an illustration of our sample chamber design.

Based upon the data collected by Glock et al. (2019)[15] as well as preliminary experiments, we were aware of the possibility of multiple types of patterns occurring within the same sample chamber. Therefore, we collected a series of large overview images via tile stitching, such as shown in Figs. 4.2 and 4.3.

Fig. 4.2 shows an overview image (A) as well as an individual field-of-view (B) for 1 μM MinD and 1 μM MinE-wildtype, revealing that while for this condition, static spot patterns clearly constituted the most dominant pattern, dynamic patterns occurred at certain positions in the sample chamber. Acquiring a second overview image about 40 minutes later (not shown) revealed that the dynamic patterns had disappeared, leaving only the spot patterns within this region. The complementary condition of 1 μM MinD and 1 μM MinE-ΔMTS shown in Fig. 4.3 reveals that using the truncated mutant produced predominantly dynamic wave patterns in this experiment. Another interesting aspect of this particular overview image is the local variation of the pattern type along the horizontal direction of this image. While traveling waves were found in the central area, we found static patterns occurring along the edges of the channel.

Acquiring and stitching large-scale overview images confirmed – as was reported previously[15] – that multiple types of patterns (both static and dynamic) can co-occur within the same sample chamber. Also, we found that patterns develop and change over time. Supplementary Fig. 4.7 (page 186) shows an example of a pattern which developed and morphed over the first hour following protein injection. Therefore, we concluded that the dominant pattern of a specific condition (i.e. a specific concentration ratio of MinD and MinE) has to be determined after a minimum incubation period to give the pattern time to develop. Also, we decided to probe it systematically at the central area of the sample channel, where we assume potential edge effects to be of lower significance.

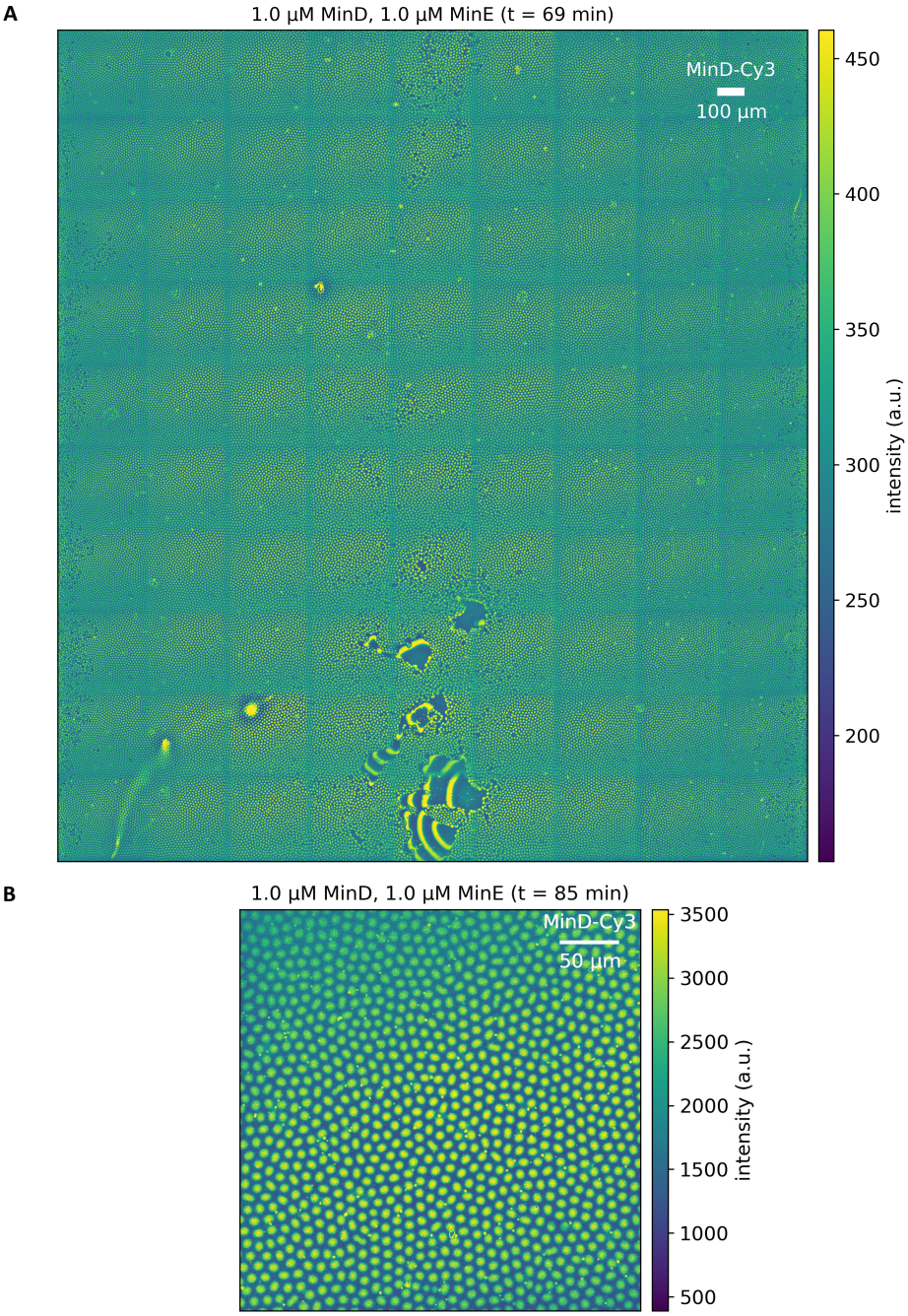


Figure 4.2: **Min patterns at 1 μM MinD and 1 μM MinE-wildtype. A** Overview image taken for 1 μM MinD, 1 μM MinE-wildtype and 2.5 mM ATP showing image data for channel MinD-Cy3, at time t=69 min after injection of protein solution. The overview shows spots as the dominant pattern, with some traveling wave patterns in the center, which would later disappear. **B** Single field-of-view of spot pattern, taken at t=85 min after injection.

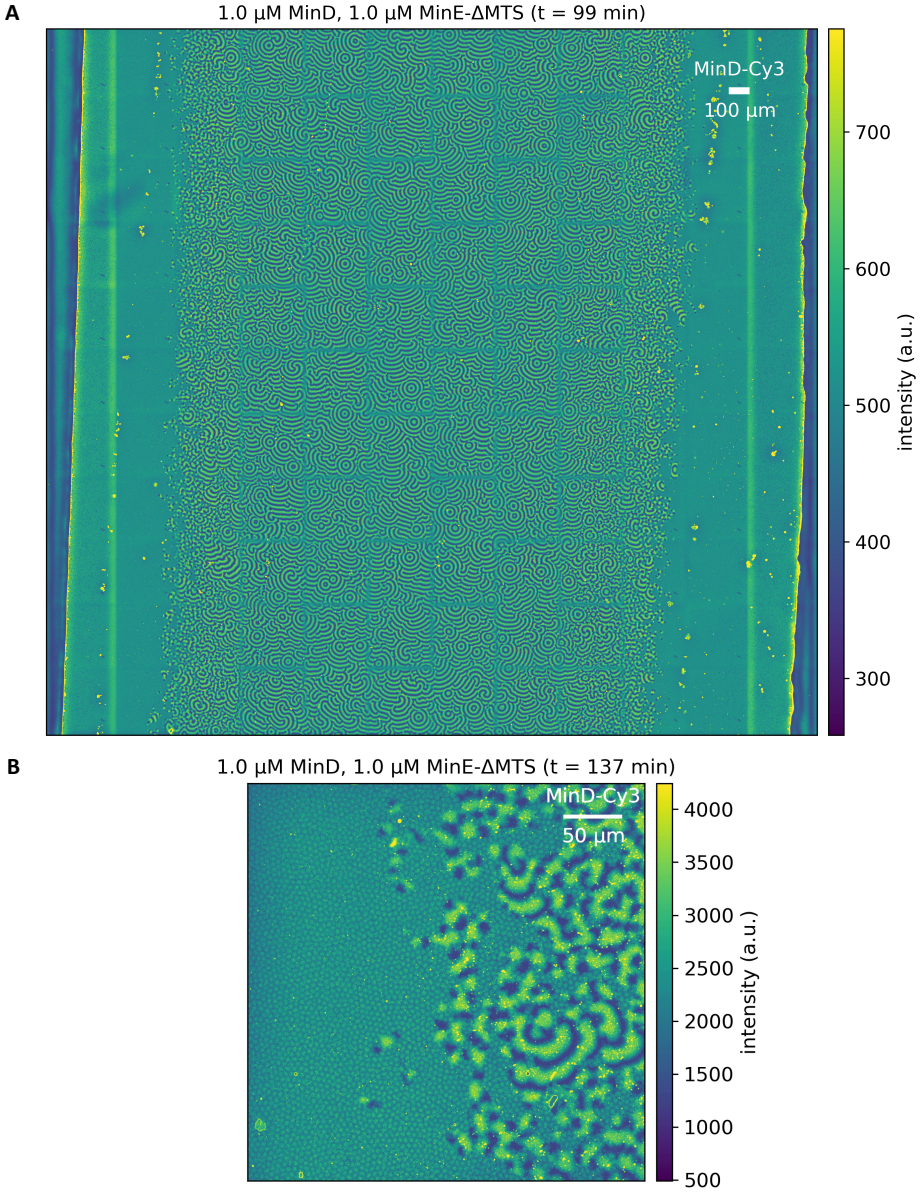


Figure 4.3: **Min patterns at 1 μM MinD and 1 μM MinE-ΔMTS. A** Overview image taken for 1 μM MinD, 1 μM MinE-ΔMTS and 2.5 mM ATP, showing image data for channel MinD-Cy3, at time t=99 min after injection of protein solution. The overview shows that dynamic traveling waves and spirals constitute the dominant pattern, while there are static patterns visible along the channel edges. **B** Single field-of-view taken at t=137 min at domain edge between dynamic and static domain.

4.2.3. CLASSIFICATION AND QUANTIFICATION OF PATTERNS

As our study focuses on the influence of MinE membrane-binding on the properties of Min patterns, we decided to collect image data for Min patterns at different MinD/MinE ratios for both MinE-wildtype and MinE-ΔMTS. Image data were acquired as two types: 1) Large overview images stretching over a rectangular area extending up to the edges of the channel (about 3 mm x 2 mm), and 2) movies taken at several (at least 3) individual positions within the central region of these images (with one field-of-view covering an area of 337 μm x 337 μm). While the identification of the dominant pattern was complicated by the observation that patterns could vary both spatially within the sample chamber, as well as locally over time, the acquisition of overview images allowed us to identify the most dominant pattern of a given set of parameters. We decided to identify the dominant pattern as the most frequently occurring pattern type found in the center area of the channel after an incubation period of at least 90 minutes.

To allow for quantification of a given pattern's characteristic length scale and (where applicable) velocity, time series were acquired at distinct central positions exhibiting the dominant pattern of the sample. In order to achieve comparability between data acquired in individual experiments, all movies intended for quantitative analysis were taken acquired within a time frame of 90 up to 150 minutes upon the injection of sample solution into the channel. A full overview of performed experiments and of the dominant as well as secondary patterns observed in them is given in table 4.1 (starting on page 182). All analysis can be performed on image data acquired for both MinD-Cy3 and MinE-Cy5. In the main text, we show analysis results for MinD-Cy3. The analysis results for the MinE-Cy5 channel are additionally provided in the Supplementary Information.

Figs. 4.4A and B show phase diagrams of the dominant patterns identified for experiments with MinE-wildtype (A) and MinE-ΔMTS (B) in the covered concentration range of up to 1.5 μM MinD and MinE, respectively. Supplementary Fig. 4.8 (page 187) shows a magnified version of these phase diagrams for a narrowed concentration range of up to 0.5 μM MinD and MinE, respectively, in order to give a clearer picture on the edges of the pattern-forming regimes in this range.

Fig. 4.4C shows the types of identified patterns, following the terminology proposed by Glock et al. (2019)[15]. We distinguish dynamic patterns (i.e. semi-periodic traveling waves and spirals) from a range of static patterns, referred to as *labyrinth*, *inverse spot* and *spot* patterns. All of these pattern types exhibit characteristic properties. Traveling waves in particular show a high density of MinD moving quickly (i.e. at velocities of about 1 μm/s) across the surface, followed immediately by a high density front of MinE. Hence, they are referred to as dynamic as opposed to static patterns. Labyrinth patterns show narrow, labyrinthine structures of regions high in MinD interlaced with complimentary regions high in MinE. Inverse spots show a high surface coverage of MinD, spotted with small regions of MinE. Spots, on the other hand, are small regions of high MinD coverage, with circles of MinE surrounding them. While these pattern types do in fact change and evolve, they are referred to as static because they only visibly change over the course of minutes rather than seconds.

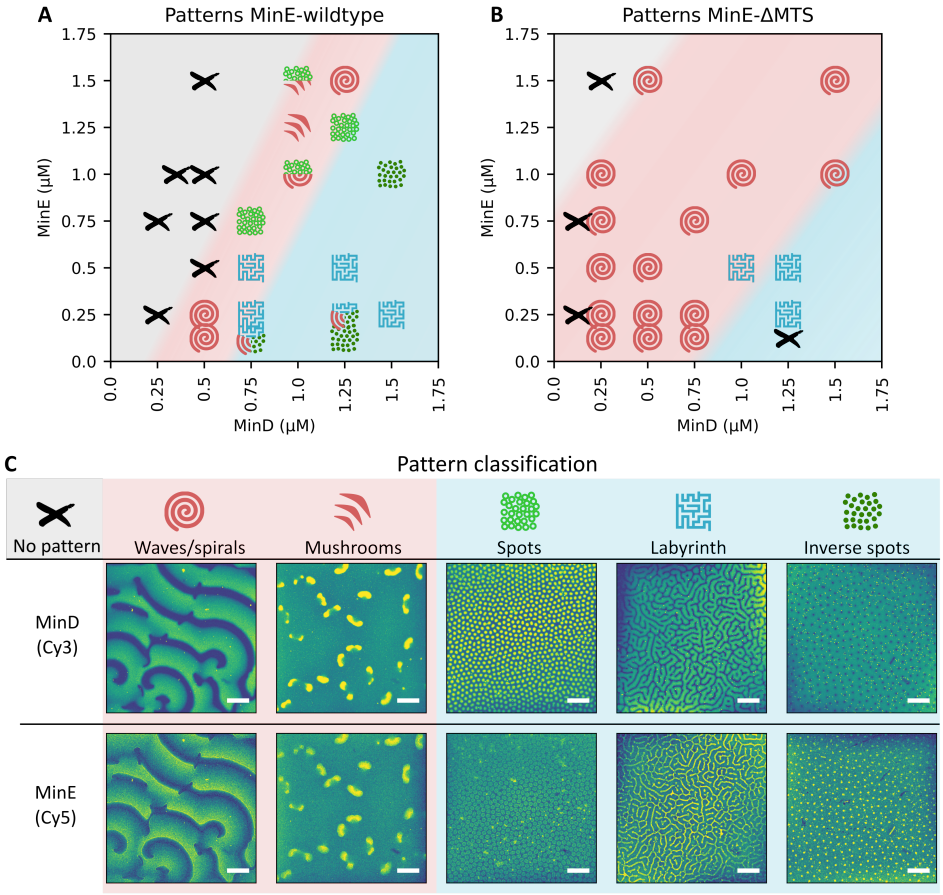


Figure 4.4: **Pattern classification.** **A** Pattern classification for experiments with MinE-wildtype, based on image data acquired for MinD-Cy3. Overlays of multiple symbols indicate either co-occurrence of dominant patterns in the same experiment or occurrence of different dominant patterns in different experiments for the same parameters (see table 4.1 on page 182 for an overview of outcome per individual experiment). **B** Pattern classification for experiments with MinE-ΔMTS. **C** Exemplary patterns and their corresponding symbols denoting their occurrence in A and B. Scale bars are 50 μm. Top row: Examples of image data acquired for MinD-Cy3 of waves/spirals (i.e. dynamic patterns), labyrinth patterns, inverse spots (small patches of MinE surrounded by MinD), spots (small patches of MinD with a circle of MinE) and no pattern formation. Bottom row: Idem for image data acquired for MinE-Cy5. Red background shade indicates a dynamic pattern, blue background shade indicates a static pattern.

To allow for a quantitative comparison of the patterns' properties to simulation results and address the *in vitro* vs. *in silico* length scale discrepancy described before, we quantified the pattern's characteristic length using autocorrelation analysis as discussed in a previous publication (chapter 2 or [18]). From our collected results, we find that dynamic traveling wave patterns tend to have both larger characteristic length scales and broader distributions thereof than static patterns. Therefore, we distinguish between dynamic and static patterns in the representation of our analysis results by showing them in separate figures.

Fig. 4.5 provides an overview of our results obtained for dynamic patterns, showing snapshots and analysis results for image data on the MinD-Cy3 channel. For comparison, Supplementary Fig. 4.9 (page 188) shows the same for MinE-Cy5 data. As can be observed in Fig. 4.5 panels C and D, the data for the MinE-wildtype does not allow for determining clear trends within the wavelengths due to the relative scarcity of dynamic patterns, while the MinE-ΔMTS data show that wavelengths decrease for constant MinD and larger MinE concentrations. Traveling wave patterns exhibit a range of length scales (i.e. wavelengths) of about 20-80 μm, as illustrated in Fig. 4.5 by exemplary image data showing dynamic patterns for MinE-wildtype (A) and MinE-ΔMTS (B). Fig. 4.5C and D show the collected analysis results for the length scales of traveling wave patterns depicted as heatmaps. These heatmaps indicate that for constant MinD concentration, dynamic patterns tend to exhibit a factor 2 smaller wavelengths for increasing amounts of MinE.

Supplementary Fig. 4.10 (page 190) shows the collected analysis results of characteristic length scales for static patterns. Our analysis of static pattern's characteristic length scales indicate that they exhibit rather little variation independent of pattern type and without recognizable trends with respect to protein concentration ratios, varying from 10 to 20 μm.

The dynamic patterns also allow us to perform an analysis of their propagation velocity using a previously introduced methodology[18] (see chapter 2). Briefly, we use optical flow to identify wave crest locations as well as propagation directions thereof, and then calculate their translocation by framewise comparison. Knowing the time difference between frames then allows to directly calculate the wave crests' propagation velocity.

Figs. 4.5E and F show the analysis results (again for MinE-wildtype and MinE-ΔMTS) depicted as heatmaps. Complementary to the trend of decreasing wavelengths for higher MinE-ΔMTS concentration, the wave propagation velocities tend to increase for increasing MinE concentrations.

Performing quantification of length scales (and velocity, for dynamic patterns) for every time series provides a distribution for both length scale and velocity. The mean (± standard error of the mean) and median values of these analyses for every measured condition are represented as bar plots in Supplementary Figs. 4.11 (page 191) and 4.12 (page 192). These plots provide overviews on the occurrence of dominant patterns and quantification results per individual experiment, as opposed to being averaged over repeats (where applicable).

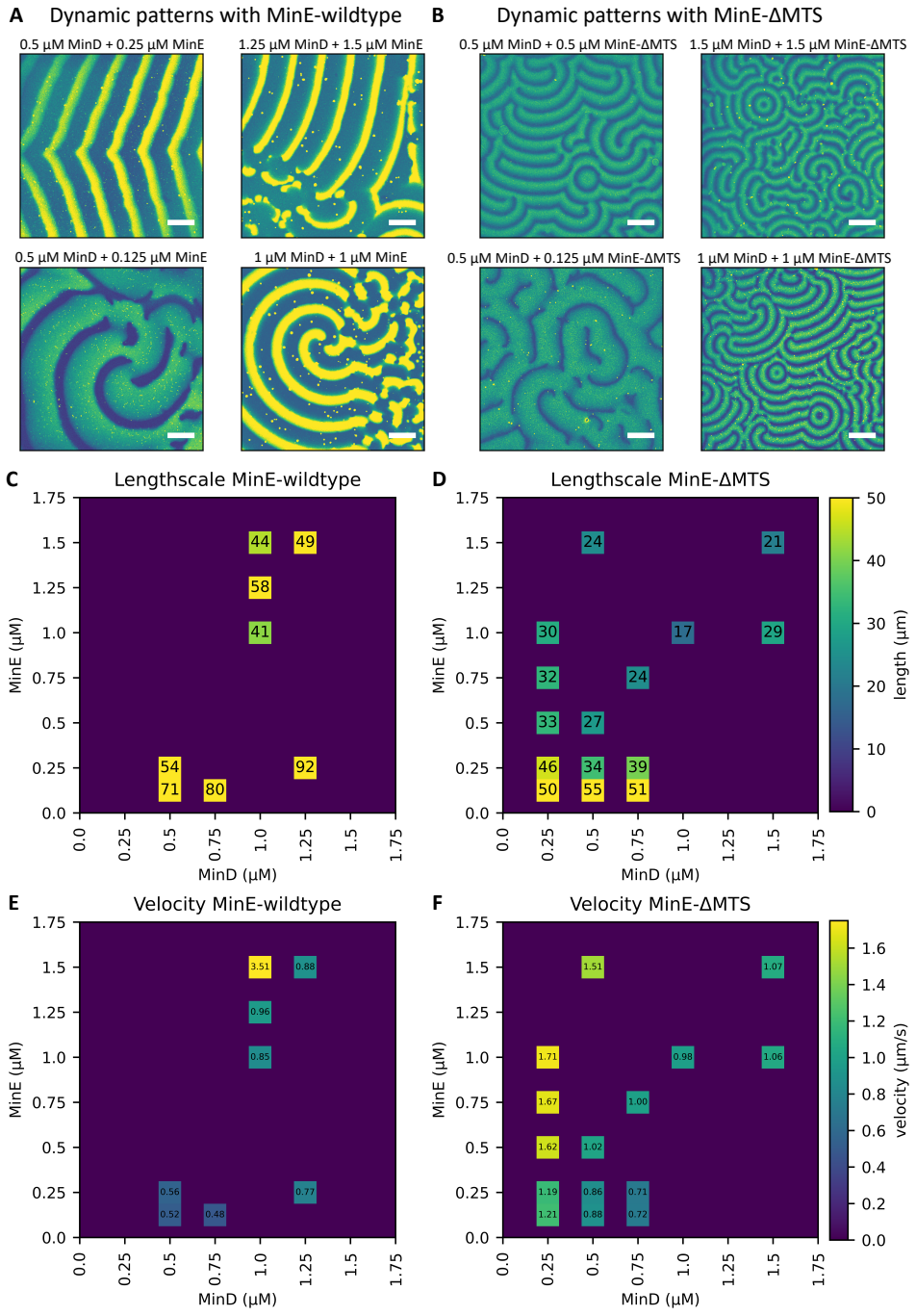


Figure 4.5: **Quantification of characteristic length scales and velocities for traveling wave patterns. A** Exemplary image for dynamic patterns with MinE-wildtype. **B** Idem for MinE-ΔMTS. **C** Characteristic length scale of patterns for MinE-wildtype, quantified via autocorrelation and median-averaged over multiple areas and/or experiments. **D** Idem for MinE-ΔMTS. *Caption continues on next page.*

Figure 4.5: **E** Characteristic velocity determined from framewise comparison of wave crest points for MinE-wildtype, median-averaged over multiple areas and/or experiments. **F** Idem for MinE-ΔMTS. Full analysis results for C and D (characteristic lengths) given in Supplementary Fig. 4.11 (page 191). Full analysis results for E and F (velocities) given in Supplementary Fig. 4.12 (page 192). All quantifications are based upon images acquired for MinD-Cy3. Scale bars in A and B are 50 μm.

4.3. DISCUSSION

In this chapter, we presented the experimental results of a project carried out in collaboration with the Frey group. Our results reproduce the core findings of data presented in Glock et al. (2019)[15] for MinE-wildtype. Importantly, this includes the observation of different types of static patterns – as opposed to the formerly dominant observation of traveling wave patterns over wide concentration ranges[7] – as well as the co-occurrence of qualitatively different pattern types for the same MinD/MinE conditions. However, our data extend upon the findings by Glock et al. by a) a quantitative analysis of the patterns' properties, i.e. characteristic length scale and propagation speed, and b) the creation of a phase diagram for a truncated mutant MinE-ΔMTS. Another more subtle difference is that while Glock et al. (2019)[15] performed experiments with MinE-His as well as MinE-wildtype (with cleaved His-tag) and His-MinD, we used MinD and MinE will all His-tags removed, aiming for best comparability to *in vivo* experiments.

In general, our experiments show that while MinE-wildtype tends to form static patterns over a wide range of the experimentally covered parameter regime, the truncated mutant MinE-ΔMTS leans heavily towards dynamic patterns (traveling wave patterns and spirals). We follow the terminology of Glock et al. (2019) in classifying the static patterns we observed as spots, inverse spots and labyrinth patterns. Additionally, we found that for some conditions, MinE-wildtype would exhibit what mushroom patterns, as also described by Vecchiarelli et al. (2016)[14] – though these experiments were for different membrane composition and His-tagged protein.

While Glock et al. (2019)[15] already commented on the occurrence of multiple patterns within a single sample chamber, we provide large-scale acquisitions which show that this is a common phenomenon, occurring in about 25 % of our experiments (34 % of experiments with MinE-wildtype and 16 % of experiments with MinE-ΔMTS). We notice that the type of pattern observed can depend on the location within the sample chamber, notably the distance from the edge. Whether this effect arises from local differences in concentration or is a consequence of the sample's geometry is not clear at the moment. The parabolic Poisson flow profile would indicate that the highest concentration of protein should be found in the central region of the channel. However, as our experiments re-confirm the intrinsic multistability of Min protein patterns[19], it is difficult to make deductions about this observation.

Indeed, we found that in some experiments even within the central regions of the sample channel, dynamic and static patterns can co-occur and intermingle rather than separate into domains. Examples for this are given in Supplementary Fig. 4.15A (on page 195). Also, we find that in different runs of the same experimental condition, a qualitatively different type of pattern can be observed (see table 4.1 on page 182 or Supplementary Fig. 4.11 on page 191 for an overview). Further, while we aim to provide a comprehensive overview on our quantitative analysis results for the patterns' dominant length scale and/or propagation velocity in the form of heatmaps (Figs. 4.5C-F and 4.10B), there are additional features to the patterns which are not captured by the analysis framework which we apply here. While spot patterns in our experiments tend to exhibit similar spot size independent of concentration, their distribution density as well as spatial arrangement across the surface can vary with the protein concentration, as illustrated by the snapshots given in Supplementary Fig. 4.15B. All of these features and observations show once again how astonishingly rich in variety the Min protein system actually is.

The data presented in this chapter is going to serve as the experimental basis of an ongoing theoretical study of the Min system, investigating whether inclusion of a certain probability p for persistent membrane binding (compare Fig. 4.1C) might be crucial for finally achieving a quantitative match between simulation results and *in vitro* experiments. Mechanochemical interactions have previously been proposed as playing a potentially important role in protein pattern formation[20], and supported lipid bilayers have been shown to exhibit mechanical properties distinct from free-standing lipid systems, such as vesicles[21]. However, the cell membrane of *E. coli* is generally connected to a cell wall, again rendering it mechanically different from a free system like a vesicle. Another relevant point to consider in this context is membrane-crowding. A substantial fraction of the *E. coli* cell membrane is in fact composed of protein, which effectively means it is a very different environment from a bare supported lipid bilayer. Min proteins have been shown to affect the lateral distribution of components embedded in as well as attached to the membrane[22, 23]. Hence, in reverse, an influence of such components on the local kinetics of the Min pattern is imaginable. Taking all of these considerations into account, it seems reasonable to us to introduce the probability for persistent membrane-binding p as an environmentally-dependent parameter which can assume different values in these distinct settings (as has also been suggested for other model parameters of the Min system[24]).

4.4. MATERIALS & METHODS

4.4.1. SUV PREPARATION

Chloroform-suspended lipids (DOPG:DOPC in a ratio 33:67, with 0.05–0.10 % mol Atto-390-DOPE) were mixed in a glass vial, then dried with a nitrogen gun and further left to dry in a desiccator for at least 30 minutes. Next, they were resuspended in SUV buffer (150 mM KCl, 25 mM TRIS pH 7.4-7.5) at a concentration of 5 mg/mL and left to swell at room temperature for at least 1 hour. After swelling, they were vortexed for about 20 seconds and sonicated for 30 minutes. SUVs were produced using an Avanti Mini-Extruder

(Avanti Polar Lipids). The extruder was pre-heated on a hotplate set to 45 ^{o}C and remained there throughout the procedure. The lipid solution was extruded through a filter membrane of pore size 100 nm for 21 times, followed by another 21 times of extrusion using filters with a pore size of 30 nm. The uneven number of filtering counts ensured that the lipid solution ended up in the originally empty one of the two syringes in order to avoid taking along aggregates that might accumulate in the first syringe. The resulting SUV solution was aliquoted into portions of 10 μL and stored at 4 ^{o}C for up to 1 week.

4.4.2. PROTEIN PURIFICATION, HIS-TAG REMOVAL AND LABELLING

Tag-free versions of Min proteins were expressed as SUMO-fusions, and purified essentially as described previously[25] with the following modifications: Following elution from the NiNTA matrix, Min proteins were dialyzed overnight to lysis buffer in the presence of $\tilde{1}$ μM homemade Ulp1403-621 protease[26]. Subsequently, Ulp1403-621 and the cleaved SUMO domain were removed by re-applying the sample to the NiNTA matrix and collecting the unbound fraction.

4.4.3. SLIDE PREPARATION AND CLEANING

For flow cells, we used thick glass slides as cover slides, and microscope slides (thickness 1.5) for imaging. To create inlets and outlets, holes were drilled in the cover slides using a diamond drill. Microscope slides and cover slides were then placed into Teflon containers and cleaned by sequential sonication in deionized water for 5 minutes, Acetone for 15 minutes, KOH (1 M) for 1 hour and Ethanol for 1 hour. Between sonication steps, the containers were rinsed with deionized water several times and sonicated in water for 5 minutes, in order to thoroughly remove the preceding solution. Next, the slides were cleaned with acid Piranha (H_2SO_4 and H_2O_2 in a ratio 5:1), rinsed with plenty of deionized water and stored in fresh Ethanol for up to several months.

4.4.4. SAMPLE PREPARATION

Flow channels were prepared using thick cover slides and regular microscope slides cleaned as described in Sec. 4.4.3 and stored in Ethanol. Both slides were dried using a nitrogen gun, placed in a glass dish and subsequently plasma-cleaned with oxygen plasma at 50 W for 1 minute. Stripes of double-sided tape were cut on a clean plastic surface using a razor blade and placed between the inlet/outlet ports in order to create 10 parallel channels spaced along the long axis of the slide. One channel would be of 70 μm height (determined by the tape) and roughly of 3 mm width and 2 cm length. The microscope slide was placed on top of the scaffold of tape, protruding pieces of tape were cut with a razor blade and the microscope slide was fixed in place by gentle pressing down on the taped areas with a pipette tip. The edges of the channels were sealed using 5-Minute-Epoxy. Finally, pipette tips cut to about 1 cm height were placed onto the inlet/outlet ports and fixed in position with 5-Minute-Epoxy. The last step creates makes it easier to place pipette tips filled with a given solution (lipid, buffer or protein solution) on top of

the inlet without chance of leakage. Flow channels created in this way were used for up to 1 week.

For each experiment, an aliquot of SUV solution (stored at 5 mg/mL at 4 $^{o}\circ$C) was diluted to a concentration of 1 mg/mL in 150 mM KCl, 25 mM TRIS (pH 7.4-7.5 at room temperature) and 4 mM $MgCl_2$, then sonicated for 15 minutes. Next, the solution was injected into the flow cell using a pipette tip and incubated at 37 ^{O}C for 1 hour. The flow cell was then rinsed with at least 400 μL of Min buffer (150 mM KCl, 25 mM TRIS pH 7.4-7.5 and 5 mM $MgCl_2$) using a syringe pump, pulling buffer from a freshly placed pipette tip into the flow channel at a rate of 200 μL per minute.

Protein solutions at the indicated concentrations were pre-incubated at room temperature with ATP for 30 minutes before injection into the flow channel from a fresh pipette tip, again using the syringe pump at 200 μL per minute. At least 200 μL of protein solution were injected to ensure the flow channel got filled up completely.

4.4.5. FLUORESCENCE MICROSCOPY

Microscope data was acquired using a spinning disc confocal microscope, comprising a Crest X-light V3 spinning disc unit (50 μm pinhole size with 250 μm pinhole spacing) connected to an inverted microscope stand (Nikon Eclipse Ti-2), using CELESTA light engine as fluorescence excitation source. The device was controlled using the software NIS Elements (Nikon).

Image detection was achieved with Photometrics Kinetix sCMOS (10.24 Megapixel active array size, 29.4 mm diagonal sensor area), set to 2x2 binning and 12-bit dynamic range. To minimalize effects of inhomogeneous illumination within the imaged area, we imaged in regions-of-interest covering 1024x1024 pixels. MinD-Cy3 was imaged using 561 nm (40 mW) and MinE-Cy5 was imaged using 640 nm (24 mW) lasers, with excitation times ranging from 100-300 ms each, depending on protein concentration.

4.4.6. IMAGE ACQUISITION, RENDERING AND ANALYSIS

Imaging data was acquired either as large-scale overview and later on assembled via tile stitching or as movies at individual positions. Image rendering and analysis (as well as all subsequent data analysis) was performed using Python.[27] Analysis was performed analogously, yet separately, on MinD-Cy3 and MinE-Cy5 channels.

Large-scale overviews were acquired as individual tiles with an overlap of 10%, preprocessed and stitched into larger images. Here, preprocessing involved applying a high-pass-filter to every individual frame in order to reduce effects of inhomogeneous illumination across the imaged area, followed by homogenization of images by setting them to the same median intensity value. Subsequently, tiles were stitched with overlapping regions being weighted with linear gradients (ranging from 1 to 0 towards the image edges) and added to each other.

Movies were taken within a time frame of 90 to 150 minutes after sample injection for at least 3 individual positions around the center of the sample chamber, which we considered to be the most representative pattern for the given condition. Images were acquired for at least one, up to several minutes at imaging rates from 1 to 5 seconds between frames. Image processing of movies involved again application of a high-pass filter, with the mask being determined from the first frame and kept constant for all subsequent frames. Quantification of the pattern's properties was performed on preprocessed movie files (tiff format) as described previously.[18] A slightly extended version of the published code associated with the publication[18] (available on Zenodo at `https://zenodo.org/record/6724666`) was used for image analysis. Lengthscale analysis was performed for all frames of every image stack via 2D autocorrelation analysis. Velocity analysis was performed for the image stack's first 10 frames, choosing the function's parameters as follows: Parameters for the velocity analysis were chosen as follows: The range, within which the corresponding translocated wave crest is sampled when comparing one frame to another, was automatically determined as approximately half the wavelength from autocorrelation analysis performed on the first frame. Sampling happened at subpixel resolution of 0.25 times the pixel width. The kernels for image smoothing were chosen as extending over a quarter of the wavelength.

4.5. SUPPLEMENTARY INFORMATION

4.5.1. EXPERIMENTAL DATA: OVERVIEW

The following table provides an overview on experimental data used in the figures shown throughout chapter 4. In the category "MinE", the abbreviation *wt* refers to the wildtype.

We identify the "dominant pattern" as being the pattern that is found at the center of a sample channel after at least 90 minutes of incubation. As described above, other patterns were regularly observed in the same channel, either transiently (early on, compare Supplementary Fig. 4.7) or along the edges of the channel (compare Supplementary Fig. 4.3).

A star (*) after the description of the dominant pattern indicate some peculiarity in the form of a deviation from regularly observed characteristics of the identified pattern type.

ID	MinD-Cy3 (μM)	MinE-Cy5 (μM)	MinE type	dominant pattern	other patterns
1	0.250	0.250	wildtype	no pattern	
2	0.500	0.500	wildtype	no pattern	
3	0.750	0.750	wildtype	spots	
4	1.000	1.000	wildtype	spots	waves/spirals
5	1.250	1.250	wildtype	spots	waves/spirals
6	0.250	0.250	deltaMTS	waves/spirals	
7	0.500	0.500	deltaMTS	waves/spirals	
8	1.000	1.000	deltaMTS	waves/spirals	mesh

9	0.250	0.500	deltaMTS	waves/spirals	
10	0.500	0.250	deltaMTS	waves/spirals	
11	0.250	0.750	deltaMTS	waves/spirals	
12	0.750	0.250	deltaMTS	waves/spirals	labyrinth
13	0.250	1.000	deltaMTS	waves/spirals	
14	0.250	0.500	deltaMTS	waves/spirals	
15	0.500	0.250	deltaMTS	waves/spirals	
16	0.250	0.750	deltaMTS	waves/spirals	
17	0.750	0.250	deltaMTS	waves/spirals	labyrinth
18	0.250	1.000	deltaMTS	waves/spirals	
19	0.250	0.250	deltaMTS	waves/spirals	
20	0.500	0.500	deltaMTS	waves/spirals	
21	0.750	0.750	deltaMTS	waves/spirals	
22	1.500	1.500	deltaMTS	waves/spirals	
23	0.250	0.750	wildtype	no pattern	
24	0.350	1.000	wildtype	no pattern	
25	0.500	0.250	wildtype	waves/spirals	spots
26	0.750	0.250	wildtype	labyrinth	
27	0.250	0.125	deltaMTS	waves/spirals	
28	0.125	0.250	deltaMTS	no pattern	waves/spirals
29	1.250	0.250	deltaMTS	unclear	
30	0.500	0.125	wildtype	waves/spirals	
31	0.750	0.125	wildtype	inverse spots	
32	0.750	0.500	wildtype	labyrinth	
33	0.750	0.125	deltaMTS	waves/spirals	
34	0.125	0.750	deltaMTS	no pattern	
35	0.500	1.500	deltaMTS	waves/spirals	
36	1.500	1.000	deltaMTS	waves/spirals	mesh
37	0.250	1.500	deltaMTS	no pattern	
38	0.500	0.750	wildtype	no pattern	
39	0.500	1.000	wildtype	no pattern	
40	0.500	1.500	wildtype	no pattern	
41	1.000	1.000	wildtype	waves/spirals	spots
42	1.250	1.500	wildtype	waves/spirals	spots
43	1.500	0.250	wildtype	labyrinth	inverse spots
44	0.500	0.125	deltaMTS	waves/spirals	
45	0.125	0.750	deltaMTS	no pattern	
46	1.250	0.125	deltaMTS	no pattern	
47	1.250	0.250	deltaMTS	labyrinth*	
48	0.500	0.125	wildtype	waves/spirals	
49	0.750	0.125	wildtype	waves/spirals; labyrinth	labyrinth; inverse spots
50	1.250	0.250	wildtype	waves/spirals; inverse spots	inverse spots
51	0.500	0.250	wildtype	waves/spirals	labyrinth

52	0.500	0.125	wildtype	waves/spirals	labyrinth; inverse spots
53	0.500	0.050	wildtype	waves/spirals	labyrinth; inverse spots
54	0.500	0.010	wildtype	no pattern	
55	1.000	1.500	wildtype	mushroom	
56	0.500	0.250	deltaMTS	waves/spirals	
57	0.500	0.125	deltaMTS	waves/spirals	
58	0.500	0.050	deltaMTS	no pattern; waves/spirals	
59	0.500	0.010	deltaMTS	no pattern	
60	0.500	0.050	wildtype	waves/spirals	labyrinth; inverse spots
61	0.500	0.250	wildtype	waves/spirals	
62	1.000	1.500	wildtype	mushroom	
63	1.500	1.000	wildtype	inverse spots	
64	1.250	0.050	wildtype	no pattern	
65	1.250	0.125	wildtype	inverse spots	
66	1.250	0.250	wildtype	labyrinth; inverse spots	
67	1.250	0.500	wildtype	labyrinth	
68	1.000	1.250	wildtype	mushroom	waves/spirals; spots
69	0.500	0.010	wildtype	no pattern	
70	1.000	1.500	wildtype	spots* (bursts?)	
71	1.250	0.050	wildtype	no pattern	
72	0.500	0.010	deltaMTS	no pattern	
73	0.500	0.050	deltaMTS	waves/spirals	
74	1.000	0.500	deltaMTS	labyrinth	waves/spirals
75	1.250	0.500	deltaMTS	labyrinth	

4.5.2. SUPPLEMENTARY FIGURES

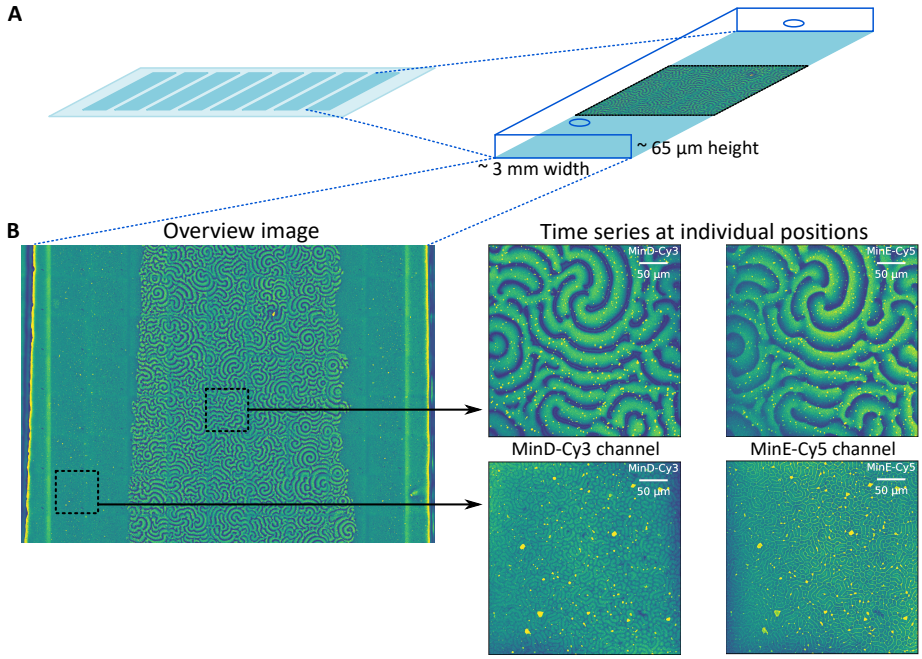


Figure 4.6: **Experimental setup. A** Multiple parallel sample channels on one glass-based device. Protein solution is injected via entry ports on the top glass slide. Images are acquired on the lower glass surface. **B** Overview images were assembled via stitching of sequentially acquired fields-of-view. Time series (movies) for quantitative analysis of the pattern's spatial and temporal characteristics were acquired around the center of the channel. In cases in which multiple types of patterns were present within the channel (as in the example image, showing traveling waves in the center and labyrinth patterns along the edges), quantitative analysis was only performed for the most dominant pattern, occurring in the central area.

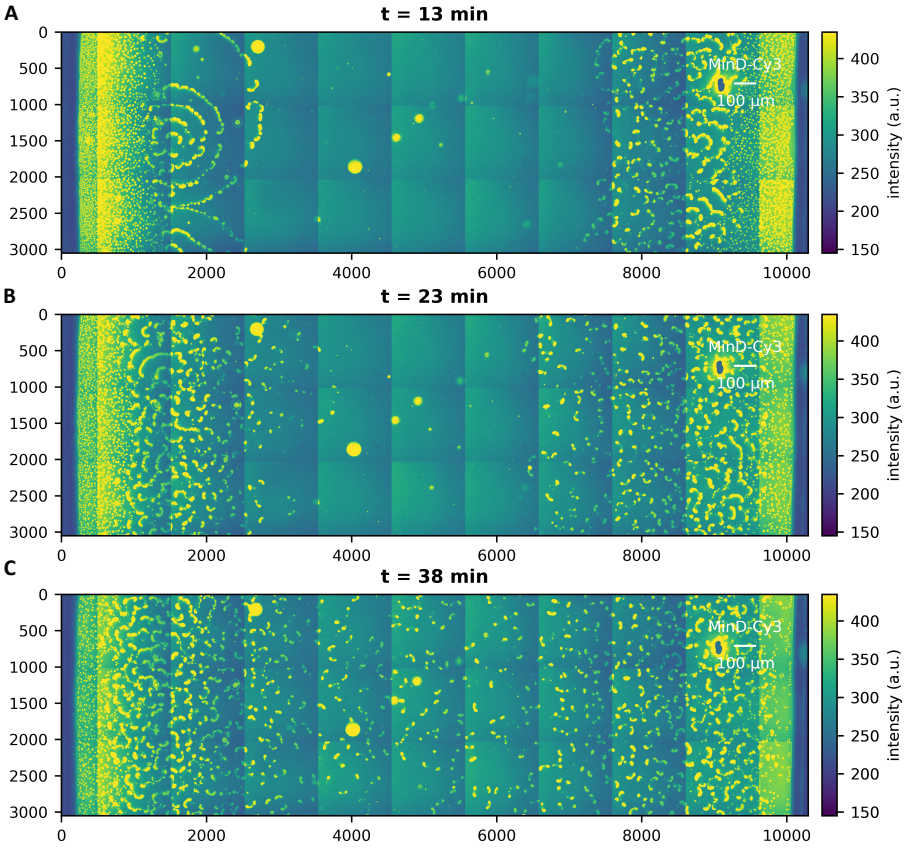


Figure 4.7: **Time-lapse shows pattern's development.** Snapshots of a sample channel's cross-section acquired for 1 μM MinD and 1.5 μM MinE-ΔMTS **A** at t = 13 min, **B** at t = 23 min, and **C** at t = 38 min after injection.

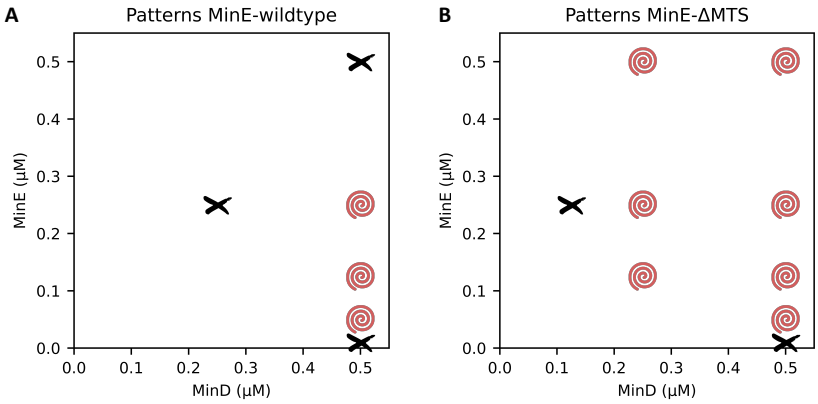


Figure 4.8: **Pattern classification and characteristic length scales, limited concentration range. A** Pattern classification for experiments with MinE-wildtype. **B** Pattern classification for experiments with MinE-ΔMTS.

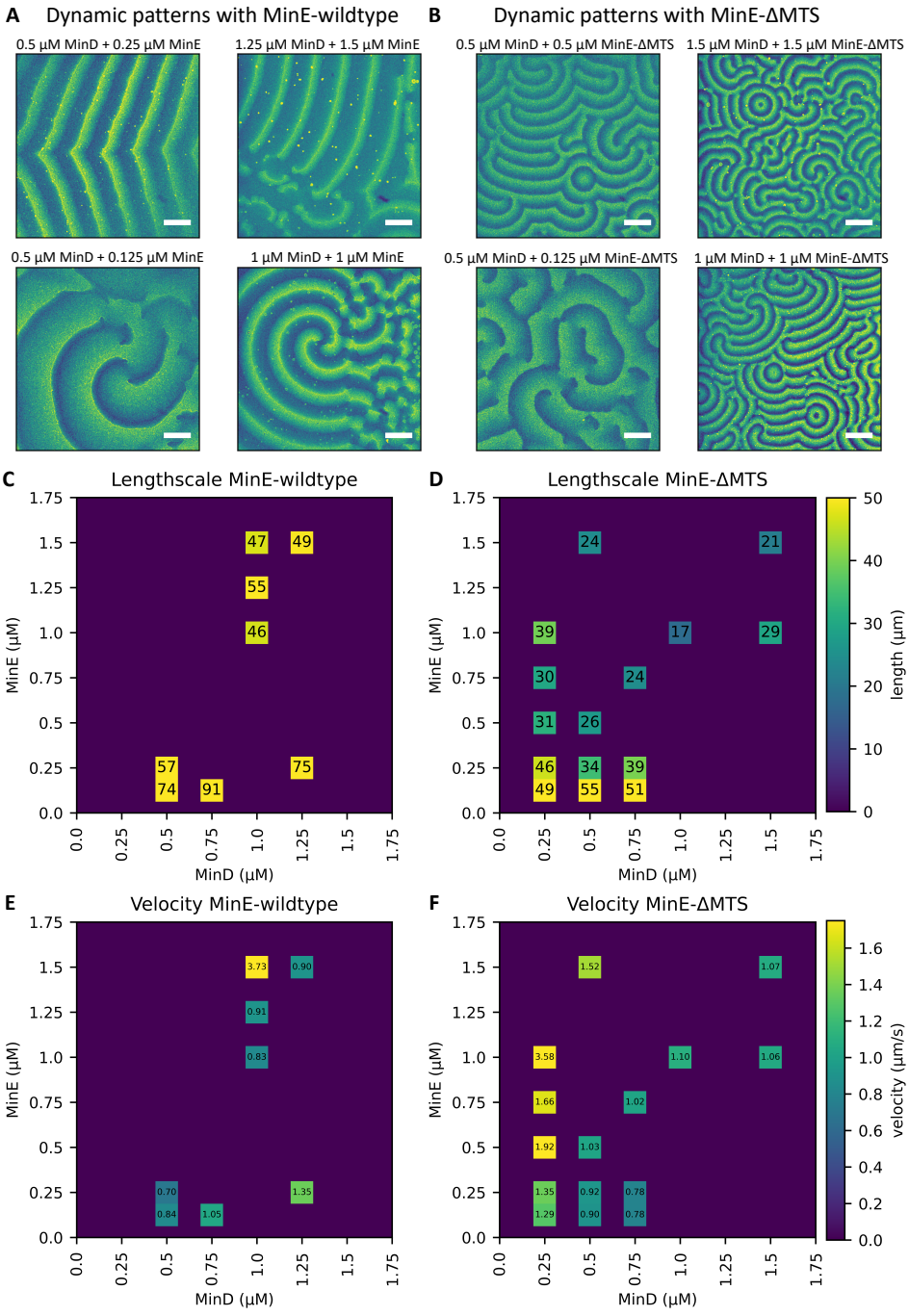


Figure 4.9: **Quantification of characteristic length scales and velocities for traveling wave patterns, image data for channel MinE-Cy5.** *Caption continues on next page.*

Figure 4.9: **A** Exemplary image for dynamic patterns with MinE-wildtype. **B** Idem for MinE-ΔMTS. **C** Characteristic length scale of patterns for MinE-wildtype, quantified via autocorrelation and median-averaged over multiple areas and/or experiments. **D** Idem for MinE-ΔMTS. **E** Characteristic velocity determined from framewise comparison of wave crest points for MinE-wildtype, median-averaged over multiple areas and/or experiments. **F** Idem for MinE-ΔMTS. Full analysis results for C and D (characteristic lengths) given in Supplementary Fig. 4.13 (page 193). Full analysis results for E and F (velocities) given in Supplementary Fig. 4.14 (page 194). All quantifications are based upon images acquired for MinE-Cy5. Scale bars in A and B are 50 μm.

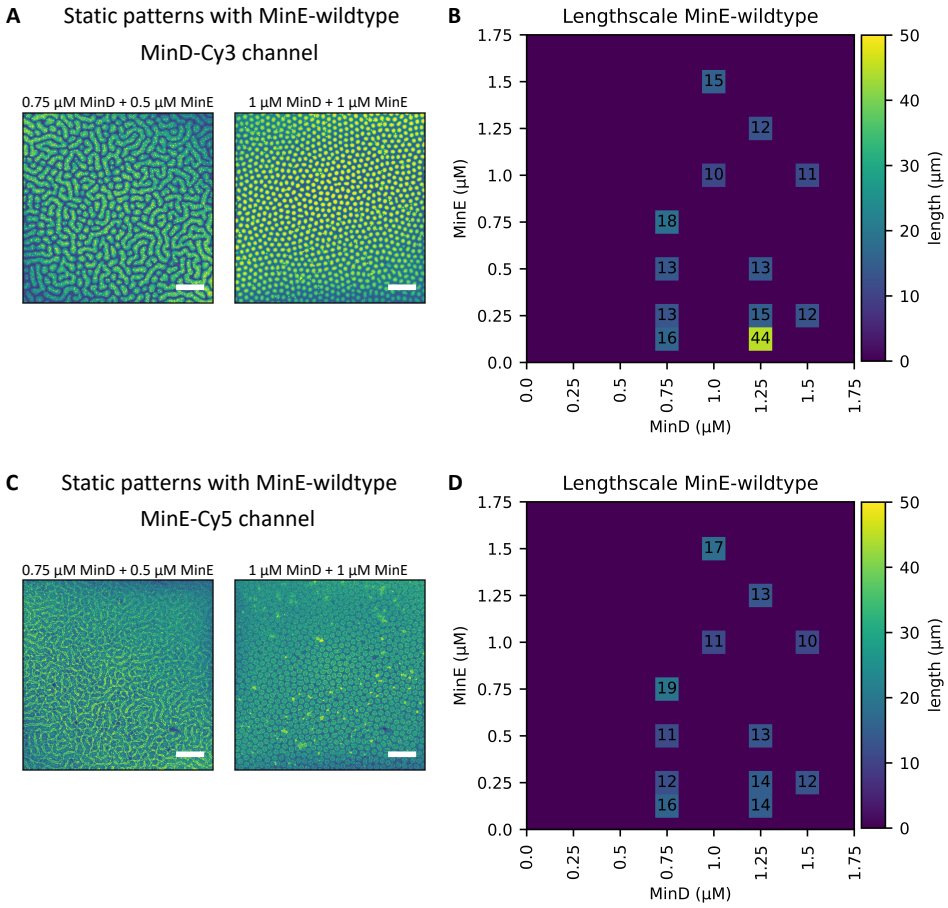


Figure 4.10: **Quantification of characteristic length scales for static patterns. A** Examples of image data acquired for MinD-Cy3 channel, showing static patterns as obtained when using MinE-wildtype. Scalebars 50 μm. **B**. Characteristic length scale of patterns for MinE-wildtype on image data for MinE-Cy5, quantified via autocorrelation and averaged over multiple areas. Full analysis results for static patterns observed with MinE-wildtype as well as MinE-ΔMTS are given in Supplementary Fig. 4.11 (on page 191). **C** Examples of image data acquired for MinE-Cy5 channel, showing static patterns as obtained when using MinE-wildtype. Scalebars 50 μm. **B**. Characteristic length scale of patterns for MinE-wildtype on image data for MinE-Cy5, quantified via autocorrelation and averaged over multiple areas. Full analysis results for static patterns observed with MinE-wildtype as well as MinE-ΔMTS are given in Supplementary Fig. 4.13 (on page 193).

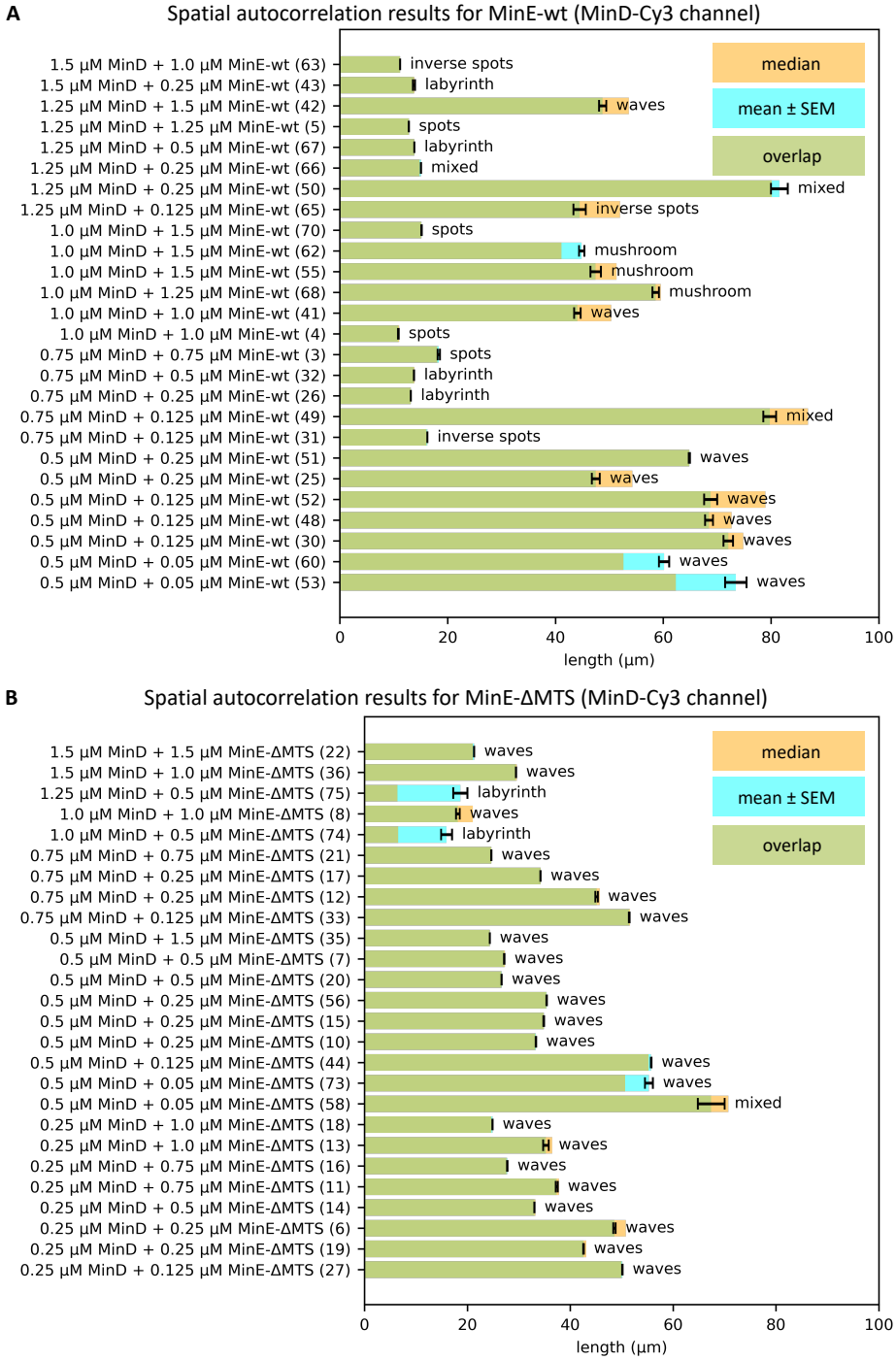


Figure 4.11: An overview of spatial autocorrelation analysis results for quantification of a given pattern's characteristic length scale, based on image data for channel MinD-Cy3. The experiment ID (given in brackets) refers to the ID given in table 4.1.

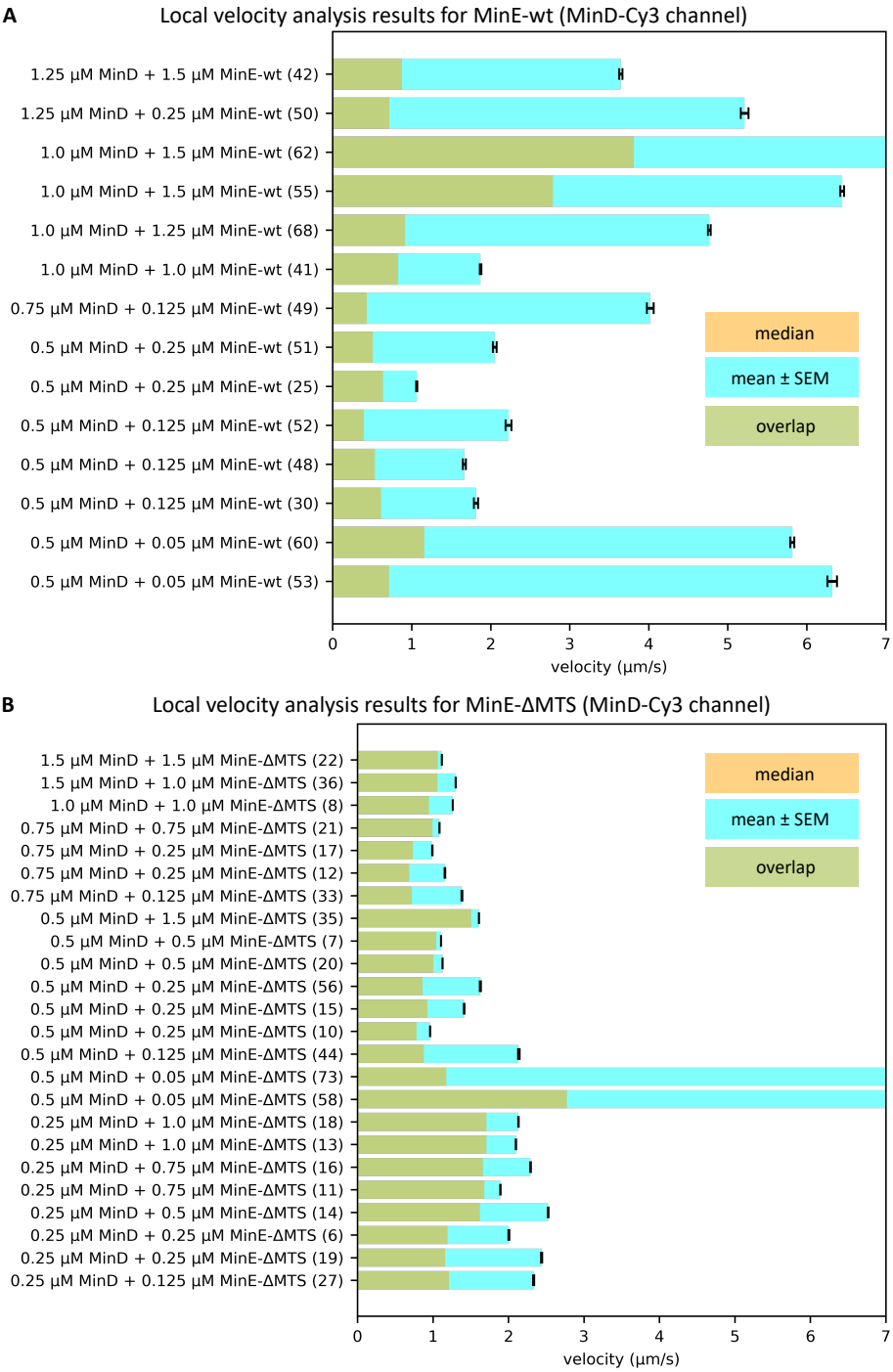


Figure 4.12: An overview of local velocity analysis results for quantification of a given dynamic pattern's characteristic velocity, based on image data for channel MinD-Cy3. The experiment ID (given in brackets) refers to the ID given in table 4.1.

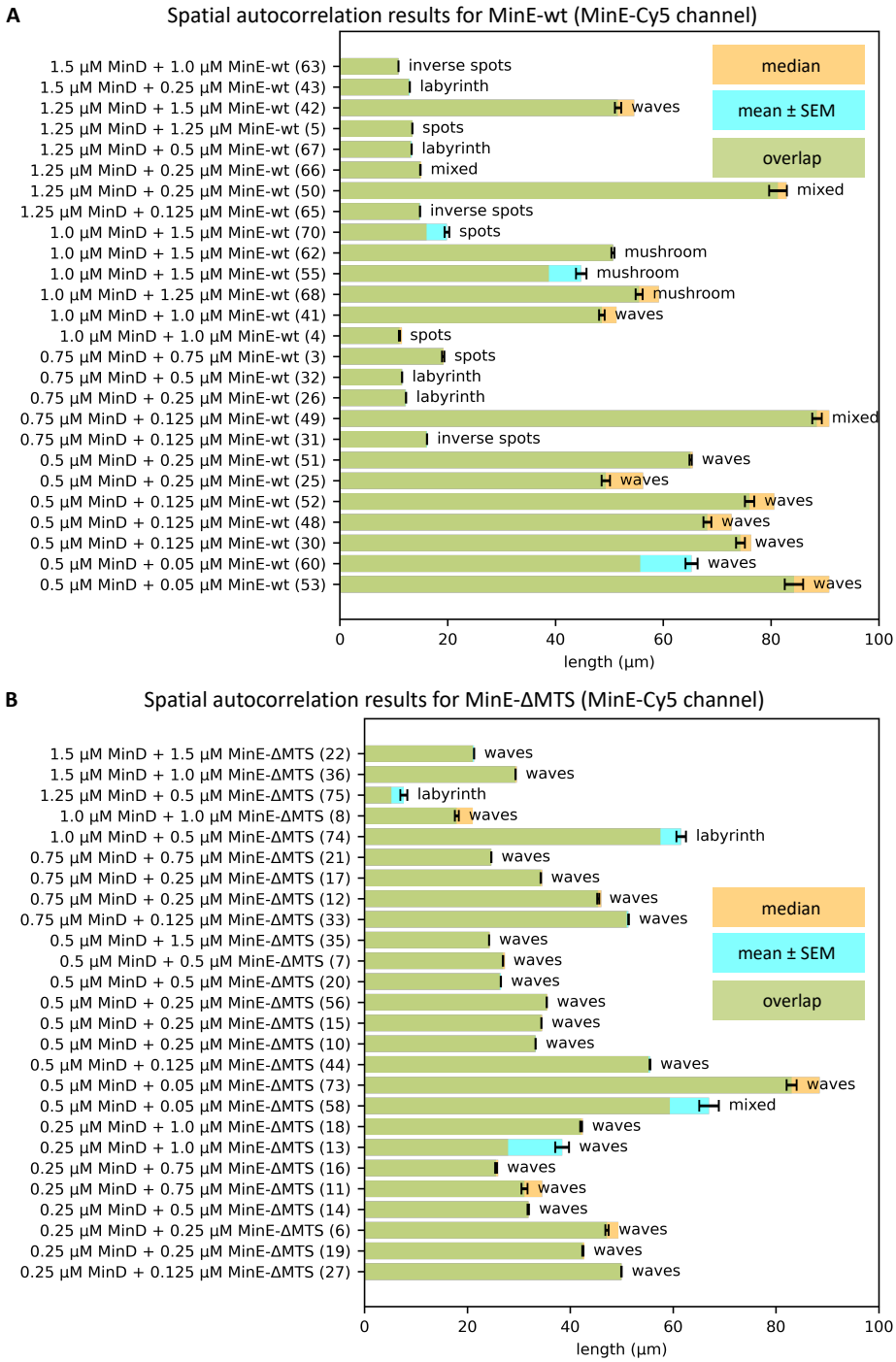


Figure 4.13: An overview of spatial autocorrelation analysis results for quantification of a given pattern's characteristic length scale, based on image data for channel MinE-Cy5. The experiment ID (given in brackets) refers to the ID given in table 4.1.

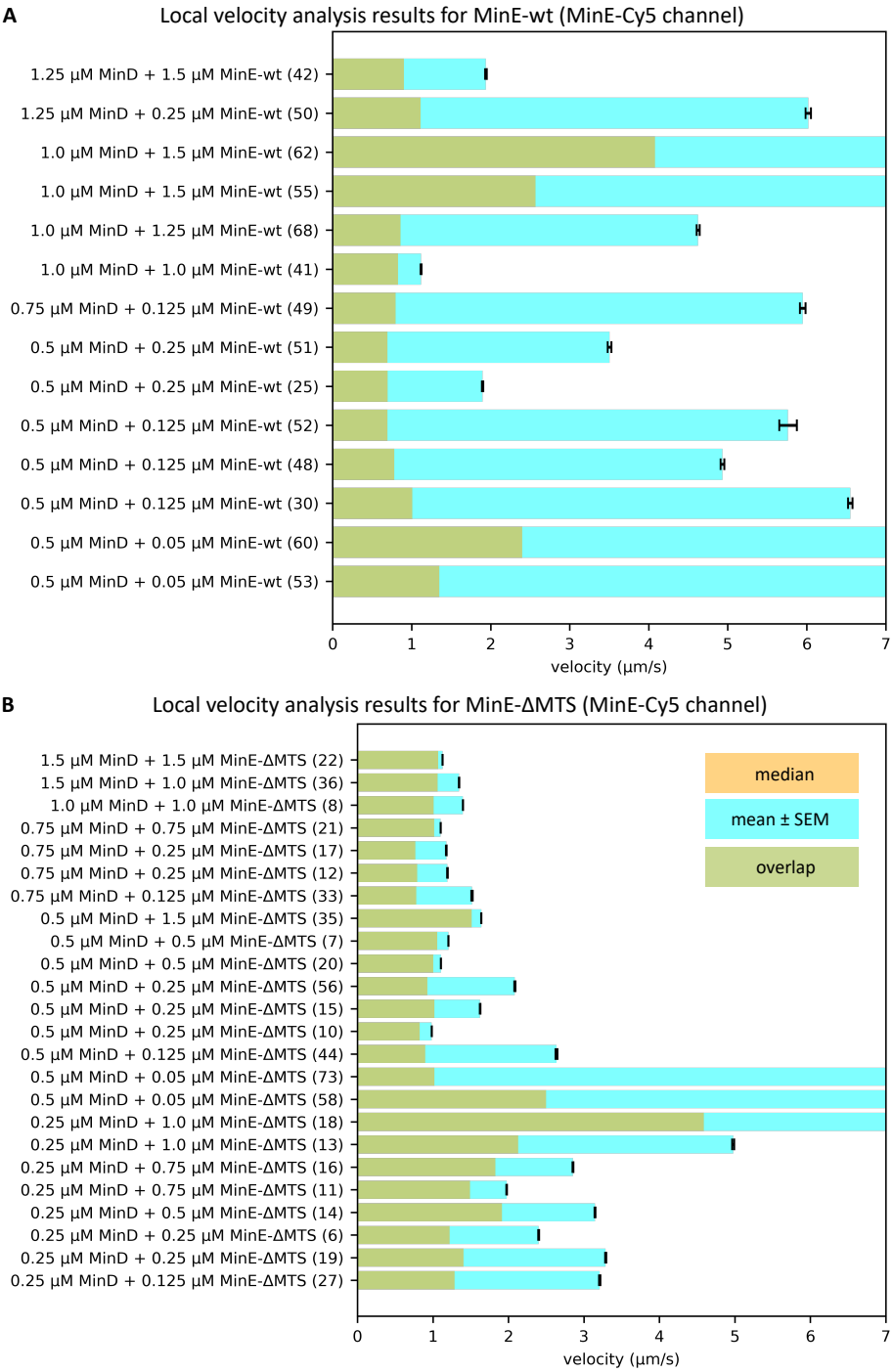


Figure 4.14: An overview of local velocity analysis results for quantification of a given dynamic pattern's characteristic velocity, based on image data for channel MinE-Cy5. The experiment ID (given in brackets) refers to the ID given in table 4.1.

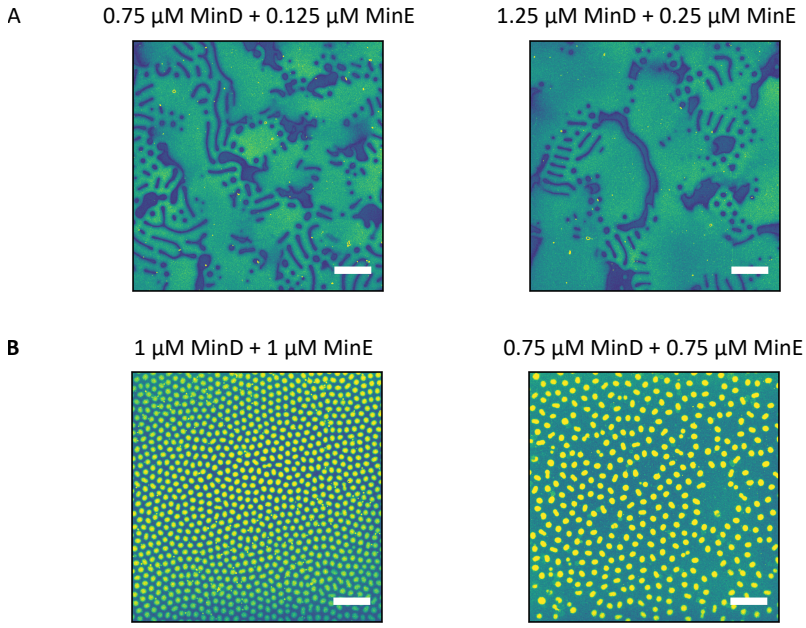


Figure 4.15: **Example images for additional observations. A** Left: 0.75 μM MinD, 0.125 μM MinE (at t=101 min). Right: 1.25 μM MinD, 0.25 μM MinE. **B** Left: 1.0 μM MinD, 1.0 μM MinE (at t= 89 min). Right: 0.75 μM MinD, 0.75 μM MinE (at t= 99 min). Image data for MinD-Cy3. All scalebars indicate 50 μm.

REFERENCES

[1] J. Halatek and E. Frey. "Rethinking pattern formation in reaction–diffusion systems". In: *Nature Physics* 14.5 (May 2018), pp. 507–514. ISSN: 1745-2473, 1745-2481. DOI: 10.1038/s41567-017-0040-5. URL: http://www.nature.com/articles/s41567-017-0040-5 (visited on 11/27/2019).

[2] H. I. Adler et al. "MINIATURE *escherichia coli* CELLS DEFICIENT IN DNA". In: *Proceedings of the National Academy of Sciences* 57.2 (Feb. 1967), pp. 321–326. ISSN: 0027-8424, 1091-6490. DOI: 10.1073/pnas.57.2.321. URL: https://pnas.org/doi/full/10.1073/pnas.57.2.321 (visited on 11/17/2023).

[3] Lawrence I Rothfield and Chun-Rui Zhao. "How Do Bacteria Decide Where to Divide?" In: *Cell* 84.2 (Jan. 1996), pp. 183–186. ISSN: 00928674. DOI: 10.1016/S0092-8674(00)80971-X. URL: https://linkinghub.elsevier.com/retrieve/pii/S009286740080971X (visited on 11/17/2023).

[4] H. Meinhardt and P. A. J. de Boer. "Pattern formation in Escherichia coli: A model for the pole-to-pole oscillations of Min proteins and the localization of the division site". In: *Proceedings of the National Academy of Sciences* 98.25 (Dec. 4, 2001), pp. 14202–14207. ISSN: 0027-8424, 1091-6490. DOI: 10.1073/pnas.251216598. URL: http://www.pnas.org/cgi/doi/10.1073/pnas.251216598 (visited on 11/22/2021).

[5] Martin Loose et al. "Spatial Regulators for Bacterial Cell Division Self-Organize into Surface Waves in Vitro". In: *Science* 320.5877 (May 9, 2008), pp. 789–792. ISSN: 0036-8075, 1095-9203. DOI: 10.1126/science.1154413. URL: https://www.science.org/doi/10.1126/science.1154413 (visited on 11/17/2021).

[6] Kiyoshi Mizuuchi and Anthony G Vecchiarelli. "Mechanistic insights of the Min oscillator via cell-free reconstitution and imaging". In: *Physical Biology* 15.3 (Mar. 1, 2018), p. 031001. ISSN: 1478-3975. DOI: 10.1088/1478-3975/aa9e5e. URL: http://stacks.iop.org/1478-3975/15/i=3/a=031001?key=crossref.18bf29cccb7b7223b142cdbecfc43d0d (visited on 11/22/2019).

[7] Beatrice Ramm, Tamara Heermann, and Petra Schwille. "The E. coli MinCDE system in the regulation of protein patterns and gradients". In: *Cellular and Molecular Life Sciences* 76.21 (Nov. 2019), pp. 4245–4273. ISSN: 1420-682X, 1420-9071. DOI: 10.1007/s00018-019-03218-x. URL: http://link.springer.com/10.1007/s00018-019-03218-x (visited on 11/22/2019).

[8] Sophie Tschirpke et al. *A guide to the in vitro reconstitution of Cdc42 GTPase activity and its regulation.* preprint. Biochemistry, Apr. 24, 2023. DOI: 10.1101/2023.04.24.538075. URL: http://biorxiv.org/lookup/doi/10.1101/2023.04.24.538075 (visited on 11/17/2023).

[9] Fridtjof Brauns et al. "Bulk-surface coupling identifies the mechanistic connection between Min-protein patterns in vivo and in vitro". In: *Nature Communications* 12.1 (Dec. 2021), p. 3312. ISSN: 2041-1723. DOI: 10.1038/s41467-021-23412-5. URL: http://www.nature.com/articles/s41467-021-23412-5 (visited on 06/03/2021).

[10] Sabrina Meindlhumer et al. “Directing Min protein patterns with advective bulk flow”. In: *Nature Communications* 14.1 (Jan. 27, 2023), p. 450. ISSN: 2041-1723. DOI: 10.1038/s41467-023-35997-0. URL: https://www.nature.com/articles/s41467-023-35997-0 (visited on 03/25/2023).

[11] Jonas Denk et al. “MinE conformational switching confers robustness on self-organized Min protein patterns”. In: *Proceedings of the National Academy of Sciences* 115.18 (May 1, 2018), pp. 4553–4558. ISSN: 0027-8424, 1091-6490. DOI: 10.1073/pnas.1719801115. URL: http://www.pnas.org/lookup/doi/10.1073/pnas.1719801115 (visited on 07/28/2020).

[12] Anthony G. Vecchiarelli et al. “Differential affinities of MinD and MinE to anionic phospholipid influence Min patterning dynamics *in vitro*: Flow and lipid composition effects on Min patterning”. In: *Molecular Microbiology* 93.3 (Aug. 2014), pp. 453–463. ISSN: 0950382X. DOI: 10.1111/mmi.12669. URL: http://doi.wiley.com/10.1111/mmi.12669 (visited on 11/29/2019).

[13] Beatrice Ramm et al. “The MinDE system is a generic spatial cue for membrane protein distribution in vitro”. In: *Nature Communications* 9.1 (Dec. 2018), p. 3942. ISSN: 2041-1723. DOI: 10.1038/s41467-018-06310-1. URL: http://www.nature.com/articles/s41467-018-06310-1 (visited on 01/17/2020).

[14] Anthony G. Vecchiarelli et al. “Membrane-bound MinDE complex acts as a toggle switch that drives Min oscillation coupled to cytoplasmic depletion of MinD”. In: *Proceedings of the National Academy of Sciences* 113.11 (Mar. 15, 2016), E1479–E1488. ISSN: 0027-8424, 1091-6490. DOI: 10.1073/pnas.1600644113. URL: http://www.pnas.org/lookup/doi/10.1073/pnas.1600644113 (visited on 11/22/2019).

[15] Philipp Glock et al. “Stationary Patterns in a Two-Protein Reaction-Diffusion System”. In: *ACS Synthetic Biology* 8.1 (Jan. 18, 2019), pp. 148–157. ISSN: 2161-5063, 2161-5063. DOI: 10.1021/acssynbio.8b00415. URL: https://pubs.acs.org/doi/10.1021/acssynbio.8b00415 (visited on 11/05/2021).

[16] Ziyuan Ren et al. *Robust and resource-optimal dynamic pattern formation of Min proteins in vivo*. preprint. Biophysics, Aug. 16, 2023. DOI: 10.1101/2023.08.15.553443. URL: http://biorxiv.org/lookup/doi/10.1101/2023.08.15.553443 (visited on 11/08/2023).

[17] Martin Loose et al. “Min protein patterns emerge from rapid rebinding and membrane interaction of MinE”. In: *Nature Structural & Molecular Biology* 18.5 (May 2011), pp. 577–583. ISSN: 1545-9993, 1545-9985. DOI: 10.1038/nsmb.2037. URL: http://www.nature.com/articles/nsmb.2037 (visited on 11/22/2019).

[18] Sabrina Meindlhumer, Jacob Kerssemakers, and Cees Dekker. “Quantitative analysis of surface wave patterns of Min proteins”. In: *Frontiers in Physics* 10 (Aug. 3, 2022), p. 930811. ISSN: 2296-424X. DOI: 10.3389/fphy.2022.930811. URL: https://www.frontiersin.org/articles/10.3389/fphy.2022.930811/full (visited on 09/19/2022).

[19] Fabai Wu et al. “Multistability and dynamic transitions of intracellular Min protein patterns”. In: *Molecular Systems Biology* 12.6 (June 2016), p. 873. ISSN: 1744-4292, 1744-4292. DOI: 10.15252/msb.20156724. URL: https://www.embopress.org/doi/10.15252/msb.20156724 (visited on 10/07/2023).

[20] Andriy Goychuk and Erwin Frey. “Protein Recruitment through Indirect Mechanochemical Interactions”. In: *Physical Review Letters* 123.17 (Oct. 21, 2019), p. 178101. ISSN: 0031-9007, 1079-7114. DOI: 10.1103/PhysRevLett.123.178101. URL: https://link.aps.org/doi/10.1103/PhysRevLett.123.178101 (visited on 11/29/2019).

[21] Andrea Alessandrini and Paolo Facci. “Nanoscale mechanical properties of lipid bilayers and their relevance in biomembrane organization and function”. In: *Micron* 43.12 (Dec. 2012), pp. 1212–1223. ISSN: 09684328. DOI: 10.1016/j.micron.2012.03.013. URL: https://linkinghub.elsevier.com/retrieve/pii/S0968432812000844 (visited on 03/23/2024).

[22] Yu-Ling Shih et al. “Active Transport of Membrane Components by Self-Organization of the Min Proteins”. In: *Biophysical Journal* 116.8 (Apr. 2019), pp. 1469–1482. ISSN: 00063495. DOI: 10.1016/j.bpj.2019.03.011. URL: https://linkinghub.elsevier.com/retrieve/pii/S0006349519301973 (visited on 10/13/2022).

[23] Beatrice Ramm et al. “A diffusiophoretic mechanism for ATP-driven transport without motor proteins”. In: *Nature Physics* 17.7 (July 2021), pp. 850–858. ISSN: 1745-2473, 1745-2481. DOI: 10.1038/s41567-021-01213-3. URL: http://www.nature.com/articles/s41567-021-01213-3 (visited on 10/05/2021).

[24] Lukas Wettmann, Mike Bonny, and Karsten Kruse. “Effects of geometry and topography on Min-protein dynamics”. In: *PLOS ONE* 13.8 (Aug. 30, 2018). Ed. by Lev Tsimring, e0203050. ISSN: 1932-6203. DOI: 10.1371/journal.pone.0203050. URL: https://dx.plos.org/10.1371/journal.pone.0203050 (visited on 10/13/2022).

[25] Yaron Caspi and Cees Dekker. “Mapping out Min protein patterns in fully confined fluidic chambers”. In: *eLife* 5 (Nov. 25, 2016), e19271. ISSN: 2050-084X. DOI: 10.7554/eLife.19271. URL: https://elifesciences.org/articles/19271 (visited on 11/22/2019).

[26] N. Baranova and M. Loose. “Chapter 21 - Single-molecule measurements to study polymerization dynamics of FtsZ-FtsA copolymers”. In: *Cytokinesis*. Ed. by Arnaud Echard. Vol. 137. Methods in Cell Biology. Academic Press, 2017, pp. 355–370. DOI: https://doi.org/10.1016/bs.mcb.2016.03.036. URL: https://www.sciencedirect.com/science/article/pii/S0091679X16300280.

[27] Guido Van Rossum and Fred L. Drake. *Python 3 Reference Manual*. Scotts Valley, CA: CreateSpace, 2009. ISBN: 1441412697.

5

DESIGNING SURFACE PATTERNS BASED ON DNA OLIGOMERS

In this chapter, we summarize the current state of a new project carried out in collaboration with the theoretical biophysics group of Erwin Frey. The aim of this project is the bottom-up construction of a system based on DNA hybridization that is capable of forming surface patterns, in analogy to the surface patterns formed by Min proteins. The emphasis of this chapter is on the conceptual work that went into the design of the system, while we also describe the initial experimental work that went into it so far.

While we have not yet been able to observe such surface patterns, we have made significant advances in our understanding of what is required for a pattern to emerge out of an initially homogeneous distribution of the system components. We hope to lay the foundation for successfully establishing this as a model system for pattern formation in the future.

This chapter contains contributions from Sabrina MEINDLHUMER, Eva BERTOSIN, Henrik WEYER, Ching Yee LEUNG, Jaco VAN DER TORRE, Alex JOESAAR, Laeschkir WÜRTHNER, Erwin FREY and Cees DEKKER.

5.1. INTRODUCTION

5.1.1. MINIMUM REQUIREMENTS FOR PATTERN FORMATION

Pattern formation has fascinated people throughout history.[1] When Alan Turing published his seminal work on the foundations of reaction-diffusion-based pattern formation in 1952,[2] it provided a starting point for systematic research on this subject in the context of biology. Seven decades later, a plethora of systems have been studied experimentally and theoretically, which at their very core, function by the astonishingly simple mechanism first proposed by Turing.[3] Thanks to the extensive research efforts, we now have a fair deal of understanding on the properties that a system of molecules needs to possess in order to be able to form patterns.

The minimum requirement for pattern formation appears to be a combination of specific intermolecular interactions coupled with a transport mechanism. In many cases, this transport is provided by diffusion, leading to what is referred to as reaction-diffusion systems. Different types of reaction networks are able to produce patterns, so long as they contain some form of nonlinear process.[4, 5] In the case of the Min-protein system, this nonlinearity is presumably provided by the cooperative membrane recruitment of MinD, i.e., the recruitment of MinD-ATP from the bulk by already membrane-bound MinD-ATP. [4]

Here, we argue that the research field of pattern formation would benefit from the bottom-up implementation of a synthetic, DNA-based system that is capable of forming surface patterns, akin to membrane patterns formed by intracellular systems. Fig. 5.1 shows what a pattern-forming system based on DNA oligomers could look like on a conceptual level. Generally speaking, the system would need to be such that it is capable of forming and maintaining concentration patterns on a surface.[4]

So far, Min proteins constitute the most thoroughly studied model system for intracellular pattern formation, not least because they have been shown to be capable of forming both dynamic and static surface patterns on planar lipid membrane.[6, 7, 8]. Systematically varying parameters and gradually extending and improving modeling of this system has lead to a fairly good, though still incomplete understanding of the Min system's underlying mechanisms.[9, 10, 11, 12, 4, 8] The engineering and use of mutant variants of Min proteins is an important strategy for further improving these models,[13, 10, 7, 14] but comes with the technical difficulties of predicting just how a certain modification will affect the protein's action and structure. Here, relying on a DNA-based rather than a protein-based model system would pose significant technical advantages such as the high flexibility and tunability of hybridized DNA nanostructures.[15] Once implemented, such a DNA-based system would allow to systematically modify the components' base sequences and to examine the system's response to the resulting kinetic changes both experimentally and theoretically.[16, 17]

5.1.2. DNA-BASED OSCILLATORS

A similar strategy has been applied in other fields. DNA nanotechnology is a vast research field which comprises the hybridization-driven engineering of 2D- or 3D- structures from DNA oligomers, which are designed to fulfill certain functions. The technical possibility of synthesizing DNA of any sequence allows for a lot of freedom when creating these building blocks, leading to a wide range of applications that have been and continue to be explored.[18, 15, 19] Using DNA as source material for bioengineering poses restrictions due to the limited number of available components, that being four bases with two types of specific pairing (A-T and G-C) versus the 21 amino acids classically available in proteins. However, exactly because of this limitation, the use of DNA also comes with a series of advantages. These include its high sequence-specificity and selectivity, leading to predictability of the resulting 3D-structure as well as of the kinetic properties[18, 15, 19]. Furthermore, components are readily available with commercial providers for biochemical synthesis.

The review by Del Gross et al. (2022)[20] proposes a distinction between "dynamic" and "dissipative" DNA nanotechnology. Here, dynamic DNA nanotechnology refers to systems in which DNA oligomers transition between different hybridization states. Dissipative systems, in contrast, employ enzymes, such as nucleases, which consume energy provided by nucleotide-triphosphates. [20] Notably, biological patterns rely on an energy source such as this, as they operate away from the system's thermodynamic equilibrium.[1] One strategy to achieve oscillatory behavior (or spatial patterning) within DNA-based systems is to employ the action of DNA-specific enzymes (such as polymerases and nickases) for production of a certain DNA-species. In these cases, the reaction requires some form of input (typically toehold-strand invasion by another DNA-strand), and is followed by enzymatic degradation of the reaction products (often by an exonuclease). It has been shown that DNA-based building blocks coupled with enzymatic activity can be employed to create oscillatory behavior in bulk[21] as well as spatio-temporal concentration patterns in one[16, 22] or two dimensions[23]. Visualization is typically done by fluorescent labeling of double-stranded reaction products via intercalating dyes. Coordinated succession of these processes allowed for local accumulation of a reaction product, followed by its degradation. Examples for such reaction networks yielding spatio-temporal patterns are given in references [23, 16, 22]. Notably, pattern-forming systems like these are distinct from most intracellular systems (such as constituted by Min protein) as they rely on local production and degradation. The Min system, in contrast, works with a fixed number of molecules that keep cycling between distinct states, and can hence be described by mass-conserving reaction-diffusion equations.[4]

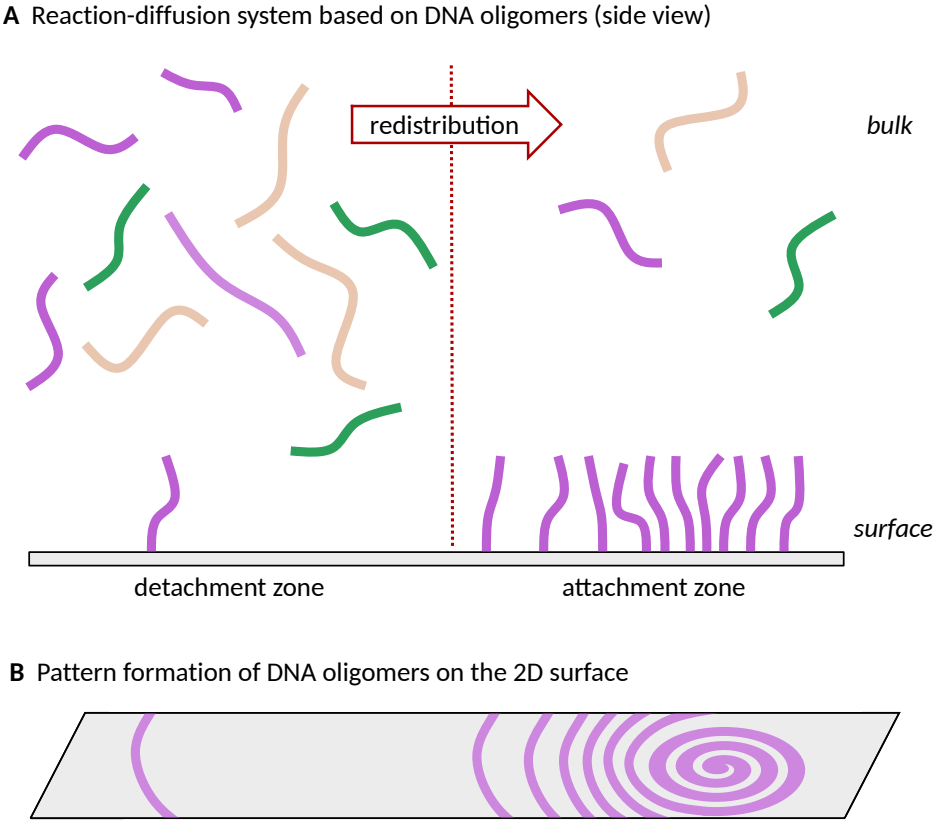


Figure 5.1: **Concept of a mass-conserving reaction-diffusion system based on DNA oligomers. A** We envision a mass-conserving reaction-diffusion system composed primarily of DNA-based components. Similar to intracellular pattern-forming systems such as the Min system, components should be able to cycle between the bulk and the surface. Oligomers in bulk are able to diffuse freely in 3D, while those on the surface should barely diffuse. The reaction kinetics at the surface should be such that gradients in surface concentration are amplified rather than attenuated, allowing for a heterogeneous steady-state to form. This requires some form of a nonlinear process (positive feedback), leading to oligomers that are transported via the bulk from a detachment zone (low surface concentration) to an attachment zone (high surface concentration). The concept is based upon schematics by Halatek et al. (2018)[4]. **B** For a suitable reaction network, patterns should be able to form at the surface. When using fluorescently labelled DNA oligomers, these surface patterns can subsequently be imaged using microscopy techniques.

Furthermore, it has been shown that, even in the absence of enzymes, it is possible to create patterns in bulk by implementing complex DNA-based chemical reaction networks.[24] For example, gradients in a bulk agarose matrix could be achieved in an enzyme-free system by relying on a reaction-diffusion mechanism when providing "fuel" DNA strands from an external reservoir.[25]. Another interesting system is the "rock-paper-scissor" reaction network, which creates oscillatory dynamics in bulk (without any enzymes) by providing the system with metastable DNA-strands that are used as fuel.[26]

In systems such as these, energy is obtained from externally provided components that are gradually converted into an energetically lower state (from "fuel" to "waste" product).[20]

5.1.3. A MASS-CONSERVING DNA-BASED SURFACE PATTERN SYSTEM

As Min proteins constitute the simplest intracellular pattern-forming system currently known to us,[4] it seems logical to use it as a starting point for designing a synthetic system. Vice versa, we expect that research on a synthetic system with controllable and tunable parameters might give us more insight into the Min system, and on how its molecular properties and kinetic rates influence the characteristics of formed patterns. Indeed, a number of important findings in research on the Min system stem from studying mutants of MinD[14] or MinE[13, 10, 7] that have slightly different properties.

For MinE in particular, it was shown that some of its molecular features can be removed in a modular fashion while retaining the system's capacity for pattern formation. For example, Glock et al. (2019) suggested a "minimal motif" version of MinE. [17] A fully synthetic, tunable system would allow for strategic implementation or omission of components and studying the effect thereof – without the risks that come with introducing mutations in proteins where protein purification may fail, protein functionality may be different from what was anticipated, or one often encounters incomplete knowledge on secondary effects that mutations might bring along. In return, this might in the long run help us to gain a better understanding of naturally occurring pattern-forming systems, in particular the Min system.

In the following, we describe our first steps in *de novo* constructing such a synthetic system capable of forming surface patterns from primarily DNA-based building blocks. Notably, we aim to design the system as mass-conserving, i.e., not relying on production and degradation, but able to facilitate the spontaneous emergence of patterns from a set of molecules in a fixed volume when provided with adequate energy input - just as the Min system.

5.2. RESULTS PART I: DESIGN OF A PATTERN-FORMING SYSTEM

5.2.1. COMPONENTS AND MECHANISMS

Looking at the Min system as our starting point, it is apparent that – although this is the simplest pattern forming system in cell biology – there is a lot of complexity hidden within it. Disregarding a list of impactful molecular details (such as MinE's conformational switching[10] or membrane binding[13]) leaves us with a core mechanism, which is often referred to as a skeleton model/network.[10] In this simplified picture, MinD-ATP binds to the membrane, where it cooperatively recruits more MinD-ATP in its immediate vicinity.[27, 28] This is followed by recruitment of MinE, which associates with membrane-bound MinD and stimulates its ATPase activity. When MinD hydrolyses its ATP to ADP, it detaches from the membrane – along with MinE. Back in bulk, MinD can undergo nucleotide exchange, which makes it available again to participate in the next reaction cycle.[4] The full process is outlined in Fig. 5.2A. Taking a look at the intermediate steps required in this model, we can make a list of structures that need to be implemented using methods available to dissipative DNA-nanotechnology:

- Cycling a key component ("DNA-D"): A DNA-based building block which is designed to go through repeated cycles of binding to and unbinding from the surface, akin to MinD.
- An antagonistic component ("DNA-E"): Another DNA-based building block which, akin to MinE, stimulates the surface-detachment of DNA-D.

As the aim is to create surface patterns, the cycling DNA-building block (DNA-D) needs to have some means of specifically and nonlinearly binding to the surface. This can be achieved by covering the surface with single-stranded DNA (ssDNA) that has a chemical end group that allows for binding to a pre-treated surface. For visualization, the cycling MinD-like component can be fluorescently labeled, allowing for observation of potentially emerging patterns on a microscope.

In the following, we present methods and components which constitute potential candidates for implementing these required steps.

5.2.2. STRAND-DISPLACEMENT REACTIONS

DNA strand-displacement reactions (SDRs) constitute a commonly used tool in DNA nanotechnology that accounts for intermediate steps in numerous applications, [24, 29, 30], including DNA-based oscillatory systems[23, 22, 26]. An SDR facilitates the exchange of one partially hybridized strand for another strand. Starting from a set of two strands which are partially hybridized (i.e., consisting partly of a double-stranded and partly of a single-stranded segment), the single-stranded part serves as a "toehold" that allows for the hybridization of another piece of single-stranded DNA of complementary sequence. That newly bound strand can then displace the originally bound complementary strand by strand displacement. SDRs do not require enzymes, but rely solely on the biochemical bindings underlying DNA hybridization. [24, 29, 30]

Including SDRs in our DNA-based pattern forming system seems to be an obvious choice, as it allows for specific binding events (such as DNA-E to surface-bound DNA-D) to be implemented.

5.2.3. HELICASE AS A TOOL FOR DISASSEMBLY

Helicases are DNA-translocating enzymes that convert chemical energy into motor action that overcomes the energy barrier posed by the hybridization of double-stranded nucleic acids to unwind a DNA-duplex. Research on helicases is long-standing and active, not least because of their physiological importance, as they allow other enzymes to access single-stranded regions of formerly double-stranded nucleic acids. [31]

Helicases have been found to come in a lot of variations, such as DNA- or RNA-specific, and they may require single- or double-stranded starting points to initiate their activity. Their "processivity" – describing the number of base pairs that are sequentially unwound by a single helicase – as well as rate can vary strongly. [31]

For the purpose of our DNA-based pattern forming system, incorporating a helicase would provide some of the core-functionalities of the Min system, most specifically the reversal of a previous surface binding event under energy consumption. However, it also means introducing a DNA-processing protein component. To minimize complications, we aimed to find a reliable helicase that features a high processivity that we could include into the pattern-forming reaction scheme. The choice fell on the RepX "superhelicase" engineered by the Ha Lab and introduced by Arslan et al. (2015) [32]. *E. coli's* Rep is a DNA helicase that requires a free 3' single-stranded segment to load and that subsequently unwinds an adjacent hybridized region.[31, 32] While Rep had previously been found to exhibit a low processivity *in vitro*,[33] crystal structures pointed towards the importance of a flexible domain (2B) which was found to allow for a conformational change between two distinct states: an open and a closed state.[34] The Ha Lab could show that upon locking Rep into the closed "RepX" confirmation via internal cross-linking of the 2B domain, the increased processivity significantly, both compared to the Rep wildtype protein and the open "RepY" mutant. RepX was found to exhibit a processivity of up to 6000 base pairs (compared to 50-80 base pairs for Rep) and features an average speed of 136 base pairs per second.[32] The RepX mutant thus is an excellent candidate for incorporation into a DNA-based pattern-forming system due to its high processivity and overall reliability.

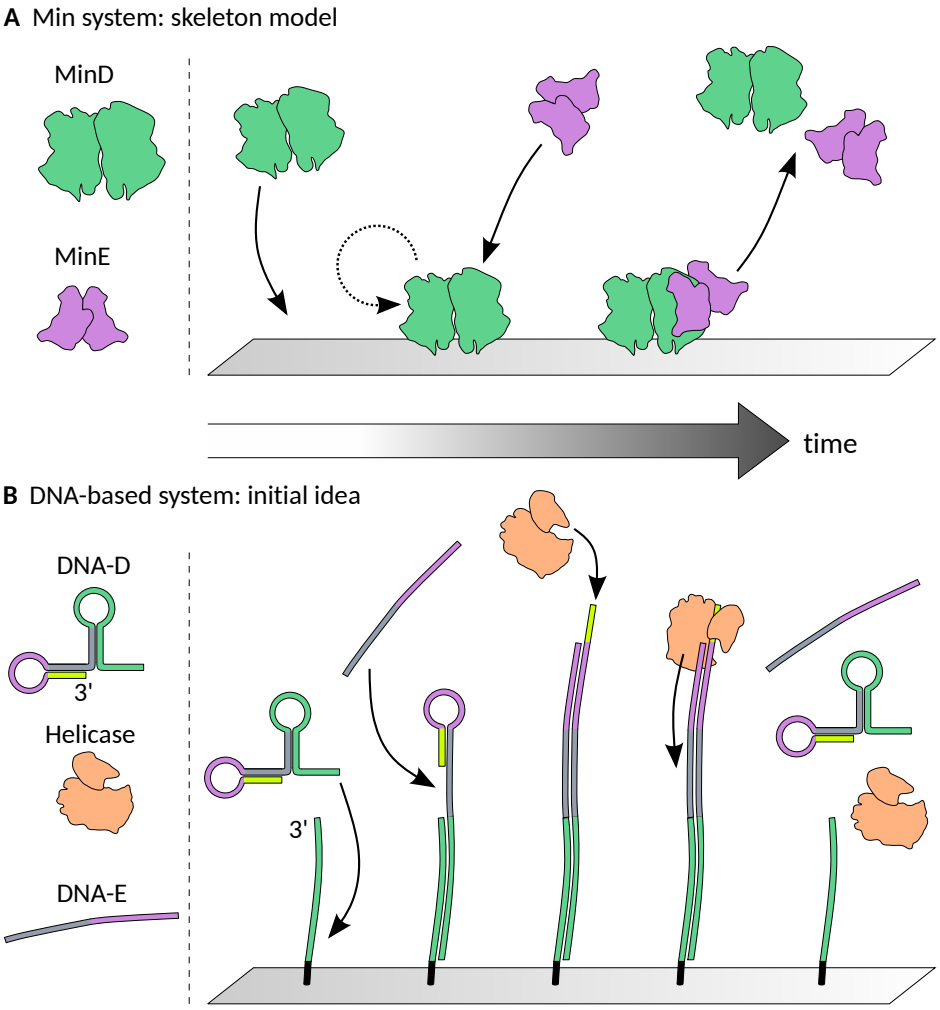


Figure 5.2: **Tentative implementation of a membrane attachment/detachment cycle.** **A** Simplified schematic representing the membrane attachment/detachment cycle of the Min system based upon the skeleton model.[10, 8]. MinD binds (cooperatively) to the surface (i.e. a lipid membrane), followed by recruitment and binding of MinE. MinE stimulates MinD's ATPase activity, leading to ATP-hydrolysis and membrane detachment of MinD. In bulk, MinD undergoes nucleotide exchange, whereupon it can subsequently undergo another cycle. The cooperative membrane recruitment is not visualized in this representation. **B** First design idea for DNA-based pattern-forming system. MinD is represented by a DNA-based building block (DNA-D). MinE is represented by a helicase that consumes energy by ATP hydrolysis. DNA-D from bulk binds to a surface-bound DNA-anchor and in doing so, partially unfolds. Subsequently, DNA-E opens up the remaining secondary structure of DNA-D via strand-displacement. A helicase recognizes the free 3' end, binds and removes DNA-D as well as DNA-E from the surface-anchor (under ATP-hydrolysis). This design was considered but finally disregarded on the basis of it not fulfilling the requirements for pattern formation. Depictions in **A** and **B** are schematized and not drawn to scale.

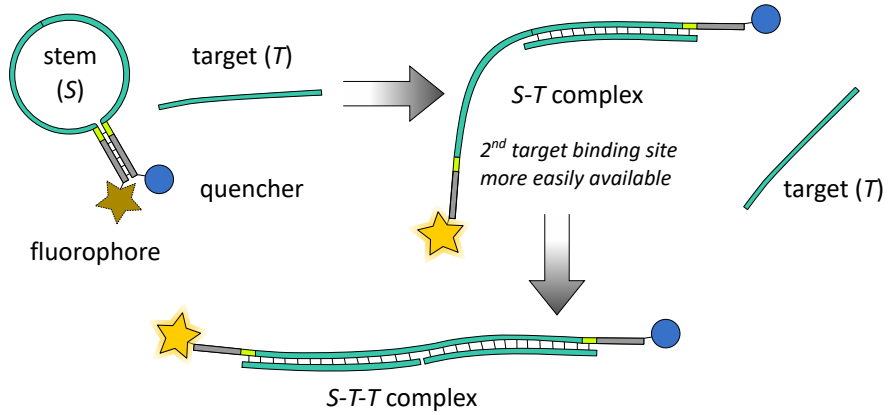
5.2.4. INITIAL DESIGN

Fig. 5.2B shows an overview on one of the first design ideas that we developed for this system. In this design, the surface is covered by linear DNA oligomers that serve as anchoring points for binding DNA-D, in analogy to the phospholipid bilayer that provides a reaction platform for initial binding of MinD. DNA-D can be implemented as containing two loops and two self-hybridized stems, with a single-stranded segment that can act as a toehold. One of these stems would need to be complementary the DNA-E, the other to the surface anchoring strand. Surface attachment of DNA-D would lead to opening up one of the latter of its two stems via strand-displacement, hence exposing part of the sequence complementary to DNA-E and leading to subsequent attachment thereof.

The cycle would be concluded by a helicase disassembling the entire DNA-D/DNA-E hybrid, leading to surface detachment. In this scheme, certain functions of MinD (ATPase activity) and MinE (triggering surface detachment) would be fulfilled by the helicase. Notably, surface detachment could only happen upon binding of DNA-E as its attachment to surface-bound DNA-D would provide the free 3' end that is required for the helicase to load.

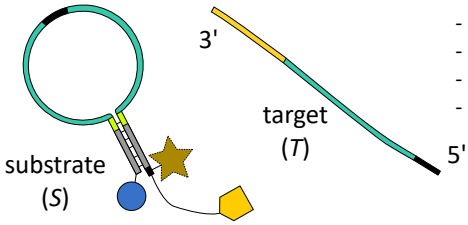
All in all, this system seems to be present a possible replication of the basic Min reaction cycle, as visualized by comparing Fig. 5.2A and B. However, further consideration indicates that this system likely would not be able to form patterns, as it does not contain a nonlinear element within its reaction scheme.[4] Hence, despite the apparent similarity, we expect that such a system will not produce surface patterns.

A Cooperative mechanism implemented using DNA *adapted from Simon et al (2014)*



S: 5' - *fluorophore* - *(C)$_6$ linker* - GGGTGG GTTCACTGTCTTA GTTCACTGTCTTA CCACCC - 3' - *quencher*
T: 5' - G TAAGACAGTGAAC C - 3'

B Modifications for re-implementation as DNA-based pattern-forming system



- extend target at 3' with poly-dT for RepX (yellow)
- add $(T)_5$ tail at 5' of target (black)
- add $(T)_5$ spacer at center of stem (black)
- add biotin-linker for surface-binding

S: 5'- *quencher* - GGGTGG GTTCACTGTCTTA $(T)_5$ GTTCACTGTCTTA CCACCC - *internal Cy5* - 3' - *biotin*
T: 5' - $(T)_5$ GTAAGACAGTGAACC $(dT)_{15}$ -3'

Figure 5.3: **A** DNA-based cooperative mechanism implemented by Simon et al. (2014) [35]. A linear "target" (*T*) binds to a partly hybridized "stem" (*S*) via a toehold and opens up its previously hybridized region. Now, a second target can bind without having to overcome the energy barrier given by opening the double-strand. Hence, the second target can bind cooperatively. The Hill coefficient was shown to depend on both the target-length and the stability of the double-strand. As a starting point, we consider the 5 GC symmetric cooperative molecular beacon and the 14-base target presented in the paper. **B** A number of modifications were made to the published sequence[35] in order to use them in an experimental DNA-based pattern-forming system. The idea of placing a fluorophore/quencher pair at the 3'/5' ends of the stem was kept, with an additional biotin-linker being added for surface binding via streptavidin later on. A poly-dT tail was added to allow for the RepX helicase to act on the *S*-*T*-*T* hybrids later[32], and poly-T spacers were added at the center of the stem as well as the 5' end of the target. Later, another fluorescent label (Cy3) would additionally be added to the target (not shown). Note that all depictions in **A** and **B** are schematized and not drawn to scale.

5.2.5. COOPERATIVITY

Below, we present how the design idea was modified to include a nonlinear element in the form of cooperative binding. Cooperativity constitutes an integral property of many pattern-forming reaction networks.[36] We reviewed the literature for implementations of cooperative behavior using DNA hybridization and found that Simon et al. (2014) [35] had introduced an example of this. Their design features a partially hybridized strand that forms a loop, referred to as "stem" ("*S*") as well as a single-strand "target" ("*T*"), which is the reverse complement to one half of *S*. The single-stranded loop part of *S* can hence act as a toehold, inducing the hybridized segment to open up and thus allow for the second *T* to bind. [35] See Fig. 5.3A for an illustration of the design by Simon et al. (2014) [35] and their strategy for cooperative target binding.

This system effectively implements cooperative binding of *T* to *S*, as the first *T*'s binding facilitates faster binding of the second *T*, as the latter no longer has to overcome the energy barrier that is associated with opening up the double-stranded hybridized segment. In order to allow for experimental detection of the open fraction via fluorescent signal in bulk assays, a fluorophore/quencher pair was placed at the 3'/5' ends of *S*, respectively. [35] This method was found to be a suitable starting point for design of a DNA-based pattern-forming system, not least because it fits the idea of implementing a minimal system, but also because it allows for controlled modification.

Notably, it was shown that lowering the energy gap between the two sequential binding events (via weakening of the hybridized stem or shortening T) led to lower Hill coefficients. For a 14-base target and a stem containing 5 GC pairs, Simon et al. (2014) measure a Hill coefficient of 1.94 ± 0.17.[35] Starting from these published sequences, it is possible to image a tentative design as comprising a RepX DNA-helicase, a 14-base target (*T*) modified to carry a 3' overhang for helicase-attachment, and a hybrid stem (*S*) to act as a substrate for cooperative binding. The modifications of the design by Simon et al. (2014) for surface-binding, fluorescence readout and helicase attachment are given in Fig. 5.3B. Fig. 5.4A shows an illustration of these components, Fig. 5.4B provides an overview of the reaction scheme as we expect it to occur.

An aspect to consider here is that the system described by Simon et al. (2014) [35] was designed to operate in thermodynamic equilibrium. However, pattern formation happens outside the thermodynamic equilibrium.[5] What is essential is for the second strand to have a higher attachment rate than the first strand, implying cooperative behavior outside of equilibrium conditions.

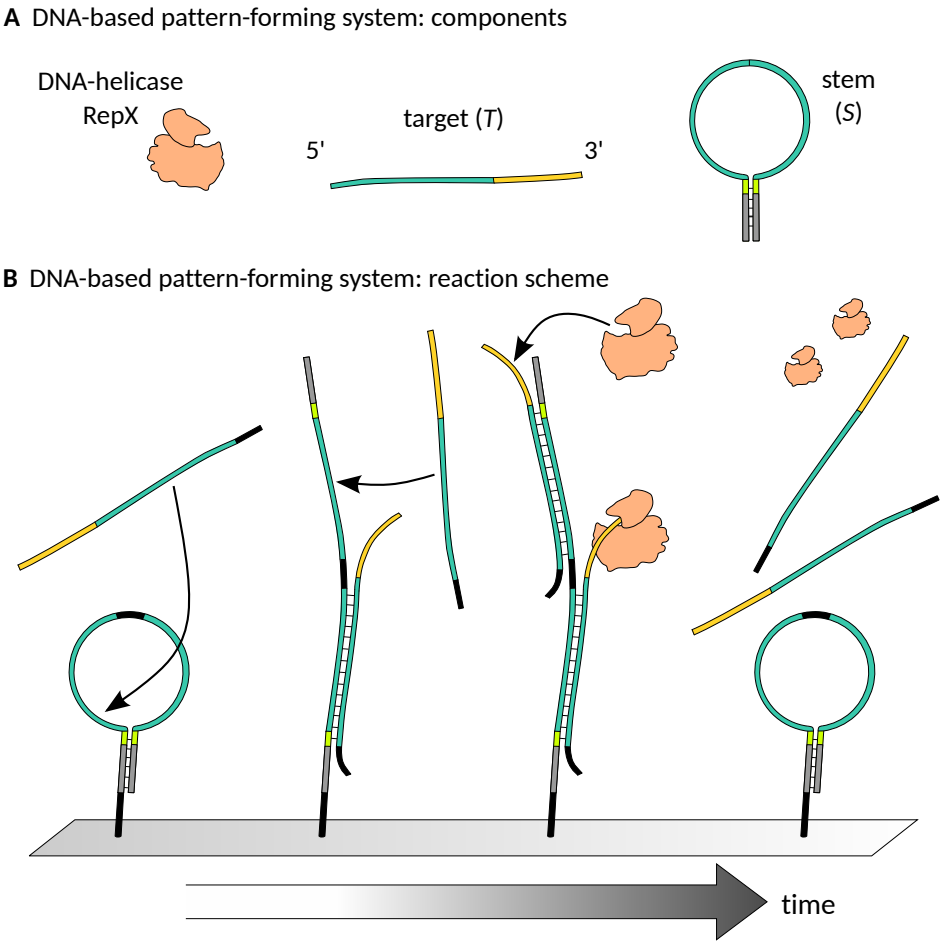


Figure 5.4: **Tentative implementation of a membrane attachment/detachment cycle.** **A** A simplified overview of the main components of our tentative design of a DNA-based pattern-forming system, disregarding modifications (such as fluorescent labels/quenchers): A RepX DNA helicase (a kind gift by Taekjip Ha) [32], a single-stranded sequence T and a single-/double-strand hybrid S [35]. **B** An illustration of the reaction scheme as it is expected to occur at a surface covered with S:T from the bulk binds to surface-bound S via a toehold, opening its double-stranded region and rendering the second binding site more readily accessible to the attachment of another T from the bulk. Note that all depictions in **A** and **B** are schematics and not drawn to scale.

5.2.6. TWO-STEP DETACHMENT MODEL

Before characterizing the kinetics of this system, we first turned to simulations to take a more generalized look at the reaction scheme and determine whether additional modifications would be necessary for the components shown in Fig. 5.3A to act as a pattern-forming system. The Frey Group (work mainly done by Henrik Weyer, Ching-Yee Leung and Laeschkir Würthner) captured the essence of the tentative design in a reaction scheme as shown in Fig. 5.5A, and analyzed it with regard to its capacity for pattern formation by performing a linear stability analysis. [4, 37, 5].

Although their model included the cooperative binding of target (*T*) to surface-bound substrate (*S*), no pattern-forming instability could be found. Hence, it was concluded that the reaction scheme constituted a linear sequence of events (first *T* binds, second *T* binds, *H* binds, both *T* are removed in one step) – but not a feedback loop. Accordingly, the system would not be able to produce reaction-diffusion patterns.

Remarkably, however, inclusion of a two-step detachment rather than single-step (i.e. sequential) detachment of both *T* segments changed this result. As illustrated in Fig. 5.5B, a helicase (*H*) that removes *T* from an *S*-*T*-*T* complex subsequently unbinds from the remaining *S*-*T*-complex, rather than proceeding its action and removing a second *T*. In the illustration of the modified reaction scheme, the additional pathways emerging from this additional requirement are highlighted in orange. As the surface density of *T* increases, more *H* is occupied in the orange circle in Fig. 5.5B (which does, however, not lead to a return of *S* into its unoccupied state). Consequently, there is less *H* available for participation in the turquoise circle in Fig. 5.5B (which would lead to full diassembly of the *S*-*T*-*H* complex), creating a double-negative feedback in the detachment of *T* from *S*.

For the required two-step detachment to be experimentally realized, we re-visited the design and sequences shown in Fig. 5.3 and considered how to modify it accordingly. As also shown in Fig. 5.4A, we opted to introduce a spacer at the center of the substrate loop, and added an extension at the 5' end of the target. With these additions, the reaction should indeed occur as illustrated in Fig. 5.4B: Rather than proceed from one target directly to the next, the helicase should now slide off after unbinding the target and be free to diffuse away.

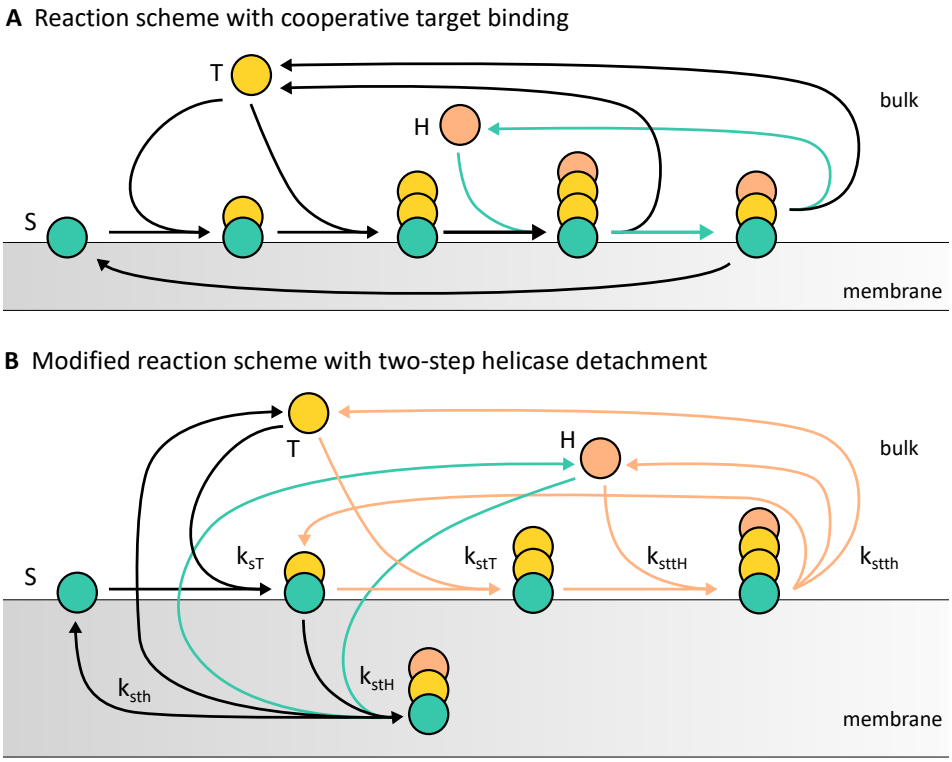


Figure 5.5: **Reaction scheme of DNA-based pattern forming system as conceptualized by Frey Group.** *S*, *T* and *H* correspond to substrate, target and helicase. **A.** Sequential detachment model: *T* from the bulk cooperatively binds to surface-bound *S*. *H* from the bulk binds to surface-bound *T* and takes both *T*s off sequentially. **B.** Two-step detachment model: *T* from the bulk cooperatively binds to surface-bound *S*. *H* from the bulk binds to surface-bound *T*, but cannot take both bound *T*s off in one action. Instead, removal of either *T* leads to release of *H* into the bulk. Consequently, the action of two *H* is needed for both *T*s to be removed and *S* to revert into its fully closed state.

5.3. RESULTS PART II: EXPERIMENTAL TESTING OF THE DNA-BASED SYSTEM

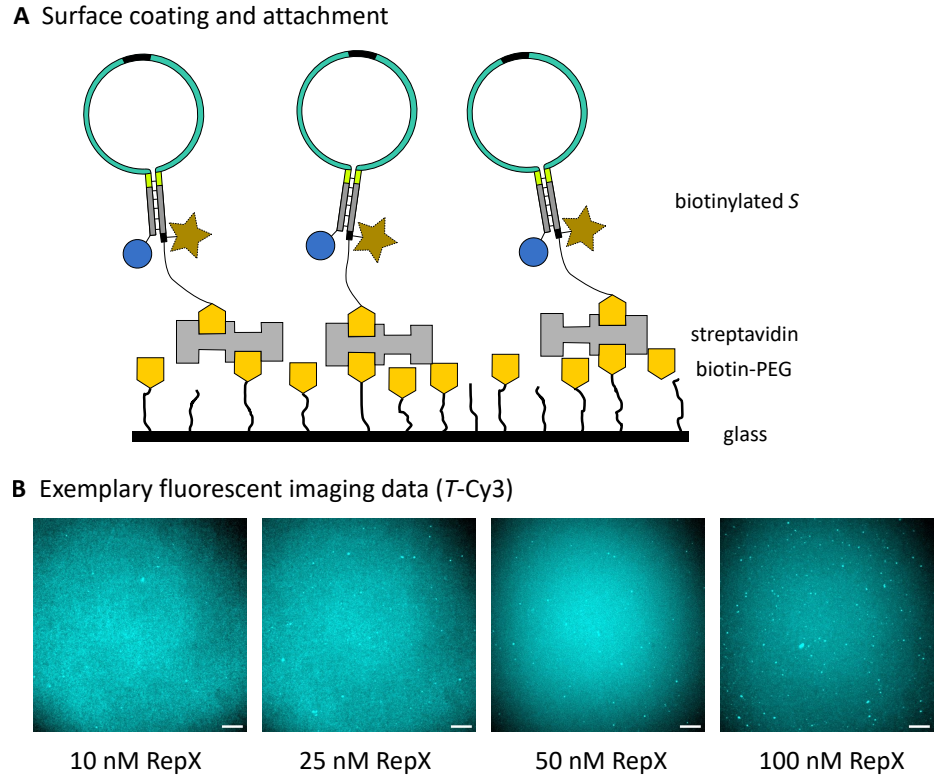


Figure 5.6: **A** To construct sample chambers, glass surfaces were thoroughly cleaned, treated with aminosilanization and coated in biotin-PEG. Following incubation of streptavidin, biotinylated *S* was injected and bound to the surface. **B** Examples of snapshots of some of the conditions tested for pattern formation. 400 nM *T*-Cy3, 5 mM ATP, 5 mM phosphoenol pyruvate (PEP) + 0.015 mg/mL pyruvate kinase (PK) for ATP regeneration, concentration of RepX as indicated. Scale bars 10 μm.

5.3.1. TESTING THE SYSTEM WITH SURFACE FLUORESCENT IMAGING

The sequences *S* and *T* as denoted in Fig. 5.4A were used including modifications for fluorescent imaging (fluorescent label Cy5 and quencher on *S*, fluorescent label Cy3 on T) and additionally a biotin-linker on *S* to function as anchoring point for surface attachment. The RepX helicase was purified and cross-linked as described by the Ha Lab [32]. For preparation of the reaction surfaces, glass slides were cleaned, pre-treated and coated with biotin-PEG (see Methods 5.4 for details). Before the experiment, the coated

glass slides were used to define several individual sample channels of roughly 70 μm height, into which aqueous solutions could be injected. These channels were subsequently incubated with streptavidin and biotinylated *S* to prepare the reaction surface for the DNA-based pattern-forming system, as illustrated in Fig. 5.6A.

Different concentration ratios of *T* and RepX were tested in these sample channels with an *S* coating. Fluorescence imaging of the device's bottom surface was performed for both *S*-Cy5 and *T*-Cy3 using spinning-disc confocal microscopy in order to check for potential surface pattern formation. Only homogeneous surface intensities were obtained. So far, we thus were unable to observe any spatial or temporal pattern formation in any of the tested conditions. Examples of acquired images for different ratios of *T* and RepX are shown in Fig. 5.6B.

5.3.2. TESTING KINETIC RATES WITH BULK FLUORESCENCE

In order to obtain quantitative information on our implementation of the DNA-based pattern-forming system (importantly, on its reaction rates), we performed a series of bulk measurements via plate-based fluorescence assays. For this purpose, we used *S* modified with a fluorescent label (Cy5) and a quencher, but without biotin, as well as *T* without any modifications. We performed fluorescence measurements in bulk for different concentrations of *S*, *T*, RepX and ATP, for different buffer conditions, and measured the fluorescence signal of unquenched *S*-Cy5, i.e. the combined fraction of *S*-*T* and *S*-*T*-*T*.

Using the buffer conditions suggested for RepX (100 mM Tris pH 8.0, 15 mM NaCl, 10 mM $MgCl_2$)[32], we tested whether we could reproduce the Hill coefficient of 1.94 ± 0.17. [35] Results of four experiments are shown in Figs. 5.7A-D. Depending on the experiment, we measure Hill coefficients ranging from 1.35 up to 2.57. While there is significant variation among individual results, all experiments indicated cooperativity, i.e. a Hill coefficient larger than 1. For experiments Fig. 5.7C and D, for which a higher coverage of data points at the upper end of the slope was chosen than for those shown in A and B, the results for the Hill coefficient were more comparable to the published value.

Next, we performed a series of fluorescence measurements of *S* (with a fluorophore-quencher-pair), *T* and RepX. Measurements like these, along with cooperativity assays (Fig. 5.7), are going to be the foundation of further investigations of the system, as will be described in section 5.3.3. First, keeping constant concentrations of *S* and *T*, we varied the concentration of RepX, as show in Fig. 5.8A, and monitored Cy5 fluorescence intensity of the course of a few hours.

We observed that within the few minutes that had passed between mixing of all samples and measuring them on the plate reader, the reaction had already progressed to a point where fluorescence in samples with high RepX concentration was clearly lowered compared to samples with no or less RepX. Here, lower fluorescence means more quenching, as RepX removes bound *T* from *S*, which subsequently reassumes its partially self-hybridized state. Further, within roughly one hour, all fluorescence traces approached

the baseline (without Repx), indicating that activity had ceased. This posed the question of whether ATP levels could be a limiting factor for helicase activity in this setting.

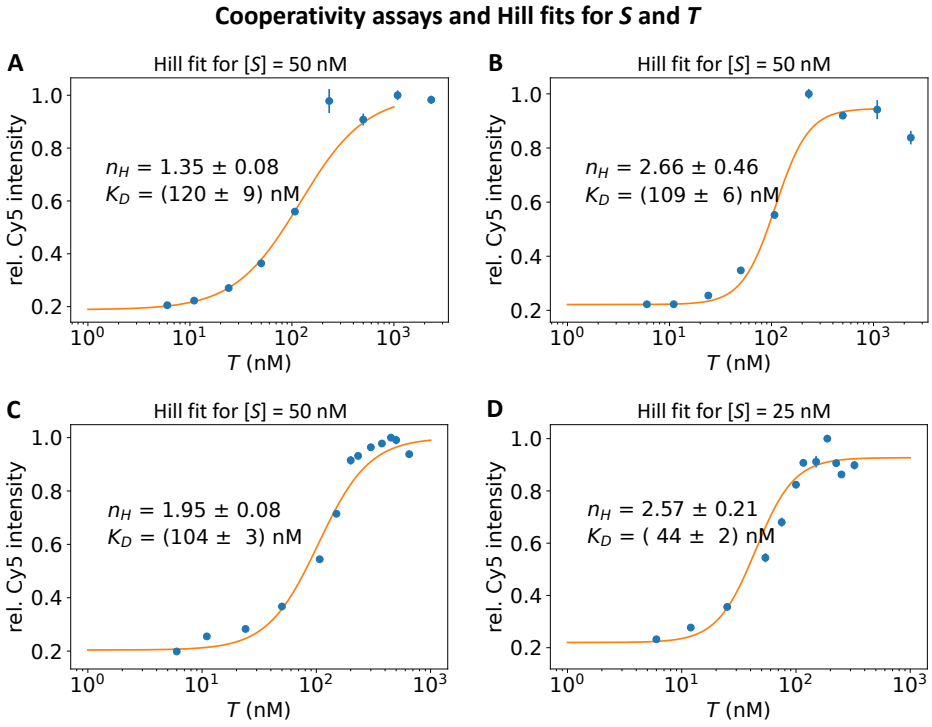


Figure 5.7: Results of cooperativity assay (varying $[T]$ for constant $[S]$) for 4 independent experiment, with each data point in every experiment being an average of technical triplicates of 3 parallel sample chambers of 50 μL volume. S and T buffered in 100 mM Tris pH 8.0 (21°, 15 mM NaCl, 10 mM $MgCl_2$. Measurements taken at room temperature after one hour of incubation. Hill equation was defined as $\Theta(x,\Theta_0,\Theta_H,n_H,K_D) := \Theta_0+(\Theta_H-\Theta_0)*x^{n_H}/(K_D^{n_H}+x^{n_H})$, with x denoting the concentration of ligand (i.e. target), n_H the Hill-coefficient, K_D the equilibrium dissociation constant, Θ_0 the intensity value at $x = 0$ and Θ_H the intensity for saturating conditions. Results for K_D and n_H shown along with the plots.

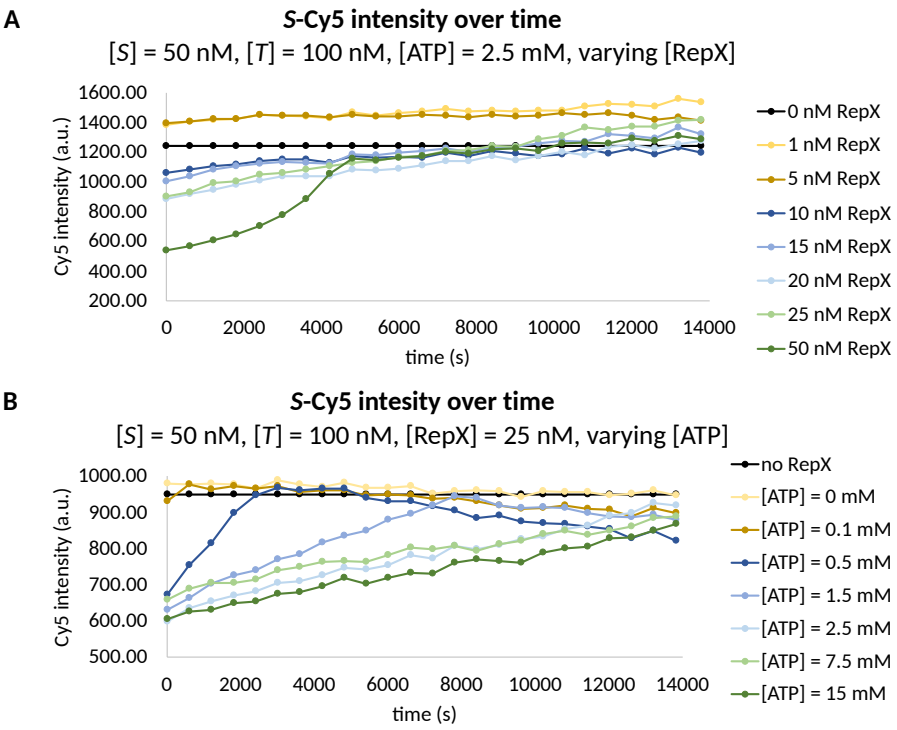


Figure 5.8: **A** Results of fluorescence intensity measurements in bulk over time for varying [RepX] for constant [*S*] and [*T*] at constant ATP concentration of 2.5 mM. **B** Results of bulk measurements for constant [*S*], [*T*] and [RepX], with varying ATP concentration. For both **A** and **B**, each data point is derived as an average of technical triplicates of 3 parallel sample chambers of 50 μL volume, error bars not shown. To account for bleaching and evaporation over the course of several hours of measurement, we assumed samples without RepX to stay at constant fluorescent value and under this assumption, re-scaled all value accordingly. All components were buffered in 100 mM Tris pH 8.0, 15 mM NaCl, 10 mM $MgCl_2$, and measurements were taken at room temperature after pre-incubation of *S* and *T* for about one hour and about 30 minutes after addition of RepX.

Therefore, to assess the risk of ATP depletion, we also performed measurements for constant concentrations of *S*, *T* and RepX, but different amounts of ATP. The results are given in Fig. 5.8B as fluorescence (Cy5) intensities over time. The traces show that for higher ATP concentrations, it does indeed take considerably longer, i.e. several hours, for the fluorescence to return to the baseline (which corresponds to *S* and *T* without RepX). For concentrations of 2.5 mM ATP and higher, fluorescence traces are comparable. Hence, we conclude that ATP depletion could indeed pose an issue for concentrations lower than 2.5 mM, which needs to be taken into account for all experiments.

5.3.3. SIMULATION-GUIDED SEQUENCE REDESIGN

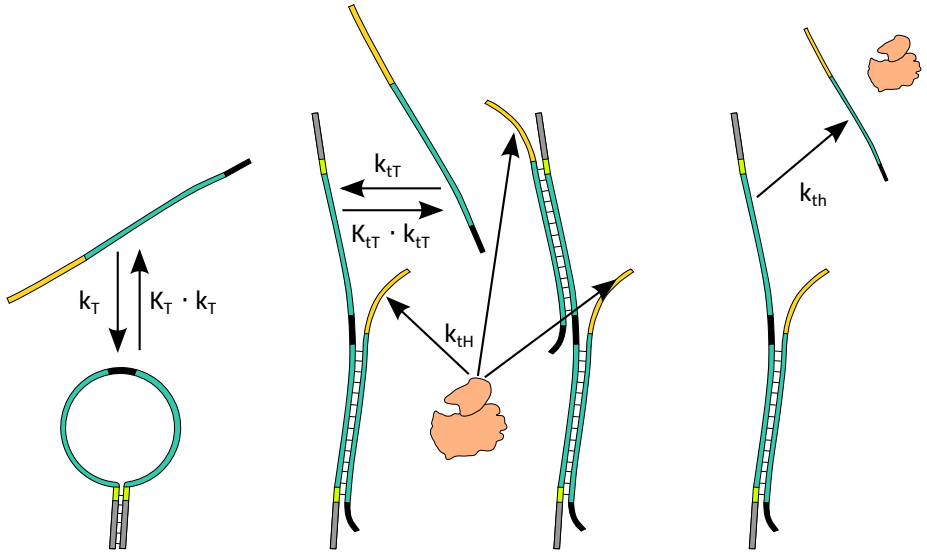


Figure 5.9: The DNA-based system in its current form contains the following free reaction parameters: k_T, K_T, k_{tT}, K_{tT}, k_{tH}, k_{th}.

Fig. 5.9 provides an overview on the free reaction parameters of the DNA-based system in its current design. In principle, the dissociation constants K_T and K_{tT} can be obtained from assays such as shown in Fig. 5.7A-D, kinetic rate parameters k_T, k_{tT} and k_{tH} can be fitted based on data such as shown in Fig. 5.8A and using values for a fixed time point (for example t=6000 s). However, as not all required information is experimentally accessible yet, simulations have to partially rely on estimated or literature values.

Depending on how these parameters are chosen, the outcome can be qualitatively different (i.e. patterns/no patterns) and quantitatively different (i.e. for which concentration ratios patterns are expected). When relying primarily on literature values (assuming K_T/K_{tT}=1050 based on Simon et al., 2014 [35] and k_{th}=2/s based Arslan et al., 2015 [32]), simulations predict that no pattern formation will occur. In contrast, when relying on equilibrium constants provided by the software tool NUPACK[38] , simulations indicate that with the current sequences, patterns are indeed possible under suitable conditions – that being low bulk height and a high density of S on the surface.

nupack.org, Copyright 2006-2024 Caltech, accessed 2024/01/23

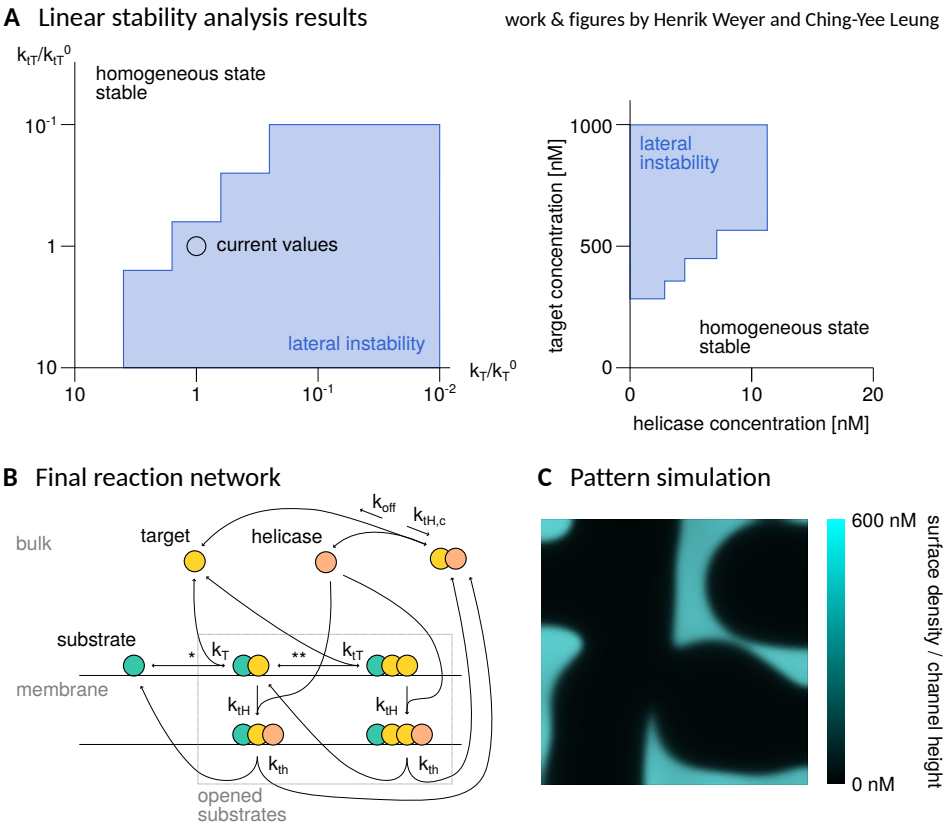


Figure 5.10: **Linear stability analysis and simulations of DNA-based pattern forming system as performed by Frey Group. Work performed by Henrik Weyer, Ching-Yee Leung and Laeschkir Würther under the supervision of Erwin Frey. Figures prepared by Henrik Weyer and Ching-Yee Leung. A.** Left: Linear stability analysis indicates the occurrence of lateral instabilities for a range of kinetic parameters. The fitted values for parameters obtained from bulk measurements indicate, that pattern formation is potentially possible for the current sequence design. Right: The expected concentration regime of target and helicase concentration, within which a lateral instability occurs. **B** The symbol * denotes dissociation constant K_T, the symbol ** denotes the dissociation constant K_{tT}. K_T = 0.01 nM, K_{tT} = 0.002 nM, k_T^0 = 0.0006/2 nM-1s-1, k_{tT}^0 = 0.003/2 nM-1s-1, $k_{tH,c}$ = 0.09 nM-1s-1, k_{tH} = 0.09/2 nM-1s-1, k_{th} = 2 s-1, k_{off} = 0.5 s-1, ρ_S = 2000 nM (eff. substrate concentration), D_m = 0 µm2s-1 (membrane diffusion), D_c = 50 µm2s-1 (bulk diffusion). **C** Pattern simulation result from finite-element method on 2D domain with Comsol Multiphysics 6.1. Opened stem oligomers are shown. ρ_T = 500 nM (average total target concentration), ρ_H = 10 nM (average total helicase concentration), D_m = 0.0003 μm2s-1, k_T $k_T^0/4$, $k_{tT} = k_T^0$, T = 104 s (simulation time), L = 100 μm (side length of simulation domain).

Figure 5.10 (kindly prepared by Henrik Weyer and Ching-Yee Leung) provides an overview on the current status of simulation results Figure 5.10A shows the results of linear stability analysis, which is a method that indicates where within the parameter space patterns can emerge spontaneously. In the left plot, shaded areas show ranges of kinetic in which pattern formation occurs. In the right plot, the same is shown for T versus RepX concentration, which is particularly helpful as a guidance for future experiments. Figure 5.10B shows the final reaction network that was used for simulations. Notably, Figure 5.10C shows a simulation result of a surface pattern that is predicted for the currently assumed kinetic parameters of the system.

Based upon the kinetic parameters fitted for the system based on fluorescence measurements in bulk (such as shown in Fig. 5.8), the current result is that the design is in principle capable of pattern formation, but is situated at the edge of the pattern-forming parameter space (Fig. 5.10A). However, measurement errors and fitting uncertainties could shift the system in either direction – meaning, that in reality it could be located slightly deeper inside the pattern-forming regime as well as just outside of it. Hence, at the moment, while it cannot yet rigorously be concluded whether the system with its current sequence design is going to be able to produce pattern in actual experiments, simulation results indicate that it should be possible. A slight redesign of the so-far used DNA sequences is under consideration, with the intent to find parameters that locate the system into a more robust pattern-forming regime.

5.4. DISCUSSION & OUTLOOK

In this chapter, we summarized the current status of an ongoing project that aims to establish a synthetic, DNA pattern-forming system based a mass-conserving reaction-diffusion mechanism. Starting from conceptual work on a sketch board, we made multiple iterations to end up with a design for such a system which should be capable of forming surface patterns, given the right conditions.

As initial experimental work did not yet yield successful observation of patterns, it became evident that finding the set of (ratios of) concentrations for generating patterns with this synthetic system is a non-trivial pursuit, given the very large multi-dimensional parameter space involved. Screening conditions at random without any starting point within the parameter space clearly harbors the risk of missing out on patterns which might emerge either at different conditions, or at tested conditions but at an unknown time or length scale. Hence, we turned to simulations to guide us in our search for patterns within the wide parameter space. For this, a thorough quantification of the system's parameters such as kinetic rates is needed to provide information that can be used in simulations to deliver a more accurate outcome. While only experiments can in the end reveal whether our approach is functional, simulations can predict concentration ranges and help us determine which system parameter would increase the likelihood of pattern formation. The success thereof thus critically depends on continued tight collaboration between experimental and theoretical scientists.

As the capability of our components' base sequences for pattern formation is in question, we plan to design and order a series of alternative sequences for experimental verification. We have designed such sequences via random modification (replacement or addition of bases) and computation of their equilibrium constants using NUPACK[38]. The next step will be to perform extensive bulk measurements of these candidates and determine, whether in our experimental setting, they actually push the reaction parameters in a direction which favors surface pattern formation.

Practically, we plan to use intercalating dyes with high specificity for double-stranded versus single-stranded DNA. Using intercalating dyes instead of labeled DNA will significantly reduce the cost of the oligomers and therefore allow for a broader and more thorough screening. Once the most favorable candidates have been identified, these can be ordered with modifications required for surface attachment and tested for pattern formation using fluorescence microscopy.

Other practical aspects to consider are the surface coating and height of the sample chamber. Current simulation results (not shown) indicate that the chance for surface pattern formation would increase considerably for lower bulk height (ideally, of a few micrometers) and higher surface coverage of stem oligomers (*S*). Lower bulk heights can be achieved by using thinner spacers between the top and bottom glass slides. Increasing the coverage of *S* on the reaction surface might require an alternative method of coating and will require further investigation. Our current surface coating strategy relies on pegylation with biotin-PEG, which according to preliminary estimations based on fluorescence imaging yielded a surface coverage in the order of about 1000 functional stem oligomers per μm^2 (data not shown). Increasing this number by about a factor 10 – either by optimization of the current surface coating method, or by using another strategy – would significantly enhance the chance of pattern formation.

While we have so far not been able to create surface patterns with this system, we have made important first steps in its development. We have explored experimental and simulation tools, which we can continue to use in the future of the project. We are convinced that the research field of (intracellular) pattern formation would greatly benefit from the implementation of such a system, as it would allow for controlled modifications and systematic coordination of theoretical and experimental study.

5.5. MATERIALS & METHODS

Chemicals were bought from Sigma Aldrich unless specified otherwise. Labelled and unlabeled DNA was ordered from Integrated DNA Technologies (IDT):

S: GGGTGG GTTCACTGTCTTA TTTTT GTTCACTGTCTTA CCACCC
T: TTTTT GTAAGACAGTGAACC TTTTTTTTTTTTTTT

For fluorescence microscopy imaging, *T* was ordered with label 5'-Cy3 and *S* was ordered with

- an internal Cy5 after stem close to 3' end,
- a 5' Iowa Black® RQ (ideal for Cy5), and
- a 3' biotin-linker.

For bulk measurements, sequence *S* with the same fluorophore/quencher pair, but without biotin-linker and sequence **T** without fluorescence label were used. Upon delivery, DNA was dissolved to a stock solution of 100 μM in TE buffer and stored at -20°.

RepX was purified and cross-linked as described by the Ha Lab.[32]

Fluorescence microscopy images were acquired using an Olympus IX-81 inverted microscope equipped with an Andor Revolution XD spinning disk system. For excitation of *T*-Cy3 and *S*-Cy5, laser lines 561 nm and 640 nm were used.

Glass slides were extensively cleaned using sonication in deionized water, acetone and 1 M KOH followed by Piranha cleaning, aminosilanized and subsequently coated in biotin-PEG. Glass-based devices were assembled from coated glass slides using double-sided tape of about 70 μm height, forming channels of roughly 0.5 mm x 2.5 mm size. Sample solution could be injected with pipette tips through entry ports drilled into the top slide.

Microplate assays were performed in 384-well plates (Corning 384 Flat Bottom black polystyrene, catalog number 3575) and measured using plate readers manufactured by Tecan (infinite 200Pro) or Agilent (BioTek Synergy H1 Multimode Reader).

REFERENCES

[1] Eric Karsenti. "Self-organization in cell biology: a brief history". In: *Nature Reviews Molecular Cell Biology* 9.3 (Mar. 2008), pp. 255–262. ISSN: 1471-0072, 1471-0080. DOI: 10.1038/nrm2357. URL: https://www.nature.com/articles/nrm2357 (visited on 11/17/2023).

[2] Alan Turing. "The chemical basis of morphogenesis". In: *Philosophical Transactions of the Royal Society of London. Series B, Biological Sciences* 237.641 (Aug. 14, 1952), pp. 37–72. ISSN: 2054-0280. DOI: 10.1098/rstb.1952.0012. URL: http://www.royalsocietypublishing.org/doi/10.1098/rstb.1952.0012 (visited on 11/22/2019).

[3] François Schweisguth and Francis Corson. "Self-Organization in Pattern Formation". In: *Developmental Cell* 49.5 (June 2019), pp. 659–677. ISSN: 15345807. DOI: 10.1016/j.devcel.2019.05.019. URL: https://linkinghub.elsevier.com/retrieve/pii/S1534580719303910 (visited on 01/08/2020).

[4] J. Halatek, F. Brauns, and E. Frey. "Self-organization principles of intracellular pattern formation". In: *Philosophical Transactions of the Royal Society B: Biological Sciences* 373.1747 (May 26, 2018), p. 20170107. ISSN: 0962-8436, 1471-2970. DOI: 10.1098/rstb.2017.0107. URL: https://royalsocietypublishing.org/doi/10.1098/rstb.2017.0107 (visited on 11/22/2019).

[5] Tom Burkart et al. "Control of protein-based pattern formation via guiding cues". In: *Nature Reviews Physics* (May 16, 2022). ISSN: 2522-5820. DOI: 10.1038/s42254-022-00461-3. URL: https://www.nature.com/articles/s42254-022-00461-3 (visited on 05/25/2022).

[6] Martin Loose et al. "Spatial Regulators for Bacterial Cell Division Self-Organize into Surface Waves in Vitro". In: *Science* 320.5877 (May 9, 2008), pp. 789–792. ISSN: 0036-8075, 1095-9203. DOI: 10.1126/science.1154413. URL: https://www.science.org/doi/10.1126/science.1154413 (visited on 11/17/2021).

[7] Philipp Glock et al. "Stationary Patterns in a Two-Protein Reaction-Diffusion System". In: *ACS Synthetic Biology* 8.1 (Jan. 18, 2019), pp. 148–157. ISSN: 2161-5063, 2161-5063. DOI: 10.1021/acssynbio.8b00415. URL: https://pubs.acs.org/doi/10.1021/acssynbio.8b00415 (visited on 11/05/2021).

[8] Beatrice Ramm, Tamara Heermann, and Petra Schwille. "The E. coli MinCDE system in the regulation of protein patterns and gradients". In: *Cellular and Molecular Life Sciences* 76.21 (Nov. 2019), pp. 4245–4273. ISSN: 1420-682X, 1420-9071. DOI: 10.1007/s00018-019-03218-x. URL: http://link.springer.com/10.1007/s00018-019-03218-x (visited on 11/22/2019).

[9] Anthony G. Vecchiarelli et al. "Differential affinities of MinD and MinE to anionic phospholipid influence Min patterning dynamics *in vitro*: Flow and lipid composition effects on Min patterning". In: *Molecular Microbiology* 93.3 (Aug. 2014), pp. 453–463. ISSN: 0950382X. DOI: 10.1111/mmi.12669. URL: http://doi.wiley.com/10.1111/mmi.12669 (visited on 11/29/2019).

[10] Jonas Denk et al. “MinE conformational switching confers robustness on self-organized Min protein patterns”. In: *Proceedings of the National Academy of Sciences* 115.18 (May 1, 2018), pp. 4553–4558. ISSN: 0027-8424, 1091-6490. DOI: 10.1073/pnas.1719801115. URL: http://www.pnas.org/lookup/doi/10.1073/pnas.1719801115 (visited on 07/28/2020).

[11] Yaron Caspi and Cees Dekker. “Mapping out Min protein patterns in fully confined fluidic chambers”. In: *eLife* 5 (Nov. 25, 2016), e19271. ISSN: 2050-084X. DOI: 10.7554/eLife.19271. URL: https://elifesciences.org/articles/19271 (visited on 11/22/2019).

[12] Kiyoshi Mizuuchi and Anthony G Vecchiarelli. “Mechanistic insights of the Min oscillator via cell-free reconstitution and imaging”. In: *Physical Biology* 15.3 (Mar. 1, 2018), p. 031001. ISSN: 1478-3975. DOI: 10.1088/1478-3975/aa9e5e. URL: http://stacks.iop.org/1478-3975/15/i=3/a=031001?key=crossref.18bf29cccb7b7223b142cdbecfc43d0d (visited on 11/22/2019).

[13] Simon Kretschmer, Katja Zieske, and Petra Schwille. “Large-scale modulation of reconstituted Min protein patterns and gradients by defined mutations in MinE’s membrane targeting sequence”. In: *PLOS ONE* 12.6 (June 16, 2017). Ed. by Colin Johnson, e0179582. ISSN: 1932-6203. DOI: 10.1371/journal.pone.0179582. URL: https://dx.plos.org/10.1371/journal.pone.0179582 (visited on 05/17/2023).

[14] Simon Kretschmer et al. “Increasing MinD’s Membrane Affinity Yields Standing Wave Oscillations and Functional Gradients on Flat Membranes”. In: *ACS Synthetic Biology* 10.5 (May 21, 2021), pp. 939–949. ISSN: 2161-5063, 2161-5063. DOI: 10.1021/acssynbio.0c00604. URL: https://pubs.acs.org/doi/10.1021/acssynbio.0c00604 (visited on 07/27/2022).

[15] Pongphak Chidchob and Hanadi F Sleiman. “Recent advances in DNA nanotechnology”. In: *Current Opinion in Chemical Biology* 46 (Oct. 2018), pp. 63–70. ISSN: 13675931. DOI: 10.1016/j.cbpa.2018.04.012. URL: https://linkinghub.elsevier.com/retrieve/pii/S1367593118300231 (visited on 11/19/2023).

[16] Anton S. Zadorin et al. “Synthesis of Programmable Reaction-Diffusion Fronts Using DNA Catalyzers”. In: *Physical Review Letters* 114.6 (Feb. 9, 2015), p. 068301. ISSN: 0031-9007, 1079-7114. DOI: 10.1103/PhysRevLett.114.068301. URL: https://link.aps.org/doi/10.1103/PhysRevLett.114.068301 (visited on 11/25/2019).

[17] Philipp Glock et al. *Design of biochemical pattern forming systems from minimal motifs*. preprint. Biophysics, June 11, 2019. DOI: 10.1101/666362. URL: http://biorxiv.org/lookup/doi/10.1101/666362 (visited on 11/22/2019).

[18] Thomas E. Ouldridge et al. “DNA hybridization kinetics: zippering, internal displacement and sequence dependence”. In: *Nucleic Acids Research* 41.19 (Oct. 2013), pp. 8886–8895. ISSN: 1362-4962, 0305-1048. DOI: 10.1093/nar/gkt687. URL: https://academic.oup.com/nar/article-lookup/doi/10.1093/nar/gkt687 (visited on 01/18/2022).

[19] Jinny X. Zhang et al. “Predicting DNA hybridization kinetics from sequence”. In: *Nature Chemistry* 10.1 (Jan. 2018), pp. 91–98. ISSN: 1755-4330, 1755-4349. DOI: 10.1038/nchem.2877. URL: http://www.nature.com/articles/nchem.2877 (visited on 09/19/2022).

[20] Erica Del Grosso et al. “Dissipative DNA nanotechnology”. In: *Nature Chemistry* 14.6 (June 2022), pp. 600–613. ISSN: 1755-4330, 1755-4349. DOI: 10.1038/s41557-022-00957-6. URL: https://www.nature.com/articles/s41557-022-00957-6 (visited on 11/19/2023).

[21] Kevin Montagne et al. “Programming an *in vitro* DNA oscillator using a molecular networking strategy”. In: *Molecular Systems Biology* 7.1 (Jan. 2011), p. 466. ISSN: 1744-4292, 1744-4292. DOI: 10.1038/msb.2010.120. URL: https://onlinelibrary.wiley.com/doi/abs/10.1038/msb.2010.120 (visited on 11/22/2019).

[22] Anton S. Zadorin et al. “Synthesis and materialization of a reaction–diffusion French flag pattern”. In: *Nature Chemistry* 9.10 (Oct. 2017), pp. 990–996. ISSN: 1755-4330, 1755-4349. DOI: 10.1038/nchem.2770. URL: http://www.nature.com/articles/nchem.2770 (visited on 11/25/2019).

[23] Adrien Padirac et al. “Spatial Waves in Synthetic Biochemical Networks”. In: *Journal of the American Chemical Society* 135.39 (Oct. 2, 2013), pp. 14586–14592. ISSN: 0002-7863, 1520-5126. DOI: 10.1021/ja403584p. URL: https://pubs.acs.org/doi/10.1021/ja403584p (visited on 11/22/2019).

[24] David Soloveichik, Georg Seelig, and Erik Winfree. “DNA as a universal substrate for chemical kinetics”. In: *Proceedings of the National Academy of Sciences* 107.12 (Mar. 23, 2010), pp. 5393–5398. ISSN: 0027-8424, 1091-6490. DOI: 10.1073/pnas.0909380107. URL: https://pnas.org/doi/full/10.1073/pnas.0909380107 (visited on 03/24/2024).

[25] John Zenk et al. “Stable DNA-based reaction–diffusion patterns”. In: *RSC Advances* 7.29 (2017), pp. 18032–18040. ISSN: 2046-2069. DOI: 10.1039/C7RA00824D. URL: http://xlink.rsc.org/?DOI=C7RA00824D (visited on 01/18/2022).

[26] Niranjan Srinivas et al. “Enzyme-free nucleic acid dynamical systems”. In: *SYNTHETIC BIOLOGY* (2017), p. 11.

[27] Atsushi Miyagi et al. “High-Speed Atomic Force Microscopy Reveals the Inner Workings of the MinDE Protein Oscillator”. In: *Nano Letters* 18.1 (Jan. 10, 2018), pp. 288–296. ISSN: 1530-6984, 1530-6992. DOI: 10.1021/acs.nanolett.7b04128. URL: https://pubs.acs.org/doi/10.1021/acs.nanolett.7b04128 (visited on 06/28/2022).

[28] Tamara Heermann et al. “Local Self-Enhancement of MinD Membrane Binding in Min Protein Pattern Formation”. In: *Journal of Molecular Biology* 432.10 (May 2020), pp. 3191–3204. ISSN: 00222836. DOI: 10.1016/j.jmb.2020.03.012. URL: https://linkinghub.elsevier.com/retrieve/pii/S0022283620302333 (visited on 10/14/2021).

[29] David Yu Zhang and Georg Seelig. “Dynamic DNA nanotechnology using strand-displacement reactions”. In: *Nature Chemistry* 3.2 (Feb. 2011), pp. 103–113. ISSN: 1755-4330, 1755-4349. DOI: 10.1038/nchem.957. URL: https://www.nature.com/articles/nchem.957 (visited on 03/24/2024).

[30] Friedrich C Simmel, Bernard Yurke, and Hari R Singh. “Principles and Applications of Nucleic Acid Strand Displacement Reactions”. In: *Chem. Rev.* (2019).

[31] Basudeb Bhattacharyya and James L. Keck. “Grip it and rip it: Structural mechanisms of DNA helicase substrate binding and unwinding”. In: *Protein Science* 23.11 (Nov. 2014), pp. 1498–1507. ISSN: 0961-8368, 1469-896X. DOI: 10.1002/pro.2533. URL: https://onlinelibrary.wiley.com/doi/10.1002/pro.2533 (visited on 11/08/2023).

[32] Sinan Arslan et al. “Engineering of a superhelicase through conformational control”. In: *Science* 348.6232 (Apr. 17, 2015), pp. 344–347. ISSN: 0036-8075, 1095-9203. DOI: 10.1126/science.aaa0445. URL: https://www.science.org/doi/10.1126/science.aaa0445 (visited on 12/03/2021).

[33] Taekjip Ha et al. “Initiation and re-initiation of DNA unwinding by the Escherichia coli Rep helicase”. In: *Nature* 419.6907 (Oct. 2002), pp. 638–641. ISSN: 0028-0836, 1476-4687. DOI: 10.1038/nature01083. URL: http://www.nature.com/articles/nature01083 (visited on 01/26/2022).

[34] Sergey Korolev et al. “Major Domain Swiveling Revealed by the Crystal Structures of Complexes of E. coli Rep Helicase Bound to Single-Stranded DNA and ADP”. In: *Cell* 90.4 (Aug. 1997), pp. 635–647. ISSN: 00928674. DOI: 10.1016/S0092-8674(00)80525-5. URL: https://linkinghub.elsevier.com/retrieve/pii/S0092867400805255 (visited on 04/07/2024).

[35] Anna J. Simon et al. “Using the Population-Shift Mechanism to Rationally Introduce “Hill-type” Cooperativity into a Normally Non-Cooperative Receptor”. In: *Angewandte Chemie International Edition* 53.36 (Sept. 1, 2014), pp. 9471–9475. ISSN: 14337851. DOI: 10.1002/anie.201403777. URL: https://onlinelibrary.wiley.com/doi/10.1002/anie.201403777 (visited on 11/24/2021).

[36] J. Halatek and E. Frey. “Rethinking pattern formation in reaction–diffusion systems”. In: *Nature Physics* 14.5 (May 2018), pp. 507–514. ISSN: 1745-2473, 1745-2481. DOI: 10.1038/s41567-017-0040-5. URL: http://www.nature.com/articles/s41567-017-0040-5 (visited on 11/27/2019).

[37] Fridtjof Brauns, Jacob Halatek, and Erwin Frey. “Phase-Space Geometry of Mass-Conserving Reaction-Diffusion Dynamics”. In: *Physical Review X* 10.4 (Nov. 19, 2020), p. 041036. ISSN: 2160-3308. DOI: 10.1103/PhysRevX.10.041036. URL: https://link.aps.org/doi/10.1103/PhysRevX.10.041036 (visited on 11/17/2021).

[38] Joseph N. Zadeh et al. “NUPACK: Analysis and design of nucleic acid systems”. In: *Journal of Computational Chemistry* 32.1 (Jan. 15, 2011), pp. 170–173. ISSN: 0192-8651, 1096-987X. DOI: 10.1002/jcc.21596. URL: https://onlinelibrary.wiley.com/doi/10.1002/jcc.21596 (visited on 01/23/2024).

6

CONCLUSIONS AND OUTLOOK TO FUTURE RESEARCH

In this short final chapter, I provide a brief overview on the main outcome of 4+ years of PhD research, the context within which it was performed, and the novel conclusions that can be drawn from it.

Pattern formation has become a vast research field[1, 2, 3, 4, 5], and so has the effort to bottom-up construct synthetic cells[6, 7, 8, 9]. Min research is in many aspects situated at the intersection of these areas. However, the research presented within this thesis can primarily be considered to be a contribution to fundamental research on (Min) pattern formation.

The simplicity of the Min system makes it attractive to both experimental and theoretical researchers, and an impressive amount of work has been done on this system over the last two decades in particular. For a starting researcher, as I was in 2019, this can present itself as both impressive and discouraging. Different groups have contributed and published on the Min system over the years, yielding a considerable body of literature that can be hard to get a good overview on. Becoming part of such a research effort poses the questions of where will be the best place to start, and where to go from there.

Very broadly speaking, one can take this research into two different directions. One approach is to consider Min proteins as an already established, well-studied system and employ it as a tool in another discipline, such as synthetic cell research[10, 11, 12], biosensing or molecular transport[13, 14]. Following this bioengineering approach certainly presents a promising route for future research, and efforts are already ongoing. Another, though connected, approach is to look into ways of how to better understand the Min protein system on a fundamental level – meaning, to get a full grasp on all the details within its reaction mechanism – and in the long run, to obtain insight into (in-

tracellular) pattern formation as a whole.[4, 15] This is the approach that underlies the work presented in this thesis.

The first project that I got to work on was the study on how Min protein patterns respond to bulk flow, which constitutes chapter 3 of this thesis. Based on an idea proposed by Prof. Erwin Frey, this project relied on using flow as an external, adjustable parameter that can help to reveal underlying reaction mechanisms. Fridtjof Brauns and Jernej Rudi Finžgar looked into modeling the Min system' response to flow, while I performed *in vitro* experiments on Min surface patterns in flow channels. While we could see by eye that patterns would tend to propagate upstream for high MinE:MinD ratios and downstream for low concentration ratios, interpretation of analysis results turned out to be non-trivial. Even in the absence of flow, Min patterns would show directional tendencies, making it hard to understand what behavior was actually a response to flow and what was just local variation in alignment of patterns.

Hence, Jacob Kerssemakers and I looked for ways to (semi-)automatize analysis, and we came up with methods on image processing that performed this task for us. The outcome of this work is given in this thesis' chapter 2. All code associated with this is available online, and we hope that it can directly be useful or provide guidance for someone working on a similar image analysis task in the future.

The projects presented in chapters 4 and 5 are ongoing at the moment of this writing and might still be subject to considerable change. Chapter 4 aims to directly address the issue of discrepancies in patterns' length scales between experimental and simulation results by considering the effect of MinE membrane binding[16]. It therefore falls in the category of fundamental research work on Min pattern formation, with the simulations performed by Henrik Weyer and Mingqi Yan. The work is currently ongoing. However, as of the moment of this writing preliminary results indicate that we are on a good path to successfully addressing the length scale discrepancy and improve models to a point, where they reproduce the observed patterns' quantitative aspects as well. If this expectation holds true, this work is likely not going to be the final step, but a significant one.

Chapter 5 describes a project, which is in some aspects a mixture between the fundamental research approach and the bioengineering approach, though its goal is to study pattern formation on a general level. Regarding Min proteins very abstractly as a model system, the goal of this project is to bottom-up construct a synthetic pattern-forming system from DNA oligomers. This system should share essential features with intracellular pattern-forming systems. In particular, it should function by a mass-conserving reaction diffusion mechanism capable of producing surface patterns – such as observed for the Min system, which can be considered a "role model" for the synthetic system.

Having such a synthetic pattern-forming system available would be of great interest to both theoretical and experimental researchers working on pattern formation. Using components consisting of DNA would allow to freely modify the structure, and in doing so, tune the system's reaction kinetics. This, in turn, would allow to systematically explore the parameter space and test, how well current simulation models perform by comparing them to experiments. As this project is currently in an exploratory phase, the

work is ongoing and supported by Ching-Yee Leung and Henrik Weyer, whose simulations provide important guidance on how to tune parameters and experimental conditions to achieve surface pattern formation within this system. Future experimental work will focus on optimizing conditions and testing a range of DNA oligomer designs for their potential for surface pattern formation.

One can ask, at this point, whether the questions posed by this research line are worth pursuing. After all, it may appear that the Min system is generally quite well understood, and the basic reaction schemes have already found their way into textbooks[17]. However, as in many cases, the devil is in the detail. While the Min system is intrinsically simple and robustly accomplishes symmetry breaking in live cells, it is also known to be multistable[18] and highly sensitive towards environmental conditions[19, 20]. Therefore, drawing generalized conclusions from the collected assortment of experiments is complicated by heterogeneity in experimental methods (such as lipid bilayer preparation[21], protein purification[22], sample chamber geometry[23]) as well as analysis and interpretation of results.

Indeed, as outlined in chapters 3 and 4, there are still considerable quantitative discrepancies between *in vitro* experimental results and simulation results, strongly suggesting that more work is needed to improve the current models to a point where they can reliably predict a given experimental settings' pattern outcome. While the work presented in chapter 4 at the moment appears to be a promising contribution to solving this riddle, it is very likely not the last question posed by this system. For example, the experiments presented in chapter 3 (effect of bulk flow on Min protein) were still performed with His-tagged Min proteins, while for chapter 4 we already had protein free of such purification artifacts[22] available.

While such differences can be considered in modeling, they still make it more challenging to gain a complete (and intuitive) understanding of the system, and repetitions of formerly performed experiments would be of interest. How, for example, will stationary patterns[22] behave in microfluidic confined chambers?[23] How will they react to bulk flow?[24] New experiments have to be designed careful in a way that allows us to systematically disentangle the different experimental parameters and relate them to specific molecular mechanisms within the reaction cycle. This experimental work has to happen in close collaboration with theoretical researchers in order to improve the models we have of the system to a point where they can accurately predict the pattern occurring within a given setting. I am convinced that this goal is in reach, and that future research would benefit greatly from more data collection. Here, the focus should be on systematic (ideally automatized) parameter screening and analysis of quantitative properties, as well as open publishing of full datasets to serve as an easily accessible foundation for modeling.

However, at the same time, I would encourage interested or starting researchers to be bold and try new things on the system. While we do not understand every aspect about this system by far, we understand it reasonably well to an extent where technical applications are possible. That includes integrating Min proteins into systems such as is done in synthetic cells, but could also mean using them for a completely different purpose,

for example as a sensor for lipid membrane properties. Further, optical imaging as well as single molecule techniques keep improving, and in doing so continue to present new opportunities for research which should be taken advantage of. It would be a pity to not keep studying a system as elegantly simple, yet astonishingly versatile, as the Min system as our possibilities to do so expand.

REFERENCES

[1] Alan Turing. "The chemical basis of morphogenesis". In: *Philosophical Transactions of the Royal Society of London. Series B, Biological Sciences* 237.641 (Aug. 14, 1952), pp. 37–72. ISSN: 2054-0280. DOI: 10.1098/rstb.1952.0012. URL: http://www.royalsocietypublishing.org/doi/10.1098/rstb.1952.0012 (visited on 11/22/2019).

[2] Eric Karsenti. "Self-organization in cell biology: a brief history". In: *Nature Reviews Molecular Cell Biology* 9.3 (Mar. 2008), pp. 255–262. ISSN: 1471-0072, 1471-0080. DOI: 10.1038/nrm2357. URL: https://www.nature.com/articles/nrm2357 (visited on 11/17/2023).

[3] Philip Ball. "Forging patterns and making waves from biology to geology: a commentary on Turing (1952) 'The chemical basis of morphogenesis'". In: *Philosophical Transactions of the Royal Society B: Biological Sciences* 370.1666 (Apr. 19, 2015), p. 20140218. ISSN: 0962-8436, 1471-2970. DOI: 10.1098/rstb.2014.0218. URL: https://royalsocietypublishing.org/doi/10.1098/rstb.2014.0218 (visited on 02/22/2024).

[4] J. Halatek, F. Brauns, and E. Frey. "Self-organization principles of intracellular pattern formation". In: *Philosophical Transactions of the Royal Society B: Biological Sciences* 373.1747 (May 26, 2018), p. 20170107. ISSN: 0962-8436, 1471-2970. DOI: 10.1098/rstb.2017.0107. URL: https://royalsocietypublishing.org/doi/10.1098/rstb.2017.0107 (visited on 11/22/2019).

[5] François Schweisguth and Francis Corson. "Self-Organization in Pattern Formation". In: *Developmental Cell* 49.5 (June 2019), pp. 659–677. ISSN: 15345807. DOI: 10.1016/j.devcel.2019.05.019. URL: https://linkinghub.elsevier.com/retrieve/pii/S1534580719303910 (visited on 01/08/2020).

[6] Yaron Caspi and Cees Dekker. "Divided we stand: splitting synthetic cells for their proliferation". In: *Systems and Synthetic Biology* 8.3 (Sept. 2014), pp. 249–269. ISSN: 1872-5325, 1872-5333. DOI: 10.1007/s11693-014-9145-7. URL: http://link.springer.com/10.1007/s11693-014-9145-7 (visited on 02/25/2020).

[7] Petra Schwille. "Division in synthetic cells". In: *Emerging Topics in Life Sciences* 3.5 (Nov. 11, 2019). Ed. by Hagan Bayley, pp. 551–558. ISSN: 2397-8554, 2397-8562. DOI: 10.1042/ETLS20190023. URL: https://portlandpress.com/emergtoplifesci/article/3/5/551/220562/Division-in-synthetic-cells (visited on 07/15/2022).

[8] Alessandro Groaz et al. "Engineering spatiotemporal organization and dynamics in synthetic cells". In: *WIREs Nanomedicine and Nanobiotechnology* 13.3 (May 2021). ISSN: 1939-5116, 1939-0041. DOI: 10.1002/wnan.1685. URL: https://onlinelibrary.wiley.com/doi/10.1002/wnan.1685 (visited on 07/13/2022).

[9] Lorenzo Olivi et al. "Towards a synthetic cell cycle". In: *Nature Communications* 12.1 (Dec. 2021), p. 4531. ISSN: 2041-1723. DOI: 10.1038/s41467-021-24772-8. URL: http://www.nature.com/articles/s41467-021-24772-8 (visited on 07/21/2022).

[10] Thomas Litschel et al. “Beating Vesicles: Encapsulated Protein Oscillations Cause Dynamic Membrane Deformations”. In: *Angewandte Chemie International Edition* 57.50 (Dec. 10, 2018), pp. 16286–16290. ISSN: 14337851. DOI: 10.1002/anie.201808750. URL: http://doi.wiley.com/10.1002/anie.201808750 (visited on 11/22/2019).

[11] Elisa Godino et al. *Cell-free biogenesis of bacterial division proto-rings that can constrict liposomes*. preprint. Synthetic Biology, Mar. 30, 2020. DOI: 10.1101/2020.03.29.009639. URL: http://biorxiv.org/lookup/doi/10.1101/2020.03.29.009639 (visited on 03/31/2020).

[12] Shunshi Kohyama, Adrian Merino-Salomon, and Petra Schwille. *In vitro assembly, positioning and contraction of a division ring in minimal cells*. preprint. In Review, Feb. 17, 2022. DOI: 10.21203/rs.3.rs-1284300/v1. URL: https://www.researchsquare.com/article/rs-1284300/v1 (visited on 07/27/2022).

[13] Beatrice Ramm et al. “A diffusiophoretic mechanism for ATP-driven transport without motor proteins”. In: *Nature Physics* 17.7 (July 2021), pp. 850–858. ISSN: 1745-2473, 1745-2481. DOI: 10.1038/s41567-021-01213-3. URL: http://www.nature.com/articles/s41567-021-01213-3 (visited on 10/05/2021).

[14] Meifang Fu et al. “Mechanochemical feedback loop drives persistent motion of liposomes”. In: *Nature Physics* 19.8 (Aug. 2023), pp. 1211–1218. ISSN: 1745-2473, 1745-2481. DOI: 10.1038/s41567-023-02058-8. URL: https://www.nature.com/articles/s41567-023-02058-8 (visited on 04/16/2024).

[15] Tom Burkart et al. “Control of protein-based pattern formation via guiding cues”. In: *Nature Reviews Physics* (May 16, 2022). ISSN: 2522-5820. DOI: 10.1038/s42254-022-00461-3. URL: https://www.nature.com/articles/s42254-022-00461-3 (visited on 05/25/2022).

[16] Martin Loose et al. “Min protein patterns emerge from rapid rebinding and membrane interaction of MinE”. In: *Nature Structural & Molecular Biology* 18.5 (May 2011), pp. 577–583. ISSN: 1545-9993, 1545-9985. DOI: 10.1038/nsmb.2037. URL: http://www.nature.com/articles/nsmb.2037 (visited on 11/22/2019).

[17] Erwin Frey et al. “Protein Pattern Formation”. In: *Physics of Biological Membranes*. Ed. by Patricia Bassereau and Pierre Sens. Cham: Springer International Publishing, 2018, pp. 229–260. ISBN: 978-3-030-00628-0 978-3-030-00630-3. DOI: 10.1007/978-3-030-00630-3_10. URL: http://link.springer.com/10.1007/978-3-030-00630-3_10 (visited on 10/14/2021).

[18] Fabai Wu et al. “Multistability and dynamic transitions of intracellular Min protein patterns”. In: *Molecular Systems Biology* 12.6 (June 2016), p. 873. ISSN: 1744-4292, 1744-4292. DOI: 10.15252/msb.20156724. URL: https://www.embopress.org/doi/10.15252/msb.20156724 (visited on 10/07/2023).

[19] Kiyoshi Mizuuchi and Anthony G Vecchiarelli. “Mechanistic insights of the Min oscillator via cell-free reconstitution and imaging”. In: *Physical Biology* 15.3 (Mar. 1, 2018), p. 031001. ISSN: 1478-3975. DOI: 10.1088/1478-3975/aa9e5e. URL: http://stacks.iop.org/1478-3975/15/i=3/a=031001?key=crossref.18bf29cccb7b7223b142cdbecfc43d0d (visited on 11/22/2019).

[20] Beatrice Ramm, Tamara Heermann, and Petra Schwille. “The E. coli MinCDE system in the regulation of protein patterns and gradients”. In: *Cellular and Molecular Life Sciences* 76.21 (Nov. 2019), pp. 4245–4273. ISSN: 1420-682X, 1420-9071. DOI: 10.1007/s00018-019-03218-x. URL: http://link.springer.com/10.1007/s00018-019-03218-x (visited on 11/22/2019).

[21] Anthony G. Vecchiarelli et al. “Differential affinities of MinD and MinE to anionic phospholipid influence Min patterning dynamics *in vitro*: Flow and lipid composition effects on Min patterning”. In: *Molecular Microbiology* 93.3 (Aug. 2014), pp. 453–463. ISSN: 0950382X. DOI: 10.1111/mmi.12669. URL: http://doi.wiley.com/10.1111/mmi.12669 (visited on 11/29/2019).

[22] Philipp Glock et al. “Stationary Patterns in a Two-Protein Reaction-Diffusion System”. In: *ACS Synthetic Biology* 8.1 (Jan. 18, 2019), pp. 148–157. ISSN: 2161-5063, 2161-5063. DOI: 10.1021/acssynbio.8b00415. URL: https://pubs.acs.org/doi/10.1021/acssynbio.8b00415 (visited on 11/05/2021).

[23] Yaron Caspi and Cees Dekker. “Mapping out Min protein patterns in fully confined fluidic chambers”. In: *eLife* 5 (Nov. 25, 2016), e19271. ISSN: 2050-084X. DOI: 10.7554/eLife.19271. URL: https://elifesciences.org/articles/19271 (visited on 11/22/2019).

[24] Sabrina Meindlhumer et al. “Directing Min protein patterns with advective bulk flow”. In: *Nature Communications* 14.1 (Jan. 27, 2023), p. 450. ISSN: 2041-1723. DOI: 10.1038/s41467-023-35997-0. URL: https://www.nature.com/articles/s41467-023-35997-0 (visited on 03/25/2023).

ACKNOWLEDGEMENTS

At the end of my PhD trajectory, it is evident that a great many people have in some way supported, accompanied, guided and shaped me – more than I could ever list here. Academic research is not perfect, but it is a global effort to broaden our knowledge on the world around us, and I am happy to have contributed to it a little in these last years. Finding oneself in a life situation in which one can pursue this line of work is a privilege, for which I would like to express my gratitude to family members, friends, colleagues, supervisors and teachers who helped to get me to this point. While the following list is bound to remain incomplete, there are of course a few people whom I would like to thank here in particular.

First, I would like to sincerely thank my PhD supervisor Prof.dr. **Cees Dekker** for giving me the opportunity to work and learn under his guidance for these past few years. Cees, what continues to impress me is your sharp critical thinking and willingness to address the big questions – be it in science or beyond. You introduced pattern formation as a research topic in your lab simply because you thought it was amazing and important to study, and I am happy that I could contribute to these efforts. Thank you also for allowing all the lab outings and various social gatherings in order to create and maintain the remarkably positive and supportive group atmosphere in your lab, which I have come to greatly appreciate. I am convinced that the time in your group has given me time to grow and improve in many ways, professionally and personally, and I am grateful for that.

Importantly, I would like to express my everlasting gratitude towards my mother **Michaela Meindlhumer** and my father **Christian Meindlhumer**. Both of you have supported me my entire life and made it possible for me to receive the education without which I would not be where I am today. For that – and a lot more, of course – I would like to sincerely thank you. *Ihr habt mich den gesamten Weg über unterstützt und mir die Ausbildung ermöglicht, die mich an diesen Punkt in meinem Leben gebracht hat. Dafür – und natürlich für vieles mehr – möchte ich mich sehr bei euch bedanken.*

Who has to be credited especially is of course my husband, **Julian Hofer**. Julian, you have supported me in so many ways: Morally by having the courage to move to a foreign country with me, emotionally by standing by my side during stressful times, and even professionally by giving me tips on how to improve my coding. Living in Delft with you was a gift and a joy, and I am astonished by how much you have developed and accomplished during the time we spent here. Somehow we even managed to organize our Austrian wedding from afar while living in the Netherlands, which seems crazy in retrospect, but turned out amazing. I am looking forward to moving with you to a new place yet again, and continuing to build our life together.

Cees Dekker Lab went through quite some personnel rotation over the 4+ years that I could be part of it, and there are many (former) colleagues whose input, support and company was invaluable to both my research and to me personally. I am genuinely grateful for having gotten to know you all, including those among you who I did not get to spend a lot of time with and who therefore, might not find their names on this list. For simplicity's sake, I will address many of you from here on in alphabetical order:

Alberto Blanch Jover, thank you so much for helping me get started with the first Min protein experiments – it is fair to say I would have been quite lost in the beginning without your kind support. **Alejandro Martin Gonzalez**, to get right to the point: Thank you for being an amazing friend. Whether it's organizing a lab trip or a game night, with you on board, it is bound to turn out epic (sometimes literally). **Aleksandre Japaridze**, or Sandro, you left our office shortly after I started, but fortunately, you continued to stick around. Wish you all the best with your company and family! **Alessio Fragasso**, it was great having you in the office – genuinely enjoyed your company and of course, guitar solos. **Alex Joesaar**, thanks a lot for all your input and very insightful contributions to the DNA-pattern project, and all the best! **Allard Katan**, thank you for great conversations and support in the lab. Also, thanks for your patience while training me on the group's AFM. Say hi to your cats from me! **Anders Barth**, thanks for providing our office with some much-needed levelheadedness and calm, at least for the most part. Wish you all the best, let us know if you are around Munich! **Angeliki Goutou**, or Angel, thanks a lot for purifying the marvelous helicase and for being a lot of fun to be around. **Anthony Birnie**, thanks a lot for all the lab training and support that you gave me in the beginning. Your instructions and tips were essential to me getting those lipid bilayers done. **Ashmiani van den Berg**, your Min proteins do wonders, and so do you – hope you keep on dancing, whether you are in the lab or elsewhere! **Bert van Herck**, the future of synthetic cell research – you are going to split those vesicles one day. You joined right before a lab trip, which is quite a brave thing to do. Wish you all the best! **Brian Analikwu**, our double-movie-star, who spreads good mood (and loops) wherever he goes. As another rising star of the SMC team, it feels almost redundant, but regardless: Wish you all the best for your future! **Charu Sharma**, it amazed me how fast you picked up working with vesicles – synthetic cell research will benefit from you for sure. Glad we could get to know each other, wish you all the best! **Chenyu Wen**, it was great fun preparing Chinese food with you for the lab trip. All the best for your new position, good luck learning Swedish this time! **Eli van der Sluis**, thank you for all the support regarding proteins! *Ik dank je ook voor jouw geduld met mijn Nederlands en voor de mogelijkheid om te oefenen.* **Eva Bertosin**, I am so glad you developed an interest in patterns and joined the project with your expertise in DNA origami – thanks a lot for everything and all the best for your future research & beyond! **Jaco van der Torre**, aka the grandmaster of the lab, impressively knowledgeable and always willing to support, or simply chat (a lot). Thank you so much for helping me out with more things than I could possibly recount here! Special thanks go of course also to **Jacob Kerssemakers**, whose work on Min patterns started long before I joined, and whose experience and creativity in all matters concerning image data analysis (and way beyond) never cease to amaze. Thank you for all the help and the very memorable conversations. **Justas Ritmejeris**, never saw anyone else look that good with a blonde wig. By the end of this year, you will be the most senior PhD student in this

lab, so bear it with pride. Wish you all the best! **Martin Holub**, we started just a month after each other, and we went through the joy of cleanroom training together (before I dropped out of that). Aside from that, it was always great chatting with you when you permitted yourself a break from all the lab work. All the best for your future path, wherever it may lead you, and keep thinking ~~inside~~ out of the box! **Milos Tišma**, we started our PhD contracts merely two weeks apart and spent a lot of time together in our office. I am glad to have gotten to know you as a friend over these years, and I have no doubt the future holds many more amazing things for you to achieve. And I must admit, I will miss you playing the Sad Serbian Song. **Minco Polinder**, thanks for the ride to Groningen and opportunity to exchange experiences on wedding planning, and I wish you all the best for your future! **Nicola De Franceschi**, as you were the most experienced member of the SynCell team when I started my PhD, I really appreciate you taking the time to help me learn lots of the skills that I absolutely needed in the lab. Thanks a lot for working together, and I hope you continue to enjoy your work and life in Poland! **Nils Klughammer**, the conscience of the office, always ready to chat/discuss and help out when needed. Julian and I really enjoyed attending climate demos with you, Tanja, and of course Lola. We wish only the best to the three of you! **Paola De Magistris**, thank you very much for your kindness, I genuinely enjoyed the conversations we had over the years. Academia surely profits from someone who is as passionate about teaching as you are. Wish you only the best! **Pinyao He**, I am really happy you were part of the lab during my first two years – Julian and I certainly enjoyed having hotpot with you in Rotterdam. Looking forward to seeing you again in the future! **Rafael Bezerra De Lira**, your arrival surely started a new era of the SynCell team, and I am curious to see what else you will achieve! **Roman Barth**, the youngest among our generation of PhD students, but the most experienced within the lab nevertheless. Whether it's flow cells, Python code or cooking eggplants, you master it, and no doubt you will continue to do so in your next career steps. Wish all the best to both you and Irina! **Richard Janissen**, though I sadly failed to teach you proper Austrian dialect, you certainly taught me a trick or two when it comes to making flow cells, so thanks a lot! Sincerely wish you all the best for your future. **Theo Koenig**, somehow you keep coming back to this lab, and every time you are welcomed with open arms for a good reason! It was great having you around, and I am glad that you left with a good impression back when I gave you and some other students a lab tour. All the best for your next steps, wherever they may take you. **Shuo Wang**, though we did not get to spend a lot of time together, I was really glad you joined the lab and enjoyed talking to you about science and more! **Sonja Schmid**, you left not too long after I started, yet still we kept meeting on several occasions (sometimes unexpectedly), and I really enjoyed talking to you every single time. I am impressed by your strong dedication to science, and wish you all the best for your future! **Xin Shi**, this group really benefitted from having you around, being as kind and knowledgeable as you are, and cooking Chinese food with Chenyu and you at the lab trip surely was fun. Hope you continue to have an amazing time in Belgium, wish you all the best! **Wayne Yang**, never shy of bringing up a controversial topic for discussion, but at the same time a remarkably kind person to talk to. Julian and I are hoping for future board game sessions, be it in Switzerland or elsewhere. Until then, all the best! **Xiuqi Chen**, thanks a lot for the very helpful travel advice!

Of course, there are lots of other people outside the group within the Bionanosicence department that I got to work with or talk to over the last couple of years. Thanks a lot to Prof. Dr. **Gijsje Koenderink** as well as her former PhD student **Lennard van Buren** for early collaborative work on DynA, together with Nicola De Franceschi.
Further, thanks to all the people who provided me with training and continuous support on equipment, in particular microscopes. That includes **Michal Shemesh**, whose dedication to keeping things up and running was vital to my work these last few years.

Fortunately for us all, modern research can benefit from the possibility of international collaborations. Research on (Min protein) pattern formation is exemplary of this development, as continues to be a shared topic of interest among experimental and theoretical scientists.
The work of these recent years would not have been possible in its form without the insights provided by Prof.dr. **Erwin Frey** and his theoretical biophysics group. Prof.dr. Frey, I remember talking to you on my first visit to Delft as you happened to be in town, and being fascinated by your depth of understanding and clear way of explaining complex concepts. Thank you very much for the great exchange and collaboration we had over these years.
This gratitude extends to several current and former members of Frey Group with whom I could be in regular contact, and who shared my interest in everything related to patterns: **Fridtjof Brauns** and **Jernej Rudi Finžgar**, who were willing to go with and against the flow with us. **Henrik Weyer**, **Ching-Yee Leung** and **Laeschkir Würthner**, who were brave enough to help us tackle the challenge of creating synthetic surface patterns (and the first two of which were even brave enough to enter a lab and pick up a pipette). **Mingqi Yan** and again Henrik, who worked out an improved model of the Min system, hoping to solve the longstanding riddle of why our observations differ from their simulation results.

Last but certainly not least, I would like to thank the students that I had the opportunity to work with throughout the years: **Sofie van Dorst**, who picked up working with Min proteins faster than I could look, and did some amazing work with them. All the best for your own PhD! Next was **Viktor Gilin**, who joined me for a short student project to do some preliminary work on our DNA-pattern idea. All the best to you as well for the rest of your studies! You certainly picked an excellent supervisor for your bachelor project with Eva. Finally, **Mandy Grooters**, who will continue the work on DNA-patterns for her master project, also guided by Eva. I wish you all the patterns that we dreamed of, and thereafter all the best for your future.

CURRICULUM VITÆ

Sabrina Christina Michaela MEINDLHUMER

21-02-1995 Born in Linz, Austria.

EDUCATION

2005–2013 Secondary School
Ramsauergymnasium, Linz, Austria

2013–2016 Bachelor Studies in Technical Physics
Johannnes Kepler Universität, Linz, Austria

2016–2019 Master Studies in Biophysics
Johannnes Kepler Universität, Linz, Austria

2019-2024 **PhD in Bionanoscience**
Delft University of Technology, Delft, The Netherlands

Thesis: Spiraling towards understanding in vitro Min protein surface patterns

Promotor: Prof.dr. C. Dekker

LIST OF PUBLICATIONS

3. **N. De Franceschi, R. Barth, S. Meindlhumer, A. Fragasso, C. Dekker**, *Dynamin A as a one-component division machinery for synthetic cells*, Nature Nanotechnology **19**, 70–76 (2024).

2. **S. Meindlhumer, F. Brauns, J. Finžgar, J. Kerssemakers, C. Dekker, E. Frey**, *Directing Min protein patterns with advective bulk flow*, Nature Communications **14**, 450 (2023).

1. **S. Meindlhumer, J. Kerssemakers, C. Dekker**, *Quantitative analysis of surface wave patterns of Min proteins*, Frontiers in Physics **10**, 930811 (2022).